

---

# **Cavity Optomechanics and Optical Frequency Comb Generation with Silica Whispering-Gallery-Mode Microresonators**

**Albert Schließer**

---

Dissertation  
an der Fakultät für Physik  
der Ludwig-Maximilians-Universität  
München

vorgelegt von  
Albert Schließer  
aus München

Erstgutachter: Prof. Dr. Theodor W. Hänsch

Zweitgutachter: Prof. Dr. Jörg P. Kotthaus

Tag der mündlichen Prüfung: 21. Oktober 2009

*Meinen Eltern gewidmet.*

---

# Danke

An dieser Stelle möchte ich mich bei allen bedanken, deren Unterstützung maßgeblich für das Gelingen dieser Arbeit war.

Prof. **Theodor Hänsch** danke ich für die Betreuung der Arbeit und die Aufnahme in seiner Gruppe zu Beginn meiner Promotion. Seine Neugier und Originalität, die die Atmosphäre in der gesamten Abteilung prägen, sind eine Quelle der Motivation und Inspiration.

In dieser Abteilung war auch die *Independent Junior Research Group “Laboratory of Photonics”* von Prof. **Tobias Kippenberg** eingebettet. Als erster Doktorand in dieser Gruppe danke ich Tobias für die Gelegenheit, an der Mikroresonator-Forschung am MPQ von Anfang an mitzuwirken. Ich bin ihm auch zu Dank verpflichtet für die tollen Rahmenbedingungen, die er mit beispiellosem Elan und Organisationstalent innerhalb kürzester Zeit schuf — und die mit *Independent* wohl wesentlich treffender beschrieben sind denn mit *Junior*. Aus den ungezählten Diskussionen physikalischer Fragestellungen und Ideen aller Art, und seiner sportliche Herangehensweise an die Herausforderungen des Forschungsalltags habe ich einiges gelernt.

Ich möchte auch Prof. **Jörg Kotthaus** danken, für die Möglichkeit der Probenherstellung im Reinraum seiner Gruppe, und sein Interesse am Fortgang dieser Arbeit. Ich freue mich, dass er sich schließlich auch dazu bereit erklärt hat, das Zweitgutachten zu übernehmen.

Anfang 2006 bestand das *“Laboratory of Photonics”* noch aus zwei leeren Laborräumen. Ich hatte das Glück, zu dieser Zeit im Frequenzkammerlabor der Hänsch-Gruppe mitarbeiten zu können. Die Zusammenarbeit mit **Christoph Gohle** und **Thomas Udem** hat mein Wissen in Sachen Frequenzmetrologie und Laserspektroskopie definitiv erweitert und viel Spaß gemacht—im Labor genauso wie in der U-Bahn und im Biergarten (wo es natürlich nicht immer um Physik geht).

Und weiter: Ohne die zahlreichen Leihgaben aus dem Frequenzkammerlabor hätte das *“Laboratory of Photonics”* wohl einen schwierigeren Start gehabt am MPQ. Zusammen mit dem tatkräftigen Engagement der Master-Studenten **Aurélien Kuhn** und **Rui Ma** beim Einkauf und Aufbau der experimentellen Apparaturen konnten wir so schon nach wenigen Monaten die ersten Experimente mit Mikroresonatoren beginnen, und noch im selben Jahr die ersten Ergebnisse veröffentlichen.

**Pascal del’Haye**, der in dieser Zeit zu uns stieß, bewies dabei ein äußerst geschicktes Händchen beim Herstellen immer besserer Proben. Es hat mich

---

gefreut, dass er, und auch **Georg Anetsberger** sich nach ihrer Diplomarbeit dazu entschieden haben, bei uns weiterzumachen. Georg war mir nicht nur ein sehr angenehmer Bürokollege, er leistete auch Schlüsselbeiträge zum Verständnis der mechanischen Güten. Vielleicht folgt **Johannes Hofer**, mit dem ich jetzt an den kristallinen Resonatoren arbeite, ja ihrem Beispiel.

Mit meinen Mitstreitern **Olivier Arcizet** und **Rémi Rivière** habe ich gelernt, was es bedeutet, ein schwieriges Experiment durchzuführen. Ohne Rémis effiziente Laborarbeit und seinen durch Rückschläge aller Art unbeeindruckten Einsatz wären die kryogenen Experimente nicht gelungen. Olivier ist nicht nur ein begabter Experimentalist, sondern brachte aus Paris auch derart umfangreiches physikalisches Wissen mit, dass die Diskussionen mit ihm immer eine Bereicherung waren.

Am Forschungscampus Garching und ganz besonders am MPQ ist eine erstklassige Infrastruktur und eine Fülle von Expertenwissen konzentriert, wovon ich vielfältig profitieren konnte. Auf der wissenschaftlichen Seite möchte ich mich besonders bei **Wilhelm Zwerger**, **Ignacio Wilson-Rae**, **Janis Alnis**, **Thomas Becker** und **Ronald Holzwarth** bedanken. Auf der technischen Seite leisteten unser Elektroniker **Helmut Brückner** und die Techniker **Charly Linner** und **Wolfgang Simon** unschätzbare Hilfe beim Aufbau eines jeden neuen Experiments. Wolfgangs Fähigkeiten, die exotischsten Probleme in einer eingeschobenen halben Stunde zu lösen, grenzen zuweilen an Zauberkunst. **Achim Marx** sei für den Zugang zu dem erstklassigen Elektronenmikroskop am Walther-Meißner Institut gedankt. **Fritz Keilmann** danke ich nicht nur für wertvollen Rat und Unterstützung, sondern auch die Einladung zu den schönen Ausflügen in die Alpen. **Christina Becker**, **Ingrid Herrmann** und **Gabi Geschwendtner** sei für ihre Unterstützung in administrativen Angelegenheiten gedankt. Es ist traurig, dass ich **Rosemarie Lechner** für ihre besonders tatkräftige Hilfe nicht mehr persönlich danken kann.

Wissenschaftliches Arbeiten erfordert Ausdauer, und oft die Fähigkeit, ein Problem aus verschiedenen Richtungen anzugehen. Ohne die anregende Gesellschaft und den **Humor** meiner Kolleg(inn)en **Xiaoqing**, **Thomas**, **Max**, **Katha**, **Jens**, **Christoph**, **Birgitta**, **Andreas** und **Ali** wäre das sicher beträchtlich schwieriger gewesen. Auf keinen Fall hätte ich auch den Ausgleich durch die stets amüsanten freitäglichen Zusammenkünfte mit **Christian**, **Matthias**, **Martin**,  $\mu$  und **Simon** missen wollen.

Von meinen Freunden und meiner Familie habe ich sehr viel Unterstützung erfahren, wann immer es darauf ankam. Dafür bin ich sehr dankbar.

# Zusammenfassung

In dieser Arbeit werden nichtlineare optische Effekte in den Flüstergalleriemoden von Glas-Mikroresonatoren untersucht. Insbesondere werden optomechanische Effekte, und die Erzeugung von Frequenzkämmen studiert.

Das in einem Resonator gespeicherte optische Feld koppelt über seinen Strahlungsdruck an die mechanischen Freiheitsgrade der Resonatorwände. Im Rahmen dieser Arbeit wurden optische Mikroresonatoren entwickelt, in denen das in Flüstergalleriemoden gespeicherte Licht eine starke optomechanische Kopplung an mechanische Moden mit besonders geringer Dissipation und hoher Oszillationsfrequenz (30–120 MHz) aufweist.

Wir beobachten und analysieren den Effekt der *dynamischen Rückwirkung*, bei der der Strahlungsdruck die Bewegungsdynamik der mechanischen Mode modifiziert. Insbesondere demonstrieren wir erstmalig, wie dieser Effekt dazu benutzt werden kann, eine mechanische Mode durch Laserlicht abzukühlen. Die effektive Temperatur der mechanischen Mode wird dabei durch die Messung von Positionsfluktuationen mithilfe optischer Interferometrie bestimmt. Am Schrotrausch-Limit werden dadurch Ungenauigkeiten von  $1 \cdot 10^{-18} \text{ m}/\sqrt{\text{Hz}}$  erreicht, die unterhalb der erwarteten quantenmechanischen Nullpunktsfluktuationen der mechanischen Mode liegen.

Wir demonstrieren die Laserkühlung erstmalig auch im “aufgelösten Seitenband”-Regime, in dem die Photonenspeicherzeit wesentlich länger ist als eine mechanische Oszillationsperiode, wie es zur Grundzustandskühlung erforderlich ist. Heizmechanismen technischer Natur werden durch die Verwendung rauscharmer Laser und einer kryogenen Experimentumgebung unterdrückt. Damit wird die Okkupation der mechanischen Mode bis auf  $\langle n \rangle = 63 \pm 20$  Anregungsquanten reduziert. Es konnte auch gezeigt werden, dass die interferometrische Positionsmessung eine nahezu ideale quantenmechanische Messung darstellt, mit einem Rückwirkung-Ungenauigkeits-Produkt nahe dem Quantenlimit. Damit sind alle wesentlichen Bedingungen für die Beobachtung von Quanteneffekten in mesoskopischen Oszillatoren erfüllt.

In einer unabhängigen Serie von Experimenten wird die Kerr-Nichtlinearität in Glas-Mikroresonatoren untersucht. Durch Vierwellen-Mischen entsteht eine Kaskade von Seitenbändern zu einem Dauerstrichlaser. Die Linien dieses diskreten Spektrums überspannen mehr als 500 nm. Die relative Abweichung der Linienfrequenzen von einem äquidistanten Kamm-Spektrum wird in Präzisionsmessungen auf  $7 \cdot 10^{-18}$  beschränkt. Damit steht eine neuartige, ultrakompakte Quelle für optische Frequenzkämme mit hohen Repetitionsraten (80 GHz–1 THz) zur Verfügung, mit möglichen Anwendungen in der Astronomie und Telekommunikationstechnologie.



# Abstract

In this thesis, I report on the exploration of non-linear optical phenomena in silica whispering gallery mode (WGM) microcavities. In particular, optomechanical interactions, and the generation of optical frequency combs due to the Kerr non-linearity of silica are investigated.

Radiation pressure couples the optical field stored in a microcavity to mechanical degrees of freedom of its boundary. Our systematic survey of the mechanical modes present in silica WGM microcavities has enabled engineering devices which exhibit strong optomechanical coupling between high-quality, radio-frequency (30–120 MHz) mechanical radial-breathing modes and ultra-high finesse optical WGMs.

The finite build-up time of the intracavity field leads to complex dynamics in the optomechanical interaction. We observe and analyze the effect of *dynamical backaction*, in which the radiation-pressure force modifies the dynamics of the mechanical mode. In particular, we demonstrate for the first time, how this effect can be exploited to optically cool a mechanical mode. Quantum-noise limited optical interferometry is employed for the measurement of mechanical displacement fluctuations, from which the effective temperature of the mode is inferred. An imprecision at the level of  $1 \cdot 10^{-18} \text{ m}/\sqrt{\text{Hz}}$  is reached, below the expected quantum mechanical zero-point position fluctuations of the mechanical mode.

For the first time, we demonstrate laser cooling also in the “resolved-sideband regime”, in which the optical photon storage time exceeds the mechanical oscillation period, as required for ground-state cooling. Technical sources of heating are eliminated by using low-noise lasers, a  $^4\text{He}$ -cryogenic environment for the experiment and suppressing laser absorption. Occupations down to  $\langle n \rangle = 63 \pm 20$  mechanical excitation quanta are achieved in this manner.

Simultaneously, we are able to assess the perturbation of the mechanical mode due to the process of measurement (measurement backaction). The optical techniques employed here are shown to operate in a near-ideal manner according to the principles of Quantum Measurement, displaying a backaction-imprecision product close to the quantum limit.

In an independent set of experiments, we show that the high intensities circulating in silica WGM microcavities give rise to strong optical four-wave mixing due to the material’s Kerr nonlinearity. Starting from a continuous-wave pump laser, broad, discrete optical spectra are formed by a cascade of optical sidebands to the pump. These “comb” spectra span more than 500 nm, and consist of lines spaced roughly by the cavity’s free spectral range.

An optical frequency comb based on a mode-locked laser is used as a reference to determine the homogeneity of the microcavity comb lines’ spacing in the frequency domain. The microcavity comb lines are found to be

---

equidistant at a relative level of  $7 \cdot 10^{-18}$ , in spite of the presence of cavity dispersion. We have therefore demonstrated a novel, ultracompact source of optical frequency combs with applications in astronomy and telecommunication technology.

# List of publications

## Peer-reviewed journal articles

- [1] A. Schliesser, P. Del’Haye, N. Nooshi, K.J. Vahala, and T. Kippenberg. Radiation pressure cooling of a micromechanical oscillator using dynamical backaction. *Physical Review Letters*, 97:243905, 2006.
- [2] A. Schliesser, C. Gohle, T. Udem, and T. W. Hänsch. Complete characterization of a broadband high-finesse cavity using an optical frequency comb. *Optics Express*, 14(13):5975–5983, 2006.
- [3] P. Del’Haye, A. Schliesser, O. Arcizet, T. Wilken, R. Holzwarth, and T. Kippenberg. Optical frequency comb generation from a monolithic microresonator. *Nature*, 450:1214–1217, 2007.
- [4] C. Gohle, B. Stein, A. Schliesser, T. Udem, and T. W. Hänsch. Frequency Comb Vernier Spectroscopy for Broadband, High-Resolution, High-Sensitivity Absorption and Dispersion spectra. *Physical Review Letters*, 99:263902, 2007.
- [5] R. Ma, A. Schliesser, P. Del’Haye, A. Dabirian, G. Anetsberger, and T. Kippenberg. Radiation-pressure-driven vibrational modes in ultrahigh-Q silica microspheres. *Optics Letters*, 32:2200–2202, 2007.
- [6] G. Anetsberger, R. Rivière, A. Schliesser, O. Arcizet, and T. J. Kippenberg. Ultralow-dissipation optomechanical resonators on a chip. *Nature Photonics*, 2:627–633, 2008.
- [7] P. Del’Haye, O. Arcizet, A. Schliesser, R. Holzwarth, and T. J. Kippenberg. Full stabilization of a microresonator-based optical frequency comb. *Physical Review Letters*, 101:053903, 2008.
- [8] A. Schliesser, R. Rivière, G. Anetsberger, O. Arcizet, and T. Kippenberg. Resolved-sideband cooling of a micromechanical oscillator. *Nature Physics*, 4:415–419, 2008.

- [9] A. Schliesser, G. Anetsberger, R. Rivière, O. Arcizet, and T. J. Kippenberg. High-sensitivity monitoring of micromechanical vibration using optical whispering gallery mode resonators. *New Journal of Physics*, 10:095015, 2008.
- [10] A. Schliesser, O. Arcizet, R. Rivière, G. Anetsberger, and T. Kippenberg. Resolved-sideband cooling and position measurement of a micromechanical oscillator close to the Heisenberg uncertainty limit. *Nature Physics*, 5:509–514, 2009.
- [11] O. Arcizet, R. Rivière, A. Schliesser, G. Anetsberger, and T. J. Kippenberg. Cryogenic properties of optomechanical silica microcavities. *Physical Review A*, 80:021803(R), 2009.
- [12] G. Anetsberger, O. Arcizet, Q. P. Unterreithmeier, R. Rivière, A. Schliesser, E. M. Weig, J. P. Kotthaus, and T. J. Kippenberg. Near-field cavity optomechanics with nanomechanical oscillators. *Nature Physics*, accepted, 2009.

## Book chapters

- [13] O. Arcizet, A. Schliesser, P. Del’Haye, R. Holzwarth, and T. J. Kippenberg. Optical frequency comb generation in monolithic microresonators. In A. Matsko, editor, *Practical applications of microresonators in optics and photonics*, chapter 11, pages 483–506. CRC press, 2009.
- [14] A. Schliesser and T. Kippenberg. Cavity optomechanics with silica microresonators. In E. Arimondo, P. Berman, and C. C. Lin, editors, *Advances in atomic, molecular and optical physics*, volume 58. Elsevier Academic Press, 2010 (in preparation).

## Patent applications

- [15] C. Gohle, A. Schliesser, and T. W. Hänsch. Method and device for optical Vernier spectroscopy. European (EP 06026763) and US (US 12/520577) patent applications, 2007.
- [16] P. Del’Haye, T. Kippenberg, and A. Schliesser. Method and apparatus for optical frequency comb generation using a monolithic microresonator. European (EP 07009067) and US (US 60.916045) patent applications, 2007.

# Contents

|  |            |
|--|------------|
| <b>Danke</b>   | <b>iii</b> |
| <b>Zusammenfassung</b>   | <b>v</b>   |
| <b>Abstract</b>  | <b>vii</b> |
| <b>List of publications</b>  | <b>ix</b>  |
| <b>1 Silica microresonators: versatile vehicles for Quantum Optics</b> | <b>1</b>   |
| 1.1 Introduction . . . . .   | 1          |
| 1.2 Properties of optical whispering gallery modes . . . . .           | 2          |
| 1.2.1 Mode shapes and resonance frequencies . . . . .                  | 2          |
| 1.2.2 Optical losses . . . . .   | 5          |
| 1.3 Fabrication of silica microtoroids . . . . .                       | 7          |
| 1.3.1 Photolithography and silica wet etch . . . . .                   | 7          |
| 1.3.2 Silicon dry etch . . . . .                                       | 7          |
| 1.3.3 Laser reflow . . . . .   | 9          |
| 1.4 Coupling to whispering gallery mode resonators . . . . .           | 10         |
| 1.4.1 Fiber tapers . . . . .   | 10         |
| 1.4.2 Theoretical description of coupling . . . . .                    | 12         |
| 1.5 Optical nonlinearities . . . . .                                   | 18         |
| 1.5.1 Thermal nonlinearity . . . . .                                   | 19         |
| 1.5.2 Raman nonlinearity . . . . .                                     | 23         |
| 1.5.3 Kerr nonlinearity . . . . .                                      | 24         |
| <b>2 Cavity optomechanics</b>  | <b>25</b>  |
| 2.1 Introduction . . . . .   | 25         |
| 2.2 Theory of optomechanical interactions . . . . .                    | 31         |
| 2.2.1 Classical description and elementary phenomena . . . . .         | 31         |
| 2.2.2 Formal framework: quantum Langevin equations . . . . .           | 39         |
| 2.3 Silica WGM resonators as optomechanical systems . . . . .          | 41         |
| 2.3.1 Optical properties of WGM microresonators . . . . .              | 42         |

## CONTENTS

---

|          |  |            |
|----------|--|------------|
| 2.3.2    | Mechanical properties of WGM silica microresonators                            | 43         |
| 2.3.3    | Optomechanical coupling . . . . .  | 57         |
| 2.4      | Ultrahigh-sensitivity interferometric motion transduction . . .                | 64         |
| 2.4.1    | Theoretical limits in displacement sensing . . . . .                           | 64         |
| 2.4.2    | Experimental techniques . . . . .  | 69         |
| 2.4.3    | Observation and analysis of quantum and thermal noise                          | 75         |
| 2.5      | Observation of dynamical backaction . . . . .                                  | 77         |
| 2.5.1    | Optical spring and optical damping . . . . .                                   | 78         |
| 2.5.2    | Cooling by dynamical backaction . . . . .                                      | 81         |
| 2.5.3    | Radiation pressure versus thermal effects . . . . .                            | 83         |
| 2.6      | Resolved-sideband cooling . . . . .  | 87         |
| 2.6.1    | Ground state cooling: the atomic physics case . . . . .                        | 88         |
| 2.6.2    | Limitations of radiation-pressure cooling using dynamical backaction . . . . . | 90         |
| 2.6.3    | Resolved-sideband cooling of a silica microtoroid . . .                        | 93         |
| 2.6.4    | Direct sideband spectroscopy . . . . .   | 99         |
| 2.7      | Approaching the quantum ground state . . . . .                                 | 101        |
| 2.7.1    | Implementation . . . . .   | 102        |
| 2.7.2    | Cooling towards the quantum ground state . . . . .                             | 112        |
| 2.7.3    | Assessing measurement backaction . . . . .                                     | 114        |
| 2.8      | Conclusion . . . . .   | 116        |
| 2.9      | Outlook . . . . .  | 119        |
| <b>3</b> | <b>Generation of frequency combs in silica microresonators</b>                 | <b>125</b> |
| 3.1      | Introduction . . . . .   | 125        |
| 3.2      | Physics of the comb generation process . . . . .                               | 127        |
| 3.3      | Verification of the comb components' equidistance . . . . .                    | 129        |
| 3.4      | Dispersion in toroidal microresonators . . . . .                               | 133        |
| 3.5      | Conclusion . . . . .   | 134        |
| <b>A</b> | <b>Constants, symbols and relations</b>  | <b>137</b> |
| A.1      | Silica material constants . . . . .  | 137        |
| A.2      | Table of symbols . . . . .   | 138        |
| A.3      | Frequently used relations . . . . .  | 139        |
| <b>B</b> | <b>Calculations</b>  | <b>141</b> |
| B.1      | Integrating displacement spectra . . . . .                                     | 141        |
| B.2      | Noise transfer of a lossy cavity . . . . .                                     | 143        |
| <b>C</b> | <b>Useful experimental techniques</b>  | <b>147</b> |
| C.1      | Fiber loop cavity . . . . .  | 147        |
| C.2      | Locking of the cooling laser . . . . .   | 149        |
|          | <b>Bibliography</b>  | <b>151</b> |

# Chapter 1

## Silica microresonators: versatile vehicles for Quantum Optics

### 1.1 Introduction

For many years, whispering gallery modes in silica microspheres, created by melting an optical fiber using intense mid-infrared laser radiation or a hydrogen torch, have been appreciated in the community of Quantum Optics for their extraordinarily high optical quality factors exceeding  $10^9$  and a simultaneously microscopic mode volume [17–19], both of which are all-important figures of merit for studies of non-linear optics [17, 20, 21], low-threshold lasers [20, 22–24], cavity quantum electrodynamics [25–27], or biophysical applications [28, 29]. However, these devices were not amenable to fabrication techniques developed in microelectronics, which can provide parallel, precisely reproducible processing of many geometries, and potential integration with other electrical or micromechanical functionality.

In an effort to combine the ultrahigh quality factors possible in silica whispering gallery mode resonators, and a chip-based platform, the group of Prof. Kerry Vahala at the California Institute of Technology developed a process in which the preform for the resonator is lithographically defined into a silica layer on top of a silicon wafer. The result of this development—the invention of silica microtoroids [30–32]—has proven to be a most versatile platform for experiments in Quantum Optics.

This chapter gives an elementary introduction to silica microresonators (both spheres and toroids) used in this work. After introducing elementary concepts required to describe the properties of WGMs in section 1.2, section 1.3 summarizes the fabrication process of silica microtoroids as it was carried out in the cleanroom of Prof. Kotthaus’ group at Ludwig-Maximilians-Universität, and in our labs at the Max-Planck-Institute of Quantum Optics (MPQ). In section 1.4 the tapered-fiber coupling technique is introduced

## **1. Silica microresonators: versatile vehicles for Quantum Optics**

both theoretically and experimentally, and the linear optical properties of fiber-coupled microtoroids produced in this work are shown. Finally, section 1.5 reviews the basic optical non-linear effects observed in the fabricated resonators.

### **1.2 Properties of optical whispering gallery modes**

Mie's theory [33] of light scattering from spherical dielectric particles predicts sharp resonances for a number of optical wavelengths. They are due to resonant optical modes within the spheres, in which the light orbits closely to the sphere's surface. In a simplified picture, light rays within the sphere, incident on the dielectric-air interface under a shallow angle, can be thought to repetitively bounce off the surface due to total internal reflection. If an integer multiple of the light's wavelength matches the (effective) pathlength along the circumference, scattering is enhanced. For these modes, the term "whispering gallery modes" (WGMs) was coined by an analogy to an acoustic phenomenon studied by Lord Rayleigh [34]: In the gallery of the 32-m diameter dome of St. Paul's cathedral in London, a word whispered against the stone wall can be clearly conceived at the opposite side of the gallery. Rayleigh explained this phenomenon by the fact that sound waves travel close to the wall around the circumference of the dome.

In this work, silica WGM resonators as shown in figure 1.1 are used. Compared to earlier studies with liquid droplets, silica resonators allow studying a single localized resonator for extended amounts of time. Most of the studies presented in this work were done with silica microtoroids. However, due to their higher symmetry, spheres are more amenable to some of the theoretical analysis to follow in this section. For moderate major/minor diameter ratios, toroids deviate only slightly from the discussed predictions. For rigorous discussion of the toroids' properties, it is necessary to resort to numerics or perturbation theory [35–41].

#### **1.2.1 Mode shapes and resonance frequencies**

To determine the optical resonance modes of a dielectric sphere of radius  $R$  and refractive index  $n$ , the vectorial Helmholtz equation

$$\Delta \vec{E}(\vec{r}) + k(r)^2 \cdot \vec{E}(\vec{r}) = 0 \quad (1.1)$$

and  $\vec{\nabla} \cdot \vec{E}(\vec{r}) = 0$  must be fulfilled, where  $\vec{E}(\vec{r})$  is the electric field, and  $k$  its wavenumber, with  $k(r) = nk_0$  inside the sphere and  $k(r) = k_0$  outside the sphere. For a homogenous medium, the solutions for the field are well known, and can be analytically calculated using Debye's potentials [42]. For a discussion at a greater level of detail, see for example references [43, 44]. In short, two classes of solutions, TE-modes and TM-modes can be derived

## 1.2 Properties of optical whispering gallery modes

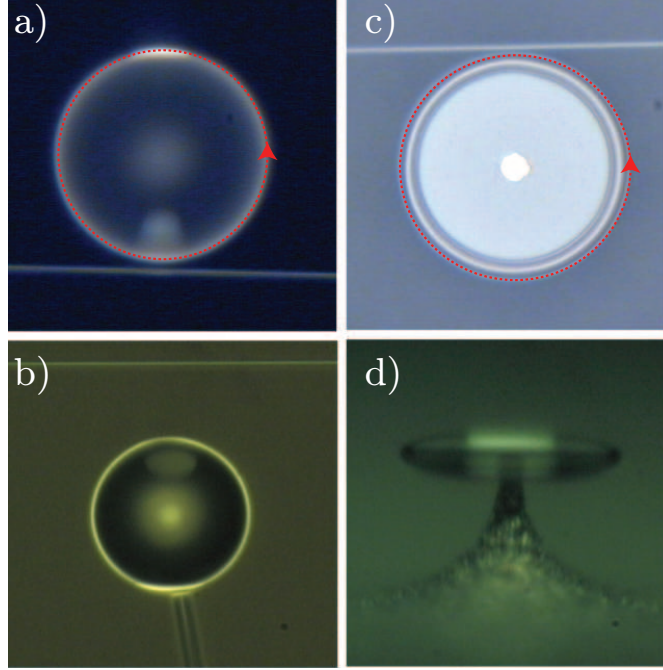


Figure 1.1: Whispering gallery mode resonators used in this work. The light orbits along the circumference of a silica microsphere (a), top view, b), side view) or silica microtoroid (c), top view, d), side view) as indicated by the dotted red arrow in the top views (about  $100 \mu\text{m} \times 100 \mu\text{m}$ ). The thin line is the silica taper used for coupling, as described in section 1.4.

from the scalar Helmholtz equation which separates into a radial and an orthoradial equation, and the corresponding fields read

$$\vec{E}_{\ell,m}^{\text{TE}}(r, \theta, \varphi) = E_0 \frac{f_\ell(r)}{k_0 r} \vec{Y}_\ell^m(\theta, \varphi) \quad (1.2)$$

$$\vec{B}_{\ell,m}^{\text{TE}}(r, \theta, \varphi) = -\frac{i}{ck_0} \vec{\nabla} \times \vec{E}_{\ell,m}^{\text{TE}}(r, \theta, \varphi) \quad (1.3)$$

and

$$\vec{E}_{\ell,m}^{\text{TM}}(r, \theta, \varphi) = -\frac{i}{ck_0 n^2} \vec{\nabla} \times \vec{B}_{\ell,m}^{\text{TM}}(r, \theta, \varphi) \quad (1.4)$$

$$\vec{B}_{\ell,m}^{\text{TM}}(r, \theta, \varphi) = -\frac{iE_0}{c} \frac{f_\ell(r)}{k_0 r} \vec{Y}_\ell^m(\theta, \varphi), \quad (1.5)$$

where  $\vec{Y}_\ell^m(\theta, \varphi)$  is the vector spherical harmonic

$$\vec{Y}_\ell^m(\theta, \varphi) = \frac{1}{\sqrt{\ell(\ell+1)}} \vec{\nabla} Y_\ell^m(\theta, \varphi) \times \vec{r} \quad (1.6)$$

## 1. Silica microresonators: versatile vehicles for Quantum Optics

---

derived from the standard scalar spherical harmonic functions,

$$Y_\ell^m(\theta, \varphi) = \sqrt{\frac{2\ell + 1}{4\pi} \frac{(\ell - m)!}{(\ell + m)!}} P_\ell^m(\cos(\theta)) e^{im\varphi}, \quad (1.7)$$

with the associated Legendre functions  $P_\ell^m$ . The radial dependence is essentially described by the function  $f_\ell(r)$ , the solution of the Riccati-Bessel equation

$$f_\ell(r) = \begin{cases} nk_0 r j_\ell(nk_0 r) & = \sqrt{\frac{\pi nk_0 r}{2}} J_{\ell+1/2}(nk_0 r) & \text{for } r < R \\ \alpha k_0 r h_\ell(k_0 r) & = \alpha \sqrt{\frac{\pi k_0 r}{2}} H_{\ell+1/2}(k_0 r) & \text{for } r > R \end{cases} \quad (1.8)$$

where  $j_\ell$  and  $h_\ell$  ( $J_\ell$  and  $H_\ell$ ) are the spherical (cylindrical) Bessel and Hankel functions of the first kind, respectively and  $\alpha$  is a real constant.

The continuity conditions of the fields at the boundary require

$$nk_0 R j_\ell(nk_0 R) = \alpha k_0 R h_\ell(k_0 R) \quad (1.9)$$

$$n^s [nk_0 R j_\ell(nk_0 R)]' = \alpha [k_0 R h_\ell(k_0 R)]' \quad (1.10)$$

where the prime denotes the derivative of the function with respect to the argument ( $nk_0 R$  on the left-hand-side,  $k_0 R$  on the right-hand side) and  $s = +1$  for TE-modes and  $s = -1$  for TM-modes. These characteristic equations not only determine the constant  $\alpha$ , but also the resonant wavenumbers  $k_0$  and thus resonance frequencies  $\omega_c = ck_0$  of the WGM.

For each index  $\ell$ , equation (1.10) supports an infinite number of solutions due to the oscillatory nature of the Bessel and Hankel functions. These solutions may be enumerated with an index  $q$ . As it determines the number of nodes of the electric field within the sphere, it is often referred to as the radial mode number, in contrast to the polar mode number  $\ell$  and the azimuthal mode number  $m \in \{-\ell, \dots, +\ell\}$ . The modes which are usually referred to as whispering gallery modes are modes with lowest  $q$  (few, or in the largest part of the literature, no node within the sphere), and high  $\ell$ , with  $|m| \sim \ell$ . We emphasize that for a perfect sphere, the resonance frequency of the WGM is independent of  $m$ , as the characteristic equation is independent of  $m$ . In practice, residual eccentricity however lifts this degeneracy. In this case, only the counterpropagating modes  $+m$  and  $-m$  remain degenerate. Note that the TE and TM modes are physically distinct in that for TE modes, the electric field points essentially in polar direction (along the unit vector  $\vec{e}_\theta$ ), and the magnetic field essentially in radial direction (along the unit vector  $\vec{e}_r$ ), and vice versa for TM modes. The mode shapes of the most important WGMs in a sphere have been mapped in beautiful experiments with a near-field probe [45, 46].

For spheres, a number of useful approximations in the experimentally relevant limit of high  $\ell$  have been developed [44]. This can also be used to

## 1.2 Properties of optical whispering gallery modes

---

obtain approximative solutions to the characteristic equations, to derive the resonance frequencies of WGMs [38,47]. In this case, the resonance frequency  $\nu_\ell$  of the fundamental mode with index  $\ell$  is approximately given by

$$\nu_\ell = \frac{c}{2\pi n R} \left( \ell + 1/2 + \eta_1 \left( \frac{\ell + 1/2}{2} \right)^{1/3} + \dots \right), \quad (1.11)$$

where  $c$  is vacuum speed of light,  $n$  the refractive index,  $R$  the cavity radius and  $-\eta_1$  the first zero of the Airy function ( $\eta_1 \approx 2.34$ ).

Toroidal geometries, due to their reduced symmetry, are not amenable to a closed-form analytical solution. However, both numerical simulation using finite-element methods [35,36,39,40,48] and a perturbative analytical approach [38,39] have been successfully used to derive the resonance frequencies and mode shapes of toroids. For moderate inverse aspect ratios (ratio of minor to major diameter) and minor diameters of several optical wavelengths, toroids support fundamental modes with no nodes in radial and polar direction, similar to the fundamental modes with  $|m| = \ell$  observed in spheres. In this regime, toroids also exhibit quasi-TE and quasi-TM modes. In contrast to spheres, however, the number of modes with nodes in the polar direction is vastly reduced, which leads to a sparse resonance spectrum. For small minor diameters of only a few wavelengths, the toroidal modes experience a strong transverse confinement similar to a fiber taper, which alters both resonance frequencies and mode volumes dramatically from the situation of a sphere [35,36,39].

### 1.2.2 Optical losses

A perfect optical resonator would store light for infinite amounts of time. Due to different loss mechanisms, the optical energy stored in a WGM decays over a timescale  $\tau$  or, alternatively at a rate

$$\kappa = 1/\tau. \quad (1.12)$$

The storage time  $\tau$  is often expressed in the form of the resonator's *quality factor*, a crucial figure of merit in many applications of optical cavities, for example as a laser cavity, for experiments in cavity quantum-electrodynamics or cavity optomechanics. It is defined by comparing the photon storage time  $\tau$  with the oscillation period of the field in the cavity

$$Q \equiv \tau \omega_c = \omega_c / \kappa \quad (1.13)$$

where  $\omega_c$  is the optical resonance frequency of the cavity.

For silica microresonators, there are several sources of optical loss, all of which reduce the cavity photon storage time  $\tau$ . In particular, optical absorption of the silica material, scattering in the bulk or at surface inhomogeneities, absorption by surface contaminants and radiative loss may reduce

## 1. Silica microresonators: versatile vehicles for Quantum Optics

the cavity storage time. In addition, intentional coupling to a propagating mode using, for example, a fiber taper as described below, leads to an additional reduction of storage time. Usually these losses are quantified by rates  $\tau_{\text{mat}}^{-1}$ ,  $\tau_{\text{sca}}^{-1}$ ,  $\tau_{\text{con}}^{-1}$ ,  $\tau_{\text{rad}}^{-1}$  and  $\tau_{\text{ex}}^{-1}$ , respectively, and the total loss rate is given by

$$\kappa = \tau^{-1} = \tau_{\text{mat}}^{-1} + \tau_{\text{sca}}^{-1} + \tau_{\text{con}}^{-1} + \tau_{\text{rad}}^{-1} + \tau_{\text{ex}}^{-1}. \quad (1.14)$$

The losses intrinsic to the resonator are often summarized to an intrinsic loss rate

$$\tau_0^{-1} = \tau_{\text{mat}}^{-1} + \tau_{\text{sca}}^{-1} + \tau_{\text{con}}^{-1} + \tau_{\text{rad}}^{-1}. \quad (1.15)$$

and an intrinsic quality factor is defined with the corresponding contributions

$$Q_0^{-1} = (\omega_c \tau_0)^{-1} = Q_{\text{mat}}^{-1} + Q_{\text{sca}}^{-1} + Q_{\text{con}}^{-1} + Q_{\text{rad}}^{-1}. \quad (1.16)$$

Losses in ultraclean silica at visible and near-infrared wavelengths are very low. A material-limited quality factor, given simply by  $Q_{\text{mat}} = 2\pi n/\alpha\lambda$ , where  $\alpha$  is the absorption coefficient with contributions from both absorption and Rayleigh scattering, as high as  $\sim 10^{10}$  at 633 nm has been predicted, and values close to this limit have been observed [49]. For longer wavelengths, silica absorption is even weaker, enabling  $Q_{\text{mat}}$  of  $10^{11}$  and more [50].

Radiation loss is due to insufficient light confinement by the curved surface of the resonator. For the resonators used in this (and most other) work, this loss mechanism is typically negligible. For example, for spheres with diameters in excess of  $20 \mu\text{m}$ , and toroids with major and minor diameters of  $60 \mu\text{m}$  and  $2 \mu\text{m}$ , respectively, the radiative losses alone would allow  $Q_{\text{rad}} > 10^{11}$  in the visible and near-infrared wavelength range [35, 39].

Another possible source of loss is scattering of light at residual surface inhomogeneities [50]. During the reflow process, surface tension renders the boundary of spheres or toroids nearly atomically smooth, however it has been shown that redeposition of evaporated silica can lead to sub-wavelength surface defects [36]. The surface-scattering limited quality factor is roughly  $Q_{\text{sca}} \propto \lambda^3/\sigma^2 B^2$ , where  $\sigma$  is the root-mean-square surface roughness and  $B$  the correlation length, which were measured to amount to 2 nm and 5 nm, respectively, in a typical sphere [19]. The exact losses induced by such roughness critically depend on the light intensity at the surface compared to the total energy stored in the mode. Silica microtoroids with their small mode volume have been observed to be scattering-loss limited at quality factors of a few hundred million [51], while in silica spheres of larger diameter (e.g.  $750 \mu\text{m}$ ) quality factors up to  $8 \cdot 10^9$  were reported [49], close to the estimated limit by surface scattering  $Q_{\text{sca}}$  [50].

As most experiments are conducted under ambient conditions, a very important loss contribution comes from chemically adsorbed water at the surface of the highly hygroscopic silica [19, 49, 51]. In particular for near-infrared wavelengths close to  $1.5 \mu\text{m}$ , where water absorption is strong, even a monolayer of water molecules at the surface can lead to significant losses,

### 1.3 Fabrication of silica microtoroids

---

leading to maximum quality factors of about  $3 \cdot 10^8$  for a  $60 \mu\text{m}$  sphere [51]. Degradation of  $Q_{\text{con}}$  has been observed to occur on a timescale of about 100 s and partial recovery using a  $400^\circ\text{C}$ -bakeout was demonstrated [49].

### 1.3 Fabrication of silica microtoroids

In this section, the standard process to fabricate silica microtoroidal WGM resonators, as implemented at Ludwig-Maximilians-Universität and the Max-Planck-Institute of Quantum Optics is described.

#### 1.3.1 Photolithography and silica wet etch

The starting material are undoped (resistivity  $> 0.2 \Omega\text{m}$ ) silicon wafers. On the wafers' (100)-surface a silicon oxide with a thickness of 1 to  $3 \mu\text{m}$  has been thermally grown, either by wet or dry oxidation. We obtained the wet oxidized wafers from Virginia Semiconductor, while the dry oxidized samples were generously provided by the semiconductor laboratory of the Max-Planck Society (HLL, Munich). Using standard UV lithography techniques implemented with a Karl Süss MJB 3 mask aligner, arrays of circular pads with diameters ranging from 20 to  $200 \mu\text{m}$  are transferred to a positive photoresist (Shipley S-1813) spun on the  $\text{SiO}_2$  surface. After hardening, these resist pads serve as etching mask in the subsequent step, in which all uncovered  $\text{SiO}_2$  is etched away using a buffered oxide etchant containing hydrofluoric acid in the reaction



Only the silica protected by the photoresist remains on the Si surface. After chemical removal of the resist, the wafer carries arrays of circular silica pads. An example of such a pad is shown in figure 1.2. Note that the wedged rim results from an isotropic underetch of the resist pad by the hydrofluoric acid.

The etched wafers are (protected against silicon spalls by an auxiliary resist layer) cleaved into pieces of ca.  $7 \text{mm} \times 25 \text{mm}$  containing 35 silica pads each. The auxiliary resist is finally removed and the chips are thoroughly cleaned, one by one, with acetone, isopropanol and deionized water. Optionally, the chips can be cleaned in addition using 'Piranha solution' (i.e. concentrated sulfuric acid and hydrogen peroxide) or an oxygen plasma to remove all organic contaminants remaining from the lithographic process.

#### 1.3.2 Silicon dry etch

For the confinement of light in the silica pads, the silicon substrate beneath it must be at least partly removed in order to ensure a low-refractive index surrounding to the part of the silica structure trapping the light. To this end, an etching technique is employed, which etches silicon highly selectively, i.e.

## 1. Silica microresonators: versatile vehicles for Quantum Optics

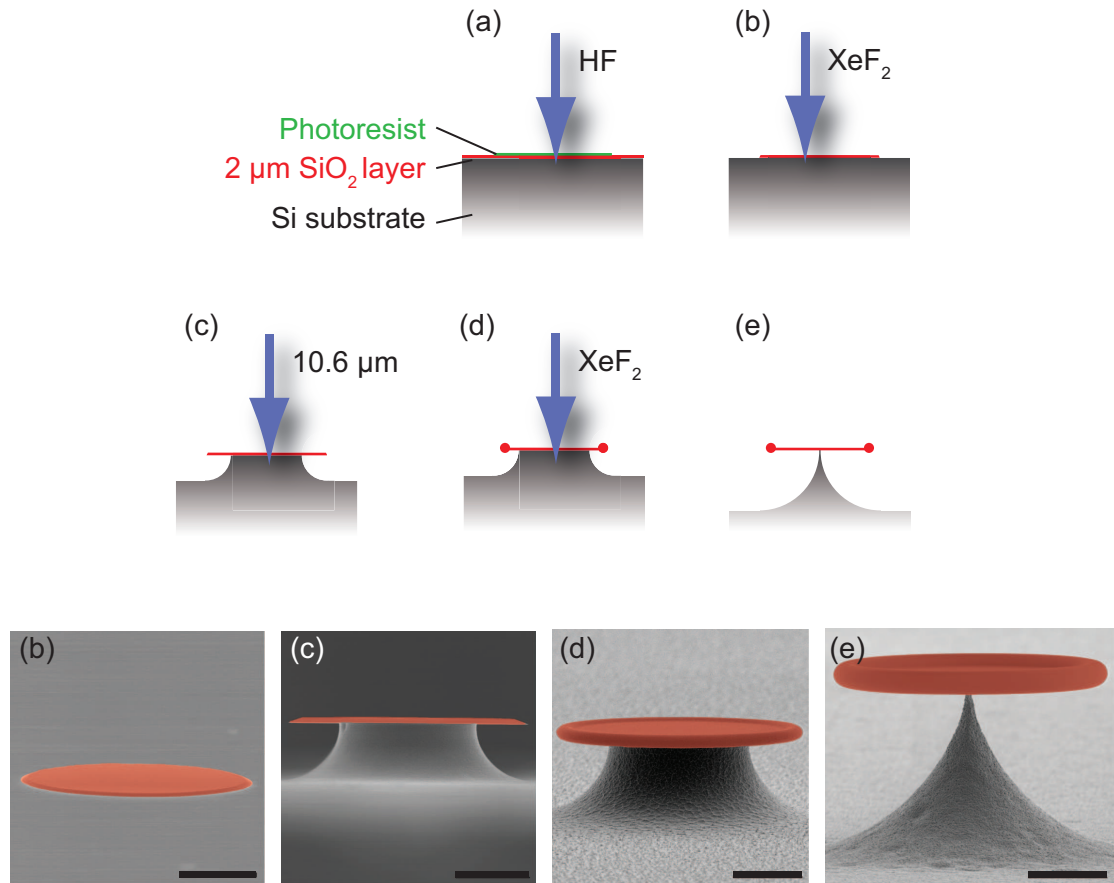
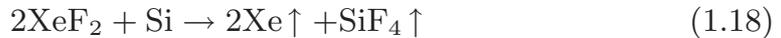


*Figure 1.2:* Fabrication of silica microtoroids (see text for details). (a) Using standard photolithography, disks are defined on a silicon wafer carrying a thin (1-3  $\mu\text{m}$ ) layer of native oxide. The disks are transferred into the oxide by etching with buffered HF solution. (b) After the resist is removed, the silica disks are underetched using gaseous  $\text{XeF}_2$ . It etches silicon selectively and isotropically, leaving a silica disk supported by a rotationally symmetric silicon pillar. (c) Reflow with a  $\text{CO}_2$  laser beam melts the free-standing part of the silica disk, and a toroidal rim is formed due to surface tension. The pillar serves as a preform in this process, stopping the melting process due to its excellent heat conductivity. (d) If desired, a second etch with  $\text{XeF}_2$  reduces the pillar diameter further, leaving only a needle support of the silica structure. Bottom panels show scanning-electron micrographs during various steps in the fabrication process (different samples). Silica structures are marked with red false-coloring (scale bars are 20  $\mu\text{m}$ ).

### 1.3 Fabrication of silica microtoroids

about 1000-times faster than silica, and isotropically. This technique [52] is based on a surface reaction of fluor with silicon,



which proceeds via (i) non-dissociative adsorption of gaseous  $\text{XeF}_2$  on the Si surface, (ii) dissociation of the adsorbate, (iii) reaction between adsorbed F atoms and the Si surface, and (iv) desorption of the volatile products into the gas phase.

In our lab, this reaction is implemented using an apparatus similar to the one described in ref. [53]. Using a simple computer-controlled vacuum system, the samples are subjected to repeated “pulses” of  $\text{XeF}_2$  gas sublimated from a reservoir. The pressure of the gas in the etching chamber and the duration of one pulse can be set by the control program, typical values are 400 Pa and 60 s. The etching rate is approximately constant, depends however on the total area of the chip(s) etched in one run. A typical single-chip order of magnitude is  $\sim 1.5 \mu\text{m}$  per etching pulse with the parameters described above. The resulting disk structures can themselves already support WGMs with quality factors up to  $5 \cdot 10^7$  [54,55].

#### 1.3.3 Laser reflow

To eliminate residual roughness of the edge of the disk cavities, a laser reflow process is applied to the disks [30]. A strong mid-IR laser beam ( $\lambda = 10.6 \mu\text{m}$ ) is applied to the disks one-by-one. Light at this wavelength is absorbed very efficiently by even the thin silica disks (absorption depth  $\sim 34 \mu\text{m}$  at room temperature [56]). Together with the poor heat conductivity of silica ( $\sim 1.4 \text{ W/K m}$ ), a pronounced temperature dependence of the extinction coefficient with a dramatic increase at higher temperatures [56] gives rise to a thermal runaway process heating the silica rim above the melting temperature of silica at about  $1650^\circ\text{C}$ . The central part of the disk remains nearly at room temperature, as the supporting silicon pillar is transparent for mid-IR light and provides an effective heat sink.

Once the disk periphery has contracted to a toroidal structure due to surface tension, the absorption cross section of the rim is reduced, and being coupled more strongly to the silicon heat sink, the glass structure cools below the melting point, even if the laser radiation is still incident. In this manner, the reflow-process is self-terminating, producing toroids with a high rotational symmetry provided by the silicon pillar preform.

In the setups we use at MPQ, the employed lasers (Synrad 48-1, and Synrad 48-2, alternatively) are specified to emit a clean  $\text{TEM}_{00}$  mode (more than 95% of the power is emitted in this mode) with a specified  $1/e^2$ -beam diameter of 3.5 mm and full divergence angle of 4 mrad. At a distance of ca. 1.3 m, a convex  $f = 100 \text{ mm}$  ZnSe lens is placed into the beam. According to standard Gaussian beam optics, it is expected to produce a  $2w_0 = 230 \mu\text{m}$

## 1. Silica microresonators: versatile vehicles for Quantum Optics

diameter waist in its focal plane, with the intensity  $I(x, y, z)$  obeying the relation

$$I(x, y, z) = \frac{2P}{\pi w(z)^2} e^{-2(x^2+y^2)/w(z)^2} \quad (1.19)$$

with  $w(z)^2 = w_0^2 (1 + z^2/z_0^2)$  and  $z_0 = w_0^2\pi/\lambda$ . In the center of the focus, the peak intensity amounts to about  $4.8 \text{ kW/cm}^2$  for a typical applied average power of  $P = 1 \text{ W}$ . To vary the applied power, but also to flatten the transverse intensity profile, it proved advantageous to move the toroids slightly out of the focal plane (cf. figure 1.3).

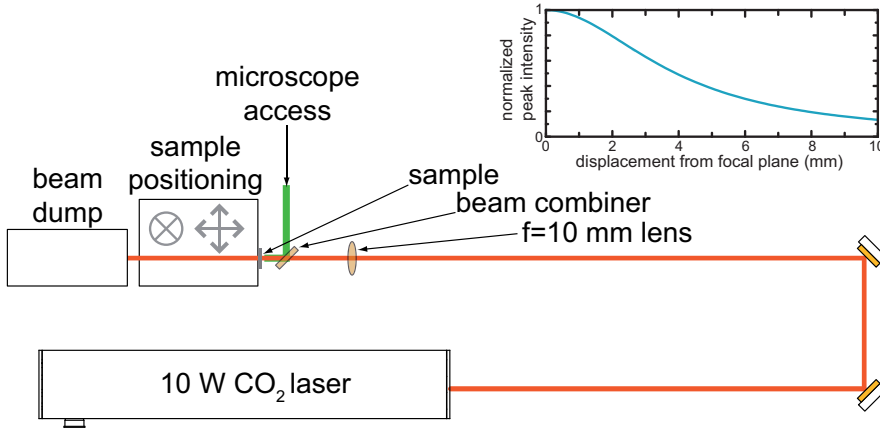


Figure 1.3: Setup used for the reflow of silica microtoroids. A 10 W CO<sub>2</sub>-laser is focused using a ZnSe lens. The sample is placed on a mount close to the focal plane and can be precisely positioned using micro-actuators. The sample can be viewed through a microscope, the image of which is aligned to the laser beam. The silica disks are positioned one-by-one, and illuminated with the laser beam until they have the desired toroidal shape. Inset shows the dependence of the laser peak intensity as a function of the displacement of the sample from the focal plane.

### 1.4 Coupling to whispering gallery mode resonators

In this section, the coupling of light into and out of the whispering-gallery modes will be described. Coupling is accomplished using tapered optical fibers, via the overlap of the evanescent field of these waveguides and the evanescent portion of the WGM. The main properties of these tapers and their fabrication at MPQ will be reviewed. The theoretical approach used to model the coupled waveguide-resonator system was adapted from H. A. Haus [57, 58].

#### 1.4.1 Fiber tapers

Fiber tapers are produced by pulling single-mode optical fiber while heating it with a hydrogen torch. As a result, the central part of the taper is essentially a cylindrical silica rod with a diameter on the order of the light's wavelength.

## 1.4 Coupling to whispering gallery mode resonators

---

This rod is an optical waveguide due to the index contrast of silica and the surrounding air (or vacuum). The modes of such a simple dielectric cylindrical waveguide are well-known, and for small enough diameters  $2R$ , the waveguide supports only a single propagating mode. In transverse (radial) direction, the field of this mode drops exponentially, over the characteristic length  $\gamma_f^{-1}$ , where [59]

$$\gamma_f = \alpha_f \frac{K_1(\alpha_f R)}{K_0(\alpha_f R)}, \quad (1.20)$$

$K_0$  and  $K_1$  being the modified Hankel functions of zero and first order, and

$$\alpha_f = \sqrt{\beta_f^2 - k^2 n_{cl}^2} \quad (1.21)$$

is obtained from the characteristic equation

$$k_f \frac{J_1(k_f R)}{J_0(k_f R)} = \alpha_f \frac{K_1(\alpha_f R)}{K_0(\alpha_f R)} \quad (1.22)$$

with zero and first order cylindrical Bessel functions  $J_0$  and  $J_1$ . This yields also the propagation constant  $\beta_f$  together with

$$k_f = \sqrt{k^2 n_f^2 - \beta_f^2}, \quad (1.23)$$

where  $n_f$  and  $n_{cl}$  are the refractive indices of the taper and the surrounding material, respectively. Variation of the taper radius (which, in a coupling experiment, can be simply achieved by displacing the taper along its symmetry axis) enables continuous tuning of the propagation constant in the taper, in order to match it with the propagation constant of the WGM of interest [59]. In this case, if the taper is approached tangentially to the WGM resonator, the fields in the taper and WGM can remain in phase over the extended interaction length (“phase matching”), enabling highly efficient coupling.

We have produced single-mode fiber tapers for various wavelengths between 633 nm and 1550 nm from standard single-mode fiber (mostly by Nufern). The main part of the setup is shown in figure 1.4: Two clamps hold the fiber above a torch, the flame of which is fed by pure hydrogen at a controlled flow. Two high-quality translation stages symmetrically pull the clamps apart. During the pulling, the transmission of test laser light at the desired wavelength is continuously monitored. After several seconds of pulling, transmission usually oscillates in time. This is due to multimode interference: as long as the taper supports a second mode, which is also slightly fed in the transition region between the core-cladding single mode fiber and the cylindrical silica waveguide in the center, multimode interference leads to a length-dependent transmission. Typically pulling is interrupted when the second mode dies off.

## 1. Silica microresonators: versatile vehicles for Quantum Optics

Reproducibly crafting low-loss ( $< 5\%$ ) tapers becomes increasingly challenging with decreasing wavelength. Position and size of the flame have to be controlled, requiring a torch mounted on translation stages with sub-millimetric reproducibility as well as a mass-flow-controller (MKS) for the hydrogen flux and an environment protected from air currents. The pulling speed must be precisely adjusted, in this case using computer-controlled drivers of the translation stages (Newport MFA). Finally, the acrylate buffer applied as a protection layer over the fiber cladding has to be completely removed before applying the flame to the fiber. Mechanical stripping and thorough wiping with a clean tissue and isopropanol are usually sufficiently effective. For the shortest wavelengths, extending the heated region by moving the flame along the fiber during pulling (“flame brushing”) [60] proved advantageous.

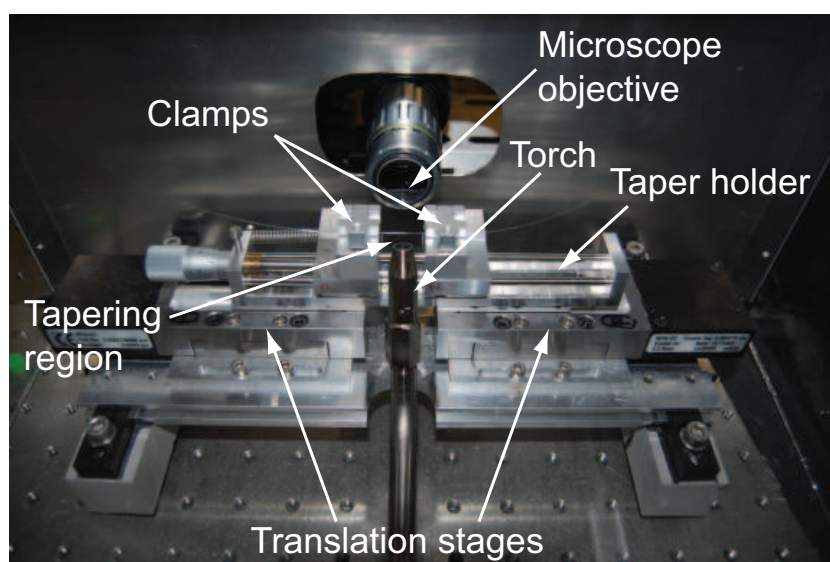


Figure 1.4: Setup used to craft tapered fibers. Two clamps, sliding on two rails of the taper holder, hold a piece of stripped single-mode fiber above the flame of a hydrogen torch. By symmetrically pulling apart the clamps using two translation stages, a fiber taper is formed in the central region.

### 1.4.2 Theoretical description of coupling

#### Coupled-mode theory

The temporal dynamics and steady states of the coupled waveguide-resonator system are most conveniently described by introducing the complex scalar *mode amplitude*  $\tilde{a}(t)$  [57, 58], which is normalized such that  $|\tilde{a}(t)|^2$  is the energy (or number of photons, just by rescaling by  $\hbar\omega_1$ ) stored in the WGM. The electric field at some location  $\vec{r}_0$  of the WGM can be thought of as being proportional to one of its quadratures, for example its real part. In general,

## 1.4 Coupling to whispering gallery mode resonators

the electric field pattern can be written

$$\vec{E}(\vec{r}, t) \propto \text{Re}(\vec{v}(\vec{r}) \cdot \tilde{a}(t)), \quad (1.24)$$

where the complex-valued  $\vec{v}(\vec{r})$  accommodates the mode's spatial and polarization degrees of freedom. Using time reversal symmetry and energy conservation [57], the mode amplitude can be shown to follow a time evolution according to

$$\dot{\tilde{a}}(t) = \left(-i\omega_c - \frac{\kappa}{2}\right) \tilde{a}(t) + \frac{\tilde{s}_{\text{in}}(t)}{\sqrt{\tau_{\text{ex}}}}, \quad (1.25)$$

where  $\omega_c$  is the mode's resonance frequency,  $\kappa$  its total energy loss rate,  $\tau_{\text{ex}}^{-1}$  its coupling rate to the waveguide mode and  $\tilde{s}_{\text{in}}(t)$  the amplitude of the mode in the fiber taper. It is normalized such that  $|\tilde{s}_{\text{in}}(t)|^2$  is the power (or photon flux) impinging on the coupling region.

Typically, the driving field oscillates harmonically in time at an angular frequency  $\omega_l$ , that is<sup>1</sup>,  $\tilde{s}_{\text{in}}(t) \equiv s_{\text{in}}(t)e^{-i\omega_l t}$ . It is convenient to transform to a rotating frame using  $\tilde{a}(t) \equiv a(t)e^{-i\omega_l t}$  to obtain

$$\dot{a}(t) = \left(i\Delta - \frac{\kappa}{2}\right) a(t) + \frac{s_{\text{in}}(t)}{\sqrt{\tau_{\text{ex}}}}, \quad (1.26)$$

where the detuning of the driving field (typically derived from a laser) with respect to the cavity resonance frequency

$$\Delta = \omega_l - \omega_c \quad (1.27)$$

was introduced. It is positive (negative) for a laser with a frequency greater (smaller) than the WGM resonance frequency, a situation that will be referred to as blue-detuned (red-detuned).

For a constant drive amplitude  $s_{\text{in}}(t) \equiv \bar{s}_{\text{in}}$ , setting the time derivative to zero immediately yields the steady state solution for the mode amplitude<sup>2</sup>

$$\bar{a} = \frac{1}{-i\Delta + \kappa/2} \frac{\bar{s}_{\text{in}}}{\sqrt{\tau_{\text{ex}}}}. \quad (1.28)$$

In this steady state, the power circulating in the cavity is given by

$$|\bar{s}|^2 = \frac{|\bar{a}|^2}{\tau_{\text{rt}}} = \frac{1}{\tau_{\text{rt}}} \frac{1}{\Delta^2 + (\kappa/2)^2} \frac{|\bar{s}_{\text{in}}|^2}{\tau_{\text{ex}}} = \quad (1.29)$$

$$= \frac{4\eta_c}{\tau_{\text{rt}}\kappa} \frac{1}{1 + 4\Delta^2/\kappa^2} |\bar{s}_{\text{in}}|^2 = 2\eta_c \frac{\mathcal{F}}{\pi} \frac{1}{1 + 4\Delta^2/\kappa^2} |\bar{s}_{\text{in}}|^2, \quad (1.30)$$

<sup>1</sup>The negative sign in the exponent was chosen to make the resulting discussion congruent with the quantum mechanical formulation later in this work, coinciding with the choice of Haus [58].

<sup>2</sup>Both  $\tilde{a}(t)$  and  $a(t)$  will be referred to as mode amplitude in the following, as they denote the same physical entity in two different frames.

## 1. Silica microresonators: versatile vehicles for Quantum Optics

a Lorentzian with full-width-half-max (FWHM) linewidth of the loss rate  $\kappa$ . In the last line, the finesse

$$\mathcal{F} = \frac{\text{free spectral range}}{\text{resonance linewidth}} = \frac{\tau_{\text{rt}}^{-1}}{\kappa/2\pi} = \frac{c}{nR\kappa}, \quad (1.31)$$

$\tau_{\text{rt}}$  being the round-trip time of light in the cavity, was introduced together with the coupling parameter

$$\eta_c = \frac{\tau_0}{\tau_0 + \tau_{\text{ex}}}. \quad (1.32)$$

The importance of the finesse is immediately evident from (1.30): For a symmetric cavity ( $\eta_c = 1/2$ ), the enhancement of intracavity power compared to launched power is  $|\bar{s}/\bar{s}_{\text{in}}|^2 = \mathcal{F}/\pi$  on resonance  $\Delta = 0$ .

The transmitted light amplitude, i.e. the amplitude of the light emerging from the fiber taper after the coupling region, can then be written as [57]<sup>3</sup>

$$s_{\text{out}}(t) = s_{\text{in}}(t) - \frac{a(t)}{\sqrt{\tau_{\text{ex}}}} \quad (1.33)$$

which from (1.28) is

$$\begin{aligned} \bar{s}_{\text{out}} &= \bar{s}_{\text{in}} - \frac{\bar{a}}{\sqrt{\tau_{\text{ex}}}} = \\ &= \frac{\tau_{\text{ex}} - \tau_0 - 2i\tau_{\text{ex}}\tau_0\Delta}{\tau_{\text{ex}} + \tau_0 - 2i\tau_{\text{ex}}\tau_0\Delta} \bar{s}_{\text{in}} = \\ &= \frac{(1 - 2\eta_c)\kappa/2 - i\Delta}{\kappa/2 - i\Delta} \bar{s}_{\text{in}} \end{aligned} \quad (1.34)$$

in the steady state. The transmitted power (or photon flux) is in this case

$$\begin{aligned} |\bar{s}_{\text{out}}|^2 &= \frac{(\tau_{\text{ex}} - \tau_0)^2 + (2\tau_{\text{ex}}\tau_0\Delta)^2}{(\tau_{\text{ex}} + \tau_0)^2 + (2\tau_{\text{ex}}\tau_0\Delta)^2} |\bar{s}_{\text{in}}|^2 = \\ &= \left( 1 - \frac{(\tau_{\text{ex}}\tau_0)^{-1}}{(\kappa/2)^2 + \Delta^2} \right) |\bar{s}_{\text{in}}|^2 \\ &= \left( 1 - \frac{\eta_c(1 - \eta_c)\kappa^2}{(\kappa/2)^2 + \Delta^2} \right) |\bar{s}_{\text{in}}|^2, \end{aligned} \quad (1.35)$$

a Lorentzian dip of FWHM linewidth  $\kappa$ .

---

<sup>3</sup>Often, the sign of  $s_{\text{out}}$  is chosen the opposite way, as in most cases it constitutes a signal reflected from a cavity. For our geometry, the chosen sign convention is physically more meaningful. In the limit of no coupling,  $s_{\text{out}}$  must be equal to  $s_{\text{in}}$ .

## 1.4 Coupling to whispering gallery mode resonators

---

### Coupling regimes

A unique property of taper-coupled silica microresonators is that the coupling strength can be continuously adjusted by tuning the taper-resonator gap. This allows to access different coupling regimes [61]:

- undercoupled regime, in which the losses are dominated by intrinsic losses of the cavity:  $\tau_0^{-1} > \tau_{\text{ex}}^{-1}$  ( $\eta_c < 1/2$ ). The magnitude of the field coupled back from the resonator into the taper is smaller than the field propagating in the taper.
- critical coupling, for which the intrinsic cavity loss rate and the coupling rate to the fiber taper mode are equal:  $\tau_0^{-1} = \tau_{\text{ex}}^{-1}$  ( $\eta_c = 1/2$ ). For critical coupling, a resonant field leaking back from the cavity and the field propagating in the taper have equal magnitude but their phase is shifted by  $\pi$ . This leads to zero power transmission of the system on resonance.
- overcoupled regime, in which the coupling rate to the taper exceeds the intrinsic loss rate  $\tau_0^{-1} < \tau_{\text{ex}}^{-1}$  ( $\eta_c > 1/2$ ). The magnitude of the field coupled back from the resonator into the taper is larger than the field propagating in the taper.

For applications in quantum optics, it is often desirable that the cavity mode be mainly coupled to a single well-controlled spatial mode, through which the light leaves the cavity. All other loss channels of the cavity admit quantum vacuum into the cavity mode, often degrading the quality of a measurement. In the case of fiber taper-coupling, the propagating mode to which the cavity mode should be coupled is the fundamental mode of the fiber taper. If the taper is approached to the cavity, the coupling rate to this mode increases exponentially,  $\tau_{\text{ex}}^{-1} \propto e^{-\gamma_f d}$ , while the intrinsic loss rate of the cavity  $\tau_0^{-1}$  is constant, so for a small enough coupling gap, the cavity mode can be coupled dominantly to the taper mode (overcoupled regime). However, there may also be other loss channels mediated by the taper in the vicinity of the cavity mode. In particular, light may couple to higher-order modes in the taper, which later die off in the transition to the normal single-mode fiber; or the presence of the taper may simply scatter part of the light into free-space modes. The degree of overcoupling that can be reached by bringing the taper closer to the cavity may thus be limited. Introducing the rates  $\tau_{\text{ho}}^{-1}$  and  $\tau_{\text{rad}}^{-1}$  for the two taper-induced loss processes described above, one may define the parameter of the *ideality*  $I$  of the coupler using

$$I = \frac{\tau_{\text{ex}}^{-1}}{\tau_{\text{ex}}^{-1} + \tau_{\text{ho}}^{-1} + \tau_{\text{rad}}^{-1}}. \quad (1.36)$$

Fiber taper-coupled microresonators have been shown to exhibit idealities of at least 99.97%, while simultaneously very strong overcoupling ( $\tau_{\text{ex}}^{-1} \sim$

## 1. Silica microresonators: versatile vehicles for Quantum Optics

$10^4(\tau_0^{-1} + \tau_{\text{ho}}^{-1} + \tau_{\text{rad}}^{-1})$ ) can be achieved if the diameter of the taper is chosen appropriately [62].

### Coupling of counter-propagating modes by scattering

As described in section 1.2, the counterpropagating modes in spheres (mode numbers  $\pm m$ ) are frequency-degenerate, and the same applies to WGMs in toroids for symmetry reasons. The propagation direction of the light in the coupling taper therefore determines which mode is going to be excited. However, light scattering both in the bulk and at surface inhomogeneities can lead to a significant population of the mode in which light orbits in the opposite direction. This was observed early on in the research on microspheres [63], and has been dedicated attention both in theory and experiment [50, 64, 65].

The basic features of this effect can be understood from a simple model based on coupled mode theory [64]. If the two modes are coupled with a coupling rate  $\gamma$ , the mode amplitudes of the pumped mode orbiting clockwise (cw) and the unpumped mode orbiting counter-clockwise (ccw) evolve according to

$$\dot{a}_{\text{cw}}(t) = (i\Delta - \kappa/2)a_{\text{cw}}(t) + i\frac{\gamma}{2}a_{\text{ccw}}(t) + \frac{s_{\text{in}}(t)}{\sqrt{\tau_{\text{ex}}}} \quad (1.37)$$

$$\dot{a}_{\text{ccw}}(t) = (i\Delta - \kappa/2)a_{\text{ccw}}(t) + i\frac{\gamma}{2}a_{\text{cw}}(t). \quad (1.38)$$

In steady state, these equations are solved in a straightforward manner by

$$\bar{a}_{\text{cw}} = \frac{1}{2} \left( \frac{1}{\kappa/2 - i(\Delta + \gamma/2)} + \frac{1}{\kappa/2 - i(\Delta - \gamma/2)} \right) \frac{\bar{s}_{\text{in}}}{\sqrt{\tau_{\text{ex}}}} \quad (1.39)$$

$$\bar{a}_{\text{ccw}} = \frac{1}{2} \left( \frac{1}{\kappa/2 - i(\Delta + \gamma/2)} - \frac{1}{\kappa/2 - i(\Delta - \gamma/2)} \right) \frac{\bar{s}_{\text{in}}}{\sqrt{\tau_{\text{ex}}}}, \quad (1.40)$$

evidently a resonance doublet. Under these conditions, the eigenmodes of the system are superpositions of cw- and ccw-orbiting modes with a fixed phase relation, that is, standing waves with a  $\cos(m\varphi)^2$  and  $\sin(m\varphi)^2$  azimuthal intensity dependence.

Both a transmitted field

$$s_{\text{tra}}(t) = s_{\text{in}}(t) - \frac{a_{\text{cw}}(t)}{\sqrt{\tau_{\text{ex}}}} \quad (1.41)$$

and a reflected field

$$s_{\text{ref}}(t) = -\frac{a_{\text{ccw}}(t)}{\sqrt{\tau_{\text{ex}}}} \quad (1.42)$$

may then be coupled back into the fiber.

## 1.4 Coupling to whispering gallery mode resonators

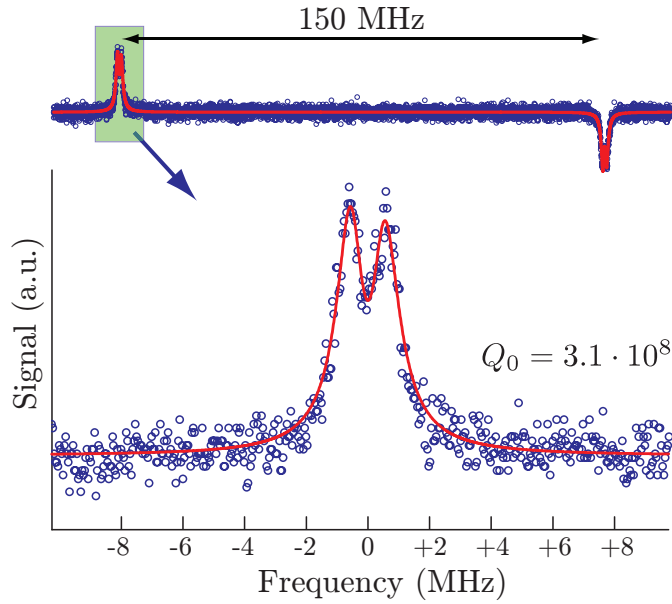


Figure 1.5: Measurement of optical linewidth and modal coupling rate of a toroidal microresonator using frequency modulation spectroscopy. Inset shows the full trace, with the two signatures when a modulation sideband is scanned over the cavity resonance. The modulation frequency (here 74.76 MHz) directly provides a calibration of the trace. Measured in the undercoupled regime, the intrinsic linewidth of 1.1 MHz and a splitting of 1.0 MHz can be extracted. At the wavelength  $\lambda = 968$  nm, this corresponds to an intrinsic quality factor of  $3.1 \cdot 10^8$ .

Figure 1.5 shows a resonance trace obtained from a toroid with a high quality factor, and exhibiting also modal splitting. The data were taken in the undercoupled regime, and the fit yields an intrinsic linewidth of  $\tau_0^{-1}/2\pi = 1.1$  MHz and a splitting of  $\gamma/2\pi = 1.0$  MHz. To enhance the signal-to-noise ratio, these data were taken using a frequency-modulation technique [43, 66], in which the incident laser is phase-modulated at a radio frequency  $\Omega_{\text{rf}}$ . The detected photocurrent of a detector placed at the exit of the fiber taper is demodulated at the same frequency, with the phase of the reference signal adjusted in order to obtain the absorptive features shown in figure 1.5.

Note that the coupling conditions (undercoupled, critically coupled, overcoupled) are also modified by the presence of strong modal splitting. In particular, reaching the critical coupling point, at which transmission vanishes for resonant excitation, requires a coupling rate of  $\tau_{\text{ex}}^{-1} = \tau_0^{-1} \sqrt{1 + \tau_0^2 \gamma^2}$  [64]. For this coupling strength, the reflected signal also gets maximized. Figure 1.6 shows the transmission and reflection of a toroid with a slightly more pronounced modal splitting of  $\tau_0 \gamma = 3.5$ .

To obtain these data, a laser at  $\lambda = 1500$  nm was swept across the WGM resonance repetitively. Both transmitted and reflected optical powers were recorded as traces with a digital oscilloscope. A piezoelectric translation stage was used to slowly approach the taper to the toroid. For each trace, the position of the translation stage was recorded. In the data analysis, the

## 1. Silica microresonators: versatile vehicles for Quantum Optics

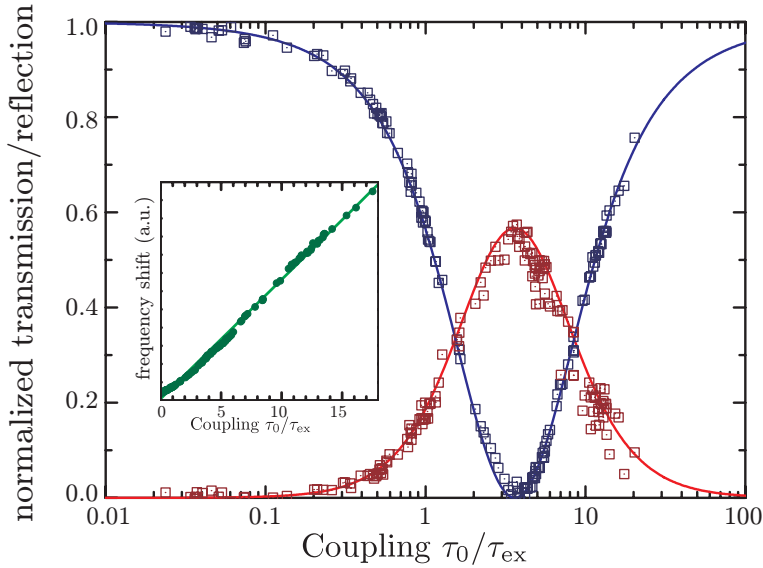


Figure 1.6: Normalized optical transmission and reflection from two coupled counterpropagating WGM excited by a fiber taper. By approaching the taper, the coupling rate  $\tau_{\text{ex}}^{-1}$  is slowly increased. The inset shows the simultaneously recorded optical resonance shift as a function of coupling strength. See text for more details.

square magnitude of transmission (1.41) and reflection (1.42) were used as fit models, with the steady-state amplitudes (1.39) and (1.40) of the two counterpropagating modes. This allowed to deduce the coupling strength  $\tau_0/\tau_{\text{ex}}$  as well as the normalized transmission  $(1 - 2\kappa\tau_{\text{ex}}^{-1}/(\gamma^2 + \kappa^2))^2$  and reflection  $4\gamma^2\tau_{\text{ex}}^{-2}/(\gamma^2 + \kappa^2)^2$  from each trace. Interestingly, an optical resonance frequency shift was also observed when the taper was approached. This is due to the presence of the taper with its refractive index in the evanescent field of the WGM. Figure 1.7 shows the dependence of the extracted coupling strength on the taper position. An exponential dependence is clearly observed, with a  $1/e$ -characteristic length of  $\sim 810$  nm.

### 1.5 Optical nonlinearities

Silica WGM resonators concentrate high optical power in small volumes, which leads to an enhancement of optical non-linearities: A typical 300,000-optical finesse toroid of  $60\ \mu\text{m}$  major diameter already achieves circulating intensities on the order of  $100\ \text{MW}/\text{cm}^2$  for launched powers below  $50\ \mu\text{W}$ . Such intensities can easily drive optical nonlinearities. Due to the isotropic nature of the amorphous silica, the lowest order nonlinearities which can be observed are  $\chi^{(3)}$ -nonlinearities, specifically the Raman and Kerr effects, which will be briefly discussed in the following. A much stronger effective nonlinearity is borne by a thermal effect [17, 67, 68], which will be discussed first.

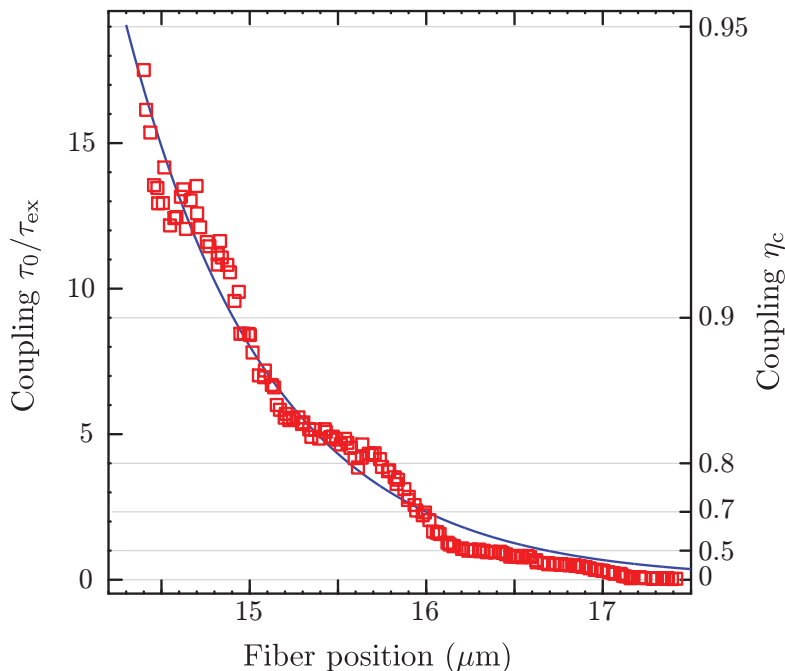


Figure 1.7: Coupling strength as a function of the fiber taper's position (abscissa has an arbitrary offset), when the taper is approached to the toroid. Red squares are data, and the full blue line is an exponential fit with a  $1/e$ -characteristic length of  $\sim 810$  nm.

### 1.5.1 Thermal nonlinearity

Due to absorption in the optical mode, the temperature of the torus changes by an amount  $\delta T$  according to

$$\rho c_p \delta \dot{T}(\vec{r}, t) = k \vec{\nabla}^2 \delta T(\vec{r}, t) + \frac{|a(t) \cdot \vec{v}(\vec{r})|^2}{\tau_{\text{abs}}}, \quad (1.43)$$

where  $\tau_{\text{abs}}^{-1}$  is the loss rate due to absorption,  $\rho$  is the density,  $c_p$  is the specific heat capacity, and  $k$  the thermal conductivity (for the numerical parameters of fused silica, see appendix A.1), and  $\vec{v}(\vec{r})$  accommodates the field distribution of the mode, and is normalized such that  $\int |\vec{v}(\vec{r})|^2 dV = 1$ . Now the time evolution of the WGM amplitude (1.25) is influenced by the temperature of the structure, as its resonance frequency is a function of the temperature distribution  $\omega_c \equiv \omega_c(\delta T(\vec{r}, t))$ .

The temperature-dependence of the resonance frequency can be due to the change in refractive index or expansion of the structure. For a *uniform* temperature distribution, the resonance frequency  $\omega_c$  should depend on the temperature changes  $\delta T$  to first order as

$$\omega_c(T + \delta T) \approx \omega_c(T) \left( 1 - \left( \alpha + \frac{1}{n} \frac{dn}{dT} \right) \delta T \right). \quad (1.44)$$

With the parameters  $dn/dT \approx 1.0 \cdot 10^{-5} \text{ K}^{-1}$  and  $\alpha \approx 5.5 \cdot 10^{-7} \text{ K}^{-1}$  (see appendix A.1) a resonance frequency shift of  $-1.44 \text{ GHz/K}$  is expected at

## 1. Silica microresonators: versatile vehicles for Quantum Optics

1550 nm. For this wavelength, we have measured a tuning coefficient of  $-1.28$  GHz/K when heating the chip with a peltier element, and a feedback controller to stabilize the temperature of the chip (figure 1.8). The deviation may be due to insufficient thermalization of the silica disk, or slightly different material parameters, which differ by up to 10% for various fabrication processes [69], and are not precisely known for silica grown on silicon wafers.

If the temperature change is induced by absorption of light, one may expect that the temperature distribution in an equilibrium situation ( $\dot{\delta T} = \dot{\tilde{a}} = 0$ ) is not uniform. Rather, the mode volume—where absorption takes place—can be assumed to be the hottest part, increasing even more the relative contribution of the thermorefractive effect. For simplicity, we replace this distribution  $\delta T(\vec{r})$  by an effective temperature  $\delta T$  seen by the optical mode, which is proportional to absorbed power,

$$\delta T = \frac{\beta |\bar{a}|^2}{\tau_{\text{abs}}}, \quad (1.45)$$

and induces a resonance frequency shift according to (1.44). Finite-element modeling suggests that for a typical toroid of  $60 \mu\text{m}$  major diameter, and a pillar diameter of  $40 \mu\text{m}$ ,  $\beta$  is on the order of  $2 \cdot 10^4$  K/W (figure 1.8), a value compatible with the measured shifts induced by absorption of a 1545 nm-laser [51].

The temperature-dependent resonance frequency gives rise to a well-known thermal bistability [17, 51, 67, 68], as the steady-state equation for the WGM amplitude

$$|\bar{a}|^2 = \frac{|\bar{s}_{\text{in}}|^2 / \tau_{\text{ex}}}{\left(\omega_1 - \omega_c + \omega_c \left(\alpha + \frac{1}{n} \frac{dn}{dT}\right) \beta |\bar{a}|^2 / \tau_{\text{abs}}\right)^2 + (\kappa/2)^2} \quad (1.46)$$

has three solutions for  $|\bar{a}|^2$  as soon as the threshold power of

$$P_{\text{thresh}} = \frac{\kappa^3 \tau_{\text{abs}} \tau_{\text{ex}}}{3\sqrt{3} \beta \left(\alpha + \frac{1}{n} \frac{dn}{dT}\right) \omega_c} \quad (1.47)$$

is reached (compare section 2.2.1, where a similar bistability is discussed in more detail). For typical parameters of a toroid ( $2\tau_{\text{abs}}^{-1} = 2\tau_{\text{ex}}^{-1} = \kappa = 2\pi \cdot 3$  MHz,  $\beta = 2 \cdot 10^4$  K/W,  $\omega_c = 2\pi \cdot 300$  THz), the threshold is already reached at ca. 50 nW, highlighting the experimental significance of this effect. Figure 1.8 illustrates the resulting hysteretic behavior of the transmission of a thermally nonlinear cavity.<sup>4</sup>

For many purposes, the temporal dynamics of the thermal effect are of importance as well. They can be assessed by solving equation (1.43) with the boundary conditions given by the shape of the silica structure.

---

<sup>4</sup>A movie [68] explaining the thermal nonlinearity is available at <http://www.opticsinfobase.org/oe/viewmedia.cfm?uri=oe-12-20-4742&seq=2>

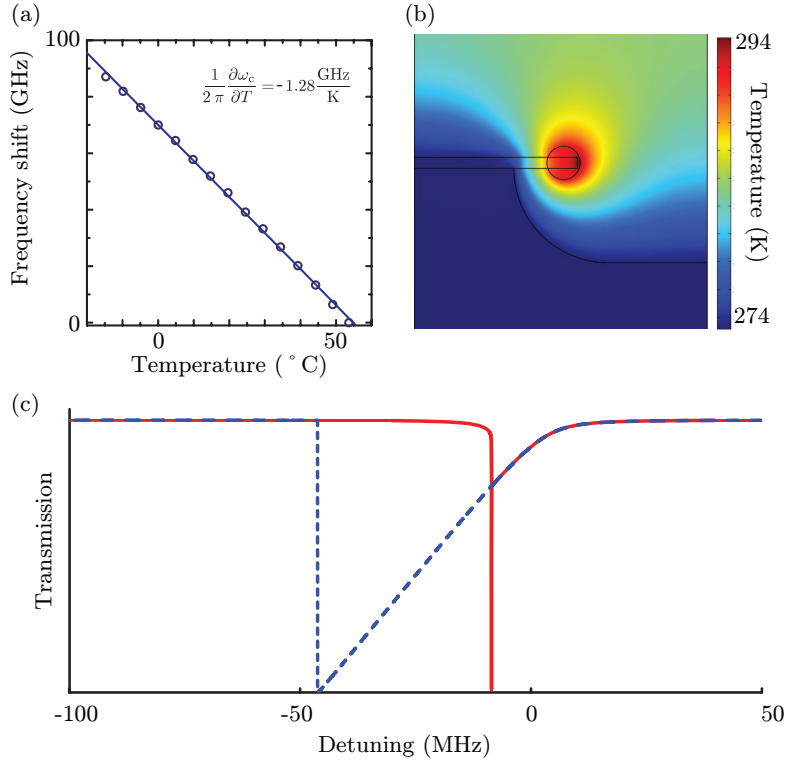


Figure 1.8: Static thermal nonlinearity. (a) Tuning of the cavity resonance frequency with externally controlled temperature. Circles are measured data, line is a fit. (b) Temperature distribution in a  $60 \mu\text{m}$ -diameter toroid and the surrounding air, in which a power of  $1 \text{ mW}$  is deposited in the optical mode volume. (c) Hysteretic transmission behavior for a laser power of  $20P_{\text{thresh}}$ . If the laser is scanned down in frequency (blue dashed line) it drags the cavity resonance down in frequency as well, and so stays resonant for a larger range of detunings. If the laser is scanned up (red line), the cavity jumps into resonance with the scanning laser while the laser is still red-detuned with respect to the cold cavity resonance frequency.

For toroids and disks, the most important mechanism of heat removal from the structure is by coupling to the silicon pillar. We may therefore set up a simplified model, in which we only calculate  $\delta T(\vec{r})$  within the silica disk, and assume it to be zero in the region  $r < R_1$  above the pillar of radius  $R_1$ . Furthermore, we may simplify the source term by approximating the optical mode with the edge of the silica disk of radius  $R$  and thickness  $d$ . The problem is then symmetric in  $z$  and  $\varphi$  and, after Fourier transform, we are left with the one-dimensional problem

$$\rho c_p i \Omega \delta T(\Omega, r) = k \frac{1}{r} \frac{\partial}{\partial r} \left( r \frac{\partial}{\partial r} \right) \delta T(\Omega, r) + \frac{|\bar{a}|^2}{\tau_{\text{abs}}} \frac{\delta(r - R)}{2\pi R d}. \quad (1.48)$$

## 1. Silica microresonators: versatile vehicles for Quantum Optics

---

To solve it, we introduce the abbreviations

$$z \equiv r/R \quad (1.49)$$

$$z_1 \equiv R_1/R \quad (1.50)$$

$$-\lambda^2 \equiv \rho c_p i \Omega R^2 / k \quad (1.51)$$

$$\mu \equiv \frac{|\bar{a}|^2}{\tau_{\text{abs}}} \frac{1}{2\pi k d} \quad (1.52)$$

$$\delta\tilde{T}(\lambda, z) \equiv \delta T(\Omega, r/R) \quad (1.53)$$

and get the ordinary differential equation

$$-\lambda^2 \delta\tilde{T}(\lambda, z) = \frac{1}{z} \frac{\partial}{\partial z} \left( z \frac{\partial}{\partial z} \right) \delta\tilde{T}(\lambda, z) + \mu \delta(z-1). \quad (1.54)$$

The homogeneous solution to this problem is

$$\delta\tilde{T}_h(\lambda, z) = c_1 J_0(\lambda z) + c_2 Y_0(\lambda z), \quad (1.55)$$

and an inhomogeneous solution is given by

$$\delta\tilde{T}_i(\lambda, z) = \frac{\mu\pi}{2} (J_0(\lambda z)Y_0(\lambda) - J_0(\lambda)Y_0(\lambda z)) \Theta(z-1), \quad (1.56)$$

with the Heaviside step function  $\Theta$ , and cylindrical Bessel functions of the first ( $J_0$ ) and second kind ( $Y_0$ ). We assume the boundary conditions

$$\delta\tilde{T}'(\lambda, 1) = 0 \quad (1.57)$$

$$\delta\tilde{T}(\lambda, z_1) = 0, \quad (1.58)$$

that is, a thermally insulated rim of the silica disk, neglecting convective heat transfer, and an unchanged temperature above the strongly conductive silicon pillar. These constraints determine the constants  $c_1$  and  $c_2$ . This yields, at the rim of the disk, where the optical mode is located, a temperature of

$$\delta\tilde{T}(\lambda, 1) = \frac{\mu}{\lambda} \frac{J_0(\lambda z_1)Y_0(\lambda) - J_0(\lambda)Y_0(\lambda z_1)}{J_1(\lambda)Y_0(\lambda z_1) - J_0(\lambda z_1)Y_1(\lambda)}. \quad (1.59)$$

From a Taylor expansion of  $\delta\tilde{T}(\lambda, 1)^{-1}$  in  $\lambda$  we obtain to lowest order in  $\Omega$

$$\delta T(\Omega, R) \approx \frac{\delta T_0}{1 + i\Omega/\Omega_1} \quad (1.60)$$

with

$$\delta T_0 = -\frac{|\bar{a}|^2}{\tau_{\text{abs}}} \frac{1}{2\pi k d} \ln(R_1/R) \quad (1.61)$$

$$\Omega_1 = -\frac{4 \ln(R_1/R)}{1 - (R_1/R)^2 + 2 \ln(R_1/R)(1 + \ln(R_1/R))} \frac{k}{\rho c_p R^2}. \quad (1.62)$$

## 1.5 Optical nonlinearities

For the static response ( $\Omega \rightarrow 0$ ), a comparison with the simulation presented in figure 1.8, with  $|\bar{a}|^2/\tau_{\text{abs}} = 1 \text{ mW}$ ,  $d = 2 \mu\text{m}$ ,  $R_1 = 20 \mu\text{m}$  and  $R = 30 \mu\text{m}$ , yields  $\delta T(0, R) = 23 \text{ K}$ , corresponding to  $\beta = 2.3 \cdot 10^4 \text{ K/W}$ , in good agreement with the simulated value of  $\beta \approx 2.0 \cdot 10^4 \text{ K/W}$ .

For high frequencies  $\Omega \gg \Omega_1$ , the approximations above break down, as the mode volume can no longer be assumed to have no extension in the radial direction. Indeed, a second cutoff can be expected when the wavelength of the thermal waves is on the order of the transverse extension of the WGM. A simple estimate for this cutoff can be obtained by assuming that the WGM has a transverse radius of  $r_0$ , and approximating (1.43) with [67, 70]

$$\rho c_p \delta \dot{T} = k \frac{1}{r_0^2} \delta T + \frac{|\bar{a}|^2}{\tau_{\text{abs}}} \frac{1}{2\pi^2 R r_0^2}, \quad (1.63)$$

one obtains again a temperature response of the form  $\delta T \propto (1 + i\Omega/\Omega_2)^{-1}$ , and the second cutoff frequency is given by

$$\Omega_2 = \frac{k}{\rho c_p r_0^2}, \quad (1.64)$$

where  $r_0$  can be obtained from finite-element modeling or approximated by  $r_0 \approx 1.8 R m^{-2/3}$  for fundamental modes in spheres, and in toroids for minor diameters greater than several wavelengths [71]. Typical orders of magnitude for silica toroidal WGM resonators are  $\Omega_1/2\pi \approx 10^3 \text{ Hz}$  and  $\Omega_2/2\pi \approx 10^5 \text{ Hz}$ , in agreement with the measurements reported in section 2.5.3.

### 1.5.2 Raman nonlinearity

The high intensities circulating in WGM of silica resonators also give rise to Raman gain in a frequency band about 13.2 THz below the frequency of the laser pumping the WGM, due to the interaction of light with vibrational modes in the silica structure. If the gain becomes large enough to exceed the losses of a second WGM within this frequency band, self-sustained optical oscillations set in. In a quantum picture, this process can be understood as the nonlinear conversion of a pump photon into a vibrational phonon and a photon at the lower ‘‘Stokes’’-frequency. The strong light confinement renders the pump power thresholds to achieve this so-called Raman lasing to unprecedentedly low light levels  $< 100 \mu\text{W}$ , and can even lead to cascaded oscillations, where several Raman sidebands are generated. The details of this process in silica microresonators have been analyzed extensively in the literature [20, 21, 32, 72–74] and will not be discussed here. Figure 1.9 shows an optical spectrum of a silica toroidal cavity pumped at a wavelength of 773 nm.

## 1. Silica microresonators: versatile vehicles for Quantum Optics

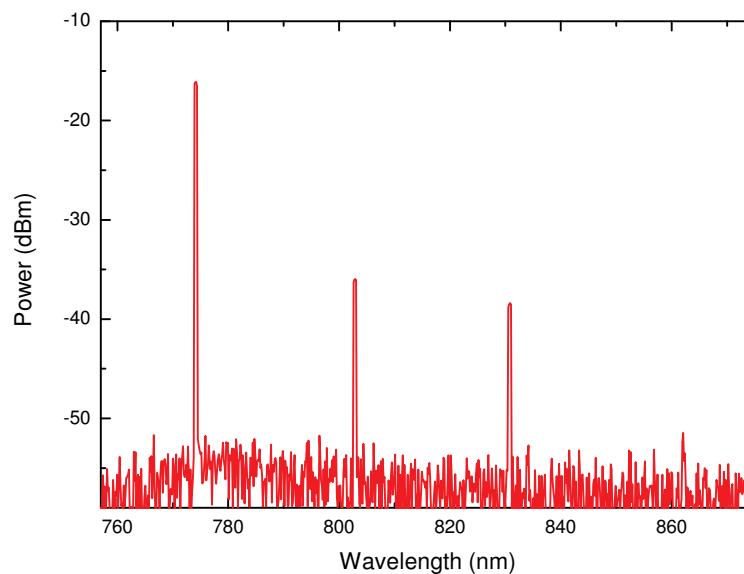


Figure 1.9: Cascaded Raman scattering from a pump laser at a wavelength of 773 nm.

### 1.5.3 Kerr nonlinearity

The Kerr nonlinearity of silica induces an intensity-dependent refractive index  $n(I) = n + n_2 I$ , where  $n_2 = 3 \cdot 10^{-20} \text{ W/m}^2$ . As a consequence, a WGM resonance frequency also depends on the launched power  $P = |s_{\text{in}}|^2$  according to

$$\omega_c(P) \approx \omega_c(0) \left( 1 - \frac{n_2}{n} \frac{1}{A_{\text{eff}}} 2\eta_c \frac{\mathcal{F}}{\pi} \frac{1}{1 + 4\Delta^2/\kappa^2} P \right), \quad (1.65)$$

where  $A_{\text{eff}}$  is the effective cross-section of the mode. This effect can lead to parametric gain and oscillation [3, 7, 75], which will be treated in more detail in chapter 3, but also to optical bistability similar to the thermal bistability discussed above. By suppressing the thermal bistability in a liquid helium bath, this effect was also observed experimentally [76]. Due to its basically instantaneous response, the Kerr effect can also be distinguished from the slower thermal effect in experiments where the laser power is modulated at high frequency [77]. Such an experiment will be described in section 2.5.3.

## Chapter 2

# Cavity optomechanics

### 2.1 Introduction

The tails of comets always point away from the sun. Kepler, in the 17<sup>th</sup> century, already conjectured from this observation that sunlight exerts a force on particles in the comet tail. Some 250 years later, Maxwell’s theory of electromagnetic radiation put this conjecture on solid theoretical grounds, yet, collecting experimental evidence for the fact that light carries momentum has eluded even the most skilled experimentalists of that age. As a famous example, Crookes attempted to construct a radiometer in which the transfer of optical momentum makes a vane spin, now famous as the “light mill” (figure 2.1). After much debate, however, it was understood that the observed rotation is mediated by the dilute gas in which the vane is kept [78]. True radiation-pressure effects, in agreement with Maxwell’s predictions, were not observed until the beginning of the 20<sup>th</sup> century, in more sophisticated experiments carried out by Lebedew in Russia [79] and Nichols and Hull in the United States [80–82].

The situation changed dramatically with the advent of lasers as highly coherent light sources in the 1970ies. It was soon suggested to *utilize* the resulting forces to manipulate the motion of mechanical objects in a controlled manner. Hänsch and Schawlow [83] and also Wineland and Dehmelt [84, 85] proposed ways to use radiation pressure to freeze out the random motion of atoms or ions (“laser cooling”), and Ashkin, Chu and coworkers conceived techniques to trap neutral particles using optical forces [86, 87]. In the decades to follow, the implementation of these ideas lead to what can be considered a true revolution in atomic physics, pivotal for discoveries such as Bose-Einstein condensation and the development of the most precise frequency standards available today.

On a fundamental level, these experiments have also soundly established that the motion of laser-cooled atoms or ions oscillating in their trapping

## 2. Cavity optomechanics

---



Figure 2.1: Radiometer used by Crookes around 1877. The pivoted vanes, each silvered and blackened on one face, are free to revolve around the central axis. Crookes observed that the vanes started to turn when illuminated by a strong light source. The origin of the effect was not radiation pressure, it was mediated by the dilute gas still present in the globe. In refined experiments by Lebedev in Russia and Hull in the US, effects of radiation pressure on mechanical objects were observed at the beginning of the 20<sup>th</sup> century. Image copyright Science Museum/SSPL, London.

potential can only be understood in quantum mechanical terms. For example, quantum fluctuations of the cooling light give rise to the Doppler limit in temperature [88]. Even more, if laser cooling to the quantum ground state is achieved [89–91], optical manipulation can be used to generate such exotic motional states as Fock or Schrödinger cat states [92].

It is a prime example of the enigmatic quantum-classical “boundary” that such quantum effects have never been observed with more massive oscillators. But it has remained an open question whether this is a mere technical challenge, or if yet unexplored mechanisms of decoherence give rise to this transition. An important impetus for *theoretical* analysis of systems in which radiation pressure acts on massive mechanical oscillators has come from the community of gravitational astronomy—for a very practical reason. In order to detect wobbles in space-time induced by gravitational waves, these scientists conceived today’s most sensitive displacement meters: kilometer-scale laser-driven interferometers, the mirrors of which are suspended as pendula to isolate them from seismic and technical noise.

Braginsky’s group at Moscow state university has played a particularly pioneering role in this regard. Embedded eventually in a very general theory of quantum measurements [93–96], they have developed a comprehensive understanding of optomechanical interactions as they occur in the fundamental building block of a gravitational wave observatory shown in figure 2.2: Monochromatic light trapped in a high-finesse cavity (a Fabry-Perot resonator in this case) exerts radiation pressure on the massive end mirrors, coupling their oscillatory motion to the light.

As early as 1967 Braginsky and coworkers recognized that radiation pressure can change the dynamics of the mechanical degree of freedom, effectively adding an optically induced viscous damping to the mirror motion. It was also soon understood that this *dynamical backaction* [97–100] could be used in principle to amplify or cool the motion of the mirror [101, 102], akin to laser cooling of atoms. While this effect can still be understood in classical terms, they also showed that true quantum effect gives rise to an unsurmountable sensitivity limit in displacement measurements of the mirror: For high enough light powers, quantum fluctuations in radiation pressure start to induce random motion in the mirror, masking the displacement to be detected [94, 103, 104], an effect now referred to as the *quantum backaction* of the measurement.

In the following years, optomechanical systems have attracted much attention by theorists in the quantum optics community, resulting in a variety of proposals exploring quantum effects in these systems. To mention just a few examples, quantum non-demolition measurements of the light intensity, or single quadratures of the mechanical displacement have been suggested early on [93, 95, 105, 106], as well as the generation of narrow-band squeezed light using the mechanical oscillator as an effective third-order nonlinearity [107, 108]. Later work has studied in great detail the possibility to generate non-classical states of motion [109], including superposition states [110], entangled states of several oscillators [111–114], or motional states entangled with optical degrees of freedom [115, 116]. As a special quantum state, it has also been suggested to cool the mechanical degree of freedom to its quantum ground state using cooling by dynamical backaction [117–122],

Observing such effects, however, has been severely complicated by several experimental challenges. First, optomechanical coupling by radiation pressure is usually weak—the momentum transfer of a single reflected photon changes the velocity of a (free) gram-scale mass by some  $10^{-24}$  m/s only. At the same time, the oscillator displacements associated with quantum effects are typically on the scale of its zero-point fluctuations  $x_{\text{ZPF}} = \sqrt{\hbar/2m\Omega_m}$ , where  $m$  and  $\Omega_m$  are its mass and the resonance frequency, respectively. For gram-scale oscillators, such as a small mirror in an interferometer, this is some ten orders of magnitude smaller than the fluctuations of a trapped atom or ion—usually at the sub-attometer scale. While dedicated experi-

## 2. Cavity optomechanics

---

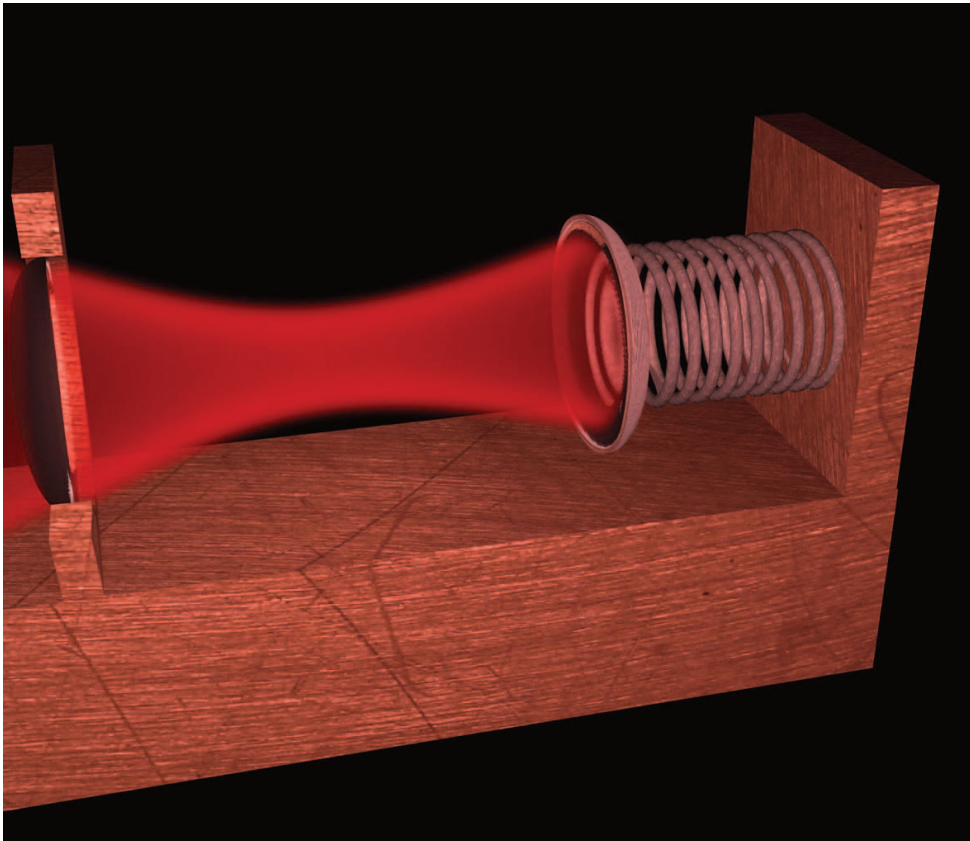


*Figure 2.2:* Artist's view of a generic optomechanical system: A Fabry-Perot resonator, consisting of two mirrors trapping near-resonant monochromatic light. One of the mirrors is mechanically compliant, here it is mounted on a spring and therefore constitutes a mechanical harmonic oscillator.

ments [123–126] have been approaching such sensitivities, another challenge persists in all room-temperature experiments: Thermal noise tends to mask quantum signatures as long as the thermal energy  $k_B T$  largely exceeds the energy scale  $\hbar\Omega_m$  of a motional quantum ( $k_B$  is the Boltzmann, and  $\hbar$  the reduced Planck constant).

In recent years, the tremendous progress in micro- and nanofabrication technologies has provided unprecedented opportunities to engineer novel mechanical devices. This potential has revived the interest in their quantum properties [127]. In a joint effort of researchers from fields as diverse as quantum optics, photonics, solid state and low-temperature physics, a vast variety of new opto- and electromechanical systems have been recently developed and characterized. Aiming at the observation of strong opto-mechanical coupling—mostly to ultimately observe quantum effects—they have formed the research field of cavity (quantum) optomechanics [128, 129]. Table 2.1 summarizes the properties of optomechanical systems studied in the last ten years, reflecting also the enormous parameter range covered.

Within this work, we have developed optomechanical systems based on the silica whispering-gallery mode (WGM) resonators introduced in chapter 1. Their compactly co-located high-quality optical and mechanical modes render them a very favorable system for the study of radiation-pressure induced optomechanical coupling. Indeed, we show in this work that basically all experimental challenges for the observation of quantum effects can be successfully tackled with this system. As an important precondition, it has been possible for the first time to demonstrate radiation-pressure cooling of a mesoscopic mechanical oscillator based on optically induced dynamical backaction. Adapting, in addition, advanced quantum optical and cryogenic techniques to this setting, we show experimentally that these systems are capable of closely approaching fundamental quantum limits—both in terms of the quality of the displacement sensitivity and the occupation of the mechanical oscillator.

In section 2.2, we first review basic theoretical concepts of optomechanics. Both an intuitive approach to understand effects such as optomechanical bistability and dynamical backaction, and a more formal approach based on the quantum Langevin equations are introduced.

Section 2.3 summarizes the properties of silica WGM resonators from the perspective of cavity optomechanics. Their optical properties are already described in chapter 1, so the attention is focused on their mechanical properties. Using analytical calculations and finite-element modeling, spatial shape, resonance frequencies and quality factors of the modes are analyzed. A detailed understanding of mechanical dissipation is developed, studying its dependence on temperature and geometry of the sample. This has allowed the design of optimized microtoroids in which mechanical quality factors are increased by more than an order of magnitude. Finally, the effective masses of the mechanical modes in this 3-dimensional structure are discussed.

## 2. Cavity optomechanics

Table 2.1: Key parameters of recently studied optomechanical systems. Earlier results are summarized in ref. [123].

| System  | Resonance frequency (Hz) | Quality factor <sup>a</sup> | Effective mass (g)   | Displacement sensitivity <sup>b</sup> (m/ $\sqrt{\text{Hz}}$ ) | References <sup>c</sup> |
|---|--------------------------|-----------------------------|----------------------|--|-------------------------|
| Internal modes of a silica mirror   | $1.86 \cdot 10^6$        | 40,000                      | $230 \cdot 10^{-3}$  | $2.0 \cdot 10^{-16}$   | [130] [131–133]         |
| Silicon torsional oscillator  | $26 \cdot 10^3$          | 4,300,000 <sup>d</sup>      | $10 \cdot 10^{-3}$   |  | [124] [134]             |
| AFM cantilevers (thermal)   | $7.28 \cdot 10^3$        | 2,000                       |                      |  | [135] [136]             |
| Silicon micromirror   | $0.81 \cdot 10^6$        | 10,000                      | $190 \cdot 10^{-6}$  | $2.0 \cdot 10^{-18}$   | [137] [138, 139]        |
| Free standing Bragg mirror  | 278 · 10 <sup>3</sup>    | 9,000                       | $400 \cdot 10^{-9}$  | $\sim 10^{-16}$  | [140] [141–143]         |
| Dielectric micromirror on silicon cantilever  | $12.5 \cdot 10^3$        | 18,000                      | $24 \cdot 10^{-9}$   | $1 \cdot 10^{-13}$   | [144] [145]             |
| Silica microtoroids   | $40.6 \cdot 10^6$        | 31,000 <sup>e</sup>         | $10 \cdot 10^{-9}$   | $1.0 \cdot 10^{-18}$   | [8] [1, 9, 10]          |
| Spiky silica microtoroids   | $38.0 \cdot 10^6$        | 80,000 <sup>f</sup>         |                      |  | [6]                     |
| Silica microspheres   | $87.2 \cdot 10^6$        | 15,600                      |                      |  | [5] [146]               |
| Chip-based silica microsphere   | $1.08 \cdot 10^9$        |                             |                      |  | [147]                   |
| Big suspended mirrors   | 173                      | 3,200                       |                      |  | [148], [149]            |
| Ultrasoft silicon cantilever  | $3.3 \cdot 10^3$         | 44,200 <sup>g</sup>         | $140 \cdot 10^{-12}$ | $1 \cdot 10^{-12}$   | [150]                   |
| Silicon cantilever  | $7 \cdot 10^3$           | 20,000                      | $2.4 \cdot 10^{-6}$  |  | [151]                   |
| Silicon nitride membrane  | $135 \cdot 10^3$         | 12,000,000 <sup>h</sup>     | $40 \cdot 10^{-9}$   | $4.5 \cdot 10^{-16}$   | [152] [153]             |
| Gold-coated silicon micropaddle   | $547 \cdot 10^3$         | 1,060                       | $11 \cdot 10^{-12}$  |  | [154]                   |
| Silica nanowire   | 193 <sup>i</sup>         |                             | $26 \cdot 10^{-9}$   |  | [155]                   |
| Mirror on a flexure mount   | 85                       | 44,500                      | 0.69                 | $3 \cdot 10^{-15}$   | [156]                   |
| Nanomechanical resonator coupled to SCMR <sup>j</sup>                                   | $1.53 \cdot 10^6$        | 300,000                     | $6.2 \cdot 10^{-12}$ | $45 \cdot 10^{-15}$  | [157] [41, 158, 159]    |
| Resonant-bar gravitational wave detector <sup>k</sup>                                   | 865                      | 1,200,000                   | $1.1 \cdot 10^{+6}$  |  | [160]                   |
| Silicon photonic circuit  | $8.87 \cdot 10^6$        | 1,850                       |                      | $18 \cdot 10^{-15}$  | [161]                   |
| Suspended mirrors in LIGO <sup>l</sup>  | $8.2 \cdot 10^6$         | $\sim 100$                  | $43 \cdot 10^{-12}$  | $2 \cdot 10^{-15}$   | [162]                   |
| Ta <sub>2</sub> O <sub>5</sub> /SiO <sub>2</sub> Bragg mirror on SigN <sub>4</sub> beam | $945 \cdot 10^3$         | 30,000 <sup>m</sup>         | $2.7 \cdot 10^{+3}$  | $2 \cdot 10^{-19}$   | [163]                   |
| e <sup>-</sup> -beam deposited nanorod  | $1.9 \cdot 10^6$         | 6,500                       | $43 \cdot 10^{-9}$   | $1 \cdot 10^{-16}$   | [164]                   |
| Silica double-disk resonator  | $8.5 \cdot 10^6$         | 4,070                       |                      | $1 \cdot 10^{-13}$   | [165]                   |
| Silicon optomechanical crystal  | $2.3 \cdot 10^9$         | 1,300                       | $330 \cdot 10^{-15}$ | $2 \cdot 10^{-15}$   | [166]                   |
| Silicon nitride nanoresonator   | $10.7 \cdot 10^6$        | 53,000                      | $3.6 \cdot 10^{-12}$ | $6.4 \cdot 10^{-16}$   | [167]                   |
| Trapped ion   | $71 \cdot 10^3$          |                             | $4.0 \cdot 10^{-23}$ |  | [12]                    |
| CaF <sub>2</sub> WGM resonator  | $1.06 \cdot 10^6$        | 136,000                     | 0.5                  |  | [168] [169]             |

<sup>a</sup> at room temperature unless noted otherwise, <sup>b</sup> experimental value, including all noise except for the mechanical mode of interest, <sup>c</sup> quoted numbers are from the references printed in bold, <sup>d</sup> at 2K, at room temperature 250,000, <sup>e</sup> at room temperature, for values at cryogenic temperatures see ref. [11], <sup>f</sup> at 410K, at room temperature 32,000, <sup>g</sup> at 4.2K, at room temperature 16,000, <sup>h</sup> at 300 mK, at room temperature 1,100,000, <sup>i</sup> the device is operated at d.c., <sup>j</sup> superconducting microwave resonator, <sup>k</sup> the resonance is a combined mechanical and electronic resonance, <sup>l</sup> laser interferometer gravitational wave interferometer. The resonance frequency is increased by electronic feedback on actuators controlling the mirror position, <sup>m</sup> at 5.3K, at room temperature 5,000

---

## 2.2 Theory of optomechanical interactions

Several quantum optical techniques for quantum-limited phase measurement of an optical field are introduced in section 2.4. The aim was to demonstrate the capability to observe zero-point fluctuations of the mechanical mode of interest. This is indeed possible with the extreme sensitivity achieved ( $10^{-18}$  m/ $\sqrt{\text{Hz}}$ ). Furthermore, signatures of several different thermal noise mechanisms are observed, and their origin is investigated.

In section 2.5, we report on our experiments demonstrating radiation-pressure induced laser cooling of a mechanical oscillator using dynamical backaction. Together with two groups in Paris and Vienna, we have first observed this long-anticipated effect in our Garching laboratory in 2006. Subsequently, we have carefully studied its dependence on the characteristic parameters of the optomechanical system. In particular, we have been interested in the regime of long intracavity photon storage times compared to the oscillation period of the mechanical oscillator.

This regime has attracted more interest as theoretical work predicted that cooling the oscillator to its quantum mechanical ground state via dynamical backaction is only possible under this condition. The results of our efforts to implement an optomechanical system operating in this so-called “resolved-sideband regime” are described in section 2.6. We demonstrated efficient radiation-pressure cooling in this regime. Classical and quantum limitations of laser cooling are discussed.

To reduce thermal noise even further, we have combined radiation pressure cooling with cryogenic precooling. The implementation of fiber-taper coupling and radiation-pressure cooling at cryogenic temperatures, and the results of these experiments are described in section 2.7. By bringing the mechanical oscillator close to its quantum ground state in these experiments, we have also been able to assess the backaction of the optical displacement detection. As a result we find that our optical measurement scheme performs in a near-ideal manner in quantum mechanical terms.

Section 2.8 concludes this chapter, summarizing the results achieved, and in section 2.9 we present ideas for future investigations using WGM resonators as optomechanical devices.

## 2.2 Theory of optomechanical interactions

### 2.2.1 Classical description and elementary phenomena

To begin the discussion of cavity optomechanics, it is useful to review some basic underlying physical concepts and simple limiting cases. Consider the generic optomechanical system depicted in figure 2.3a). The impinging field  $s_{\text{in}}(t)$  drives the cavity mode amplitude  $a(t)$  (cf. chapter 1). Part of the boundary of this mode—in the simplest case, one of the end mirrors of a Fabry-Perot cavity—is free to move, and its displacement is described by the one-dimensional variable  $x(t)$ . Irrespective of the spatial structure of both

## 2. Cavity optomechanics

the optical mode and the mechanical displacement pattern, we assume that the displacement  $x(t)$  shifts the resonance frequency of the optical mode in a linear fashion,

$$\omega'_c(t) = \omega_c + g_0 x(t), \quad (2.1)$$

where  $\omega_c$  is the cavity resonance frequency for  $x = 0$  and

$$g_0 = \frac{\partial \omega'_c}{\partial x} \quad (2.2)$$

is the optomechanical coupling constant. For the cases depicted in figure 2.3,  $g_0 = -\omega_c/L$  for a Fabry-Perot cavity of length  $L$ , and  $g_0 = -\omega_c/R$  for a WGM resonator of radius  $R$ .

### A moving cavity boundary

We will first discuss the effect of the moving boundary on the optical mode, and neglect the backaction (radiation pressure) of the light. For a monochromatic pump wave  $\bar{s}_{\text{in}} e^{-i\omega_1 t}$ , the resulting equation of motion for the intracavity field amplitude reads

$$\dot{a}(t) = \left( -i(\omega_c + g_0 x(t)) - \frac{\kappa}{2} \right) a(t) + \sqrt{\eta_c \kappa} \bar{s}_{\text{in}} e^{-i\omega_1 t}. \quad (2.3)$$

As one of the simplest cases, we analyze the response of the driven cavity to a sinusoidal oscillation in the mechanical degree of freedom. For  $x(t) = x_0 \sin(\Omega_m t)$ , the solution for the mode amplitude reads

$$a(t) = \sqrt{\eta_c \kappa} \bar{s}_{\text{in}} \sum_{n=-\infty}^{+\infty} \frac{i^n J_n(\beta)}{-i(\omega_1 + n\Omega_m - \omega_c) + \kappa/2} e^{-i(\omega_1 + n\Omega_m)t - i\beta \cos(\Omega_m t)} \quad (2.4)$$

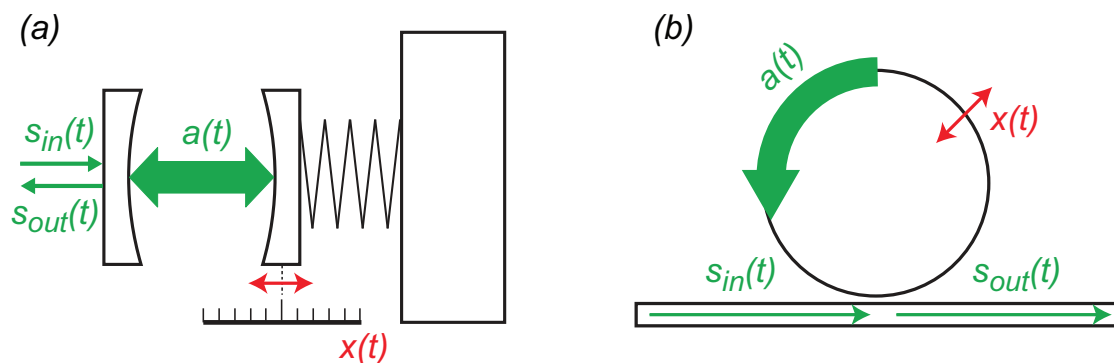


Figure 2.3: Schematic of two generic geometries of optomechanical systems. (a) Linear Fabry-Perot-type cavity with a movable mirror, pumped through a slightly transparent mirror. (b) Whispering-gallery mode resonator pumped by evanescent coupling to a waveguide. In both cases, an impinging field  $s_{\text{in}}(t)$  drives the intracavity field  $a(t)$ . The cavity resonance frequency depends on the displacement  $x(t)$  of a cavity boundary from its equilibrium position.

## 2.2 Theory of optomechanical interactions

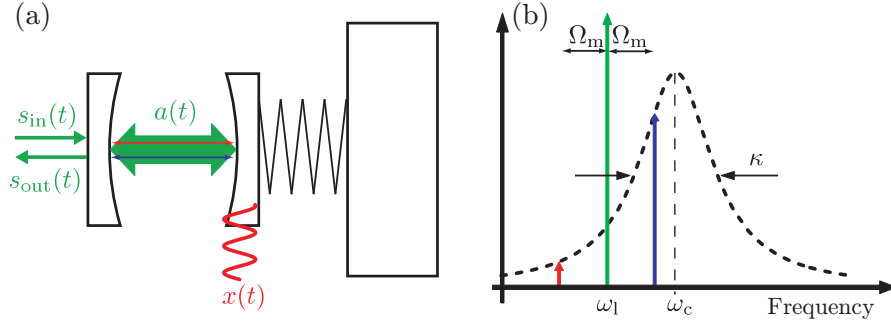


Figure 2.4: Response of a driven cavity to an oscillating end mirror (a), leading to a buildup of anti-Stokes and Stokes sidebands at frequencies  $\omega_1 + \Omega_m$  and  $\omega_1 - \Omega_m$ , weighted with the cavity Lorentzian (b).

after all transients have died off within a timescale of  $\kappa^{-1}$  [8]. Here, the  $J_n$  are the Bessel functions of the first kind and  $\beta = g_0 x_0 / \Omega_m$  is the modulation index. For small amplitudes  $x_0$ , so that  $|\beta| \ll 1$ , the intracavity field can be approximated to

$$a(t) \approx a_0(t) + a_1(t) + \mathcal{O}(\beta^2) \quad (2.5)$$

$$a_0(t) = \frac{\sqrt{\eta_c \kappa} \bar{s}_{\text{in}}}{-i\Delta + \kappa/2} e^{-i\omega_1 t} \quad (2.6)$$

$$a_1(t) = \frac{g_0 x_0}{2} \frac{\sqrt{\eta_c \kappa} \bar{s}_{\text{in}}}{-i\Delta + \kappa/2} \left( \underbrace{\frac{e^{-i(\omega_1 + \Omega_m)t}}{-i(\Delta + \Omega_m) + \kappa/2}}_{\text{anti-Stokes}} - \underbrace{\frac{e^{-i(\omega_1 - \Omega_m)t}}{-i(\Delta - \Omega_m) + \kappa/2}}_{\text{Stokes}} \right). \quad (2.7)$$

Evidently, the moving boundary acts as a modulator, building up a pair of sidebands  $a_1$  in the cavity, with weights proportional to the cavity Lorentzian evaluated at the frequencies  $\omega_1 + \Omega_m$  and  $\omega_1 - \Omega_m$  for the upper and lower sideband, respectively. These sidebands, schematically shown in figure 2.4, are also often referred to as anti-Stokes and Stokes sidebands.

The presence of these sidebands corresponds to a modulation of the intracavity stored energy  $|a(t)|^2$ , and it is easy to show that

$$\begin{aligned} |a(t)|^2 &\approx |a_0(t)|^2 + a_0(t)a_1^*(t) + a_0^*(t)a_1(t) = \quad (2.8) \\ &= \frac{\eta_c \kappa |\bar{s}_{\text{in}}|^2}{\Delta^2 + (\kappa/2)^2} \left( 1 + \right. \\ &\quad g_0 x_0 \left( \frac{\Delta + \Omega_m}{(\Delta + \Omega_m)^2 + (\kappa/2)^2} + \frac{\Delta - \Omega_m}{(\Delta - \Omega_m)^2 + (\kappa/2)^2} \right) \sin(\Omega_m t) + \\ &\quad \left. g_0 x_0 \left( \frac{\kappa/2}{(\Delta + \Omega_m)^2 + (\kappa/2)^2} - \frac{\kappa/2}{(\Delta - \Omega_m)^2 + (\kappa/2)^2} \right) \cos(\Omega_m t) \right). \quad (2.9) \end{aligned}$$

## 2. Cavity optomechanics

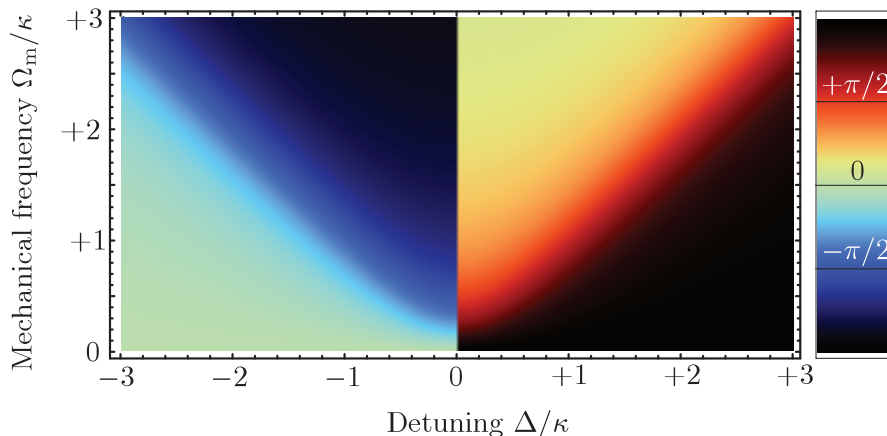


Figure 2.5: Phase lag  $\phi_{\text{lag}}$  between the oscillation of the mechanical degree of freedom and the stored optical energy (or circulating power) in the cavity, assuming  $g_0 < 0$ . For  $\pm\Delta = \Omega_m \gg \kappa$  the phase lag is exactly  $\mp\pi/2$ . The phase jump at  $\Delta = 0$  is due to a zero crossing of the oscillation amplitude of the stored optical energy.

The intracavity optical energy is modulated at the oscillation frequency  $\Omega_m$ , however, the modulation does not necessarily occur in phase with the mechanical oscillation. In fact, the phase lag depends in a non-trivial manner on the detuning  $\Delta$ , oscillation frequency  $\Omega_m$  and the cavity buildup time  $\kappa^{-1}$ , a simple calculation yields

$$\phi_{\text{lag}} = \arg \left( g_0 \Delta (\Delta^2 + (\kappa/2)^2 - \Omega_m^2 - i\Omega_m \kappa) \right), \quad (2.10)$$

which is shown in figure 2.5. The quadrature component ( $\propto \cos(\Omega_m t)$ ), the important role of which will soon become clearer, can become significant if the cavity buildup time  $\kappa^{-1}$  is comparable or larger than the oscillation period  $\Omega_m^{-1}$ . Both in-phase and quadrature component are shown in the parametric plot in figure 2.6.

### Radiation-pressure backaction: static phenomena

So far, only the effect of the mechanical on the optical degree of freedom has been considered. However, the richness of optomechanical effects arises only when the *mutual* coupling of optical and mechanical degrees of freedom is taken into account. The physical origin of the “back-action” of light on the movable cavity boundary is due to radiation pressure. In the simple case of a Fabry-Perot cavity, the force arises from the momentum flips of the photons reflected from the movable mirror, and thus

$$F_{\text{rp}}(t) = |a(t)|^2 \frac{c}{2L} 2\hbar k = \frac{|a(t)|^2 \hbar \omega_1}{L} = -\hbar g_0 |a(t)|^2, \quad (2.11)$$

where  $\hbar k$  with  $k = \omega_1/c$  is the momentum of the photons. Note that, for convenience, we switched to normalization of  $|a(t)|^2$  to photon number now,

## 2.2 Theory of optomechanical interactions

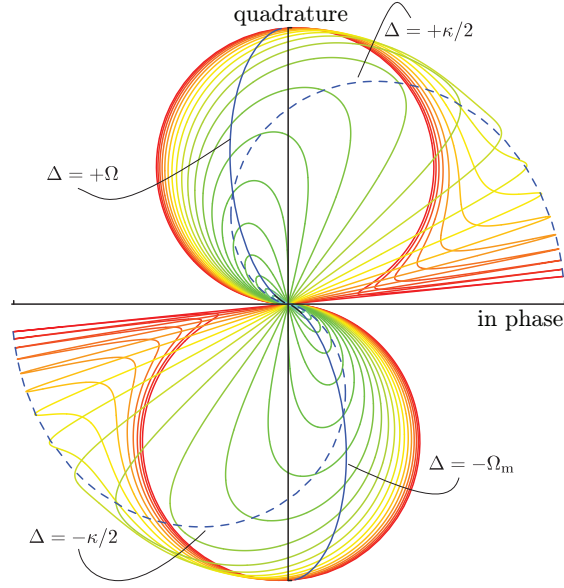


Figure 2.6: In-phase and quadrature oscillation amplitude of the intracavity energy (or circulating power) when the detuning is varied (colored curves). Different colors represent different choices of the cavity linewidth  $\kappa$ , which was changed from  $\Omega_m/10$  (green) to  $10\Omega_m$  (red) in logarithmic steps. In the blue curves, a fixed detuning was chosen (as indicated by the labels), and the cavity linewidth was varied from  $\Omega_m/10$  to  $10\Omega_m$ .

and will pursue this consistently in this chapter. Equivalently,  $|s_{\text{in}}(t)|^2$  now denotes the photon flux impinging on the coupling region.

The relation  $F_{\text{rp}}(t) = -\hbar g_0 |a(t)|^2$  is actually generally valid, it also applies to the WGM resonators, as will be derived in section 2.3.3. If the cavity boundary is free to move, the coupled equations describing the optomechanical system will then read (in a frame rotating at the laser frequency)

$$\dot{a}(t) = (i(\Delta - g_0 x(t)) - \kappa/2) a(t) + \sqrt{\eta_c \kappa} s_{\text{in}}(t) \quad (2.12)$$

$$\ddot{x}(t) + \Gamma_m \dot{x}(t) + \Omega_m^2 x(t) = -\hbar g_0 \frac{|a(t)|^2}{m_{\text{eff}}}, \quad (2.13)$$

where, for the mechanical oscillation, a resonance frequency  $\Omega_m$ , viscous damping at a rate  $\Gamma_m$ , and an effective mass  $m_{\text{eff}}$  (cf. section 2.3.3) are assumed. For a constant drive amplitude  $\bar{s}_{\text{in}}$ , these coupled nonlinear equations can be analyzed in a first step by looking for stable solutions  $a(t) = \bar{a}$ ,  $x(t) = \bar{x}$  in which all time derivatives ( $\dot{a}(t), \dot{x}(t), \ddot{x}(t)$ ) vanish, requiring simultaneously

$$\bar{a} = \frac{1}{-i(\Delta - g_0 \bar{x}) + \kappa/2} \sqrt{\eta_c \kappa} \bar{s}_{\text{in}} \quad \text{and} \quad (2.14)$$

$$m_{\text{eff}} \Omega_m^2 \bar{x} = -\hbar g_0 |\bar{a}|^2. \quad (2.15)$$

Equations (2.14) and (2.15) can be illustrated by understanding both of them as functions mapping the displacement  $\bar{x}$  to an intracavity photon number

## 2. Cavity optomechanics

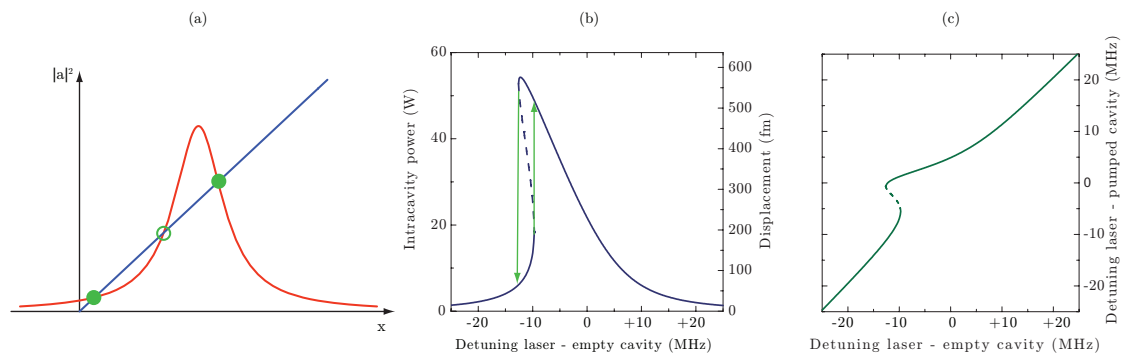


Figure 2.7: (a) Graphical representation of the self-consistent solutions of the coupled equations (2.14) (red) and (2.15) (blue) for the intracavity optical energy  $|\bar{a}|^2$  and the radiation-pressure induced displacement  $\bar{x}$  of the cavity radius. Intersections of the curves indicate possible stable (full circles) and unstable (empty circles) solutions. (b) Plot of numerical solutions for the power  $|\bar{a}|^2/\tau_{rt}$  circulating in the cavity and the radiation-pressure induced displacement for typical parameters of a silica microtoroidal optomechanical oscillator ( $R = 25 \mu\text{m}$ ,  $\kappa = 2\pi 8 \text{ MHz}$ ,  $\Omega_m = 2\pi 50 \text{ MHz}$ ,  $m_{\text{eff}} = 20 \text{ ng}$ ,  $\omega_c = 2\pi 380 \text{ THz}$ ,  $|\bar{s}_{\text{in}}|^2 = 1 \text{ mW}$ ). The dashed line indicates the unstable solutions. (c) The actual detuning  $\Delta - g_0 \bar{x}$  as a function of the detuning  $\Delta$  of the laser from the undriven cavity resonance.

$|\bar{a}|^2$ , as shown in figure 2.7. The self-consistent, physically possible solutions are given by the intersections of the two curves.<sup>1</sup> Evidently, the system has at least one solution for arbitrary parameters. For high enough powers or finesse, and/or floppy enough mechanical oscillators, two additional solutions are physically possible. The condition for their appearance is given by

$$|\bar{s}_{\text{in}}|^2 \geq \frac{\sqrt{3}}{9} \frac{\Omega_m^2 m_{\text{eff}} \kappa^2}{\eta_c \hbar g_0^2}, \quad (2.16)$$

which is derived in a straightforward manner from the requirement that the maximum slope  $3\sqrt{3}|\bar{s}_{\text{in}}|^2 \eta_c |g_0|/\kappa^2$  of the Lorentzian square modulus of (2.14) must exceed the slope  $m_{\text{eff}} \Omega_m^2/\hbar |g_0|$  corresponding to (2.15). Above this threshold, the optomechanical system displays a well-known bistable behavior, resulting, for example, in a hysteretic transmission behavior upon the variation of the input power. This effect was observed in a pioneering experiment [170] at the Max-Planck-Institute of Quantum Optics as early as 1983. Reports in the microwave domain followed soon thereafter [171].

### Radiation-pressure backaction: dynamical effects

It is even more interesting to analyze the dynamical response of such a system around an equilibrium  $(\bar{a}, \bar{x})$ . As first pointed out by Braginsky and co-workers decades ago [97, 100, 102], the dynamics of fluctuations around the equilibrium do not only display new physical effects, but are also of experimental relevance, in particular in the most sensitive gravitational wave

<sup>1</sup>Note that the phase of the complex entity  $\bar{a}$  can always be adjusted to fulfill (2.14), as it does not affect (2.15).

## 2.2 Theory of optomechanical interactions

interferometers. Keeping with the simple illustrative approach of this section, let us assume the system is in a stable equilibrium if  $a = \bar{a}$  and  $x = \bar{x}$  and analyze the dynamics of small excursions  $\delta a(t)$  and  $\delta x(t)$  if a small external force  $\delta F(t)$  is applied to the mechanical oscillator. Plugging  $a(t) = \bar{a} + \delta a(t)$ ,  $x(t) = \bar{x} + \delta x(t)$  into (2.12)–(2.13) and introducing the equilibrium detuning

$$\bar{\Delta} \equiv \omega_1 - (\omega_c + g_0 \bar{x}) \quad (2.17)$$

one finds the linearized equations

$$\dot{\delta a}(t) = (+i\bar{\Delta} - \kappa/2)\delta a(t) - ig_0\bar{a}\delta x(t) \quad (2.18)$$

$$m_{\text{eff}} \left( \ddot{\delta x}(t) + \Gamma_m \dot{\delta x}(t) + \Omega_m^2 \delta x(t) \right) = -\hbar g_0 \bar{a} (\delta a(t) + \delta a^*(t)) + \delta F(t), \quad (2.19)$$

where (2.14) and (2.15) were used, and second-order terms  $\propto \delta a(t)\delta x(t)$  or  $\propto |\delta a(t)|^2$  were dropped, as we assume  $|\delta a| \ll |\bar{a}|$ . Furthermore, without loss of generality, we have assumed real  $\bar{a} = \bar{a}^*$ , which can always be attained by adjusting the (physically irrelevant) phase of the incoming driving wave  $\bar{s}_{\text{in}}$ .

This equation system is most easily solved in the frequency domain, by applying a Fourier transformation to all involved time-dependent variables.<sup>2</sup> One then obtains

$$-i\Omega\delta a(\Omega) = (+i\bar{\Delta} - \kappa/2)\delta a(\Omega) - ig_0\bar{a}\delta x(\Omega) \quad (2.20)$$

$$-i\Omega\delta a^*(\Omega) = (-i\bar{\Delta} - \kappa/2)\delta a^*(\Omega) + ig_0\bar{a}\delta x(\Omega) \quad (2.21)$$

$$m_{\text{eff}} \left( -\Omega^2 - i\Gamma_m\Omega + \Omega_m^2 \right) \delta x(\Omega) = -\hbar g_0 \bar{a} (\delta a(\Omega) + \delta a^*(\Omega)) + \delta F(\Omega), \quad (2.22)$$

where  $\delta a^*(\Omega) = (\delta a(-\Omega))^*$  was used. Analogous to the introductory considerations of a moving boundary, we now find that a non-zero displacement amplitude  $\delta x(\Omega)$  at Fourier frequency  $\Omega$  induces anti-Stokes and Stokes sidebands of amplitudes

$$\delta a(\Omega) = \frac{-ig_0\bar{a}}{-i(\bar{\Delta} + \Omega) + \kappa/2} \delta x(\Omega) \quad (2.23)$$

$$\delta a^*(\Omega) = \frac{+ig_0\bar{a}}{+i(\bar{\Delta} - \Omega) + \kappa/2} \delta x(\Omega), \quad (2.24)$$

respectively. As above, the intracavity energy gets modulated, but now we

---

<sup>2</sup>We choose the convention  $f(\Omega) = \int_{-\infty}^{+\infty} f(t)e^{+i\Omega t} dt$ .

## 2. Cavity optomechanics

---

have to consider that this gives rise to an oscillating force,

$$\delta F_{\text{rp}}(\Omega) = -\hbar g_0 \bar{a} (\delta a(\Omega) + \delta a^*(\Omega)) = \quad (2.25)$$

$$\begin{aligned} &= -\hbar g_0^2 \bar{a}^2 \left( \frac{\bar{\Delta} + \Omega}{(\bar{\Delta} + \Omega)^2 + (\kappa/2)^2} + \frac{\bar{\Delta} - \Omega}{(\bar{\Delta} - \Omega)^2 + (\kappa/2)^2} \right) \delta x(\Omega) \\ &\quad + i\hbar g_0^2 \bar{a}^2 \left( \frac{\kappa/2}{(\bar{\Delta} + \Omega)^2 + (\kappa/2)^2} - \frac{\kappa/2}{(\bar{\Delta} - \Omega)^2 + (\kappa/2)^2} \right) \delta x(\Omega) \end{aligned} \quad (2.26)$$

The real and imaginary parts of the radiation pressure force in this representation are easily identified as being due to the in-phase and quadrature modulation of the circulating power in the cavity, which was derived above. The additional force acting on the mechanical oscillator changes its dynamical behavior, in particular its response to the external perturbation. This effect is the essence of *dynamical backaction*.

Specifically, substituting (2.26) back into (2.22), one finds a modified response of the oscillator to an external force,

$$\delta x(\Omega) = \chi_{\text{eff}}(\Omega) \delta F(\Omega) \quad (2.27)$$

with the effective susceptibility  $\chi_{\text{eff}}(\Omega)$ ,

$$\chi_{\text{eff}}(\Omega)^{-1} = m_{\text{eff}} \left( -\Omega^2 - i(\Gamma_m + \Gamma_{\text{dba}}(\Omega))\Omega + \left( \Omega_m^2 + \frac{k_{\text{dba}}(\Omega)}{m_{\text{eff}}} \right) \right). \quad (2.28)$$

The damping and spring constant induced by dynamical backaction are given by

$$\Gamma_{\text{dba}} = \frac{\hbar g_0^2 \bar{a}^2}{m_{\text{eff}} \Omega} \left( \frac{\kappa/2}{(\bar{\Delta} + \Omega)^2 + (\kappa/2)^2} - \frac{\kappa/2}{(\bar{\Delta} - \Omega)^2 + (\kappa/2)^2} \right) \quad (2.29)$$

$$k_{\text{dba}} = \frac{\hbar g_0^2 \bar{a}^2}{m_{\text{eff}}} \left( \frac{\bar{\Delta} + \Omega}{(\bar{\Delta} + \Omega)^2 + (\kappa/2)^2} + \frac{\bar{\Delta} - \Omega}{(\bar{\Delta} - \Omega)^2 + (\kappa/2)^2} \right). \quad (2.30)$$

If the induced changes of the mechanical oscillator's dynamics are small, the oscillator still behaves as a damped harmonic oscillator with effective damping and resonance frequency [1]

$$\Gamma_{\text{eff}} \approx \Gamma_m + \frac{\hbar g_0^2 \bar{a}^2}{m_{\text{eff}} \Omega_m} \left( \frac{\kappa/2}{(\bar{\Delta} + \Omega_m)^2 + (\kappa/2)^2} - \frac{\kappa/2}{(\bar{\Delta} - \Omega_m)^2 + (\kappa/2)^2} \right) \quad (2.31)$$

$$\Omega_{\text{eff}} \approx \Omega_m + \frac{\hbar g_0^2 \bar{a}^2}{2m_{\text{eff}} \Omega_m} \left( \frac{\bar{\Delta} + \Omega_m}{(\bar{\Delta} + \Omega_m)^2 + (\kappa/2)^2} + \frac{\bar{\Delta} - \Omega_m}{(\bar{\Delta} - \Omega_m)^2 + (\kappa/2)^2} \right). \quad (2.32)$$

## 2.2 Theory of optomechanical interactions

### 2.2.2 Formal framework: quantum Langevin equations

A more general formulation of optomechanical interactions than the simple but illustrative considerations in the previous section is possible within the framework of a quantum Langevin approach. This enables the full description of the quantum dynamics of an optomechanical system. In particular, effects related to the quantum nature of light can be treated in an adequate manner.

#### Hamiltonian of cavity optomechanics

Starting point of the analysis is a Hamiltonian formulation of a generic optomechanical system put forward by Law [172]. If the mechanical oscillation frequency is much smaller than the free spectral range of the cavity, so that a only a single optical mode has to be considered, the system Hamiltonian can be written as

$$\hat{H} = \hat{H}_{\text{mech}} + \hat{H}_{\text{opt}} + \hat{H}_{\text{int}} + \hat{H}_{\text{drive}} \quad (2.33)$$

$$\hat{H}_{\text{mech}} = \frac{\hat{p}^2}{2m_{\text{eff}}} + \frac{1}{2}m_{\text{eff}}\Omega_{\text{m}}^2\hat{x}^2 \quad (2.34)$$

$$\hat{H}_{\text{opt}} = \hbar\omega_{\text{c}} \left( \hat{a}^\dagger \hat{a} + \frac{1}{2} \right) \quad (2.35)$$

$$\hat{H}_{\text{int}} = \hbar g_0 \hat{x} \hat{a}^\dagger \hat{a} \quad (2.36)$$

$$\hat{H}_{\text{drive}} = i\hbar\sqrt{\eta_{\text{c}}\kappa} \left( \bar{s}_{\text{in}}\hat{a}^\dagger e^{-i\omega_1 t} - \bar{s}_{\text{in}}^*\hat{a}e^{+i\omega_1 t} \right) \quad (2.37)$$

where  $\hat{x}$  and  $\hat{p}$  are the mechanical displacement and momentum operators, and  $\hat{a}^\dagger$  and  $\hat{a}$  are the creation and annihilation operators of the considered optical mode, i. e.  $\hat{n} = \hat{a}^\dagger \hat{a}$  is the intracavity photon operator, and correspondingly, the drive amplitude  $\bar{s}_{\text{in}}$  is now normalized to photon flux at the input of the cavity  $|\bar{s}_{\text{in}}|^2 = P_{\text{in}}/\hbar\omega_1$ . Evidently, this Hamiltonian reproduces the optical resonance frequency shift upon mechanical displacement, as

$$\hat{H}_{\text{opt}} + \hat{H}_{\text{int}} = \hbar(\omega_{\text{c}} + g_0\hat{x}) \hat{a}^\dagger \hat{a}, \quad (2.38)$$

and simultaneously describes the radiation pressure force, with

$$F_{\text{rp}} = -\frac{\partial \hat{H}_{\text{int}}}{\partial \hat{x}} = -\hbar g_0 \hat{a}^\dagger \hat{a}. \quad (2.39)$$

#### Quantum Langevin equations

From the Hamiltonian, the time evolution of the operators of interest can be derived. In addition to the conservative dynamics described by (2.33), dissipation of both the optical and mechanical modes, and the corresponding

## 2. Cavity optomechanics

fluctuations are taken into account by the following set of quantum Langevin equations (QLEs) [173] (in a frame rotating at  $\omega_1$ )

$$\frac{d}{dt}\hat{a}(t) = \left(+i\Delta - \frac{\kappa}{2}\right)\hat{a}(t) - ig_0\hat{x}(t)\hat{a}(t) + \frac{(\bar{s}_{\text{in}} + \delta\hat{s}_{\text{in}}(t))}{\sqrt{\tau_{\text{ex}}}} + \frac{\delta\hat{s}_{\text{vac}}(t)}{\sqrt{\tau_0}} \quad (2.40)$$

$$\frac{d}{dt}\hat{x}(t) = \frac{\hat{p}(t)}{m_{\text{eff}}} \quad (2.41)$$

$$\frac{d}{dt}\hat{p}(t) = -m_{\text{eff}}\Omega_{\text{m}}^2\hat{x}(t) - \hbar g_0\hat{a}^\dagger(t)\hat{a}(t) - \Gamma_{\text{m}}\hat{p}(t) + \delta\hat{F}_{\text{th}}(t) \quad (2.42)$$

where the noise terms  $\delta\hat{s}_{\text{in}}$ ,  $\delta\hat{s}_{\text{vac}}$ , and  $\delta\hat{F}_{\text{th}}$  were introduced. They fulfill the commutation relations [174]

$$[\delta\hat{s}_{\text{in}}(t), \delta\hat{s}_{\text{in}}^\dagger(t')] = [\delta\hat{s}_{\text{vac}}(t), \delta\hat{s}_{\text{vac}}^\dagger(t')] = \delta(t - t') \quad (2.43)$$

and

$$\langle \delta\hat{s}_{\text{in}}(t)\delta\hat{s}_{\text{in}}^\dagger(t') \rangle = \langle \delta\hat{s}_{\text{vac}}(t)\delta\hat{s}_{\text{vac}}^\dagger(t') \rangle = \delta(t - t') \quad (2.44)$$

are the only non-zero correlators for the quantum vacuum entering the cavity from its two ports: the one through which it is pumped ( $\delta\hat{s}_{\text{in}}$ ), and the second port ( $\delta\hat{s}_{\text{vac}}$ ) representing all other loss channels. Here, zero thermal excitation of the optical mode has been assumed. In order to adequately describe the mirror undergoing Brownian motion the correlator of the mechanical driving term can be shown [173] to have the form

$$\langle \delta\hat{F}_{\text{th}}(t)\delta\hat{F}_{\text{th}}(t') \rangle = \hbar m_{\text{eff}}\Gamma_{\text{m}} \int e^{-i\Omega(t-t')} \Omega \left( \coth\left(\frac{\hbar\Omega}{2k_{\text{B}}T}\right) + 1 \right) \frac{d\Omega}{2\pi} \quad (2.45)$$

As in the previous subsection, the QLEs are simplified in the first place by considering static and the dynamical effects separately. To this end, the unitary transformations  $\hat{a}(t) = \bar{a} + \delta\hat{a}(t)$  and  $\hat{x}(t) = \bar{x} + \delta\hat{x}(t)$  with  $\langle \delta\hat{a}(t) \rangle = \langle \delta\hat{x}(t) \rangle = 0$  yields again the requirements (2.14)–(2.15) for the steady state values of intracavity field amplitude  $\bar{a}$  and displacement  $\bar{x}$ .

### Dynamics of the fluctuations

If we assume  $(\bar{a}, \bar{x})$  to be known as a stable solution of the system (which can, for example, be tested for using the Routh-Hurwitz criterion, see [107]), we can derive the Heisenberg equation of motion for the fluctuations  $\delta\hat{a}$ ,  $\delta\hat{a}^\dagger$  and  $\delta\hat{x}$ . Choosing again the phase of the input field  $\bar{s}_{\text{in}}$  such that  $\bar{a}$  is real and positive, and assuming again a strong coherent drive

$$\bar{a} \gg 1 \quad (2.46)$$

### 2.3 Silica WGM resonators as optomechanical systems

it is possible to derive linearized quantum Langevin equations for the fluctuations by dropping terms  $\propto \delta\hat{a}\delta\hat{x}$ ,  $\delta\hat{a}^\dagger\delta\hat{x}$  or  $\delta\hat{a}^\dagger\delta\hat{a}$ , yielding

$$\frac{d}{dt}\delta\hat{a}(t) = \left(+i\bar{\Delta} - \frac{\kappa}{2}\right)\delta\hat{a}(t) - ig_0\bar{a}\delta\hat{x}(t) + \frac{\delta\hat{s}_{\text{in}}(t)}{\sqrt{\tau_{\text{ex}}}} + \frac{\delta\hat{s}_{\text{vac}}(t)}{\sqrt{\tau_0}} \quad (2.47)$$

$$\frac{d}{dt}\delta\hat{a}^\dagger(t) = \left(-i\bar{\Delta} - \frac{\kappa}{2}\right)\delta\hat{a}^\dagger(t) + ig_0\bar{a}\delta\hat{x}(t) + \frac{\delta\hat{s}_{\text{in}}^\dagger(t)}{\sqrt{\tau_{\text{ex}}}} + \frac{\delta\hat{s}_{\text{vac}}^\dagger(t)}{\sqrt{\tau_0}} \quad (2.48)$$

$$\frac{d^2}{dt^2}\delta\hat{x}(t) + \Gamma_m\frac{d}{dt}\delta\hat{x}(t) + \Omega_m^2\delta\hat{x}(t) = -\frac{\hbar g_0}{m_{\text{eff}}}\bar{a}\left(\delta\hat{a}(t) + \delta\hat{a}^\dagger(t)\right) + \frac{\delta\hat{F}_{\text{th}}(t)}{m_{\text{eff}}} \quad (2.49)$$

where the Hermitian property  $\delta\hat{x}(t) = \delta\hat{x}^\dagger(t)$  was used. This set of equations is most easily solved in the Fourier domain, and we obtain

$$\left(-i(\bar{\Delta} + \Omega) + \kappa/2\right)\delta\hat{a}(\Omega) = -ig_0\bar{a}\delta\hat{x}(\Omega) + \frac{\delta\hat{s}_{\text{in}}(\Omega)}{\sqrt{\tau_{\text{ex}}}} + \frac{\delta\hat{s}_{\text{vac}}(\Omega)}{\sqrt{\tau_0}} \quad (2.50)$$

$$\left(+i(\bar{\Delta} - \Omega) + \kappa/2\right)\delta\hat{a}^\dagger(\Omega) = +ig_0\bar{a}\delta\hat{x}(\Omega) + \frac{\delta\hat{s}_{\text{in}}^\dagger(\Omega)}{\sqrt{\tau_{\text{ex}}}} + \frac{\delta\hat{s}_{\text{vac}}^\dagger(\Omega)}{\sqrt{\tau_0}} \quad (2.51)$$

$$m_{\text{eff}}\left(\Omega_m^2 - \Omega^2 - i\Gamma_m\Omega\right)\delta\hat{x}(\Omega) = -\hbar g_0\bar{a}\left(\delta\hat{a}(\Omega) + \delta\hat{a}^\dagger(\Omega)\right) + \delta\hat{F}_{\text{th}}(\Omega). \quad (2.52)$$

In the frequency domain,

$$\langle\delta\hat{s}_{\text{in}}(\Omega)\delta\hat{s}_{\text{in}}^\dagger(\Omega')\rangle = 2\pi\delta(\Omega + \Omega') \quad (2.53)$$

$$\langle\delta\hat{s}_{\text{vac}}(\Omega)\delta\hat{s}_{\text{vac}}^\dagger(\Omega')\rangle = 2\pi\delta(\Omega + \Omega') \quad (2.54)$$

and

$$\langle\delta\hat{F}_{\text{th}}(\Omega)\delta\hat{F}_{\text{th}}[\Omega']\rangle = 2\pi\delta(\Omega + \Omega')\hbar m_{\text{eff}}\Gamma_m\Omega\left(\coth\left(\frac{\hbar\Omega}{2k_{\text{B}}T}\right) + 1\right) \quad (2.55)$$

are the only non-zero correlators. Together with the input-output relations for the fluctuations

$$\delta\hat{s}_{\text{out}}(\Omega) = \delta\hat{s}_{\text{in}}(\Omega) - \sqrt{\eta_c\kappa}\delta\hat{a}(\Omega) \quad (2.56)$$

$$\delta\hat{s}_{\text{out}}^\dagger(\Omega) = \delta\hat{s}_{\text{in}}^\dagger(\Omega) - \sqrt{\eta_c\kappa}\delta\hat{a}^\dagger(\Omega) \quad (2.57)$$

these equations constitute the theoretical description of the most important effects in cavity optomechanics.

### 2.3 Silica whispering gallery-mode microresonators as optomechanical systems

Before the experiments on optomechanics are discussed, in the following, the most relevant properties of silica microresonators in the context of cavity optomechanics will be discussed.

## 2. Cavity optomechanics

---

### 2.3.1 Optical properties of WGM microresonators

The optical properties of silica microresonators were already discussed in chapter 1. Here, only the properties relevant for the purposes of cavity optomechanics are revised.

An essential precondition to render the weak effects of radiation pressure experimentally accessible is a high finesse. In a cavity of finesse  $\mathcal{F}$ , the circulating power—and thus also the radiation pressure force—is enhanced by a factor of  $\sim \mathcal{F}/\pi$  compared to the launched power. Silica microresonators can achieve finesse on the order of  $10^6$  (cf. section 1.2), exceeding even the best results achieved with Fabry-Perot cavities for cavity QED [19].

At the same time, in order to reveal dynamical effects of radiation-pressure coupling, the photon storage time should be on the order of—or ideally exceed—the period of the mechanical oscillator coupled to the resonator. In spite of the very short round-trip time of about 1 ps, the storage time can amount to several hundreds of nanoseconds thanks to the high finesse. This is about 10 times longer than the oscillation period of the mechanical modes in these devices. To ensure well-controlled optomechanical interaction, the optical mode spectrum must be well understood. In most experiments, light should only interact with one isolated optical mode. With a free spectral range  $c/2\pi nR$  in the THz range, and an easy suppression of higher-order transverse modes (at least for *microtoroids*), this requirement is easily fulfilled.

Absorption of light in the resonator, as discussed in detail in subsection 1.5.1, leads to an increase of the temperature of the structure. This is important for experiments in optomechanics for a two-fold reason. First, a temperature increase may be undesired for the observation of mechanical oscillators in a low-energy state: If the whole structure heats up, the mechanical mode of interest will be thermalized to this bath on the timescale of its intrinsic damping, usually much shorter than the timescale of the measurements made. While at room temperature, even absorbed powers on the order of 1 mW lead to relative temperature changes on the order of only 10%, heating can be much more significant at cryogenic temperatures (cf. section 2.7).

Secondly, the temperature rise leads to a change in refractive index and material expansion, resulting in an intracavity-power dependent frequency shift. This effective optical nonlinearity gives rise to optical bistability, and in particular, it renders one wing of the optical resonance dynamically unstable against inevitable perturbations in the detuning of the laser with respect to the WGM resonance. This effect is important for experiments, in which the driving laser is detuned from the optical resonance, as required for the observation of dynamical backaction [1]. It is noted here that due to the inversion of the thermorefractive coefficient  $\partial n/\partial T$  at  $\sim 8$  K, it is the red wing ( $\omega_1 < \omega_c$ ) which gets unstable at room temperature, while the blue

## 2.3 Silica WGM resonators as optomechanical systems

---

wing ( $\omega_1 > \omega_c$ ) gets unstable at cryogenic temperatures.

### 2.3.2 Mechanical properties of WGM silica microresonators

The mechanical degree(s) of freedom coupled parametrically to the WGMs in silica microresonators are simply given by the intrinsic acoustic modes of the structure. Each of the eigenmodes can be viewed, to a good approximation, as a damped harmonic oscillator, possibly driven by thermal or optical forces. In the following, the nature of these modes, in particular, their eigenfrequency, the damping mechanisms, (effective) mass, mode shapes, and coupling to the optical degrees of freedom will be discussed.

#### Acoustic modes in silica microresonators

The deformation induced by acoustic modes is described by a vector field  $\vec{u}(\vec{r}, t)$ , which denotes the displacement of an (infinitesimally small) cubic volume element at position  $\vec{r}$  and time  $t$  from its initial position. In an isotropic homogenous medium, to which no external forces are applied, the equation of motion for the displacement field reads [175]

$$\rho \ddot{\vec{u}}(\vec{r}, t) = (\lambda + \mu) \vec{\nabla}(\vec{\nabla} \cdot \vec{u}(\vec{r}, t)) + \mu \vec{\nabla}^2 \vec{u}(\vec{r}, t) \quad (2.58)$$

where the density  $\rho$  and the Lamé constants

$$\lambda = \frac{\sigma E}{(1 + \sigma)(1 - 2\sigma)} \quad (2.59)$$

$$\mu = \frac{E}{2(1 + \sigma)}, \quad (2.60)$$

with  $\sigma$  is Poisson's ratio and  $E$  Young's modulus, characterize the elastic properties of the material.

While for an infinitely extended medium, a continuum of solutions for (2.58) are obtained, for a finite-size body such as a silica sphere or toroid, the boundary conditions lead to a discrete spectrum of solutions, so that the total displacement  $\vec{u}(\vec{r}, t)$  can be decomposed into modes oscillating harmonically at a set of frequencies  $\Omega_n$ ,

$$\vec{u}(\vec{r}, t) = \sum_n \vec{u}_n(\vec{r}, t) = \sum_n c_n(t) \vec{u}_n^0(\vec{r}) = \sum_n \bar{c}_n \vec{u}_n^0(\vec{r}) e^{-i\Omega_n t}, \quad (2.61)$$

where  $c_n(t)$  is the displacement amplitude of a mode with index  $n$ ,  $\Omega_n$  its eigenfrequency and  $\vec{u}_n^0(\vec{r})$  is the spatial displacement pattern of the mode, normalized so that

$$\frac{\int_V \vec{u}_n^0(\vec{r}) \vec{u}_{n'}^0(\vec{r}) d^3r}{\int_V d^3r} = \delta_{nn'}. \quad (2.62)$$

For more sophisticated geometries, such as a silica toroid supported by a silicon pillar, it is difficult to obtain analytical solutions for the mode shapes

## 2. Cavity optomechanics

and frequencies.<sup>3</sup> In such a case, (2.58) with the corresponding boundary conditions is solved using the finite-element method (FEM). As an illustrative example, and to validate the accuracy of the FEM results, an analytical solution available for spheres is developed in the following [5, 179]. In spherical coordinates, equation (2.58) is solved in a homogeneous medium by functions

$$\vec{u}(\vec{r}, t) = \vec{\nabla}\phi_0(\vec{r}, t) + \vec{\nabla} \times \vec{\Phi}_1(\vec{r}, t) + \vec{\nabla} \times \vec{\nabla} \times \vec{\Phi}_2(\vec{r}, t) \quad (2.63)$$

derived from a scalar potential  $\phi_0$  and two vector potentials  $\vec{\Phi}_1 = (r\phi_1, 0, 0)$  and  $\vec{\Phi}_2 = (r\phi_2, 0, 0)$  with

$$\phi_q(\vec{r}, t) = \sum_{l,m} A_{qnlm} j_l\left(\frac{\Omega_{nlm}}{v_q} r\right) Y_l^m(\theta, \varphi) e^{-i\Omega_{nlm}t} \quad (2.64)$$

where  $q = 0, 1, 2$ , and  $j_l$  is the spherical Bessel function,  $Y_l^m$  is the spherical harmonic function,  $v_0 = \sqrt{(\lambda + 2\mu)/\rho}$  is the longitudinal sound velocity, and  $v_1 = v_2 = \sqrt{\mu/\rho}$  is the transverse sound velocity with  $\rho$  material density. The acoustic modes are characterized by an angular momentum mode number  $l$  ( $l = 0, 1, 2, \dots$ ), an azimuthal mode number  $m$  ( $-l \leq m \leq l$ ) and a radial mode number  $n$  ( $n = 1, 2, \dots$ ). Here,  $n = 1$  corresponds to the surface mode,  $n \geq 2$  to inner modes and  $\Omega_{nlm}$  denotes the frequency of the vibration characterized by the mode numbers  $(n, l, m)$ .

We focus now on the fundamental spheroidal mode  $(n, l, m) = (1, 0, 0)$ , for higher-order modes, see [5] and references therein. In particular, the displacement vector field is purely radial,

$$\vec{u}_{1,0,0}^0(\vec{r}) = A_{0,1,0,0} \frac{\sin(k_{1,0,0}r) - k_{1,0,0}r \cos(k_{1,0,0}r)}{r^2} \vec{e}_r, \quad (2.65)$$

where  $k_{1,0,0} = \Omega_{1,0,0}/v_0$ ,  $A_{0,1,0,0}$  is a normalization constant, and  $\vec{e}_r$  the radial unit vector. In the following, we drop the mode index  $(1, 0, 0)$  for better legibility, and an index to a vector field now denotes one of its components in a given coordinate system.

To determine the allowed values of  $k$  (and therefore  $\Omega$ ), the strain tensor

$$\varepsilon_{ij} = \frac{1}{2} \left( \frac{\partial u_i}{\partial x_j} + \frac{\partial u_j}{\partial x_i} \right) \quad (2.66)$$

is evaluated in a spherical coordinate system. For the considered mode, all non-diagonal elements vanish, and the diagonal elements read<sup>4</sup>

$$\varepsilon_{rr} = \frac{\partial u_r}{\partial r} = c(t) A \frac{(k^2 r^2 - 2) \sin(kr) + 2kr \cos(kr)}{r^3} \quad (2.67)$$

$$\varepsilon_{\theta\theta} = \frac{u_r}{r} = c(t) A \frac{\sin(kr) - kr \cos(kr)}{r^3} \quad (2.68)$$

$$\varepsilon_{\varphi\varphi} = \frac{u_r}{r} = c(t) A \frac{\sin(kr) - kr \cos(kr)}{r^3}, \quad (2.69)$$

<sup>3</sup>For simple cylinders, approximate solutions have been developed [176–178].

<sup>4</sup>For the definitions of the strain tensor in spherical coordinates see [175].

## 2.3 Silica WGM resonators as optomechanical systems

where  $c(t)$  is the excitation amplitude of the mode. The stress is related to the strain by Hooke's law, which in a lossless isotropic medium is given by

$$\sigma_{ij} = 2\mu\varepsilon_{ij} + \lambda\delta_{ij} \sum_k \varepsilon_{kk} \quad (2.70)$$

so that in this case the stress tensor  $\sigma_{ij}$  is diagonal as well,

$$\sigma_{rr} = c(t) A \frac{((\lambda + 2\mu)k^2 r^2 - 4\mu) \sin(kr) + 4\mu kr \cos(kr)}{r^3} \quad (2.71)$$

$$\sigma_{\theta\theta} = c(t) A \frac{(\lambda k^2 r^2 + 2\mu) \sin(kr) - 2\mu kr \cos(kr)}{r^3} \quad (2.72)$$

$$\sigma_{\varphi\varphi} = c(t) A \frac{(\lambda k^2 r^2 + 2\mu) \sin(kr) - 2\mu kr \cos(kr)}{r^3}. \quad (2.73)$$

Eventually, the boundary conditions for a freely oscillating sphere of radius  $R$  require that the stress is zero at its boundary ( $r = R$ ), leading to

$$\left(1 - \frac{1}{4} \frac{v_0^2}{v_1^2} k^2 R^2\right) \frac{\tan(kR)}{kR} - 1 = 0. \quad (2.74)$$

For the parameters of fused silica, this equation is solved for  $kR = 2.4005 \dots$  or

$$\frac{\Omega_m}{2\pi} \approx \frac{2280 \text{ m/s}}{R}, \quad (2.75)$$

corresponding to a resonance frequency of 91.2 MHz for a 50- $\mu\text{m}$  diameter sphere. Finite element modeling [180] yields the same result within less than 1%.

Another interesting physical entity is the potential energy stored in the deformation. It given by

$$U = \sum_{i,j} \int_V \frac{1}{2} \sigma_{ij} \varepsilon_{ij} d^3r. \quad (2.76)$$

The diagonal form of strain and stress tensors again makes the analytical evaluation of this integral simple, and yields

$$U \approx 8.69 \cdot 10^{11} \frac{\text{J}}{\text{m}^3} \cdot R \cdot x^2 \quad (2.77)$$

where  $x = \vec{u}(R, \theta, \varphi) \cdot \vec{e}_r = c(t) A (\sin(kR) - kR \cos(kR)) / R^2$  is the radial displacement of the boundary, with  $A \approx 0.427 R^2$  for silica. Figure 2.8 shows displacement, strain, stress and strain energy density of a silica sphere when the fundamental mode is excited. Results from analytic calculations and the FEM agree very well.

Figure 2.9 compares experimentally measured resonance frequencies of several silica microspheres with diameters between 30 and 100  $\mu\text{m}$  with analytical calculations. Again, very good agreement is obtained.

## 2. Cavity optomechanics

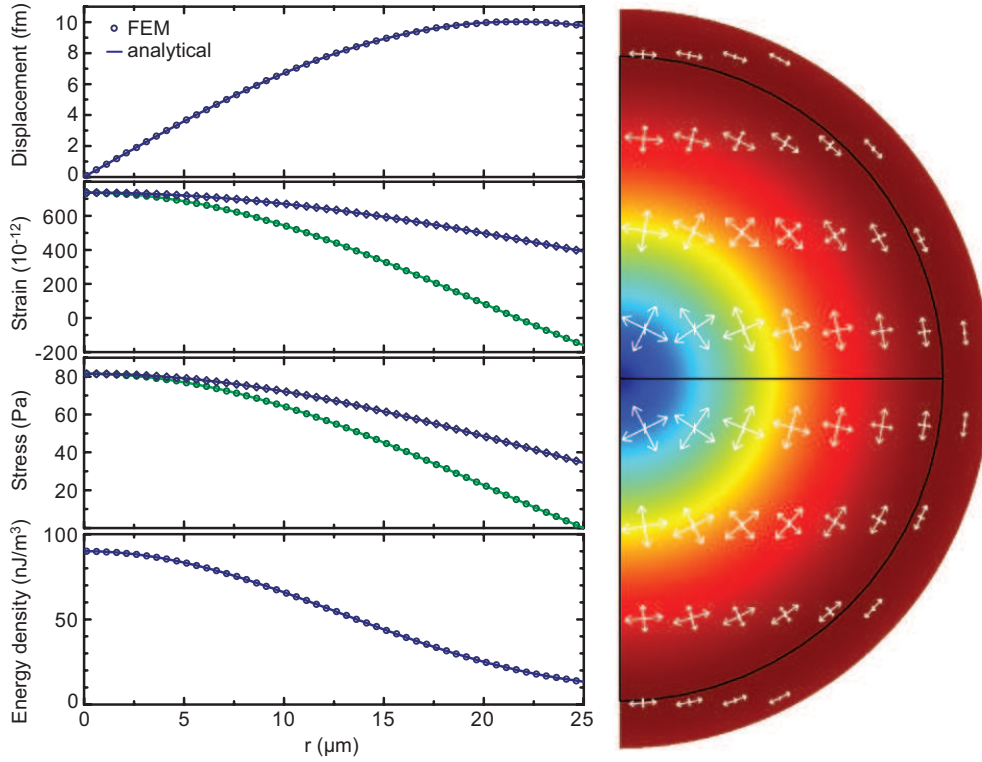


Figure 2.8: The  $(n, l, m) = (1, 0, 0)$  mode of a silica sphere. Left panels show (from top to bottom) the radial displacement  $\vec{u}(r, \theta, \varphi) \cdot \vec{e}_r$ , the strains  $\epsilon_{rr}$  (green) and  $\epsilon_{\theta\theta} = \epsilon_{\varphi\varphi}$  (blue), stresses  $\sigma_{rr}$  (green) and  $\sigma_{\theta\theta} = \sigma_{\varphi\varphi}$  (blue), and the strain energy density  $\frac{1}{2} \sum_{ij} \sigma_{ij} \epsilon_{ij}$ . Symbols are results of finite-element modeling and lines are derived from the analytical calculations, showing excellent agreement. The given magnitudes correspond to a  $50 \mu\text{m}$ -diameter sphere containing a total strain energy of  $k_{\text{B}}(300 \text{ K})/2$ . The right panel shows the exaggerated displacement profile (original sphere outlined in black), and magnitude (color coded) as well as the principal stresses (indicated by arrow lengths).

## 2.3 Silica WGM resonators as optomechanical systems

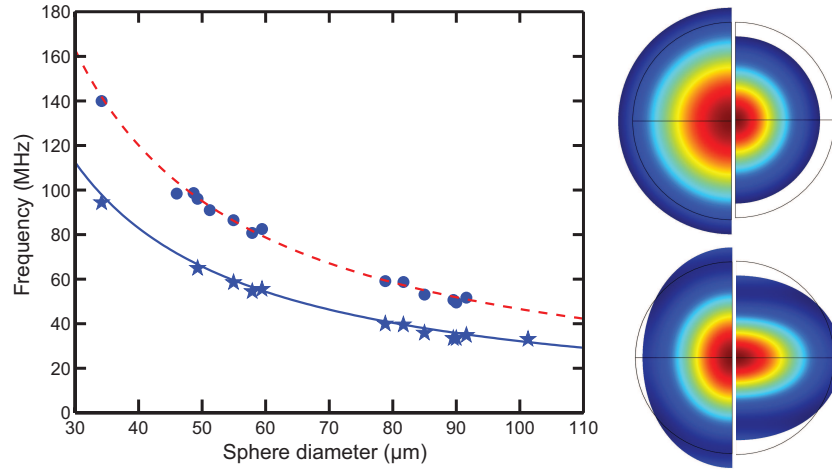


Figure 2.9: Resonance frequencies of silica microspheres for the  $(n, l) = (1, 0)$  (upper branch) and  $(n, l) = (1, 2)$  (lower branch) spheroidal resonance modes [5]. Curves are expected resonance locations for free boundary conditions, following an inverse dependence on the sphere radius with  $\Omega_m/2\pi \approx 2280 \text{ m/s}/R$  for the  $l = 0$  and  $\Omega_m/2\pi \approx 1580 \text{ m/s}/R$  for the  $l = 2$  mode. Symbols represent measured spheres. The panels on the right show the corresponding displacement patterns as obtained from the FEM. The left and right halves of the sphere show the displacement of the volume elements at two different times separated by half the oscillation period.

*Toroidal* silica resonators, sitting on top of a silicon pillar, have fewer symmetries than spheres. Such a structure must be parameterized (instead of simply the radius in the case of a sphere) by several parameters, at least by the major and minor radii of the silica torus, the radius of the silicon pillar, the thickness of the silica disk, and the offset of the symmetry planes of the disk and torus along the  $z$ -axis [181]. The shape of the silicon pillar is assumed to be rotationally symmetric, and to constitute a quarter circle in the  $r$ - $z$ -plane. The radius of this circular arch is another degree of freedom, but usually assumed to be similar to the difference of toroid and pillar radii (figure 2.10) due to the isotropic nature of the silicon etch.

The complex boundary conditions (all surfaces free, except for the bottom of the silicon pillar) render an analytical solution prohibitively difficult. We therefore use a commercial finite-element software [180] to solve (2.58)

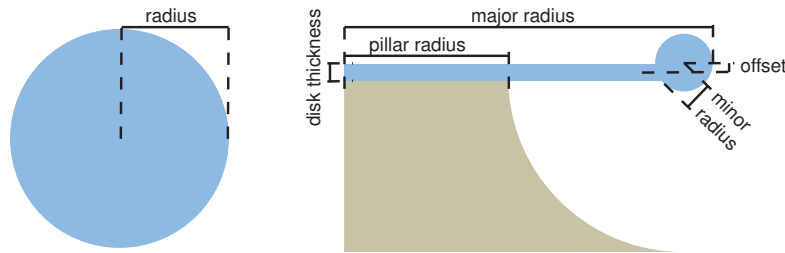


Figure 2.10: Geometric parameters required to describe a sphere (right) and a toroidal WGM resonator, where silica is shown in blue and silicon in grey.

## 2. Cavity optomechanics

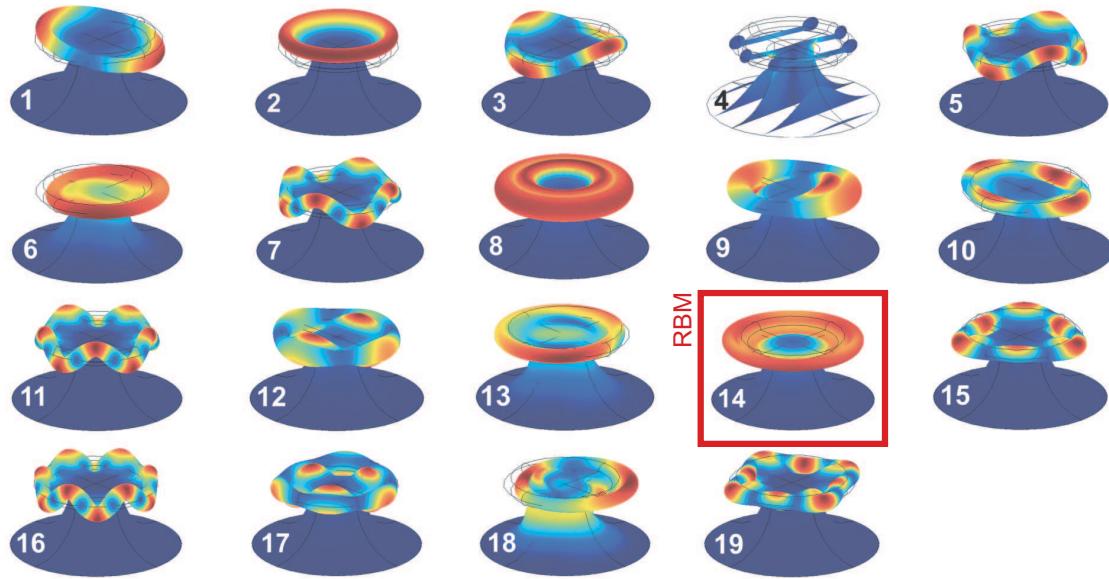


Figure 2.11: Displacement patterns of the 19 lowest-frequency modes (see text) of a toroidal microresonator as calculated using the FEM, indicated both as the deformed shape and in the color code (increasing displacement from dark blue to dark red). Mode number 4 involves mainly torsional motion, which is illustrated by plotting the displacement of originally parallel slices through the structure. Adapted from ref. [9].

on a discrete mesh consisting typically of more than 10,000 nodes which are automatically distributed in the simulation volume. Simulations can be run both assuming rotational symmetry for the modes, and in full three dimensions. Figure 2.11 shows the obtained displacement patterns for the 19 lowest-frequency modes of a toroid of major radius  $23.0 \mu\text{m}$ , pillar radius  $13.23 \mu\text{m}$ , minor radius  $2.63 \mu\text{m}$ , disk thickness  $2 \mu\text{m}$  and no offset, in a three-dimensional simulation. As shown in figure 2.12, the simulation can reproduce the frequencies measured on a real toroid to a very high accuracy [9]. Indeed, the average deviation between measured and simulated frequency is, on average, below 2%. This emphasizes the reliability of the FEM. Note also that probing of the modal displacement patterns using a scanning probe technique has confirmed the shape expected from simulations in an earlier experiment [182].

Various mode families with qualitatively different displacement patterns are recognized. Some modes involve mainly motion of the silicon pillar (number 6, 13 and 18 in figure 2.11) and are therefore irrelevant for the purpose of cavity optomechanics. A torsional mode (number 4) is also observed, but it couples only weakly to the optical modes (cf. section 2.3.3). Modes number 1, 3, 5, 7, 11 and 16 are characterized by an  $n$ -fold symmetry under rotation by an angle  $\pi/n$ , where  $n = 1 \dots 6$  in this case. These modes, sometimes referred to as “crown” modes, involve mainly sinusoidal oscillation of the toroid in the  $z$ -direction. They typically follow a quadratic dispersion relation, that is, their eigenfrequency is proportional to the square of the number

## 2.3 Silica WGM resonators as optomechanical systems

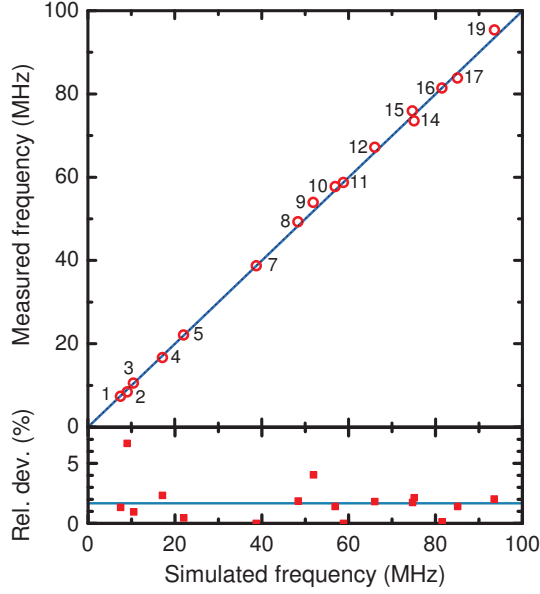


Figure 2.12: Comparison of simulated and measured frequencies of a toroidal silica microresonator. The relative deviation is below 2% on average. Adapted from ref. [9].

of nodes along the circumference [9]. Also, for each mode in this family there exists a frequency-degenerate second mode in which the positions of nodes and antinodes are swapped. In measurements on real toroids, this degeneracy is often lifted due to small deviations from perfect rotational symmetry of the structure.

In the context of cavity optomechanics, the most interesting modes are the ones with (nearly) radially symmetric displacement patterns (number 2, 8, and 14). One usually distinguishes flexural modes, in which the displacement is mainly along the  $z$ -axis (number 2 and 8), and the radial modes involving mainly radial displacement. The most important mode is the fundamental radial mode, the so-called radial breathing mode (RBM) with number 14 in figure 2.11, since it couples most strongly to the optical WGM. The RBM in the measured toroid has a frequency of 75.1 MHz, and usually lies between 30 and 120 MHz for typical toroidal geometries.

### Mechanical dissipation

Apart from its eigenfrequency  $\Omega_m$ , the most important property of the RBM is its damping rate. As in the case of the optical modes, different dissipation mechanisms lead to a release of mechanical energy stored in the RBM to other degrees of freedom. The mechanical damping rate  $\Gamma_m$  quantifies the rate at which this takes place, and is again expressed in terms of a quality factor

$$Q_m = \Omega_m / \Gamma_m. \quad (2.78)$$

## 2. Cavity optomechanics

---

The different damping mechanisms all contribute to the total damping, and the resulting quality factor can be written

$$Q_m^{-1} = Q_{\text{gas}}^{-1} + Q_{\text{clamp}}^{-1} + Q_{\text{TLS}}^{-1} + Q_{\text{other}}^{-1} \quad (2.79)$$

with contributions by surrounding gas ( $Q_{\text{gas}}^{-1}$ ), by clamping losses ( $Q_{\text{clamp}}^{-1}$ ), by two-level systems ( $Q_{\text{TLS}}^{-1}$ ) and by other damping mechanisms ( $Q_{\text{other}}^{-1}$ ).

In the initial optomechanical experiments with silica microtoroids the mechanical quality factors were around 3,000 [1]. By replacing the surrounding nitrogen gas with helium (which has lower viscosity  $\eta$  and molecular mass  $M$ ), the quality factors rose beyond 5,000, clearly indicating that the losses were dominated by gas damping. From the known drag on a sphere oscillating in a viscous fluid [183] one can expect a scaling  $Q_{\text{gas}} \propto (\eta p M)^{-1/2}$  in this regime. Reducing the pressure  $p$  of the ambient gas should therefore raise  $Q_{\text{gas}}$ . Indeed, at pressures down to about 10 mbar, in the so-called viscous regime, the quality factor was observed to increase as  $Q_{\text{gas}} \propto p^{-1/2}$ , while for lower pressures, in the molecular regime,  $Q_{\text{gas}} \propto p^{-1}$  [6]. At pressures below 1 mbar, gas damping becomes irrelevant ( $Q_{\text{gas}} \gg Q_m$ ) and the quality factor is observed to converge towards a saturation value at lower pressures. Among different toroids, there are significant variations in the range between 1,000 and 30,000 for this value. This is due to clamping losses, which strongly depend on the geometry of the sample.

To study this effect more systematically, a toroidal resonator was under-etched in several steps, to reduce the radius of the silicon pillar, and thereby increase the relative undercut, which we define as

$$\text{relative undercut} = 1 - \frac{\text{silicon pillar radius}}{\text{silica toroid major radius}}. \quad (2.80)$$

The quality factors and resonance frequencies of the RBM of six toroidal resonators on the chip were measured for each etching step (figure 2.13). While the resonance frequency reduces monotonically, the quality factors vary in a non-monotonous manner, with a distinct minimum for an undercut of about 0.7.

A series of simulations with increasing undercut reveals that the resonance frequencies of the RBM and a radially symmetric flexural mode are crossing each other for this undercut, as they have a different undercut dependence. However, the actual resonance frequencies of the structure exhibit an avoided crossing. At the same time, the modal shapes of the RBM and flexural mode hybridize in the crossing region. These two facts indicate normal mode coupling between the RBM and the flexural mode.

To corroborate this conjecture experimentally, the undercut in a different sample was again systematically increased. For each etching step, a highly sensitive measurement technique (polarization spectroscopy, cf. section 2.4) allowed the determination of the frequencies of both the RBM ( $\Omega_R$ ) and the

### 2.3 Silica WGM resonators as optomechanical systems

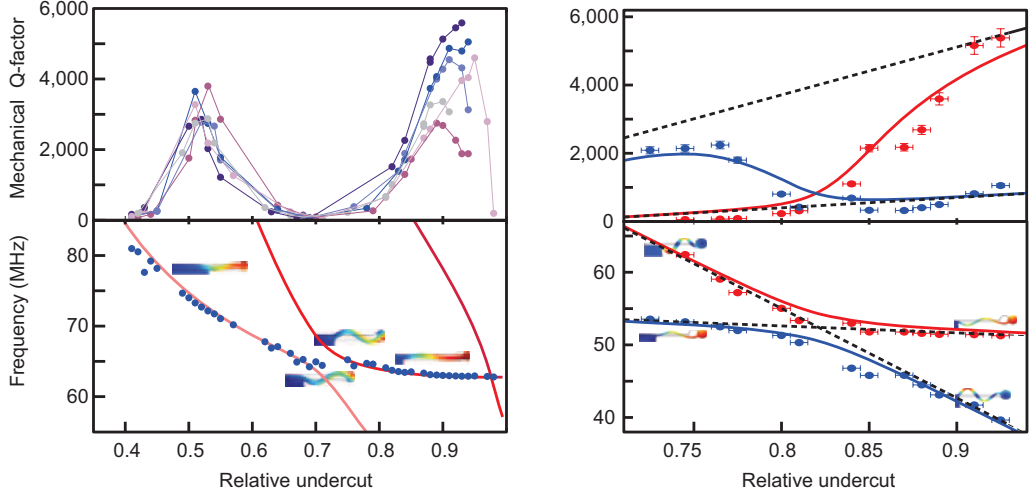


Figure 2.13: Normal mode coupling between the RBM and a flexural mode. Left panels: Measured quality factors of the RBM of six samples on the same chip as a function of relative undercut, and the resonance frequencies of one of the samples (dots). Lines in the lower panel are results of simulations, and show not only the frequency of the RBM, but also of radially symmetric flexural modes. In the region where the frequencies are similar, for a relative undercut of  $\sim 0.7$ , the quality factors are strongly reduced. Right panels: Evidence of normal mode coupling between the RBM and a flexural mode in another sample. The frequencies  $\Omega_{\pm}$  and quality factors  $Q_{\pm}$  of the experimentally observed modes (dots) can be reproduced using a model of two coupled harmonic oscillators (red and blue lines). The frequencies and quality factors of the uncoupled modes, corresponding to a pure RBM and flexural mode are assumed to depend only linearly on the relative undercut (dashed lines). Adapted from [6].

adjacent flexural ( $\Omega_F$ ) mode. Indeed, the measured frequencies and quality factors can be simultaneously reproduced using a simple model of two coupled harmonic oscillators, the intrinsic frequencies  $\Omega_R$  and  $\Omega_F$  and quality factors  $Q_R$  and  $Q_F$  of which are linearly dependent on the undercut. The frequencies  $\Omega_{\pm}$  and quality factors  $Q_{\pm}$  of the new eigenmodes are given by

$$\Omega_{\pm} + \frac{i}{2} \frac{\Omega_{\pm}}{Q_{\pm}} = \frac{1}{2} (\Omega_R + \Omega_F) + \frac{i}{4} \left( \frac{\Omega_R}{Q_R} + \frac{\Omega_F}{Q_F} \right) \pm \sqrt{\left( \frac{1}{2} (\Omega_R + \Omega_F) + \frac{i}{4} \left( \frac{\Omega_R}{Q_R} - \frac{\Omega_F}{Q_F} \right) \right)^2 + \frac{g_{im}^4}{4\Omega_R\Omega_F}} \quad (2.81)$$

where the intermode coupling  $g_{im}$  is an adjustable parameter (figure 2.13). The data in figure 2.13 can be fit using  $g_{im}/2\pi = 14$  MHz. This rather strong coupling is attributed to the asymmetry of the structure in the axial direction due to both the offset of the toroid from the disk [181], and the fact that the silicon pillar supports the disk only from below.

Summarizing the previous observations, we conclude that the admixture of a flexural displacement pattern to the RBM reduces the quality factor of the latter. This can be explained by noting that the flexural modes induce axial displacement also in the region where the silica disk is supported by

## 2. Cavity optomechanics

---

the silicon pillar. The periodic oscillation in axial direction launches acoustic waves into the pillar, through which the energy of the mode is dissipated, thereby deteriorating the quality factor.

This qualitative understanding is quantitatively supported by a simple model [6], in which the acoustic energy loss is estimated as the power radiated by a membrane of area  $A_p$  (area of the silicon pillar) oscillating with an axial displacement  $\Delta z(\vec{r})$  at frequency  $\Omega_m$

$$P_{\text{mech}} = v\rho\Omega_m^2 \int_{A_p} |\Delta z(\vec{r})|^2 d^2r, \quad (2.82)$$

where  $v$  is the sound velocity and  $\rho$  density. For geometry parameters close to the modal crossing, it was indeed found experimentally that

$$Q_{\text{clamp}} \propto \frac{\Omega_m E_{\text{mech}}}{P_{\text{mech}}}, \quad (2.83)$$

where  $E_{\text{mech}}$  is the total mechanical energy of the mode. Advantageously, both  $E_{\text{mech}}$  and  $P_{\text{mech}}$  can be simulated using FEM [6]. As an aside we note that an expression similar to (2.82) and (2.83) was obtained in a rigorous theoretical analysis based on a phonon tunneling approach [184]. To reduce  $P_{\text{mech}}$ , two strategies are immediately evident: Either the clamping area  $A_p$  is minimized, or the axial displacement  $\Delta z(\vec{r})$  in this region is reduced. Minimizing the clamping area is possible, for example, by fabricating toroids with a very strong undercut, as shown in figure 2.14, in which the silica disk is supported by a “needle pillar” of sub-micrometric diameter [8].

Alternatively, by introducing spokes into the silica disk, it was possible to strongly reduce the coupling of the radial motion to an axial displacement in the clamping region [6]. Both presented approaches yield good results with quality factors exceeding 30,000 at frequencies around 40 MHz [6, 8].

In figure 2.15 we show an overview of mechanical quality factors achieved in typical samples with different major diameters, all strongly undercut ( $> 90\%$ ) and measured in vacuum. A clear trend to higher quality factors for bigger cavity sizes (and therefore lower frequencies) is observed. The scatter in the data of neighboring toroids (with very similar reflow preform and final pillar shapes) indicates that clamping losses depend sensitively on geometry parameters. Finally, we note that we have consistently observed higher quality factors in disks than in toroids. This is attributed to a reduced offset (figure 2.10) of the oscillating mass, which, in toroids, mediates the coupling of the RBM to radially symmetric flexural modes with strong dissipation to the pillar.

The highest quality factors which were experimentally achieved at room temperature are  $Q_m \sim 50,000$  above 20 MHz. For these structures however, simulations clearly indicate  $Q_{\text{clamp}} \gg Q_m$  according to (2.83), so a different dissipation mechanism must now be dominant. A strong temperature dependence of the quality factor (allowing for values up to 80,000 at 110°C) suggests a temperature-dependent dissipation mechanism [6].

## 2.3 Silica WGM resonators as optomechanical systems

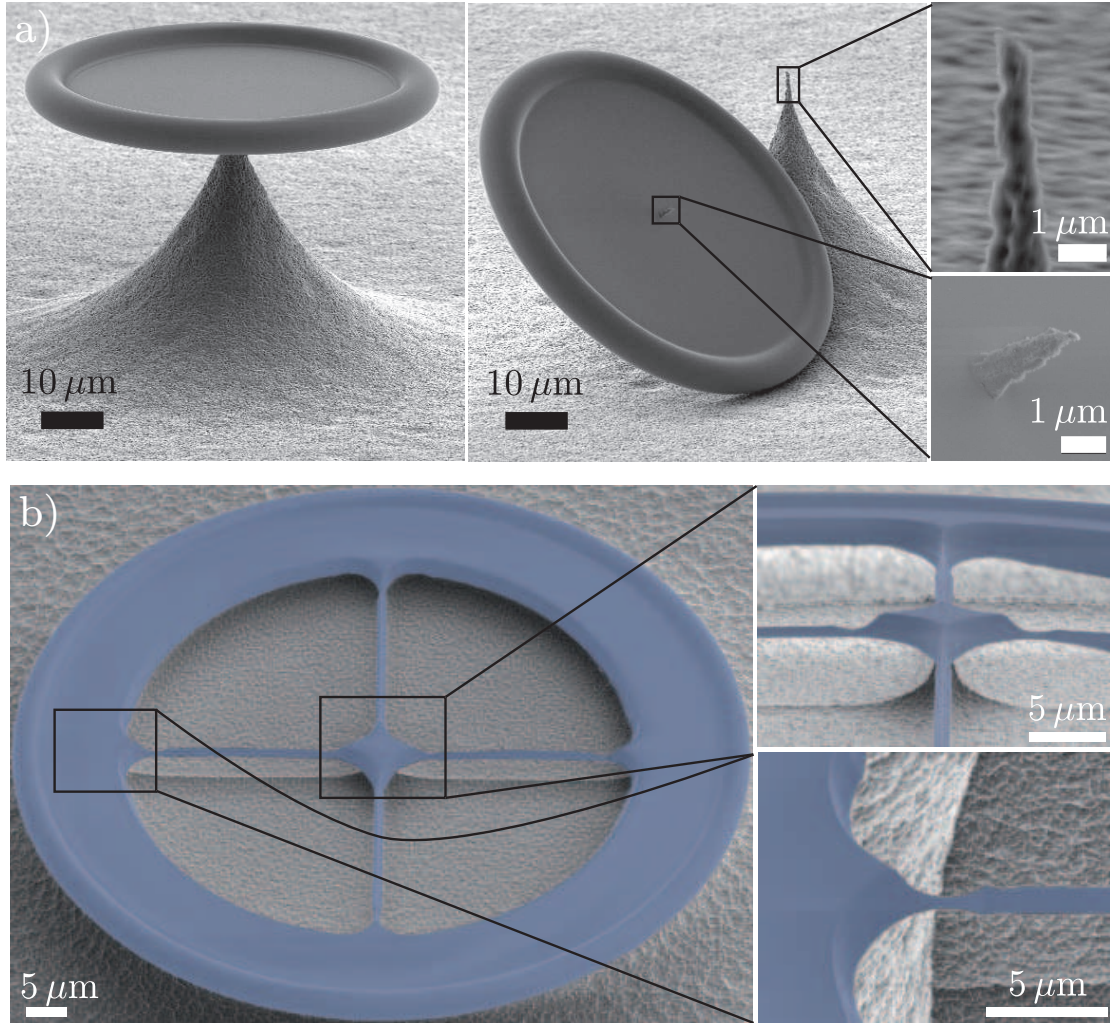


*Figure 2.14:* Silica toroidal resonators with ultralow mechanical damping. a) Reduced clamping loss by supporting the silica disk with a “needle” pillar. The central and right panels show the tip of an intentionally broken pillar, which has a sub-micron diameter. A quality factor of 30,000 is reached with such structures for a 40 MHz-RBM [8]. b) Reducing clamping loss by engineering the axial displacement in the clamping region using a “spokes” design. Such resonators achieved mechanical quality factors up to 32,000 at 38 MHz, and 50,000 at 24 MHz at room temperature [6].

## 2. Cavity optomechanics

---

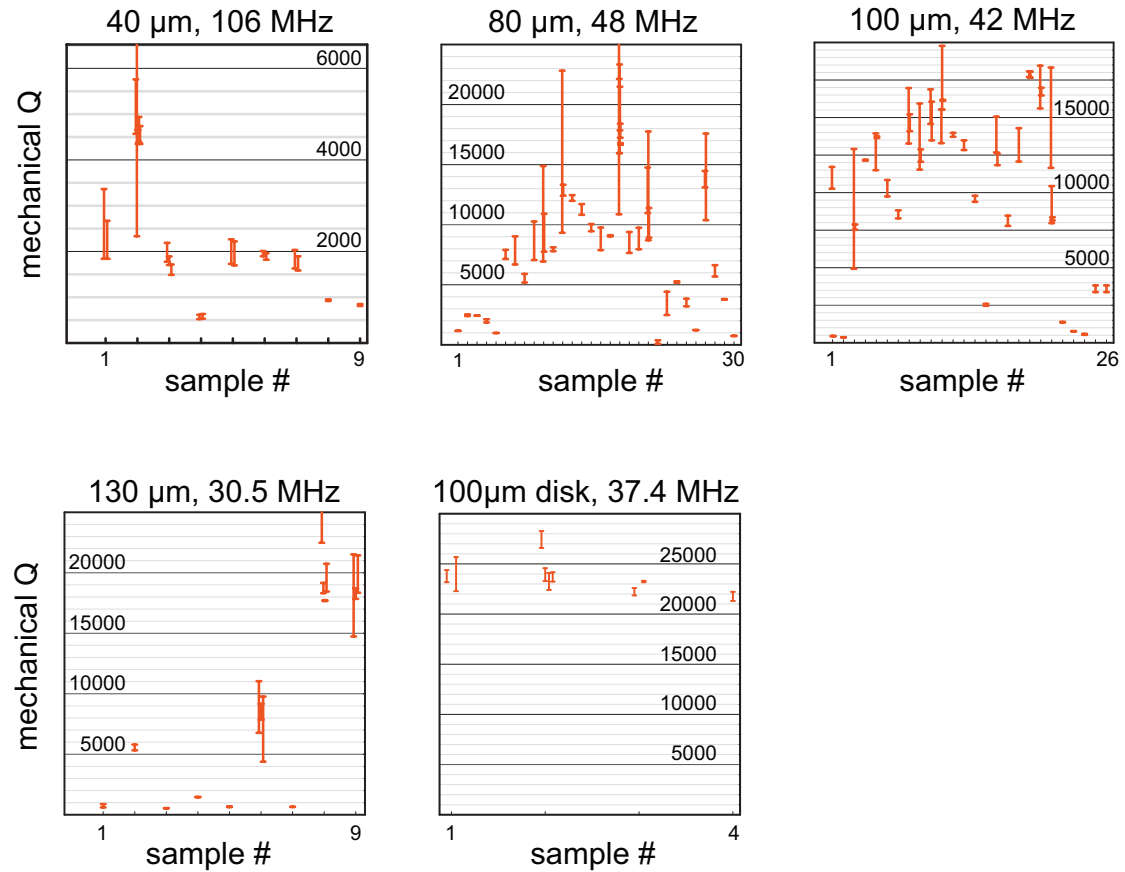


Figure 2.15: Overview of mechanical quality factors of the RBM measured in typical toroids. Major diameters of the pre-reflow disk and the approximate resonance frequency are indicated in the figure captions. Each bracket indicates the span within which the mechanical quality factor was found in a pair of measurements, in which the probing laser was red and blue detuned (dynamical backaction modifies the measured effective mechanical quality factor in opposite directions in the two cases). Groups of brackets belong to the same toroid. The last panel shows measurements taken on silica disks prior to the reflow.

### 2.3 Silica WGM resonators as optomechanical systems

Indeed, the intrinsic damping of acoustic excitations in glass is known to follow a universal behavior observed in many amorphous solids [185]. This effect is attributed to the coupling of strain fields to structural defects in the material. While the microscopic nature of these defects is not precisely known, it can be successfully modeled by a distribution of effective two-level systems (TLS) with two stable equilibria, represented by a particle in an asymmetric double-well potential [186]. These potentials are characterized by the energy difference  $\Delta$  of the ground states in both potentials (the two levels involved), and the height  $V$  of the energy barrier separating the two wells as shown in figure 2.16. Oscillating strain fields associated with an acoustic excitation modulate the energy difference  $\Delta$  between the two potential minima, and thereby couple to the TLS.

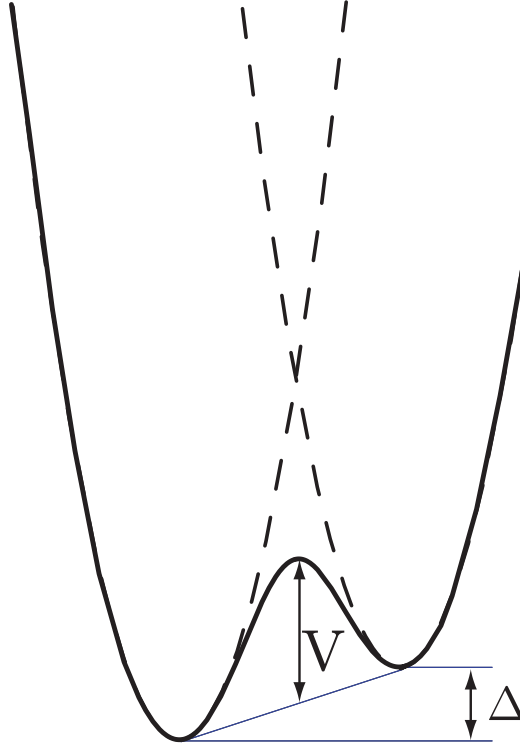


Figure 2.16: Double-well potential used to model the structural defects in glass. The two individual wells (dashed lines) are usually assumed to be identical, but to have a ground-state energy that differs by an energy  $\Delta$ . The two stable equilibria are separated by a barrier of height  $V$ .

To a very good approximation, the resulting Debye relaxation of acoustic excitations leads to a quality factor given by [187]

$$Q_{\text{TLS}}^{-1} = \frac{\gamma^2}{\rho v^2 k_{\text{B}} T} \int_{-\infty}^{+\infty} \int_0^{+\infty} P(\Delta, V) \operatorname{sech}^2 \left( \frac{\Delta}{2k_{\text{B}} T} \right) \frac{\Omega \tau}{1 + \Omega^2 \tau^2} dV d\Delta, \quad (2.84)$$

where  $\gamma = \frac{1}{2} \partial \Delta / \partial \varepsilon$  is the change of the potential asymmetry as a function of strain  $\varepsilon$ ,  $\rho$  is the density,  $v$  sound velocity, and  $P(\Delta, V)$  is the distribution

## 2. Cavity optomechanics

---

of TLS in the energy parameters  $\Delta$  and  $V$  in the sense that  $P(\Delta, V)dVd\Delta$  is a volume density of defects.

At room temperature, the relaxation between the two stable states is dominated by thermally activated processes. The relaxation time is thus given by an Arrhenius-type law

$$\tau^{-1} = \tau_0^{-1} e^{-V/k_B T} \cosh\left(\frac{\Delta}{2k_B T}\right). \quad (2.85)$$

Following the arguments given in reference [187], a sensible choice of the distribution function  $P(\Delta, V)$  yields eventually a quality factor of

$$Q_{\text{TLS}}^{-1} = C \cdot \operatorname{erf}\left(\frac{\sqrt{2}k_B T}{\Delta_c}\right) \frac{1}{k_B T} \int_0^\infty \left(\frac{V}{V_0}\right)^{-\zeta} e^{-V^2/2V_0^2} \frac{\Omega \tau_0 e^{V/k_B T}}{1 + \Omega^2 \tau_0^2 e^{2V/k_B T}} dV \quad (2.86)$$

reproducing the experimental data over four orders of magnitude in frequency (11 kHz . . . 200 MHz) and two orders of magnitude in temperature (from a few Kelvin to above room temperature) for the parameters  $V_0 = (667 \pm 21) \text{ K} \cdot k_B$ ,  $\zeta = 0.28 \pm 0.03$ ,  $\log_{10}(\tau_0/\text{s}) = -12.2 \pm 0.18$  and  $V_0/\Delta_c = 7.7 \pm 0.7$ .

While usually measured as the attenuation of large-amplitude acoustic waves in bulk material, the very same temperature dependence of the quality factor was found for the RBM of spokes toroids with sufficiently low clamping losses [11]. Figure 2.17 shows the measured quality factor of the RBMs of two samples at frequencies of 36 and 63 MHz. Simultaneously with the damping, relaxation of the TLS also leads to a change in the sound velocity, giving rise to a frequency shift of the mechanical modes, which is also shown in figure 2.17. At temperatures above 10 K, the damping can be accurately described by the model in (2.86), with a peak damping at about 50 K leading to a minimum quality factor of  $Q_{\text{TLS}} \approx 500$ .

Below 10 K, the relaxation is dominated by tunneling processes between the two equilibria [186, 189], instead of the thermally-activated relaxation. The tunneling relaxation is responsible both for the low-temperature plateau ( $Q_m \approx 1200$  at 5 K) and the roll-off at very low temperatures with  $Q_{\text{TLS}}^{-1} \propto T^3/\Omega$ . For completeness, we note that apart from damping via relaxation, at sufficiently low temperatures, direct absorption of acoustic waves by the TLS also leads to damping, which gets saturated at high enough amplitudes [186, 190].

Other damping mechanisms, as described by  $Q_{\text{other}}$ , include thermoelastic damping [191, 192], damping by anharmonicity [187], and surface effects [193]. For silica microtoroids or spheres, these effects are individually estimated to lead to limiting quality factors on the order of  $10^5$  or more. In particular when operating the resonators at cryogenic temperatures—as required for advanced experiments in cavity optomechanics—these damping mechanisms can be safely neglected against the damping due to TLS.

## 2.3 Silica WGM resonators as optomechanical systems

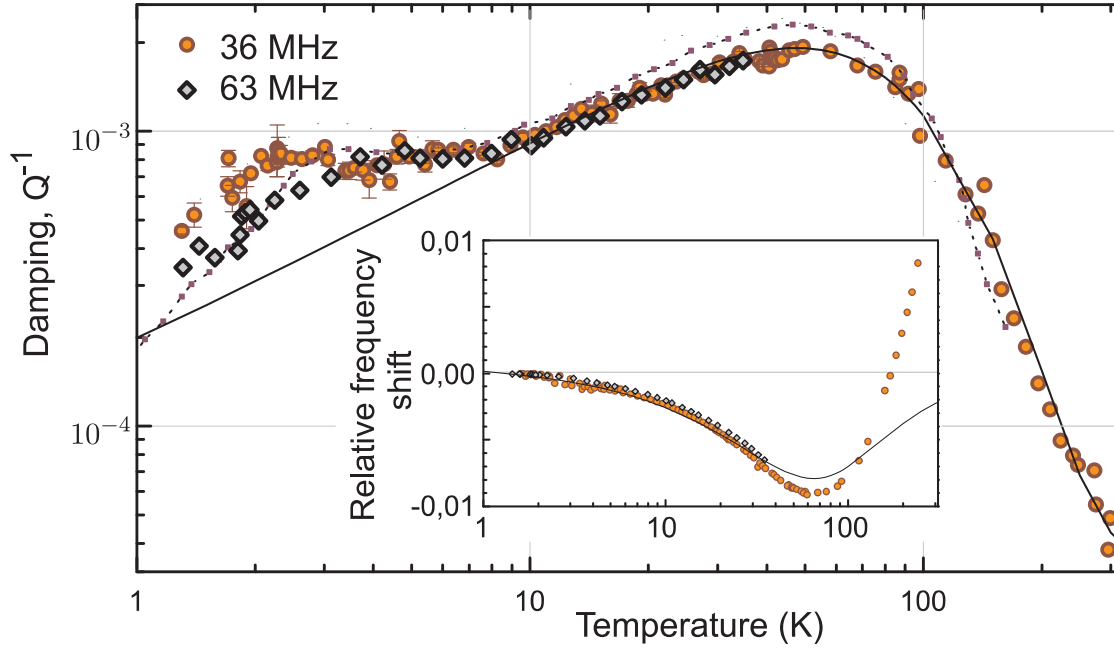


Figure 2.17: Quality factor of the RBMs of two samples which are dominated by the damping due to coupling to structural defects in glass. Solid line is a fit using the model (2.86), and the dashed lines are experimental data from an acoustic wave attenuation experiment at 40 MHz [188]. The inset shows the relative frequency shift of the RBM induced by the relaxation of TLS. Reprinted figure with permission from Arcizet *et al.*, Physical Review A **80**, 021803(R) (2009). Copyright 2009 by the American Physical Society (reference [11]).

### 2.3.3 Optomechanical coupling

In order to describe optomechanical effects in the simple way of equations (2.12) and (2.13), it is necessary to map the mechanical modes of interest to an effective one-dimensional mechanical oscillator, described by a displacement  $x$ , which parametrically modulates the optical resonance frequency through a non-zero  $g_0 = d\omega_c/dx$ . For optomechanical devices which host optical and mechanical modes with complex three-dimensional mode distribution such as silica microtoroidal resonators (figure 2.18), this mapping can be non-trivial.

#### Mapping to a scalar displacement

To formally describe this mapping, a weighting function  $\vec{w}(\vec{r})$  is introduced, mapping the displacement field  $u(\vec{r}, t)$  to a scalar displacement  $x$  according to

$$x(t) = \int_V \vec{w}(\vec{r}) \cdot \vec{u}(\vec{r}, t) d^3r = \sum_n c_n(t) \int_V \vec{w}(\vec{r}) \cdot \vec{u}_n^0(\vec{r}) d^3r \quad (2.87)$$

$$\equiv \sum_n c_n(t) \langle \vec{w}, \vec{u}_n^0 \rangle, \quad (2.88)$$

## 2. Cavity optomechanics

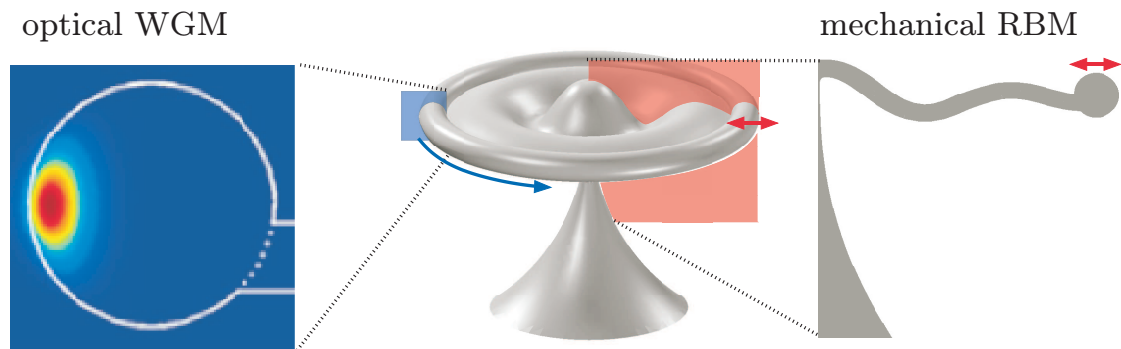


Figure 2.18: Mode shapes of optical and mechanical modes in a silica microtoroidal resonator (FEM simulations), which have to be taken into account to quantify the strength of optomechanical interaction.

where the decomposition of the displacement pattern  $\vec{u}$  as presented in eq. (2.61) is used. For each mechanical mode, the overlap integral  $\langle \vec{w}, \vec{u}_n^0 \rangle$  determines the relative strength of the transduction of the  $n$ -th mode amplitude  $c_n(t)$  into the optically sampled displacement  $x(t)$ . The *global* normalization of  $\vec{w}(\vec{r})$  is, in principle, arbitrary, as it can be compensated by an adequate choice of  $g_0 = d\omega_c/dx$ . For example, it can be chosen such that the displacement of a particular part of one mode's displacement pattern (such as the antinode of a beam's fundamental mode) directly corresponds to  $x$  [167].

For the most generic optomechanical systems, there are other obvious choices. For example, for a Fabry-Perot cavity, the normalization is chosen such that  $x$  corresponds to the center-of-mass mirror movement if it was displaced as a whole. Thus, if the laser spot on a mirror at  $z = z_0$ , which contains the mechanical modes, is given by a rotationally symmetric Gaussian with a waist of  $w_0$ , the weighting function reads [100, 194]

$$\vec{w}(\vec{r}) = \frac{2}{\pi w_0^2} e^{-2r^2/w_0^2} \delta(z - z_0) \vec{e}_z. \quad (2.89)$$

With this weighting function, the correct frequency shift is obtained using the coupling constant  $g_0 = -\omega_c/L$ , where  $L$  is the total length of the cavity.

In the case of silica WGM resonators, with their three-dimensional distributions of optical and mechanical fields, the calculation of the effective displacement is more difficult. A sensible approximation may be obtained by considering the mechanical displacement a perturbation, which does not modify the optical fields, but only displaces polarizable matter within the optical field distribution. The resulting relative frequency shift equals the relative change in the electromagnetic energy stored in the mode, as the number of stored photons, each of energy  $\hbar\omega_c$ , is conserved in the cavity [195]. The resulting frequency shifts reads

$$\frac{\delta\omega_c}{\omega_c} = \frac{\delta E_{\text{em}}}{E_{\text{em}}} = \frac{\int \frac{1}{2} E^2(\vec{r}) \vec{\nabla} \varepsilon(\vec{r}) \cdot \vec{u}(\vec{r}) d^3 r}{2 \int \frac{1}{2} E^2(\vec{r}) \varepsilon(\vec{r}) d^3 r} \quad (2.90)$$

### 2.3 Silica WGM resonators as optomechanical systems

where  $E^2(\vec{r})$  is the squared magnitude of the electric field, and the factor 2 in the denominator is due to the fact that equal amounts of energy are stored in both the electric and magnetic fields. Note however that the magnetic energy does not shift upon a displacement of the boundary, as the magnetic permeability of glass is very close to unity. For a resonator made out of a homogeneous dielectric material, the integral in the nominator is essentially a surface integral over the boundary, as  $\vec{\nabla}\varepsilon(\vec{r})$  is zero everywhere except for the surface. We use the coupling constant  $g_0 = -\omega_c/R$ , expressing the frequency shift as a consequence of an effective radius change. One then finally obtains

$$\vec{w}(\vec{r}) = -\frac{R}{E_{\text{em}}} \cdot \frac{1}{2} E^2(\vec{r}) \vec{\nabla}\varepsilon(\vec{r}). \quad (2.91)$$

As (2.91) is difficult to evaluate in complex geometries, a useful approximation is given by

$$\vec{w}(\vec{r}) \approx \frac{1}{2\pi R} \delta(z - z_0) \delta(r - R) \vec{e}_r. \quad (2.92)$$

where  $R$  is the major radius and  $z = z_0$  the plane of the equator of the toroid. This weighting function essentially considers the transverse size of the optical mode as negligibly small compared to the scales of the displacement patterns, and the resulting displacement  $x$  corresponds to the change of the cavity radius, which is sampled by the optical mode. In this work, (2.92) is applied to derive the displacement induced by the excitation of a particular WGM from the results of FEM simulations.

We finally note that in a dielectric resonator, it is important to also consider strain-optical effects, that is, a strain-dependent refractive index leading to additional resonance frequency shifts for a given excitation of the mechanical mode. This effect was indeed found to dominate the optomechanical coupling in a cryogenic sapphire microwave WGM resonator [196]. To assess the relative contribution in silica WGM microresonators, we may use the analytic expressions for the strain field (2.67)–(2.69) in a *microsphere* to calculate the corresponding change in the refractive index as experienced by the optical mode. Due to the homogeneity of the strain fields on the scale of the optical mode cross section, it can be well approximated by just evaluating the strain fields at the edge of the sphere using [197]

$$\delta(n^{-2})_{\text{TE}} = p_2 \varepsilon_{rr} + p_1 \varepsilon_{\theta\theta} + p_2 \varepsilon_{\phi\phi} \quad (2.93)$$

$$\delta(n^{-2})_{\text{TM}} = p_1 \varepsilon_{rr} + p_2 \varepsilon_{\theta\theta} + p_2 \varepsilon_{\phi\phi}, \quad (2.94)$$

where the required coefficients of the photo-elastic tensor are given by  $p_1 = 0.121$  and  $p_2 = 0.270$  [198]. This leads to an extra frequency shift by about 30% (TE modes) and 50% (TM modes), as compared to the shift induced by the displacement of the boundary alone. Evaluation of the strain-optical coupling in a toroid is not possible analytically. For typical torus geometries as used in this work, however, we can extract an extra frequency shift by less than 20% from FEM simulations, in agreement with an earlier estimate [181].

## 2. Cavity optomechanics

---

### Effective mass

As a global coupling coefficient  $g_0$  is used to quantify the coupling strength of an effective displacement  $x$  to the resonance frequency  $\omega_c$  of the cavity, it is necessary to absorb the different coupling strengths of different mechanical modes into another parameter. This parameter is referred to as the *effective mass* of the individual mechanical modes [194, 199].

An operational definition of the effective mass of one particular mode (labeled in the following with an index  $n$ ) can be derived from its potential energy  $U_n$  which can be recast from (2.76) to

$$U_n = \frac{1}{2} M_n \Omega_n (c_n(t))^2 \quad (2.95)$$

using the free-boundary conditions [194] and the definition of the moving mass

$$M_n = \int_V \rho |\vec{u}_n^0(\vec{r})|^2 d^3r. \quad (2.96)$$

As  $c_n(t)$  is experimentally not accessible, we want to express the potential energy in terms of the measured displacement of the mode,

$$x_n(t) = \int_V \vec{w}(\vec{r}) \cdot \vec{u}_n(\vec{r}, t) d^3r = c_n(t) \langle \vec{w}, \vec{u}_n^0 \rangle, \quad (2.97)$$

and therefore require

$$U_n = \frac{1}{2} m_{\text{eff},n} \Omega_n^2 (x_n(t))^2. \quad (2.98)$$

This immediately leads to the formal definition

$$m_{\text{eff},n} \equiv \frac{M_n}{\langle \vec{w}, \vec{u}_n^0 \rangle^2}. \quad (2.99)$$

In practice, (2.98) is used to calculate the effective masses from experimental data (where, for a given  $g_0$ ,  $x$  is directly measured, and  $U_n \approx k_B T/2$ ) or FEM simulations, from which  $x_n$  and  $U_n$  can be simultaneously extracted.

The effective masses of the fundamental sphere modes can be calculated analytically, as both the potential energy (2.77) and the resonance frequency (2.75) as a function of the radius  $R$  are known, yielding the numeric relation  $m_{\text{eff}} = 8470 \text{ kg/m}^3 \cdot R^3$  for silica, so about 30 ng for a 30  $\mu\text{m}$ -diameter sphere. The numerical values for the RBMs in silica microtoroids are slightly lower, in the range of 3 to 20 ng for the typical dimensions used.

## 2.3 Silica WGM resonators as optomechanical systems

---

### Forces acting on the mechanical modes

To calculate the radiation pressure force acting on the mechanical modes, it is necessary to assess the momentum transfer from the optical mode to the dielectric medium. The fundamental starting point for such an analysis in a complex geometry such as a silica WGM resonator is the flux of momentum density of the electromagnetic field in the medium [200, 201]

$$T_{ij} = -E_i D_j - H_i B_j + \frac{1}{2} \delta_{ij} \left( \sum_k E_k D_k + \sum_k H_k B_k \right), \quad (2.100)$$

where  $E$ ,  $D$ ,  $H$  and  $B$  denote the usual electric and magnetic fields, indices  $i$  and  $j$  denote the cartesian components of vectors and tensors, and  $\delta_{ij}$  is the Kronecker-delta. In vacuum, the entity  $T_{ij}$  is usually referred to as Maxwell's stress tensor. The body force  $\vec{f}$ , that is, the force density acting on the medium, is given by the divergence of this flux, plus a contribution from a temporal change of the flux density

$$f_i = - \sum_j \frac{\partial T_{ij}}{\partial x_j} - \frac{\partial}{\partial t} \frac{1}{c^2} S_i \quad (2.101)$$

where

$$\vec{S} = \vec{E} \times \vec{H} \quad (2.102)$$

is the real-valued Poynting vector. With  $\vec{D} = \epsilon \vec{E}$  and  $\vec{B} = \mu \vec{H}$  we can write this as

$$\vec{f} = -\frac{1}{2} \vec{E} \vec{E} \vec{\nabla} \epsilon - \frac{1}{2} \vec{H} \vec{H} \vec{\nabla} \mu + \left( \frac{\epsilon \mu}{\epsilon_0 \mu_0} - 1 \right) \frac{1}{c^2} \frac{\partial}{\partial t} (\vec{E} \times \vec{H}) \quad (2.103)$$

where Maxwell's equations  $\vec{\nabla} \cdot \vec{D} = 0$ ,  $\vec{\nabla} \cdot \vec{B} = 0$ ,  $\vec{\nabla} \times \vec{E} = -\mu \partial \vec{H} / \partial t$  and  $\vec{\nabla} \times \vec{H} = +\epsilon \partial \vec{E} / \partial t$  were used [200]. We will neglect in the following the last term, the so-called Abraham force.<sup>5</sup> Furthermore, we neglect the second term due to the close-to-unity magnetic permeability of normal glass and obtain finally

$$\vec{f}(\vec{r}) \approx -\frac{1}{2} E^2(\vec{r})^2 \vec{\nabla} \epsilon(\vec{r}). \quad (2.104)$$

This body force can be recast to

$$\vec{f}(\vec{r}) = \vec{w}(\vec{r}) \frac{E_{\text{em}}}{R} \equiv \vec{w}(\vec{r}) F_{\text{rp}} \quad (2.105)$$

using (2.91) and the scalar radiation pressure force from (2.39)

$$F_{\text{rp}} = -g_0 \frac{E_{\text{em}}}{\omega}. \quad (2.106)$$

---

<sup>5</sup>The nature of this force has also remained a contentious issue for decades [201].

## 2. Cavity optomechanics

---

Note that (2.105) also holds for the simplified assumptions leading to the simplified weighting function (2.92): If all optical power is concentrated to the rim of the toroid, an estimate for the force density can be derived from a simple consideration: A line element  $R d\varphi$  contains the fraction  $d\varphi/2\pi$  of the total number of  $E_{\text{em}}/\hbar\omega$  intracavity photons, where  $E_{\text{em}}$  is the total electromagnetic energy stored in the resonator. Within the time  $nR d\varphi/c$ , each photon transfers a fraction of  $\sin d\varphi \approx d\varphi$  of its momentum  $\hbar k$  to the wall, yielding eventually

$$\vec{f}(\vec{r}) = \frac{1}{Rd\varphi} \frac{d\varphi}{2\pi} \frac{E_{\text{em}}}{\hbar\omega} \frac{\hbar k d\varphi}{nR d\varphi/c} \delta(z - z_0) \delta(r - R) \vec{e}_r = \vec{w}(\vec{r}) \frac{E_{\text{em}}}{R}. \quad (2.107)$$

Irrespective of the detailed form of the weighting function, the energy of the mechanical system reads [194]

$$H = \sum_n \frac{1}{2} M_n (\dot{c}_n(t))^2 + \frac{1}{2} M_n \Omega_n^2 (c_n(t))^2 - \langle \vec{f}, \vec{u} \rangle \quad (2.108)$$

where strain-optical effects are neglected for simplicity. This leads to the following equations of motion for the mechanical mode amplitudes

$$\ddot{c}_n + \Omega_n^2 c_n = \frac{1}{M_n} \langle \vec{f}, \vec{u}_n^0 \rangle \quad (2.109)$$

or, in Fourier domain,

$$c_n(\Omega) = \frac{1}{M_n(\Omega_n^2 - \Omega^2 - i\Omega\Gamma_n)} \cdot \left( \langle \vec{f}(\Omega), \vec{u}_n^0 \rangle + F_{T,n}(\Omega) \right) \quad (2.110)$$

where the damping  $\Gamma_n$  and the corresponding fluctuational force  $F_T$  have been introduced as well. As only the projection  $x_n$  of the excitation of the mechanical mode is measured, one obtains

$$\begin{aligned} x_n(\Omega) &= \langle \vec{w}, \vec{u}_n^0 \rangle c_n(\Omega) = \frac{\langle \vec{w}, \vec{u}_n^0 \rangle}{M_n(\Omega_n - \Omega^2 - i\Omega\Gamma_n)} \cdot \left( \langle \vec{f}(\Omega), \vec{u}_n^0 \rangle + \delta F_{T,n}(\Omega) \right) \\ &= \frac{\langle \vec{w}, \vec{u}_n^0 \rangle^2}{M_n(\Omega_n - \Omega^2 - i\Omega\Gamma_n)} \left( F_{\text{rp}}(\Omega) + \frac{\delta F_{T,n}(\Omega)}{\langle \vec{w}, \vec{u}_n^0 \rangle} \right) \\ &= \frac{1}{m_{\text{eff},n}(\Omega_n - \Omega^2 - i\Omega\Gamma_n)} \left( F_{\text{rp}}(\Omega) + \frac{\delta F_{T,n}(\Omega)}{\langle \vec{w}, \vec{u}_n^0 \rangle} \right). \end{aligned} \quad (2.111)$$

The fluctuational thermal force  $\delta F_{T,n}$  used here obeys

$$\langle \delta F_{T,n}(\Omega) \delta F_{T,n}(\Omega') \rangle = 2\pi \delta(\Omega + \Omega') \hbar M_n \Gamma_n \Omega \left( \coth \left( \frac{\hbar\Omega}{2k_B T} \right) + 1 \right). \quad (2.112)$$

### 2.3 Silica WGM resonators as optomechanical systems

However, an effective thermal force  $\delta F_{\text{th},n}$  is usually introduced, in which  $M_n$  is replaced by  $m_{\text{eff},n}$ . This directly reads to desired correlator (2.55). As a consequence, the displacement fluctuations can be written as

$$x_n(\Omega) = \frac{1}{m_{\text{eff},n}(\Omega_n - \Omega^2 - i\Omega\Gamma_n)} (F_{\text{rp}}(\Omega) + \delta F_{\text{th},n}(\Omega)) \quad (2.113)$$

in the Fourier domain. This is the very one-dimensional description used in section 2.2.

As an illustration of the influence of the effective mass, figure 2.19 shows the spectrum  $\bar{S}_{xx}(\Omega)$  of the fluctuations of  $x = \sum_n x_n$  for a toroid driven by thermal noise according to (2.113). Data were extracted from FEM simulations for toroids the major radius of which has been continuously swept from 35 to 100  $\mu\text{m}$ . Frequencies are a direct simulation result, and the effective masses were extracted using (2.92). All quality factors were, for simplicity, assumed to equal 5000. Clearly, the strong signature of the RBM can be discerned for its low effective mass, on top of the background of weaker flexural modes. At a major diameter of  $\sim 75 \mu\text{m}$ , the avoided crossing discussed in section 2.3.2 is also apparent.

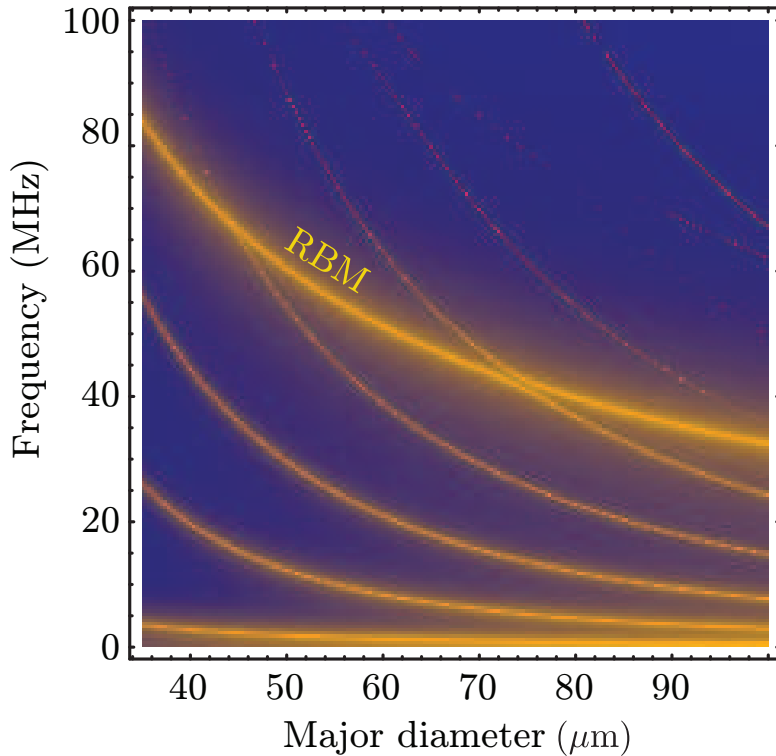


Figure 2.19: Color-coded displacement noise spectrum of a toroid with a 1  $\mu\text{m}$  thick silica disk, a 4  $\mu\text{m}$  minor diameter, 90% undercut and a varying major diameter, as simulated using FEM.

## 2. Cavity optomechanics

### 2.4 Ultrahigh-sensitivity interferometric motion transduction

As a first application, optomechanical coupling as present in WGM resonators allows to monitor mechanical displacements using the optical degree of freedom. While in early work the separation of two resonators was measured in this manner [202], we focus here on the measurement of displacements related to the internal mechanical modes of WGM resonators [9]. The principal idea of such a measurement is illustrated in figure 2.20. In the following, the theoretical limits, possible experimental implementations, and experimental results will be presented.

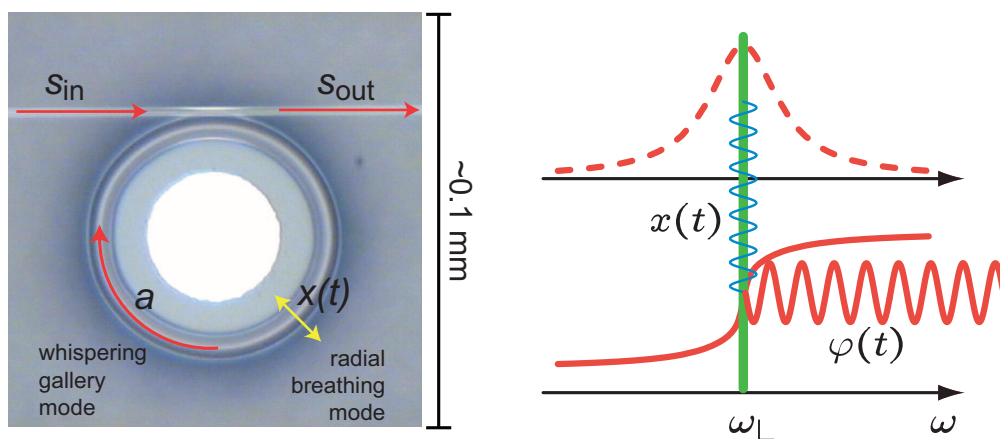


Figure 2.20: High-sensitivity displacement sensing using optomechanical coupling. Left panel: an input field  $s_{\text{in}}$  is launched into the taper and resonantly coupled to the WGM. The properties of the intracavity field  $a$  and the field  $s_{\text{out}}$  coupled back to the fiber taper are modified by the displacement  $x(t)$  of the RBM. Right panel: the launched field at frequency  $\omega_L$  (green line) acquires a phase shift that depends on the mutual detuning of laser and cavity resonance frequency (lower red curve, dashed red curve indicates the WGM Lorentzian as a reference). If the displacement  $x(t)$  modulates the WGM resonance frequency, the phase  $\varphi(t)$  of the emerging field  $s_{\text{out}}$  is also modulated. This phase modulation can be detected with quantum-limited sensitivity by comparison with an optical phase reference.

#### 2.4.1 Theoretical limits in displacement sensing

We first explore the theoretical limits in the sensitivity of the measurement, and restrict ourselves to the simple case of resonant probing  $\bar{\Delta} = 0$  (for a more general discussion, see section 2.7). In this case, the *dynamical properties* of the mechanical oscillator are not affected by the presence of the light in the cavity, that is  $\Gamma_{\text{dba}} = \Omega_{\text{dba}} = 0$  in equations (2.29) and (2.30). Still, the light can be used as a sensitive probe for the mechanical mode; in the following we discuss the performance and theoretical limitations of this method.

## 2.4 Ultrahigh-sensitivity interferometric motion transduction

### Quantum noise

To analyze the fundamental quantum limits, we directly calculate from the relations (2.50)–(2.57) the noise in the light field at the output

$$\delta\hat{s}_{\text{out}}(\Omega) = \delta\hat{s}_{\text{in}}(\Omega) - \frac{\sqrt{\eta_c\kappa}}{-i\Omega + \kappa/2} \left( -ig_0\bar{a}\delta\hat{x}(\Omega) + \frac{\delta\hat{s}_{\text{in}}(\Omega)}{\sqrt{\tau_{\text{ex}}}} + \frac{\delta\hat{s}_{\text{vac}}(\Omega)}{\sqrt{\tau_0}} \right) \quad (2.114)$$

and analogous for  $\delta\hat{s}_{\text{out}}^\dagger(\Omega)$ . For resonant probing, the mean field at the cavity output is real, and therefore the phase quadrature is directly given by

$$\delta\hat{q}_{\text{out}}(\Omega) = i \left( -\delta\hat{s}_{\text{out}}(\Omega) + \delta\hat{s}_{\text{out}}^\dagger(\Omega) \right). \quad (2.115)$$

For the symmetrized noise spectral density<sup>6</sup> of the phase quadrature at the output, defined by

$$\bar{S}_{qq}^{\text{out}}(\Omega) = \frac{1}{2} (S_{qq}^{\text{out}}(+\Omega) + S_{qq}^{\text{out}}(-\Omega)) \quad (2.116)$$

with

$$2\pi\delta(\Omega + \Omega')S_{qq}^{\text{out}}(\Omega) = \langle \delta\hat{q}_{\text{out}}(\Omega)\delta\hat{q}_{\text{out}}^\dagger(\Omega') \rangle \quad (2.117)$$

we get

$$\bar{S}_{qq}^{\text{out}}(\Omega) = 1 + \frac{4\bar{a}^2g_0^2\eta_c\kappa}{\Omega^2 + (\kappa/2)^2}\bar{S}_{xx}(\Omega) \quad (2.118)$$

with the correlators from (2.53)–(2.54). Evidently, the noise spectrum of the phase quadrature contains information on the mechanical displacement spectrum  $\bar{S}_{xx}$ , but also a background term (in this normalization, 1) which is due to the quantum noise. This background constitutes the fundamental imprecision of the measurement, and reads

$$S_{xx}^{\text{im,qn}}(\Omega) = \frac{\Omega^2 + (\kappa/2)^2}{4\bar{a}^2g_0^2\eta_c\kappa} \quad (2.119)$$

if expressed as an equivalent displacement noise. In other words, the imprecision is the *apparent* displacement noise measured in such an experiment, due to the inevitable quantum noise in the measurement of the probing light's phase quadrature.

Recast to experimentally more accessible parameters, (2.119) determines the smallest possible displacement  $\delta x_{\text{min}}(\Omega)$  which can be measured using a WGM resonator [9]

$$\frac{\delta x_{\text{min}}(\Omega)}{\sqrt{\Delta f}} = \sqrt{\bar{S}_{xx}^{\text{im,qn}}(\Omega)} = \frac{\lambda}{16\pi\mathcal{F}\eta_c\sqrt{P_{\text{in}}/\hbar\omega_l}} \sqrt{1 + \left( \frac{\Omega}{\kappa/2} \right)^2} \quad (2.120)$$

<sup>6</sup>Note that double-sided spectral densities are calculated in this chapter.

## 2. Cavity optomechanics

---

where  $\lambda$  is the wavelength in the medium and  $\Delta f$  the measurement bandwidth. Written this way, the importance of high-finesse cavities is directly evident: The smallest displacement that can be measured is roughly given by the wavelength, divided by the cavity finesse and the square root of the number of photons accumulated in the measurement time (inverse bandwidth). The term  $\sqrt{1 + 4\Omega^2/\kappa^2}$  is due to a less efficient transduction of the motion into phase shift for Fourier frequencies beyond the cavity cutoff.

As an aside, we remark that the same result can be obtained by considering the classical transduction of a displacement into the phase of the light exiting the cavity and comparing the result with the shot noise in the measurement of the light phase [8]. Importantly, (2.119) and (2.120) are independent of particular strategy used to detect the light's phase, as long as it can be achieved in a quantum-limited manner. Two strategies to accomplish this, namely homodyne and polarization spectroscopy, are described in section 2.4.2.

As first discussed by Braginsky [94], it is inevitable that the measurement of the oscillator's position disturbs it ("measurement backaction"). In the case of an optomechanical system, this is due to the fluctuations of intracavity radiation pressure [103], which can be written as

$$\delta\hat{F}_{\text{rp}}(\Omega) = -\hbar g_0 \bar{a} \left( \delta\hat{a}(\Omega) + \delta\hat{a}^\dagger(\Omega) \right) \quad (2.121)$$

in (2.52). Again from the known correlators, we obtain here

$$\bar{S}_{FF}^{\text{ba,qn}}(\Omega) = \frac{\bar{a}^2 g_0^2 \kappa \hbar^2}{\Omega^2 + (\kappa/2)^2}, \quad (2.122)$$

if the input noise is again just quantum noise. In this case, the force noise (2.122) is referred to as *quantum backaction*. Evidently, (2.119) and (2.122) fulfill the quantum-mechanically required inequality in the imprecision-backaction product [94]

$$\bar{S}_{xx}^{\text{im,qn}}(\Omega) \cdot \bar{S}_{FF}^{\text{ba}}(\Omega) = \frac{\hbar^2}{4\eta_c} \geq \frac{\hbar^2}{4}. \quad (2.123)$$

By causing *additional* displacement fluctuations in the mechanical oscillator, backaction noise also impedes the determination of the oscillator's displacement. The total uncertainty in the measurement is therefore given by

$$\bar{S}_{xx}^{\text{tot}}(\Omega) = \bar{S}_{xx}^{\text{im,qn}}(\Omega) + |\chi(\Omega)|^2 \bar{S}_{FF}^{\text{ba,qn}}(\Omega), \quad (2.124)$$

where

$$\chi(\Omega) = \frac{1}{m_{\text{eff}}(\Omega_m^2 - \Omega^2 - i\Omega\Gamma_m)} \quad (2.125)$$

is the susceptibility of the mechanical oscillator. Obviously, a tradeoff in terms of the "strength"  $\propto g_0^2 \bar{a}^2$  of the measurement has to be made, as

## 2.4 Ultrahigh-sensitivity interferometric motion transduction

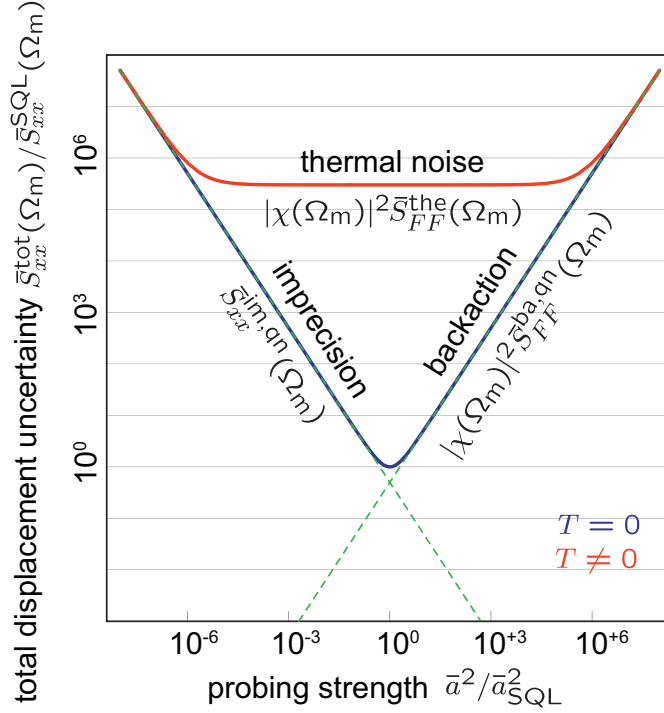


Figure 2.21: Quantum limits in the measurement of mechanical displacements (blue line). For weak probing  $\bar{a}^2 < \bar{a}_{\text{SQL}}^2$ , measurement imprecision dominates the total uncertainty, while for stronger probing  $\bar{a}^2 > \bar{a}_{\text{SQL}}^2$ , the noise in the mechanical oscillator induced by quantum backaction dominates the uncertainty. For optimum measurements with  $\bar{a}^2 = \bar{a}_{\text{SQL}}^2$ , the uncertainty is at the standard quantum limit  $\bar{S}_{xx}^{\text{SQL}}(\Omega_m) = \hbar/m_{\text{eff}}\Gamma_m\Omega_m$ . Under laboratory conditions, thermal noise is additionally present (red line).

imprecision reduces, but backaction increases for “stronger” measurements [103,104], as illustrated in figure 2.21. Optimum measurement conditions are reached for

$$\bar{a}^2 = \bar{a}_{\text{SQL}}^2 = \frac{m_{\text{eff}}\Gamma_m\Omega_m}{2g_0^2\hbar\kappa\sqrt{\eta_c}}(\Omega_m^2 + (\kappa/2)^2), \quad (2.126)$$

or, equivalently an input power of  $P_{\text{SQL}} = \hbar\omega\kappa\bar{a}_{\text{SQL}}^2/4\eta_c$ . In this case, one obtains a total uncertainty of [9]

$$\bar{S}_{xx}^{\text{SQL}}(\Omega) = \frac{\hbar|\chi(\Omega)|}{\sqrt{\eta_c}} = \frac{\hbar}{m_{\text{eff}}\sqrt{\eta_c}((\Omega_m^2 - \Omega^2)^2 + \Gamma_m^2\Omega^2)}, \quad (2.127)$$

called the *standard quantum limit* [94,103] in the case  $\eta_c = 1$ . Its peak value is calculated at  $\Omega_m$ ,

$$\bar{S}_{xx}^{\text{SQL}}(\Omega_m) = \frac{1}{\sqrt{\eta_c}} \frac{\hbar}{m_{\text{eff}}\Gamma_m\Omega_m}. \quad (2.128)$$

In this calculation we have explicitly considered the effect of the coupling conditions to the cavity, which can—as a unique feature—be varied continuously in the experiment by adjusting the gap between the coupling

## 2. Cavity optomechanics

---

waveguide and the WGM resonator. The SQL is approached most closely in the overcoupled limit  $\tau_{\text{ex}} \ll \tau_0$ . It is noteworthy that the fibre-taper coupling technique to microtoroids can deeply enter this regime, and  $100 \cdot \tau_{\text{ex}} < \tau_0$  ( $\eta_c = 99\%$ ) has been demonstrated [62].

### Laser technical noise

The previous derivation deals with the fundamental sensitivity limits. A frequent *technical* limitation is due to excess (beyond the fundamental) noise of the laser used for probing. Frequency noise in the laser, characterized by a power spectral density  $\bar{S}_{\omega\omega}(\Omega)$ , correspond to a higher level of fluctuations in the input phase quadrature,

$$\bar{S}_{qq}^{\text{in}}(\Omega) = 1 + \frac{4|\bar{s}_{\text{in}}|^2}{\Omega^2} \bar{S}_{\omega\omega}(\Omega), \quad (2.129)$$

raising the background on top of which the displacement spectrum has to be observed. Note also that most schemes to measure the phase of the light rely on a phase reference. If this reference is noisy, because it is derived from the same noisy laser, the imprecision in the displacement measurement is given simply by

$$\bar{S}_{xx}^{\text{im,fn}}(\Omega) = \frac{\bar{S}_{\omega\omega}(\Omega)}{g_0^2} \quad (2.130)$$

if the frequency noise overwhelms quantum noise in the measurement.

### Thermorefractive noise

Another important source of noise potentially preventing the measurement of mechanical displacements with quantum-limited sensitivity are fluctuations of the resonance frequency of the WGM [203] which are not related to the mechanical oscillators. For a dielectric resonator as silica microspheres or -toroids, the dominant effect to be considered here are fluctuations of the refractive index due to temperature fluctuations. At any finite mean temperature  $\bar{T}$ , the actual average temperature  $T_V$  in a volume  $V$  fluctuates according to [204]

$$\langle (T_V - \bar{T})^2 \rangle = \frac{k_B \bar{T}^2}{c_p V \rho}, \quad (2.131)$$

where  $\rho$  is the material density, and  $c_p$  the specific heat capacity. This applies in particular also to the mode volume, within which the WGM samples the temperature-dependent refractive index.

To calculate the frequency spectrum of the resulting fluctuations, Gorodetsky and Grudinin [205] have used a Langevin approach, introducing

## 2.4 Ultrahigh-sensitivity interferometric motion transduction

---

fluctuational driving terms into the dynamic equations of temperature diffusion [206, 207]. As a result, the imprecision due to thermorefractive noise in a silica WGM resonator can be estimated to amount to

$$\begin{aligned} \bar{S}_{xx}^{\text{im,tr}}(\Omega) &= R^2 \bar{S}_{\delta n/n}(\Omega) \approx \\ &\approx \frac{k_B T^2 k R}{\pi^{5/2} n^2 \rho^2 c_p^2} \frac{1}{\sqrt{d^2 - b^2}} \left( \frac{dn}{dT} \right)^2 \int_0^{+\infty} \frac{q^2 e^{-\frac{q^2 b^2}{2}}}{D^2 q^4 + \Omega^2} \frac{dq}{2\pi} \end{aligned} \quad (2.132)$$

where  $k$  is heat conductivity,  $R$  the cavity radius, and  $d$  and  $b$  the transverse mode dimensions. At low frequency ( $\lesssim 10$  MHz), this noise can dominate the measurement imprecision (cf. section 2.4.3).

### 2.4.2 Experimental techniques

#### Homodyne spectroscopy

A commonly employed technique for quantum-limited phase measurement is a balanced homodyne receiver [208], which has been used in earlier optomechanical experiments [125, 126, 209]. One possible adaptation of this technique to the ring topology of a WGM resonator is shown in figure 2.22. The probing (or signal) beam and a phase reference beam, referred to as the local oscillator (LO) are derived from the same laser, in this case a monolithic Nd:YAG laser operating at  $\lambda = 1064$  nm. This source exhibits quantum-limited amplitude and phase noise at Fourier frequencies  $\Omega/2\pi \gtrsim 5$  MHz and power levels  $P_{\text{LO}} + P \lesssim 5$  mW of interest. As tuning speed and range of this laser are limited, it was found advantageous to use a home-built external-cavity diode laser for pre-characterization of several samples until a suited toroid is found. The probing beam is sent through the coupling taper and interacts with the WGM of the studied toroid. The LO travels in the reference arm of a Mach-Zehnder interferometer over the same distance. It is finally recombined with the signal beam at a polarizing beam splitter (PBS1). Spatial mode matching of the incident beams is enhanced by using single-mode fibre as mode filter on the local oscillator. After spatial recombination, interference is enforced using a retarder plate and another polarizing beam splitter (PBS2).

As the relative phase of the two interfering beams is also subject to drifts and fluctuations, due to, for example, temperature drift of the fiber in which the reference beam propagates, active stabilization is necessary here. In one possible implementation, this is accomplished by purposely introducing a small polarization mismatch between the light in the taper region and the either predominantly TE- or TM-like WGM modes of the microcavity. The polarization component of the probing beam which does not interact with the WGM resonance can then be used to stabilize the phase of the LO (see

## 2. Cavity optomechanics

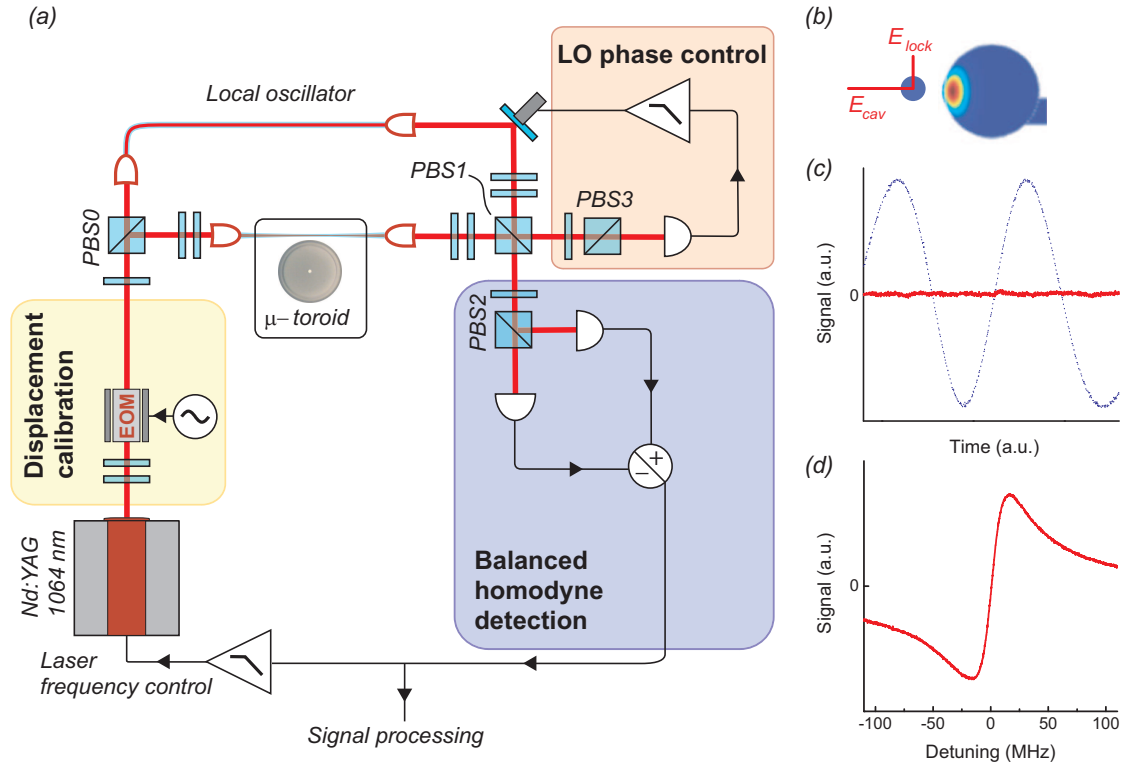


Figure 2.22: (a) Optical interferometric displacement transducer based on homodyne spectroscopy of light transmitted past the cavity (“ $\mu$ -toroid”). The phase of the local oscillator is actively stabilized (“LO phase control”). Details are given in the text. PBS0-PBS3, polarizing beam splitters. (b) Cross section through the fibre taper and the toroidal rim in the coupling region. The polarization in the taper is slightly mismatched with the polarization of the cavity mode. Thus only the part  $E_{cav}$  of the total field couples to the WGM, the other component  $E_{lock}$  can be used for the stabilization of the local oscillator phase. The components  $E_{cav}$  and  $E_{lock}$  are separated in PBS1. (c) Signal in the balanced receiver for a scanning local oscillator (dotted, blue) at low power, and for the locked LO (red). The shown locked trace was recorded for about 5 seconds. (d) Typical experimental error signal in the balanced receiver when the laser is scanned over a cavity resonance with the local oscillator locked to the appropriate phase. Adapted from ref. [9].

## 2.4 Ultrahigh-sensitivity interferometric motion transduction

figure 2.22). In this case, a dispersive signal

$$h(\Delta) = \frac{2\eta_c \kappa \Delta}{\Delta^2 + (\kappa/2)^2} \sqrt{P_{\text{cav}} P_{\text{LO}}}, \quad (2.133)$$

is obtained at the output of the balanced receiver comparing the other polarization component (which is coupled to the WGM) with the LO. Here  $P_{\text{cav}}$  and  $P_{\text{LO}}$  are the powers of the probing and local oscillator beams and  $h(\Delta)$  is the power difference measured between the two employed receivers. figure 2.22 shows an example of an experimental trace obtained when scanning the laser detuning. Evidently, due to its dispersive shape, the d.c.-component of this signal can be used to lock the laser frequency to the WGM resonance frequency using electronic feedback.

In this way, the mean detuning can be stabilized to  $\bar{\Delta} = 0$  and with  $\Delta = \bar{\Delta} - g_0 \delta \hat{x}(\Omega)$  the signal is directly given by

$$h_{\bar{\Delta}=0}(\delta x, \Omega) \approx -\frac{8\eta_c g_0 \delta x(\Omega)}{\kappa} \sqrt{\frac{P_{\text{cav}} P_{\text{LO}}}{1 + (\Omega/(\kappa/2))^2}}, \quad (2.134)$$

where the reduced signal strength for Fourier frequencies  $\Omega$  beyond the cavity cutoff can be viewed as a consequence of the reduced buildup of intracavity sidebands (2.7)<sup>7</sup>. For a strong local oscillator  $P_{\text{LO}} \gg P_{\text{cav}}$ , the detection noise is given by shot noise caused by the local oscillator beam, and the fluctuations in the detected differential power are simply  $\delta h \approx \sqrt{P_{\text{LO}} \hbar \omega_1}$ . Comparison with the signal (2.134) induced by displacements  $\delta x$  then directly give the sensitivity (2.119).

Furthermore, as (2.133) evidently only depends on the mutual detuning of laser and WGM resonance, frequency fluctuations of the laser are indistinguishable from fluctuations due to mechanical displacement. In the case of frequency noise of the laser, this leads directly to the imprecision described by (2.130). On the other hand, an intentional frequency modulation of controlled modulation depth of the laser can be utilized to calibrate the measured signals: a frequency modulation of  $\delta \omega$  corresponds to a displacement of amplitude  $g_0 \delta x$ , independent of the detuning and coupling conditions<sup>8</sup> [8, 124, 125, 205]. With the calibration at one particular modulation frequency  $\Omega_{\text{mod}}$ , the measured spectra can be absolutely calibrated at all Fourier frequencies, taking into account the reduced sensitivity beyond the cavity cutoff at  $\kappa/2$ .

### Polarization spectroscopy (Hänsch-Couillaud method)

A simplified setup may be obtained by copropagating the local oscillator in the same spatial, but orthogonal polarization mode as compared to the signal

<sup>7</sup>A more detailed calculation is presented in the supplementary information of ref. [8].

<sup>8</sup>We emphasize that for this relation to be valid for arbitrary modulation frequencies, it is necessary that the lengths of the two arms of the Mach-Zehnder interferometer are equal.

## 2. Cavity optomechanics

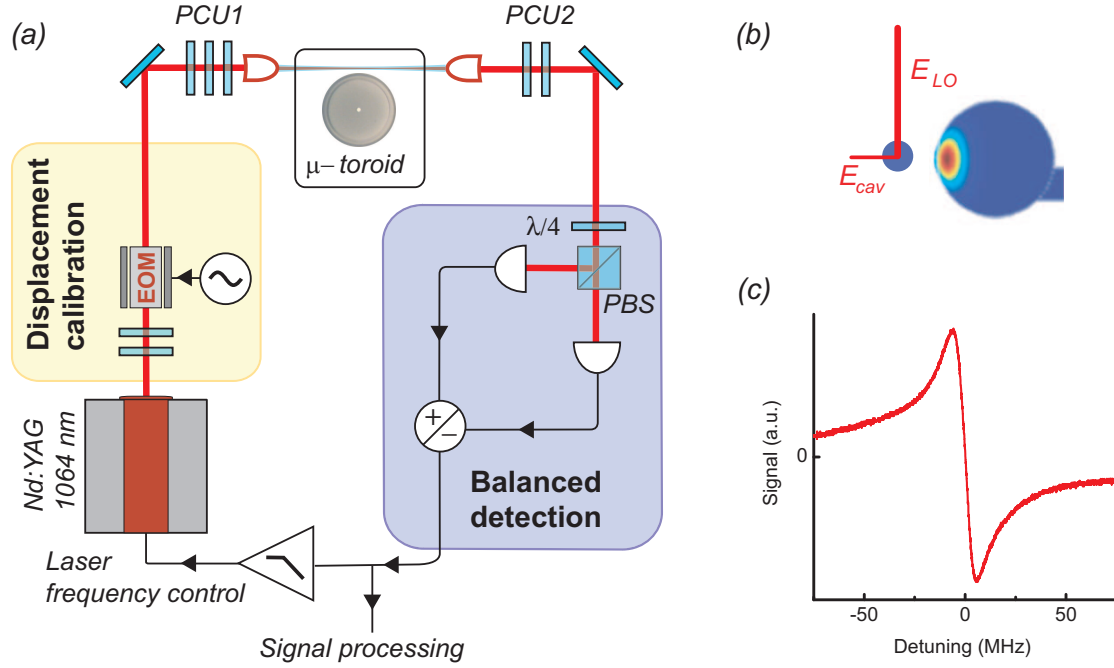


Figure 2.23: Optical interferometric displacement transducer based on polarization spectroscopy of light transmitted in the taper past the cavity (“ $\mu$ -toroid”). (a) After phase modulation with an electro-optic modulator, the polarization is prepared with a first polarization control unit (PCU1). The cavity WGM defines signal and LO polarizations. A second polarization control unit (PCU2) compensates for fibre birefringence. Polarization analysis using a  $\lambda/4$  plate and a polarizing beam splitter enforces interference of the signal and LO fields. (b) Due to the polarization non-degeneracy of the WGM in the cavity, only one polarization component of the light interacts with the mode. (c) Typical error signal obtained when the laser is scanned over a cavity resonance. Adapted from ref. [9].

beam [8]. Since the WGM modes have predominantly TE or TM character and are not degenerate, this guarantees that the local oscillator is not affected by the cavity. Due to common-mode rejection of many sources of noise in the relative phase between signal and LO (for example, frequency noise in the optical fibre), the passive stability is sufficiently enhanced to enable operation without active stabilization (figure 2.23).

Enforcing interference between local oscillator and signal beams then corresponds to polarization analysis of the light (comprising both signal and LO) emerging from the cavity. While novel in the present context of a tapered fibre coupled microcavity, this is a well established technique to derive a dispersive error signal from the light reflected from a Fabry-Perot type reference cavity, named after their inventors Hänsch and Couillaud [210].

If fiber birefringence is adequately compensated, the error signal reads

$$h(\Delta) = \frac{2\eta_c \kappa \Delta}{\Delta^2 + (\kappa/2)^2} \sqrt{P_{\text{cav}} P_{\text{LO}}}, \quad (2.135)$$

identical to (2.133), and a typical trace is shown in figure 2.23(c). This is used to lock the laser at resonance  $\bar{\Delta} = 0$  with a bandwidth of about 10 kHz.

## 2.4 Ultrahigh-sensitivity interferometric motion transduction

Calibration of the spectra may be performed as described in the previous section.

While this approach obviously allows reducing the complexity of the experiment, this arrangement proved more sensitive to slow temperature drifts in the polarization mode dispersion of the fibres employed, due to the large ratio of signal and LO powers, the magnitudes of which are only defined by the polarization state of the light in the fibre taper region. Improved stability may be obtained by reducing fibre length to its minimum of ca. 0.5 m. For reasons of flexibility and convenience, the actual fibre length totaled to several meters in our experiment. Nonetheless, sensitivities of  $10^{-18}$  m/ $\sqrt{\text{Hz}}$  are achieved in toroids using this method [8]. The intrinsic polarization selectivity of WGM renders the introduction of an additional polarizer, mandatory in the original implementation [210], obsolete. In an earlier experiment with a Fabry-Perot cavity [134], the losses associated with an intracavity polarization element limited the finesse, and therefore the attained sensitivity to  $\sim 10^{-14}$  m/ $\sqrt{\text{Hz}}$ .

### Frequency modulation spectroscopy (Pound-Drever-Hall method)

Another possible method to experimentally determine the detuning of laser and WGM resonance is frequency modulation spectroscopy as introduced by Pound, Drever and Hall [211] and discussed in great detail by Black [212]. Figure 2.24 shows a possible application of this scheme to WGM resonators. The dispersive shape of the signal can be used to lock the laser to the WGM resonance using electronic feedback. Fluctuations of the Pound-Drever-Hall (PDH) signal beyond the feedback bandwidth then indicate fluctuations of the WGM resonance frequency with respect to the laser frequency, and can therefore be used to monitor displacements.

While both homodyne and polarization spectroscopy can attain the fundamental quantum-limited displacement sensitivity (2.119), the sensitivity of the PDH method is reduced by a factor  $1 + \eta_c + (1 - 2\eta_c)^2 / 2J_1^2(\beta)$ , where  $\beta$  is the phase modulation depth and  $J_1$  a Bessel function of the first kind [213]. Note that even for a maximally overcoupled cavity with  $\eta_c \rightarrow 1$  this yields  $2 + 1/2J_1^2(\beta)$ . In practice, the displacement sensitivity using this method is often limited by electronic noise in the detector. As essentially all light used in this scheme interacts with the WGM (there is no phase reference beam in a different spatial or polarization mode), the total power levels must be kept low in order to prevent strong thermal nonlinearities. These light levels (typically a few microwatts) are not sufficient to overwhelm the electronic noise of broadband light receivers. If available at the particular wavelength of interest, a low-noise optical amplifier such as an erbium-doped fiber amplifier (EDFA) can however ameliorate this drawback [11] at the expense of a higher noise figure.

## 2. Cavity optomechanics

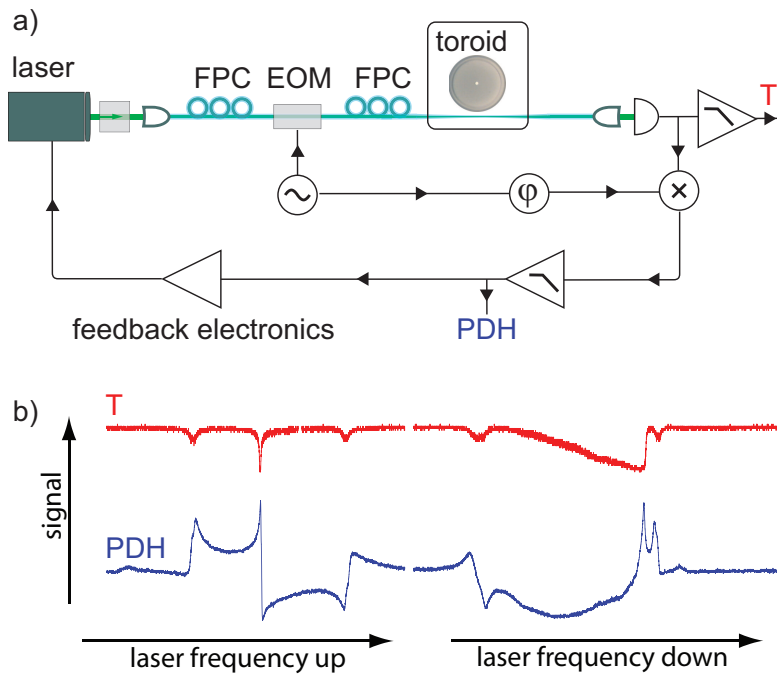


Figure 2.24: Displacement measurement using the Pound-Drever-Hall method [211]. a) The phase of the probing laser is phase-modulated at a radio-frequency of typically 50–100 MHz using a fiber-coupled electro-optic modulator (EOM). After interaction with the WGM, the detected signal is demodulated at the same frequency. The demodulation quadrature is chosen by adjusting the phase  $\varphi$  of the radio-frequency wave. In the simplest case, this can be accomplished by adjusting the length of the cable carrying the signal. The demodulated signal is low-pass filtered at a bandwidth well below the modulation signal. The resulting signal “PDH” can be used to monitor the detuning of laser and WGM resonance, and is also suited to electronically stabilize the laser frequency to the WGM. In addition, the transmission “T” of the WGM can be directly monitored. FPC, fiber polarization controller. b) Typical traces of transmission and PDH signals obtained with a silica toroidal WGM upon a laser frequency scan in the presence of thermal bistability. The satellite dips in the transmission signal appear when the modulation sidebands are scanned over the WGM frequency.

## 2.4 Ultrahigh-sensitivity interferometric motion transduction

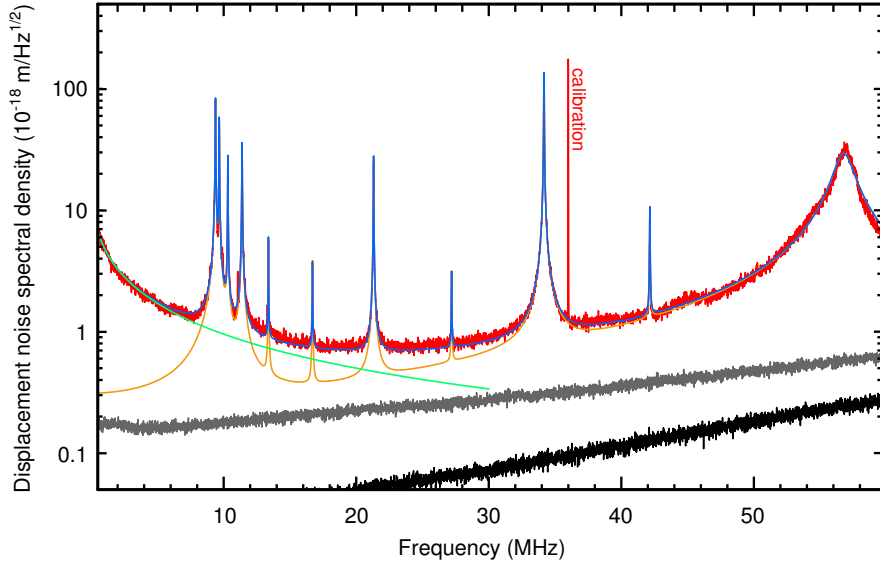


Figure 2.25: Equivalent displacement noise measured in a  $\sim 90 \mu\text{m}$ -diameter silica toroidal cavity. Red, measured trace with laser coupled to a cavity resonance, including a peak at 36 MHz due to phase modulation for calibration purposes. Gray, measured shot noise with taper retracted from the cavity and black, detector noise. Models for mechanical noise (orange line) and thermorefractive noise (green line), and sum of the two models plus the shot noise background (blue line) are also shown. Adapted from ref. [9].

### 2.4.3 Observation and analysis of quantum and thermal noise

Figure 2.25 shows data obtained using homodyne spectroscopy on a toroid of about  $45 \mu\text{m}$  radius. As long as the taper is retracted from the WGM evanescent field, quantum shot noise is observed to exceed the electronic detector noise. Note that while the detected shot noise (due to the local oscillator) is spectrally flat (white noise) to a good approximation, the equivalent displacement noise plotted in figure 2.25 exhibits a calculated  $\sqrt{1 + \Omega^2/(\kappa/2)^2}$  frequency dependence beyond the cavity cutoff at  $\kappa/2 \approx 2\pi \cdot 17 \text{ MHz}$  due to the Fourier frequency-dependent transduction (2.134).

Approaching the taper to the resonator, and locking the laser to the WGM resonance, a substantially different spectrum is observed (figure 2.25). The equivalent displacement noise is calibrated in absolute terms using an *a priori* known phase modulation at 36 MHz, as explained in subsection 2.4.2, taking also the cavity cutoff into account. While the background due to quantum measurement imprecision is at a level of  $10^{-19} \text{ m}/\sqrt{\text{Hz}}$  at low Fourier frequency, a significantly higher equivalent displacement noise level is observed when coupling the laser to the WGM.

The broad background particularly strong at low frequency can be quantitatively reproduced by the model for thermorefractive noise (2.132), when no parameters except  $b$  and the absolute magnitude are adjusted by factors of order 2. This is justified considering the approximations made in the derivation, and the incomplete knowledge on the transverse mode shape of the

## 2. Cavity optomechanics

---

WGM probed in this experiment. We note here as an aside that thermorefractive noise, measured here for the first time in a toroidal microresonator, is an important limitation for the generation of Kerr squeezing in these devices [214].

On top of these backgrounds, a sparse spectrum of peaks is observed, which are due to different mechanical modes in the spectrum. In this measurement at room temperature, the thermal Langevin force largely dominates over radiation pressure force fluctuations. Therefore, each individual mode is driven by a random thermal force according to equation (2.113), and the thermal displacement noise spectra of the individual modes add up to the total measured equivalent displacement noise

$$\bar{S}_{xx}^{\text{tot}}(\Omega) \approx \bar{S}_{xx}^{\text{im,qn}}(\Omega) + \bar{S}_{xx}^{\text{im,tr}}(\Omega) + \sum_n |\chi_n(\Omega)|^2 \bar{S}_{FF}^{\text{th},n}(\Omega), \quad (2.136)$$

where the symmetrized spectrum of the Langevin force is given, from (2.55), by

$$\bar{S}_{FF}^{\text{th},n}(\Omega) = \hbar m_{\text{eff},n} \Gamma_n \Omega \coth\left(\frac{\hbar\Omega}{2k_B T}\right) \approx 2m_{\text{eff},n} \Gamma_n k_B T, \quad (2.137)$$

where the second relation is valid as long as  $k_B T \gg \hbar\Omega$  for the frequencies of interest.

Figure 2.26 shows another example of a highly sensitive measurement, using the Hänsch-Couillaud technique in this case. Beyond the clear signatures of the RBM at around 73 MHz, fifteen other peaks related to mechanical modes are observed. Zooms on the individual peaks reveal that some are split, typically observed in modes whose degeneracy is lifted by residual asymmetry of the sample. The mode frequencies can be reproduced very accurately using finite element modeling; the peaks shown in this figure correspond to the modes discussed in section 2.3.2 (cf. also figures 2.11 and 2.12).

Finally, in figure 2.27, a zoom on the signature of a RBM of a larger sample ( $R = 38 \mu\text{m}$ ) is shown. The measurement achieves a signal-to-background ratio of nearly 60 dB determined by measurement imprecision due to detection shot noise. This dynamic range exceeds the ratio

$$\frac{|\chi(\Omega_m)|^2 \bar{S}_{FF}^{\text{the}}(\Omega_m)}{\bar{S}_{xx}^{\text{SQL}}(\Omega_m)} \approx 2\langle n \rangle. \quad (2.138)$$

We can therefore conclude that the imprecision background, at a level of  $1.1 \text{ am}/\sqrt{\text{Hz}}$ , is *below* the standard quantum limit, calculated to  $\bar{S}_{xx}^{\text{SQL}}(\Omega_m) = (2.2 \text{ am}/\sqrt{\text{Hz}})^2$  for this sample with  $\Omega_m/2\pi = 40.6 \text{ MHz}$ ,  $\Gamma_m/2\pi = 1.3 \text{ kHz}$  and  $m_{\text{eff}} = 10 \text{ ng}$ . We emphasize however, that this does not imply that measurements with a better *total* uncertainty than the standard quantum limit are possible. Quantum backaction-induced fluctuations in the mechanical displacement increase the position uncertainty, but are masked by thermal noise in this measurement.

## 2.5 Observation of dynamical backaction

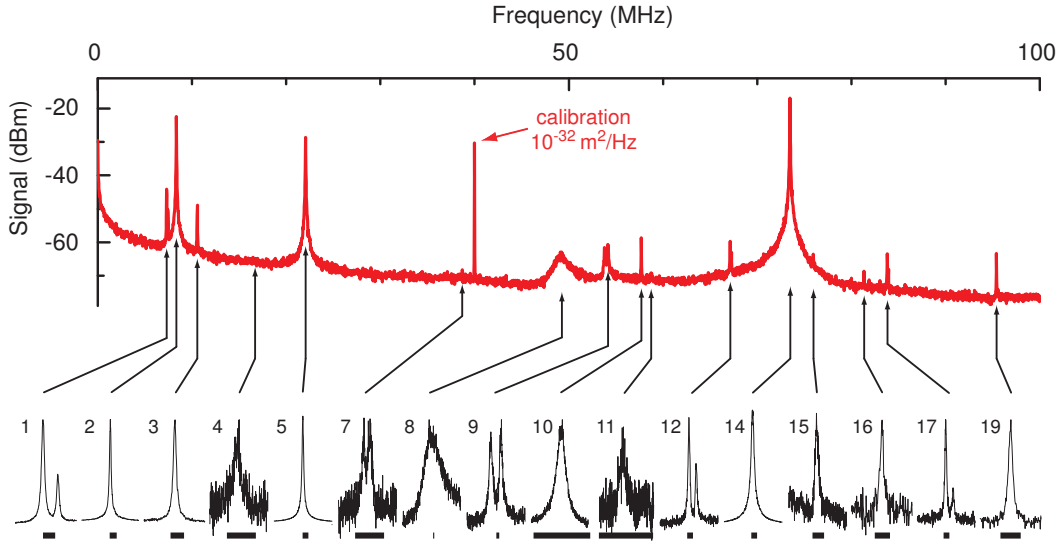


Figure 2.26: Broadband displacement noise spectrum recorded using the Hänsch-Couillaud technique (top panel). Zooms on the individual peaks (lower panels) reveal the precise frequency and linewidth of the modes (scale bar corresponds to a 100 kHz frequency span), some of which are split due to a lifted degeneracy. All observed peaks could be attributed to mechanical modes using finite element modeling (section 2.3.2). Adapted from ref. [9].

## 2.5 Observation of dynamical backaction

In contrast to the resonant probing scenario discussed in the previous section, the dynamics of the mechanical oscillator get modified by radiation-pressure backaction if the optical mode is pumped in a detuned manner. This so-called “dynamical backaction” not only modifies the effective damping and spring constant of the mechanical oscillators, but, as we will show in the following, also leads to an energy exchange between optical and mechanical modes.

Predicted as early as the 1960ies by Braginsky [97], dynamical backaction has been observed early on in mechanical devices coupled to microwave resonators [98, 99, 215–217]. In the optical domain, dynamical backaction induced by radiation pressure has been first observed by the Vahala group in 2005 in the form of an oscillatory instability and studied in great detail [181, 218–221].

Here, we present a systematic study of dynamical backaction as observed in silica microresonators, in particular its dependence on the relevant frequencies  $\kappa$ ,  $\Omega_m$  and  $\bar{\Delta}$ , and briefly introduce the oscillatory instability described above. In the second part, we focus on the case of negative detuning  $\bar{\Delta} < 0$ . In this case, the light field extracts energy from the mechanical mode, leading to the cooling of the latter. This effect was first reported by our group in Garching [1] and groups in Paris [138] and Vienna [141]. Finally, we rule out thermal nonlinearities as the origin of optomechanical interactions in silica microtoroids.

## 2. Cavity optomechanics

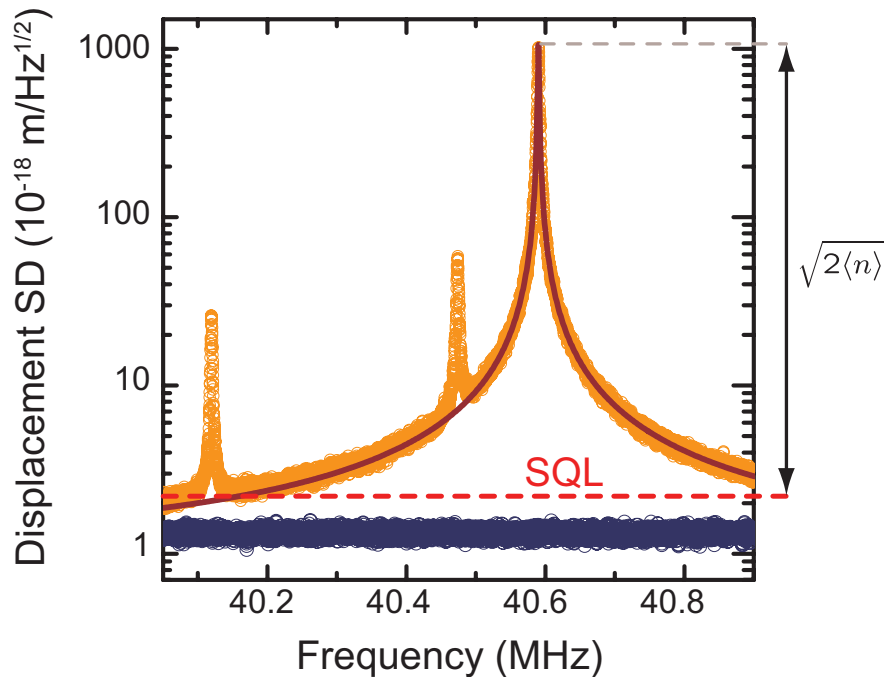


Figure 2.27: High sensitivity-measurement of the RBM of a larger sample using the Hänsch-Couillaud technique. Orange circles represent measured data, revealing also the signatures of two neighboring modes, dark red line is a Lorentzian fit. Blue circles are the recorded measurement imprecision due to detection shot noise. An excellent signal-to-background ratio of nearly 60 dB is attained, corresponding to a measurement imprecision of  $1.1 \text{ am}/\sqrt{\text{Hz}}$ , which is well below the standard quantum limit at  $2.2 \text{ am}/\sqrt{\text{Hz}}$ .

### 2.5.1 Optical spring and optical damping

For a detuned optical pump, we have found in section 2.2.1 that the presence of light modifies the dynamics of the mechanical degree of freedom when it responds to an external force. In an intuitive picture, this can be understood as the consequence of the in-phase and quadrature response of the radiation-pressure force, when the mechanical oscillator is driven by the external force. The same result is formally attained using the quantum Langevin approach. Disregarding, in a first step, the quantum fluctuations of the light ( $\delta\hat{s}_{\text{in}} = \delta\hat{s}_{\text{vac}} \rightarrow 0$ )<sup>9</sup>, the radiation pressure force fluctuations in Fourier space read

$$\delta\hat{F}_{\text{rp}}(\Omega) = i\hbar g_0^2 \bar{a}^2 \delta\hat{x}(\Omega) \left( \frac{1}{-i(\bar{\Delta} + \Omega) + \kappa/2} - \frac{1}{+i(\bar{\Delta} - \Omega) + \kappa/2} \right), \quad (2.139)$$

equivalent to (2.26). As a consequence, the mechanical oscillator reacts to the thermal Langevin force with the effective susceptibility already derived in (2.28).

<sup>9</sup>This simplification is justified as long as the thermal Langevin force largely exceeds force fluctuations due to the quantum nature of the light.

## 2.5 Observation of dynamical backaction

To confirm these predictions, a series of measurements was taken using the setup described in figure 2.28. A 980 nm-wavelength diode laser was locked to a resonance of the silica microtoroid, using simply the transmission signal as an error signal, from which an offset can be subtracted to control the detuning. Moderate optical quality factors ( $Q < 10^7$ ) and low optical powers ( $P_{\text{in}} \sim 200 \mu\text{W}$ ) ensure that thermal nonlinearities are weak enough to still allow stable locking.

Applying this procedure to both the red ( $\bar{\Delta} < 0$ ) and blue ( $\bar{\Delta} > 0$ ) wing of the optical resonance by changing the sign of the error signal, a detuning series can be recorded. From the transmission signal level with the laser locked to the side of the fringe, the relative detuning  $\bar{\Delta}/\kappa$  can be determined. At the same time, the fluctuations of the transmitted power, as recorded by the spectrum analyzer, reflect the position fluctuations of the mechanical modes.

Driven predominantly by the thermal Langevin force with its essentially frequency-independent spectrum (2.137), the measured displacement spectrum directly reveals the effective susceptibility of the mechanical mode. It is therefore possible to extract the effective damping and resonance frequency of the mode using the fit model (2.28). Figure 2.29 shows the data obtained from the 56.5 MHz-RBM of a silica microtoroid together with fits by the models (2.32) and (2.31). The measured changes in both damping and resonance frequency agree well with expectation.

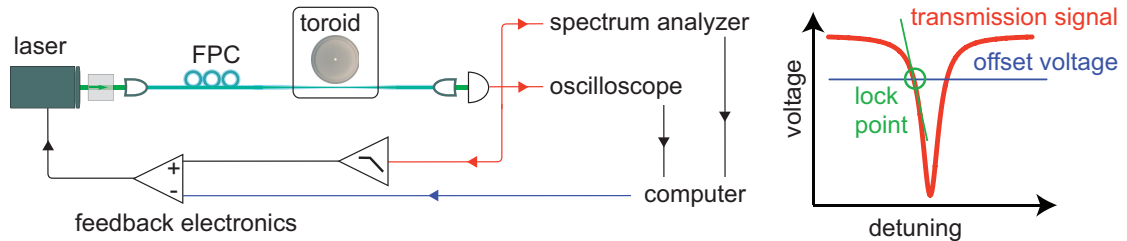


Figure 2.28: Schematic illustration of the setup used for the measurement of dynamical backaction. A diode laser is locked to the side of the optical fringe by applying an electronic, computer-controlled offset to the transmission signal. This differential signal is used as an error signal in a feedback loop actuating the laser frequency by regulating both the position of the grating in the laser cavity, and the current pumping the laser diode. Once the laser is locked, the detuning is varied in small steps by adjusting the electronic offset. For each detuning, a trace from the oscilloscope (to determine the actual residual transmission) and a noise spectrum from the electronic spectrum analyzer are taken. FPC, fiber polarization controller.

The resonance frequency shift is often referred to as “optical spring” effect [222], as it originates from an optical restoring force proportional to the displacement of the resonator. It is interesting to note that this optical force can even exceed the natural restoring force of the mechanical oscillator, and thereby totally dominate the mechanical resonance frequency [148]. For silica microresonators, due to the stiffness of the structure, this is typically

## 2. Cavity optomechanics

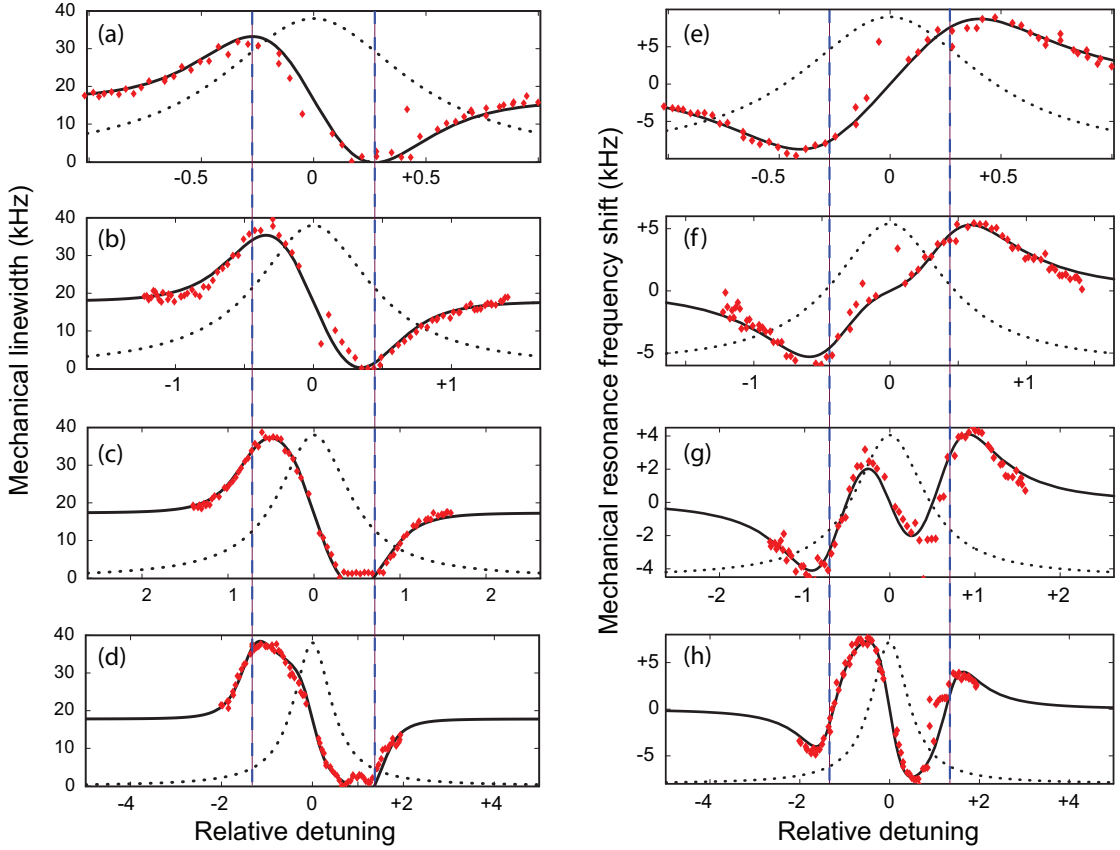


Figure 2.29: Linewidth (a–d) and mechanical resonance frequency shift (e–h) of the mechanical mode as a function of relative laser detuning  $\bar{\Delta}/\kappa$  for optical resonance linewidths  $\kappa/2\pi$  of about 207 MHz (a,e), 127 MHz (b,f), 79 MHz (c,g) and 42 MHz (d,h). Dotted lines indicate the corresponding optical resonance Lorentzian, over which the laser was tuned. Dashed blue lines marks a detuning equal to the mechanical oscillator’s frequency of 56.5 MHz and full lines are fits from the models for dynamical backaction.

not the case. In these devices however, another interesting effect occurs for narrow optical resonances ( $\kappa < \Omega_m$ ): in this case, the optical spring force changes its sign for small detunings, turning a restoring into an anti-restoring force and vice versa [1], an effect not observed in other systematic studies of dynamical backaction [138, 223].

The optically induced damping can provide both positive and negative damping. For positive detuning  $\bar{\Delta} > 0$ , the total damping can reach zero. In this case, the mechanical mode, initially driven by thermal noise, starts to oscillate regeneratively. Specifically, solving  $\Gamma_{\text{eff}} = 0$  for a threshold power, one obtains

$$P_{\text{thresh}} = \Gamma_m \frac{\bar{\Delta}^2 + (\kappa/2)^2}{\eta_c \kappa} \frac{\omega_c m_{\text{eff}} \Omega_m}{g_0^2} \times \left( \frac{\kappa/2}{(\bar{\Delta} - \Omega_m)^2 + (\kappa/2)^2} - \frac{\kappa/2}{(\bar{\Delta} + \Omega_m)^2 + (\kappa/2)^2} \right)^{-1} \quad (2.140)$$

## 2.5 Observation of dynamical backaction

for this optically driven mechanical oscillation to occur. This effect, often referred to as parametric oscillatory instability (POI), has been reported for various systems, including silica microspheres [5] with mechanical modes at up to GHz-frequencies [147]. For light powers largely exceeding the threshold, nonlinearities neglected in the linearized models presented in this work lead to complex behavior such as multistability [224] and chaos [225]. For an in-depth theoretical discussion of the oscillatory instability, including also quantum effects, we refer the reader to references [226, 227].

As an aside we note that in the regime  $\kappa \ll \Omega_m = \bar{\Delta}$  discussed in greater detail in section 2.6, one finds the interesting relation

$$P_{\text{thresh}} = 4\sqrt{\eta_c} P_{\text{SQL}}. \quad (2.141)$$

This therefore universally relevant power scale (for both dynamical and quantum backaction) is at the level of  $30 \mu\text{W}$  for typical parameters of silica microtoroids.

### 2.5.2 Cooling by dynamical backaction

As yet, we have only discussed the damping and resonance frequency of the mechanical mode and its modification by dynamical backaction. However, a major feature of light-induced damping is that it also changes the temperature of the mechanical mode. To introduce the concept of a “mode temperature”, let us first evaluate the amplitude of the displacement of a specific mode, which is driven by the thermal Langevin force, by integrating its noise spectrum over all Fourier frequencies

$$\begin{aligned} \langle \delta x^2 \rangle &= \int_{-\infty}^{+\infty} \bar{S}_{xx}(\Omega) \frac{d\Omega}{2\pi} = \int_{-\infty}^{+\infty} |\chi(\Omega)|^2 \bar{S}_{FF}^{\text{th}}(\Omega) \frac{d\Omega}{2\pi} \approx \\ &\approx \int_{-\infty}^{+\infty} \frac{2m_{\text{eff}}\Gamma_m k_B T}{m_{\text{eff}}^2 ((\Omega^2 - \Omega_m^2)^2 + \Omega^2 \Gamma_m^2)} \frac{d\Omega}{2\pi}. \end{aligned} \quad (2.142)$$

This integral can be evaluated using the residue theorem (cf. section B.1), one obtains

$$\frac{1}{2} m_{\text{eff}} \Omega_m^2 \langle \delta x^2 \rangle = \frac{1}{2} k_B T. \quad (2.143)$$

We may turn this result around and use it to introduce the mechanical mode temperature

$$T_m = m_{\text{eff}} \Omega_m^2 \langle \delta x^2 \rangle / k_B. \quad (2.144)$$

With this definition, if the mechanical mode is only driven by the Langevin force, it ends up in thermal equilibrium with its environment, and  $T_m = T$ . As an example, the root-mean-square (RMS) displacement  $\langle \delta x^2 \rangle^{1/2}$  of the RBM of a silica microtoroid is typically a few tens of femtometers at room temperature (figure 2.30).

## 2. Cavity optomechanics

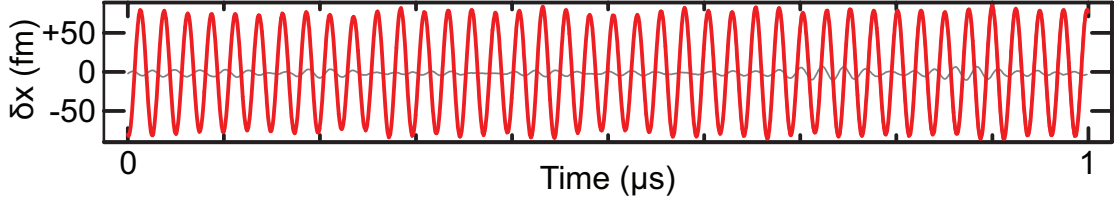


Figure 2.30: Real-time recording of the displacement of a 40.6-MHz RBM of a silica microtoroid measured using the Hänsch-Couillaud technique. A 2 MHz-wide band was filtered out of the displacement signal and selectively amplified to record the mechanical trace (red line). The gray line is a background trace recorded with the taper retracted from the cavity [8].

In the presence of detuned pumping, the mechanical susceptibility is modified due to dynamical backaction, *the thermal Langevin force, however, is not*. If, therefore, the RMS displacement is calculated from the modified spectrum

$$\bar{S}_{xx}(\Omega) = |\chi_{\text{eff}}(\Omega)|^2 \bar{S}_{FF}^{\text{th}}(\Omega) \quad (2.145)$$

one obtains

$$\frac{1}{2} m_{\text{eff}} \Omega_m^2 \langle \delta x^2 \rangle \approx \frac{1}{2} \frac{\Gamma_m}{\Gamma_{\text{eff}}} k_B T \quad (2.146)$$

as long as the mechanical oscillator can be described with its frequency-independent effective damping  $\Gamma_{\text{eff}}$  and resonance frequency  $\Omega_{\text{eff}}$  for not too strong backaction effects<sup>10</sup>. The mode temperature of the mechanical oscillator therefore is changed to

$$T_m = \frac{\Gamma_m}{\Gamma_{\text{eff}}} T = \frac{\Gamma_m}{\Gamma_m + \Gamma_{\text{dba}}} T. \quad (2.147)$$

As for  $\Gamma_{\text{dba}} > 0$  one has  $T_m < T$  the damping rate  $\Gamma_{\text{dba}}$  induced by dynamical backaction is often referred to as the laser *cooling rate*.

Indeed it can be shown that  $\Gamma_{\text{dba}}$  is the rate with which energy is transferred from the mechanical resonator to the optical field. Returning, for simplicity, to the example of a sinusoidally oscillating boundary considered in section 2.2.1 ( $x(t) = x_0 \sin(\Omega_m t)$ ), the cycle-averaged work done by the mechanical oscillator on the optical field can be calculated to

$$P_{\text{dba}} = -\frac{2\pi}{\Omega_m} \int_0^{2\pi/\Omega_m} F_{\text{rp}}(t) \dot{x}(t) dt \approx \Gamma_{\text{dba}} \left( \frac{1}{2} m_{\text{eff}} \Omega_m^2 x_0^2 \right) \quad (2.148)$$

using only the elementary relations (2.9) and (2.11).

In very general terms, this cooling effect arises by coupling the mechanical oscillator not only to the reservoir—constituted by all other mechanical modes present in the device, the gas and thermal radiation field surrounding it etc.—at room temperature, but also to the cooling laser field. Laser cooling therefore disequilibrates the oscillator with the reservoir, and brings it into

<sup>10</sup>See e. g. [121] for more general calculations.

## 2.5 Observation of dynamical backaction

a new equilibrium in which it is coupled both to the reservoir and the laser field. This field possesses an effective temperature very close to zero (see section 2.6 for the limitations), and acts as a “cold damper”, by introducing dissipation, but only very little fluctuations to the mechanical mode.

We note here that the application of cold damping schemes has a long history in physics, and has been successfully applied in systems as diverse as electrometers and particle storage rings [228–230] (here often referred to as “stochastic cooling”). Interestingly, cold damping has also been used to cool a mechanical mode of a mirror in a pioneering 1999 experiment at Laboratoire Kastler Brossel in Paris [130], and subsequently in many other experiments [137, 144, 149, 150, 231]. However, these experiments all involve a complex hybrid electronic/optical feedback loop, whereas the method presented here relies solely on the intrinsic dynamics of radiation pressure.

In figure 2.31 we show cooling results obtained on the RBM of silica microresonators at frequencies around 57 MHz. In an experimental setup essentially identical to the one described in figure 2.28, a 980-nm wavelength diode laser was locked to the red wing of an optical resonance. Note that as the thermal bistability (section 1.5.1) renders the red wing dynamically unstable under laser or cavity frequency fluctuations, special care has to be taken in the implementation of the feedback loop stabilizing the laser frequency to a given detuning (see also appendix C.2 for more details).

As the launched laser power is increased, the total damping increases, and correspondingly the width of the Lorentzian resonance. At the same time, the temperature  $T_m$  of the mode is reduced by the optical pumping. Panel (a) shows four traces for detuned pumping of a WGM mode with  $\bar{\Delta} \approx -\kappa/2 \approx -25$  MHz. For the highest pump powers, the damping is increased beyond 450 kHz, and the correspondingly reduced mode temperature is 11 K. The other panels show a systematic power series, in which a different torus was pumped at  $\bar{\Delta} \approx -0.7\kappa$  with powers between 20 and 200  $\mu$ W.

### 2.5.3 Radiation pressure versus thermal effects

In many early experiments, the optomechanical interaction has been mediated by thermal effects, sometimes referred to as “photothermal pressure” instead of radiation pressure [135, 136, 141, 154, 232]. In the following we present evidence for the fact that the optomechanical interaction in silica microtoroids is strongly dominated by radiation pressure due to the high ( $\Omega_m/2\pi \gtrsim 50$  MHz) frequencies of the RBM.

Prior work on the radiation-pressure-induced parametric oscillatory instability has provided independent evidence that radiation-pressure dominates the interaction between optical and mechanical modes [181, 220] in this system. For instance, it has been shown that the mechanical gain depends on the cavity finesse. This observation demonstrates that radiation pressure is responsible, since thermal forces only depend on the absorbed power and not

## 2. Cavity optomechanics

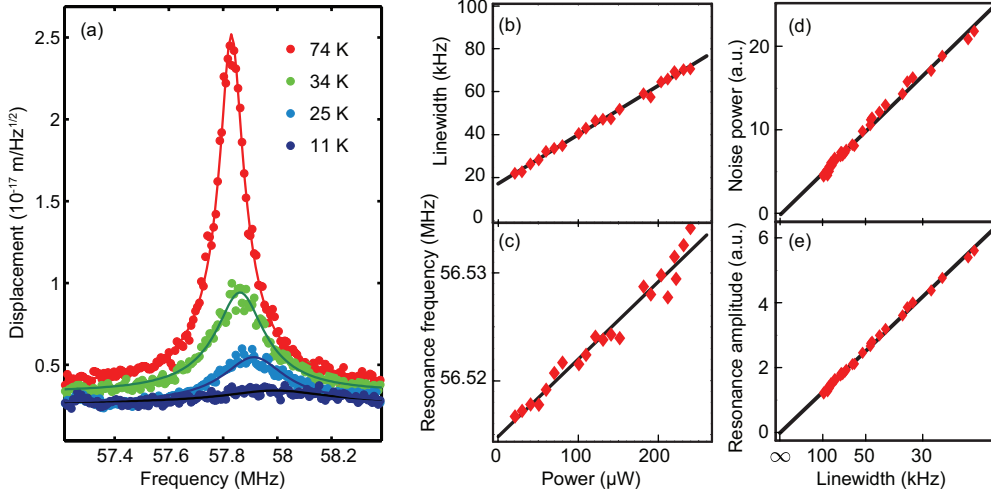


Figure 2.31: Cooling of the RBM of silica microtoroids. (a) Noise spectra of the RBM when a 50 MHz-wide WGM resonance is pumped at  $\bar{\Delta} \approx -\kappa/2$  with increasing power (0.25 mW, 0.75, 1.25 mW and 1.75 mW). The extracted increased damping rates  $\Gamma_{\text{eff}}$  correspond to mode temperatures  $T_m$  given in the legend. (b)–(e) Dependence of mechanical mode properties on the launched laser power (measured on the RBM of a different toroid). The linewidth  $\Gamma_{\text{eff}}$  and resonance frequency  $\Omega_{\text{eff}}$  vary linearly with input power in this range, and both the noise power  $\int_{-\infty}^{+\infty} \bar{S}_{xx}(\Omega) d\Omega / 2\pi \propto T_m$  and the resonance amplitude  $\sqrt{\bar{S}_{xx}(\Omega_m)}$  vary linearly with the inverse linewidth  $\Gamma_{\text{eff}}^{-1}$  as expected. Reprinted figures with permission from Schliesser *et al.*, Physical Review Letters **97**, 243905 (2006). Copyright 2006 by the American Physical Society (reference [1]).

on the cavity enhanced circulating power.

To theoretically estimate the forces due light absorption it is necessary to study the coupling of mechanical and thermal waves (or modes) of the structure. Thermodynamical considerations allow to derive the mutually coupled differential equations for temperature and displacement distributions [233], adding a coupling term proportional to the linear expansion coefficient  $\alpha$  to the heat diffusion equation (1.43) and the equations of motion of the displacement field (2.58).

For small perturbations, we may however assume that the solutions of the uncoupled system ( $\alpha \rightarrow 0$ ) are still approximately valid, and heat transport is still dominated by diffusion. In this case, the resulting temperature gradients give rise to a thermoelastic body force [233]

$$\vec{f}_{\text{te}}(\vec{r}) = -(3\lambda + 2\mu)\alpha \vec{\nabla} \delta T(\vec{r}) \quad (2.149)$$

driving the mechanical modes ( $\lambda$  and  $\mu$  are the Lamé constants). Importantly, this body force depends on the gradient of the temperature distribution.

The effective scalar thermal force on a mechanical mode with a displacement pattern  $\vec{u}_n^0$  is determined by an overlap integral  $\langle \vec{f}_{\text{te}} \vec{u}_n^0 \rangle$ . Due to the very high mechanical resonance frequencies, the diffusion length for the temperature distribution  $\lambda_D = \sqrt{2k/c_p \rho \Omega}$  becomes very short, for example about

## 2.5 Observation of dynamical backaction

50 nm for  $\Omega/2\pi = 50$  MHz. If absorption takes place in the silica, we can therefore conclude that the temperature distribution is essentially given by the energy distribution of the optical mode, and the resulting temperature modulation in the volume can be estimated at  $\delta T(\Omega) \approx 2P_{\text{abs}}/\Omega c_p \rho V_{\text{mode}}$ , typically  $\lesssim 10$  K/W for a typical 30  $\mu\text{m}$ -radius toroid—a value confirmed by finite element modeling of heat diffusion in such a geometry. Due to the nearly *symmetric* temperature distribution in radial direction with respect to the center of the optical mode, the overlap integral over the gradient of the temperature distribution can be expected to yield only a small total contribution. For a rough estimate, we may use

$$\begin{aligned} \langle \vec{f}_{\text{te}} \vec{u}_n^0 \rangle &\propto \int_V \vec{\nabla} \delta T(\vec{r}) \vec{u}_n^0(\vec{r}) d^3r \approx |\vec{u}_n^0(R)| 2\pi R d_m \int_{R-d_m}^R \partial \delta T / \partial r dr \\ &\approx |\vec{u}_n^0(R)| 2\pi R d_m \delta T(R), \end{aligned} \quad (2.150)$$

where  $d_m \ll R$  is the transverse diameter of the optical mode. Using  $\delta T(R)/P_{\text{abs}} \approx 2$  K/W for the parameters described above (again confirmed by FEM), we obtain  $\langle \vec{f}_{\text{rp}} \vec{u}_n^0 \rangle / \langle \vec{f}_{\text{te}} \vec{u}_n^0 \rangle \approx \mathcal{O}(10^2)$ . We note however that this result depends on the exact location of the heat source (absorption may also take place in a water or helium surface layer), and the cooling mechanisms provided by a surrounding medium, effects presently investigated in our group [234]. We also note that at cryogenic temperatures, thermoelastic coupling is weaker as the expansion coefficient drops below  $2 \cdot 10^{-9}$  K $^{-1}$  at 1.6 K [11, 235].

At the experimental side, we have made response measurements [219] to quantify the different nonlinearities—due to the thermal, Kerr and radiation-pressure effects—encountered in silica microtoroids. To that end, two lasers at different wavelengths (980 and 1550 nm in this case) are coupled to two WGM resonances of a single toroid. One laser, referred to as the “pump”, is amplitude modulated at a variable frequency  $\Omega$ , while the other “probe” laser is used to measure the response of the WGM frequency to the pump laser power modulation. In the simplest case, this is accomplished by tuning the probe laser to the wing of a WGM resonance, and measuring the variation of its transmission at the same frequency  $\Omega$ , most conveniently implemented using a network analyzer. Care is taken to suppress direct optical or electronic cross-talk of the pump modulation into this signal.

Figure 2.32 shows the result of such a measurement on a 29  $\mu\text{m}$ -major radius toroid. Clearly, at low frequencies ( $\Omega/2\pi < 1$  MHz), a strong modulation of the probe WGM frequency is apparent. This is due to absorption of pump light, and the consequent modulation of the temperature-dependent expansion, and refractive index of the toroid material (cf. section 1.5.1). Above this frequency, a plateau is observed in the response, due to the modulation of the refractive index seen by the probe WGM, which varies with pump power due to the non-linear refractive index of silica (Kerr effect, see section 1.5.3).

## 2. Cavity optomechanics

Finally, around a mechanical resonance, a dispersive peak is observed. This is due to the excitation of mechanical modes by the modulated pump power.

To fit the response, we use the model

$$\delta\omega_{\text{probe}}(\Omega) = \delta\omega_{\text{th}}(\Omega) + \delta\omega_{\text{K}}(\Omega) + \delta\omega_{\text{rp}}(\Omega) \quad (2.151)$$

with

$$\delta\omega_{\text{th}}(\Omega) = -\omega_c \left( \alpha + \frac{1}{n} \frac{dn}{dT} \right) \underbrace{\left( \frac{\beta_1}{1 + i\Omega/\Omega_1} + \frac{\beta_2}{1 + i\Omega/\Omega_2} \right)}_{\delta T_{\text{eff}}(\Omega)} \frac{2\pi n R}{c} \frac{\delta P_{\text{IC}}(\Omega)}{\tau_{\text{abs}}} \quad (2.152)$$

$$\delta\omega_{\text{K}}(\Omega) = -\omega_c \frac{n_2}{n} \frac{\delta P_{\text{IC}}(\Omega)}{A_{\text{eff}}} \quad (2.153)$$

$$\begin{aligned} \delta\omega_{\text{rp}}(\Omega) &= g_0 \chi(\Omega) \delta F_{\text{rp}}(\Omega) = \\ &= -\frac{\omega_c}{R} \frac{1}{m_{\text{eff}}(\Omega_{\text{m}}^2 - \Omega^2 + i\Gamma_{\text{m}}\Omega)} \frac{2\pi n}{c} \delta P_{\text{IC}}(\Omega). \end{aligned} \quad (2.154)$$

For the thermal effect, we extract cutoff frequencies  $\Omega_1 \approx 2\pi \cdot 900$  Hz and  $\Omega_2 \approx 2\pi \cdot 69$  kHz. Furthermore, using the parameters of silica (cf. appendix A.1) and  $R = 29 \mu\text{m}$  as well as  $A_{\text{eff}} \approx 2.5 \mu\text{m}^2$ , we can normalize all results to the measured Kerr response. In this manner, we extract  $\beta_1/\tau_{\text{abs}} \approx 1.8 \cdot 10^4$  K/W/100 ns and  $\beta_2/\tau_{\text{abs}} \approx 570$  K/W/100 ns. All these parameters are very well in the range expected for the thermal effects discussed in section 1.5.1.

The combination of the radiation-pressure and Kerr responses gives rise to the dispersive signature around the mechanical resonance frequency: At modulation frequencies slightly above the mechanical resonance, the mechanical degree of freedom oscillates out of phase and therefore counteracts the Kerr effect, which always reacts instantaneously to power changes. Furthermore, at the resonance frequency  $\Omega_{\text{m}}$  of the RBM we expect

$$\left| \frac{\delta\omega_{\text{rp}}(\Omega_{\text{m}})}{\delta\omega_{\text{K}}(\Omega_{\text{m}})} \right| = \frac{2\pi n^2 A_{\text{eff}}}{R n_2 \Gamma_{\text{m}} \Omega_{\text{m}} c m_{\text{eff}}} \approx 240 \quad (2.155)$$

with  $\Gamma_{\text{m}} = 15.7$  kHz derived from the fit and the numerically determined effective mass  $m_{\text{eff}} \approx 15$  ng, in very good agreement to the measured value of 260. The extrapolated thermal effect, in contrast, drops more than four orders of magnitude below the observed mechanical displacement at  $\Omega_{\text{m}}$  (cf. figure 2.32). At mechanically non-resonant frequencies, this modulation would be largely dominated by a thermorefractive effect as compared to thermoelastic effects, as  $(dn/dT)/n\alpha > 10$ . Even if enhanced by the mechanical resonance, thermoelastic contributions may therefore be estimated at or below the  $10^{-2}$ -level.

We finally note that thermally induced forces that may be related to the identified thermal effects would be out of phase (by nearly  $\pi/2$ ) with the

## 2.6 Resolved-sideband cooling

driving pump laser modulation, since the relevant radio frequencies are well beyond the thermal cutoff frequencies. As a direct consequence, the observed interference effects between mechanical displacement and the Kerr-induced modulation would form a single symmetric resonant peak, fundamentally different to the observed dispersive shape. This again confirms the dominance of radiation pressure in this system.

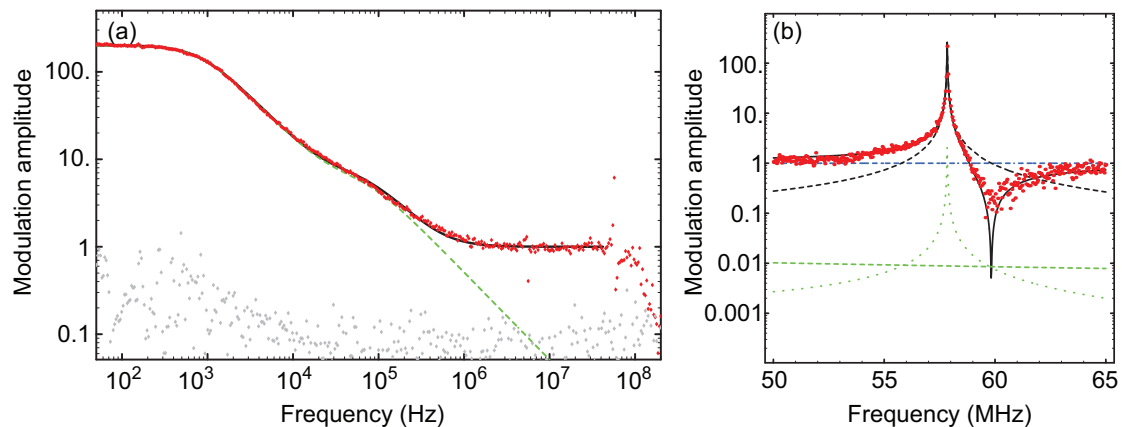


Figure 2.32: Pump-probe type response measurements of the nonlinearities present in toroidal silica microcavities. (a) Measured response (red dots) and fit (black line) modeling a two-pole low-pass thermal nonlinearity and an instantaneous Kerr effect, which becomes significant above 1 MHz. The data furthermore show a detector and cavity-induced cutoff above 100 MHz as well as indication of mechanical resonances at 5.6 and 58 MHz, though not resolved. The green dashed line shows the extrapolation of the thermal effects to higher frequencies and below the measurement background at about 0.1 (gray dots). All data are normalized to the fitted Kerr response. (b) Higher-resolution data (red points) as recorded in the vicinity of the radial-breathing mechanical resonance at  $\sim 58$  MHz. Full black line, model for the harmonic response plus a constant background due to the Kerr effect. Black and blue dashed lines illustrate the individual contributions from the harmonic response and the Kerr effect, respectively. Green dashed line indicates the extrapolated thermal response, and green dotted line the expected response if the thermally induced displacement was resonantly enhanced. All data normalized to Kerr response.

## 2.6 Resolved-sideband cooling

The successful demonstration of cooling by dynamical backaction immediately raises the question of how strongly the temperature of the mechanical oscillator can be reduced. A series of theoretical and experimental investigations revealed the fundamental [118, 119, 121, 122] and technical [8, 236, 237] limitations of radiation-pressure cooling of mechanical oscillators. In essence they showed that if all technical sources of heating are avoided, the quantum fluctuations of the cooling light field provide a fluctuating force, driving the oscillator to random motion and therefore compete with the laser cooling effect. An advantageous ratio of these two effects can however be achieved in the so-called *resolved-sideband* (RSB) regime, in which the mechanical oscil-

## 2. Cavity optomechanics

---

lation frequency  $\Omega_m$  exceeds the cavity linewidth  $\kappa$ . In this case, cooling of the mechanical oscillator to its quantum mechanical ground state is possible.

In the following, a brief outline of the required theoretical considerations will be given after a motivation by well-known results from atomic physics. In the main part of this section, experimental results—including the first demonstration of resolved sideband laser cooling of an optomechanical device—will be presented.

### 2.6.1 Ground state cooling: the atomic physics case

The quantum mechanical expectation value of the energy of a harmonic mechanical oscillator of  $\Omega_m$  and mass  $m_{\text{eff}}$  is given by

$$\langle H_{\text{mech}} \rangle = \frac{1}{2} \frac{\langle \hat{p}^2 \rangle}{m_{\text{eff}}} + \frac{1}{2} m_{\text{eff}} \Omega_m^2 \langle \hat{x}^2 \rangle = \quad (2.156)$$

$$= \hbar \Omega_m \left( \langle \hat{n} \rangle + \frac{1}{2} \right) \quad (2.157)$$

where the phonon number operator  $\hat{n} = \hat{b}^\dagger \hat{b}$  is given by the creation and annihilation operators

$$\hat{b}^\dagger = \frac{1}{2x_{\text{ZPF}}} \left( \hat{x} - i \frac{\hat{p}}{m_{\text{eff}} \Omega_m} \right) \quad (2.158)$$

$$\hat{b} = \frac{1}{2x_{\text{ZPF}}} \left( \hat{x} + i \frac{\hat{p}}{m_{\text{eff}} \Omega_m} \right) \quad (2.159)$$

with the so-called zero-point fluctuations

$$x_{\text{ZPF}} = \sqrt{\frac{\hbar}{2m_{\text{eff}} \Omega_m}}, \quad (2.160)$$

which are of the order of 100 am for typical silica microtoroidal resonators ( $m_{\text{eff}} = 10$  ng,  $\Omega_m/2\pi = 40$  MHz).

The question raised by the cooling results presented in the previous section is whether it is possible to reduce  $\langle H_{\text{mech}} \rangle$  to levels comparable with the ground-state energy  $\hbar \Omega_m/2$ . In other words, is it possible to reach the quantum ground state, in which the occupation number (the number of excitation quanta, phonons)  $\langle n \rangle$  reaches zero? In this case, deviations from the classical cooling behavior described in the previous section are clearly expected in order to prevent cooling to reach arbitrarily low energy states.

To answer this question, it is instructive to consider the results obtained in the context of laser cooling of ions (or atoms) [83–85, 238]. Trapped in a harmonic potential, these elementary particles constitute mechanical oscillators as well, their eigenfrequency  $\Omega_m$  being given by the tightness of the trap. Lasers can be used to drive electronic transitions of energy  $\hbar \omega_0$

## 2.6 Resolved-sideband cooling

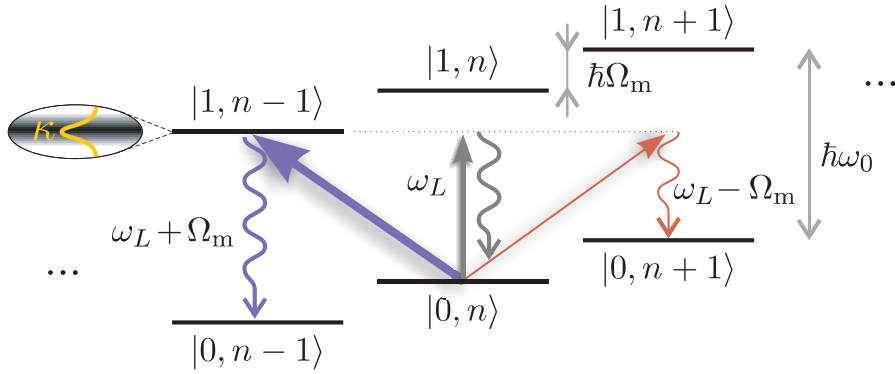


Figure 2.33: Optical sideband cooling. Laser photons of energy  $\hbar\omega_1 = \hbar(\omega_0 - \Omega_m)$  preferentially induce “red-sideband” transitions  $|0, n\rangle \rightarrow |1, n-1\rangle$  (blue arrow) if they are detuned from the carrier  $|0, n\rangle \rightarrow |1, n\rangle$  (gray arrow) and blue sideband  $|0, n\rangle \rightarrow |1, n+1\rangle$  (red arrow) transitions. As a consequence, the phonon occupation  $n$  of the mechanical oscillator is reduced when the photon gets absorbed by the atom, or, in the optomechanical case, by the cavity. Re-emission of the photon (wavy lines), on average, does not change the phonon occupation (neglecting recoil), so that a detuned laser provides cooling. Figure from ref. [8].

and lifetime  $\kappa^{-1}$ , and optical and mechanical degrees of freedom are coupled by the Doppler shift of the optical resonance if the ion is moving, and the momentum transfer of absorbed and emitted photons.

If the laser is detuned from the optical resonance, cooling can occur by favoring the absorption of a photon only in conjunction with the annihilation of a mechanical excitation quantum. Essentially, it is the phonon energy  $\hbar\Omega_m$  which makes up for the energy lack  $\hbar(\omega_0 - \omega_1)$  of the incoming photon to drive the electronic transition. If absorption takes place, the subsequently re-emitted photon has an average energy of  $\hbar\omega_0$  (neglecting recoil). It therefore carries away the additional energy of the phonon, and leaves the mechanical oscillator in a state of lower excitation  $n$  (figure 2.33).

This method is usually referred to as optical sideband cooling: an ion oscillating in its trap exhibits absorption sidebands at frequencies  $\omega_0 \pm j\Omega_m$ ,  $j \in \mathbb{N}$ , very similar to the case of a cavity discussed in section 2.2.1. If the laser is tuned to the red sideband at  $\omega_0 - \Omega_m$ , cooling transitions are resonantly enhanced as shown in figure 2.33. The quantum theory of laser cooling of trapped atoms or ions reveals that this method allows ground state cooling  $\langle n \rangle \rightarrow 0$  provided that  $\Omega_m \gg \kappa$  (neglecting recoil) [85, 238]. In this case, the lowest average occupation that can be achieved is given by

$$\langle n \rangle = \frac{\kappa^2}{16\Omega_m^2}. \quad (2.161)$$

Interestingly, this result can also be viewed as being due to the competition of the cooling effect of the detuned laser, due to an effective viscous force, and a “heating” effect due to quantum fluctuations of the light beam, giving rise to a fluctuating radiation-pressure force [88].

## 2. Cavity optomechanics

### 2.6.2 Limitations of radiation-pressure cooling using dynamical backaction

A similar analysis can be applied to cooling by dynamical backaction. To assess the fundamental cooling limits, we consider the radiation pressure force as it is obtained from the quantum Langevin equations:

$$\begin{aligned} \delta\hat{F}_{\text{rp}}(\Omega) &= i\hbar g_0^2 \bar{a}^2 \delta\hat{x}(\Omega) \left( \frac{1}{-i(\bar{\Delta} + \Omega) + \kappa/2} - \frac{1}{+i(\bar{\Delta} - \Omega) + \kappa/2} \right) \\ &\quad - \hbar g_0 \bar{a} \frac{\delta\hat{s}_{\text{in}}(\Omega)\tau_{\text{ex}}^{-1/2} + \delta\hat{s}_{\text{vac}}(\Omega)\tau_0^{-1/2}}{-i(\bar{\Delta} + \Omega) + \kappa/2} \\ &\quad - \hbar g_0 \bar{a} \frac{\delta\hat{s}_{\text{in}}^\dagger(\Omega)\tau_{\text{ex}}^{-1/2} + \delta\hat{s}_{\text{vac}}^\dagger(\Omega)\tau_0^{-1/2}}{+i(\bar{\Delta} - \Omega) + \kappa/2} \end{aligned} \quad (2.162)$$

In essence, the expression in the first line correspond to quantum backaction due to quantum fluctuations of the intracavity photon number, while the expression on the second line is due to dynamical backaction (proportional to the mechanical displacement). The latter force contribution, is usually absorbed into the effective susceptibility  $\chi_{\text{eff}}$  from (2.28), while the spectrum of the force quantum fluctuations is calculated as

$$\bar{S}_{FF}^{\text{ba,qn}}(\Omega) = \hbar^2 g_0^2 \bar{a}^2 \frac{\kappa}{2} \left( \frac{1}{(\bar{\Delta} + \Omega)^2 + (\kappa/2)^2} + \frac{1}{(\bar{\Delta} - \Omega)^2 + (\kappa/2)^2} \right) \quad (2.163)$$

$$= \frac{\hbar^2}{x_{\text{ZPF}}^2} \frac{1}{2} \left( \underbrace{\frac{g_0^2 \bar{a}^2 x_{\text{ZPF}}^2 \kappa}{(\bar{\Delta} + \Omega)^2 + (\kappa/2)^2}}_{A_-} + \underbrace{\frac{g_0^2 \bar{a}^2 x_{\text{ZPF}}^2 \kappa}{(\bar{\Delta} - \Omega)^2 + (\kappa/2)^2}}_{A_+} \right) \quad (2.164)$$

using the known correlators for the input quantum noise. We have introduced here the rates  $A_-$  and  $A_+$ , which can be shown to correspond to rates of anti-Stokes and Stokes scattering events in which phonons are annihilated or created [118, 119, 121, 239].

The remaining energy stored in the mode after cavity cooling can be evaluated by integrating the mechanical displacement spectrum. This is possible analytically if a hot mechanical reservoir  $\hbar\Omega_m \ll k_B T$  is assumed and the effective susceptibility still corresponds to a high-quality Lorentzian. Without further proof we note here that this can be safely assumed case as long as for the optomechanical coupling parameter

$$G = 2\bar{a}g_0 x_{\text{ZPF}} \quad (2.165)$$

one has  $|G| \ll \kappa$ . For higher values of  $G$ , hybridization of optical and mechanical modes set in, a regime treated in detail in [240, 241]. In the limits  $\Omega_m, \kappa \gg G, \Gamma_m$  relevant to the work presented in the following, one eventually

obtains [121]

$$\frac{1}{2}m_{\text{eff}}\Omega_m^2\langle\delta\hat{x}^2\rangle = \int |\chi_{\text{eff}}(\Omega)|^2 \left( \bar{S}_{FF}^{\text{th}}(\Omega) + \bar{S}_{FF}^{\text{ba,qn}}(\Omega) \right) \frac{d\Omega}{2\pi} = \quad (2.166)$$

$$= \frac{1}{\Gamma_{\text{eff}}} \left( \Gamma_m k_B T + \frac{A_- + A_+}{2} \hbar \Omega_m \right) \quad (2.167)$$

and therefore

$$\langle n \rangle \approx \frac{\Gamma_m}{\Gamma_{\text{eff}}} \underbrace{\frac{k_B T}{\hbar \Omega_m}}_{n_{\text{bath}}} + \underbrace{\frac{A_+}{A_- - A_+}}_{n_{\text{min}}} \quad (2.168)$$

for significant cooling  $A_- \gg A_+ \gg \Gamma_m$  (note also that in the considered limits, equal amounts of energy are stored in potential and kinetic energy).

As a consequence, even for very strong cooling  $\Gamma_{\text{eff}} \gg \Gamma_m$ , the phonon occupation cannot be reduced to arbitrarily low numbers, instead it is bound by  $n_{\text{min}}$ . Two simple limits are derived depending on the ratio of mechanical resonance frequency and optical cavity linewidth:

$$n_{\text{min}} \approx \frac{\kappa}{4\Omega_m} \quad \kappa \gg \Omega_m \quad \text{unresolved sidebands} \quad (2.169)$$

$$n_{\text{min}} \approx \frac{\kappa^2}{16\Omega_m^2} \quad \kappa \ll \Omega_m \quad \text{resolved sidebands.} \quad (2.170)$$

Evidently, the ground state  $\langle n \rangle \rightarrow 0$  can only be reached in the resolved-sideband regime, where  $\kappa \ll \Omega_m$ . Due to the non-zero occupation  $n_{\text{bath}} \approx k_B T / \hbar \Omega_m$  when in equilibrium with the thermal bath, more stringent requirements arise in laboratory experiments. In particular, both  $\kappa > \Gamma_m n_{\text{bath}}$  [240] and  $\Omega_m > \Gamma_m n_{\text{bath}}$  [119] are necessary to enable sufficiently high cooling rates without being limited by the cavity decay rate or an effectively overdamped mechanical resonator, respectively. Apart from these limits, it is desirable to work with optical resonances as narrow as possible to enable ground state cooling.

Another advantage of working in the resolved-sideband regime is that the cooling rate increases monotonously for decreasing  $\kappa$  if all other parameters are fixed. As shown in figure 2.34, if the detuning is chosen for optimum cooling rate, the intracavity power reduces as the laser is effectively detuned further from the WGM cavity resonance. This is advantageous to keep undesired nonlinearities at a low level, but also to prevent heating effects due to absorbed light. This effect is particularly relevant in cryogenic environments, where small absorbed powers may already significantly alter the temperature of the system, see section 2.7.3.

Finally, another technical imperfection in this cooling scheme may lead to a limit in the attainable occupation number. If the cooling laser frequency exhibits technical frequency noise, it is translated by the cavity into

## 2. Cavity optomechanics

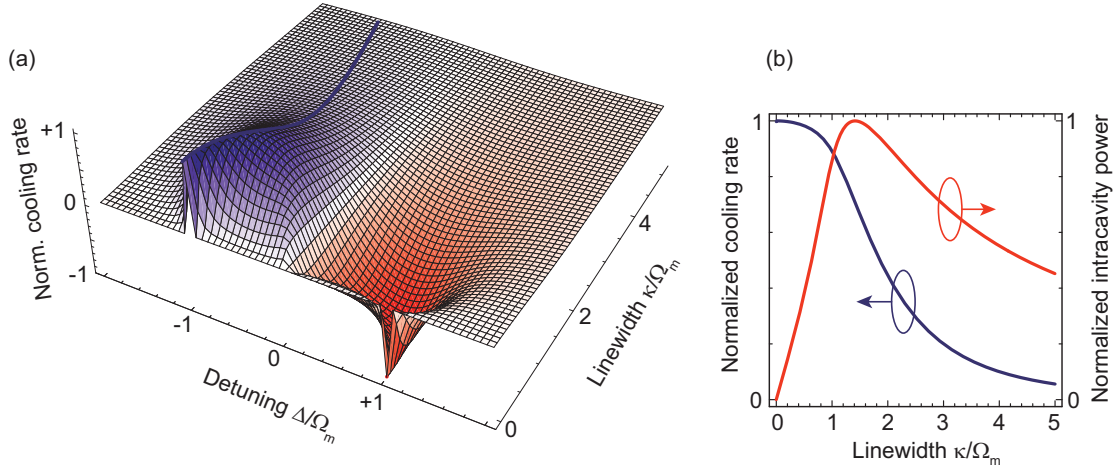


Figure 2.34: (a) Normalized cooling rate as a function of detuning and linewidth, for a fixed mechanical resonance frequency  $\Omega_m$  assuming  $G < \kappa$ . Blue line indicates the optimum detuning for a given cavity linewidth. (b) Normalized cooling rate (blue line) and intracavity power (red line) as a function of linewidth for fixed  $\Omega_m$ , if the detuning is kept at the optimum value.

a radiation pressure force noise. Laser frequency fluctuations  $\bar{S}_{\omega\omega}(\Omega)$ , with  $\bar{S}_{qq}^{\text{in}}(\Omega) = 1 + 4|\bar{s}_{\text{in}}|^2 \bar{S}_{\omega\omega}(\Omega)/\Omega^2$  lead to additional radiation-pressure force fluctuations with the spectrum

$$\bar{S}_{FF}^{\text{ba,fn}}(\Omega) = \frac{\hbar^2 \bar{a}^4 g_0^2}{\Omega} \left( \frac{\bar{\Delta}}{(\bar{\Delta} - \Omega)^2 + (\kappa/2)^2} - \frac{\bar{\Delta}}{(\bar{\Delta} + \Omega)^2 + (\kappa/2)^2} \right) \bar{S}_{\omega\omega}(\Omega), \quad (2.171)$$

which can be derived from the intracavity fluctuations of the  $p$ -quadrature (see appendix B.2). A lower limit for the occupation can then be estimated by integration of the resulting displacement noise spectrum, taking into account the modified susceptibility of the mechanical oscillator (in particular its damping  $\Gamma_{\text{dba}} \approx \Gamma_{\text{eff}}$ , cf. equation (2.29). In the linear cooling regime [240], the integrand is simply a Lorentzian, and we assume that the force noise is approximately constant within the frequency band in which the mechanical oscillator picks it up. Then one gets (cf. appendix B.1)

$$m_{\text{eff}} \Omega_m^2 \langle \delta x^2 \rangle \approx \frac{\bar{S}_{FF}^{\text{ba,fn}}(\Omega_m)}{2m_{\text{eff}} \Gamma_{\text{dba}}} = \underbrace{\bar{S}_{\omega\omega}(\Omega_m) \frac{\bar{a}^2 |\bar{\Delta}|}{\kappa \Omega_m}}_{n_{\text{fn}}} \hbar \Omega_m. \quad (2.172)$$

As will be discussed later, this result gets modified in the additional presence of thermal noise [8], not taken into account in other discussions of frequency-noise induced cooling limits which [236, 237].

### 2.6.3 Resolved-sideband cooling of a silica microtoroid

Implementing an optomechanical system which operates in the resolved-sideband regime is advantageous to suppress the effects of nonlinearities and absorption-induced heating present in most laboratory experiments. Furthermore, the analysis at the quantum level has shown that this regime is mandatory for cooling to the quantum ground state. It is interesting to note that this finding is quite generally valid, and applies in an analogous manner to a large class of systems in which a mechanical oscillator is cooled by parametric coupling to physical systems as diverse as an ion [242], a quantum dot [117], a Josephson qubit [243], a superconducting quantum interference device (SQUID) [244], a superconducting single-electron transistor (sSET) [245, 246], or a resonant electric circuit [151]. The excitations of all these systems need to have a lifetime  $\kappa^{-1}$  exceeding the oscillation period  $\sim \Omega_m^{-1}$  of the mechanical oscillator to enable ground-state cooling.

Experimental implementation of the resolved-sideband regime however proves non-trivial: in a classical optomechanical system involving a Fabry-Perot resonator, increasing the cavity length  $L$  in principle reduces  $\kappa$ , but at the same time also the coupling strength  $g_0 = -\omega_c/L$ . Also, it typically increases the waist size of the beam, which may induce diffraction losses (and therefore increase  $\kappa$  again) if, as it is typically the case, the micromechanical oscillator constitutes one of the cavity mirrors. In an integrated system such as silica microtoroids, increasing the cavity size (within the relevant range of 60 to 100  $\mu\text{m}$  diameter) typically leads only to modest improvements of  $\kappa$ , as the losses are dominated by absorption along the light propagation path. In addition to the reduced coupling  $g_0 = -\omega_c/R$ , the mechanical resonance frequency of the RBM is reduced for bigger cavity size. The first experiment demonstrating efficient resolved-sideband laser cooling was eventually performed in 2008 with silica microresonators [8], while other systems, such as superconducting microwave cavities [157] or Fabry-Perot resonators [164] followed soon thereafter.

Figure 2.35 shows data obtained with a 47  $\mu\text{m}$ -diameter toroid hosting a RBM at  $\Omega_m/2\pi = 73.5$  MHz. Using a first laser, the RBM is driven to regenerative oscillations, by pumping a WGM in a blue-detuned manner, leading to the well-known oscillatory instability [181, 218–221]. A second laser, launched into the same tapered fibre, is used to probe a different, high-Q WGM resonance of the oscillating toroid. Using optical filters to extract only the transmission signal of the probe laser, the traces shown in figure 2.35 are recorded if this laser is swept over the resonance.

Instead of a single dip, several dips are observed if the electronic signal is filtered with a low-pass filter with a cutoff far below  $\Omega_m$ . From the intracavity mode amplitude of the oscillating cavity (equation (2.7)) the low-frequency

## 2. Cavity optomechanics

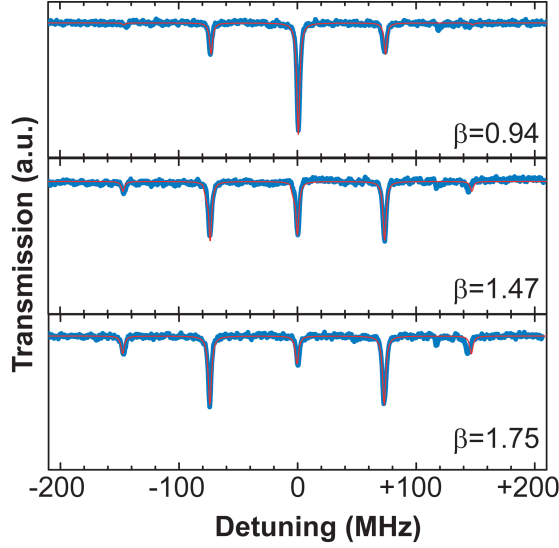


Figure 2.35: Steady-state transmission spectrum of a microtoroid when the mechanical degree of freedom is excited to picometer-scale amplitude oscillations at its resonance frequency of  $\Omega_m/2\pi = 73.5$  MHz using an auxiliary laser. The linewidth of the resonances corresponds to the optical decay rate of  $\kappa/2\pi = 3.2$  MHz, placing this device deeply into the resolved sideband regime. Blue points are experimental data, and the red lines are fits using the Bessel function expansion (eq. (2.173)) with  $\beta$ -parameters given in each panel. Figure from ref. [8].

component of the transmitted power

$$|\bar{s}_{\text{out}}^{\text{DC}}|^2 = \left( 1 - \eta_c(1 - \eta_c) \sum_n \frac{\kappa^2 J_n(\beta)^2}{(\Delta + n\Omega_m)^2 + (\kappa/2)^2} \right) |\bar{s}_{\text{in}}^2| \quad (2.173)$$

is calculated [8], where  $J_n$  are the Bessel functions and  $\beta = g_0 x_0 / \Omega_m$ . From fits using this model, it is possible to derive the amplitude  $x_0$  of the mechanical oscillation to about 5.3, 8.3 and 9.9 pm for the three traces, respectively. At the same time, these traces clearly show that the mechanical resonance frequency  $\Omega_m$ —by which the Lorentzian dips are spaced—largely exceeds the optical cavity linewidth  $\kappa$ . Indeed, the fits yield a resolved-sideband factor  $\Omega_m/\kappa \approx 23$ , due to the very high cavity finesse of 440,000.

For resolved-sideband cooling, the two lasers are used in a different way. The cooling laser is tuned below the narrow WGM, to the lower sideband at  $\bar{\Delta} = -\Omega_m$ . The second laser is used to sensitively monitor mechanical displacements and therefore tuned in resonance with a different WGM (figure 2.36). Using two completely independent laser sources helps to rule out artifacts in the displacement measurements, due to potentially induced noise correlations between the cooling beam and induced motion of the mechanical oscillator, referred to as “squashing” in feedback cooling [150].

In this experiment, sensitive monitoring of mechanical motion is accomplished using the Hänsch-Couillaud technique described in section 2.4.2. As shown in figure 2.37, a low-noise Nd:YAG laser is used for this purpose, which

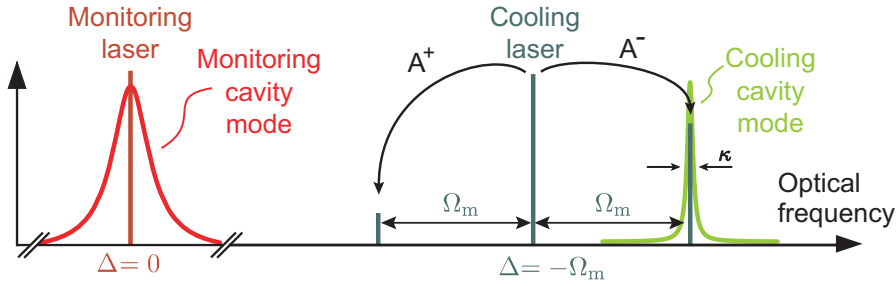


Figure 2.36: Scheme used for resolved-sideband cooling. The cooling laser at  $\lambda \approx 980$  nm (green line) is tuned to the lower sideband ( $\bar{\Delta} = -\Omega_m$ ) of a high-Q optical resonance. Resonant anti-Stokes scattering into the cavity mode, at rate  $A_-$  dominates over Stokes scattering at rate  $A_+$ . A second laser is tuned in resonance with a different WGM at  $\lambda = 1064$  nm, and used to monitor the mechanical displacements. Figure from ref. [8].

is locked to the line-center using feedback to a piezo pressing on the YAG crystal. In order to lock the cooling laser to a detuning much larger than the resonance linewidth  $\kappa$ , we use an experimental technique, in which the signal obtained by frequency modulation spectroscopy [66] is used as an error signal. Some technical details of this method are described in appendix C.2.

Figure 2.38 shows cooling results obtained with the 73.5 MHz-sample. Note that due to the strongly detuned operation, only a fraction of about  $\sim (4(\Omega_m/\kappa)^2 + 1)^{-1} \approx 5 \times 10^{-4}$  of the launched power of 3 mW, i. e. circa  $1.5 \mu\text{W}$ , is coupled into the cavity. Nonetheless, very high cooling rates up to  $\Gamma_{\text{dba}}/2\pi = 1.56$  MHz can be achieved. The mode temperatures achieved with this sample, however, remained above 20 K, due to the modest mechanical quality factor of about  $Q_m = 2,100$ , and a heating mechanism described below.

We have also recorded noise spectra of the mechanical oscillator by directly analyzing the transmitted power of the cooling laser (as explained in section 2.5). Qualitatively the same behavior of the mechanical spectra is observed when cooling, however with significantly worse signal-to-noise ratio. This renders, for example, the determination of the mode temperature extremely difficult for strong cooling. Furthermore, for cooling laser powers on the order of 3 mW, significant deformations of the mechanical spectra from their originally Lorentzian shape were observed. The particular shapes were strongly dependent on the detuning and coupling conditions. Figure 2.39 shows one example in which a resonance doublet appeared. We note that such an doublet would in principle be expected when entering the regime of strong optomechanical coupling, in which optical and mechanical modes hybridize [240, 241].

To achieve lower mode temperatures, a second cooling run was initiated. We used a larger toroid (radius  $R = 28 \mu\text{m}$ ) with a RBM at  $\Omega_m/2\pi = 40.6$  MHz and  $\Gamma_m/2\pi = 1.3$  kHz, corresponding to a very high mechanical quality factor of 30,000. The broadband displacement spectrum recorded with this sample using the Hänsch-Couillaud technique (cooling laser is off)

## 2. Cavity optomechanics

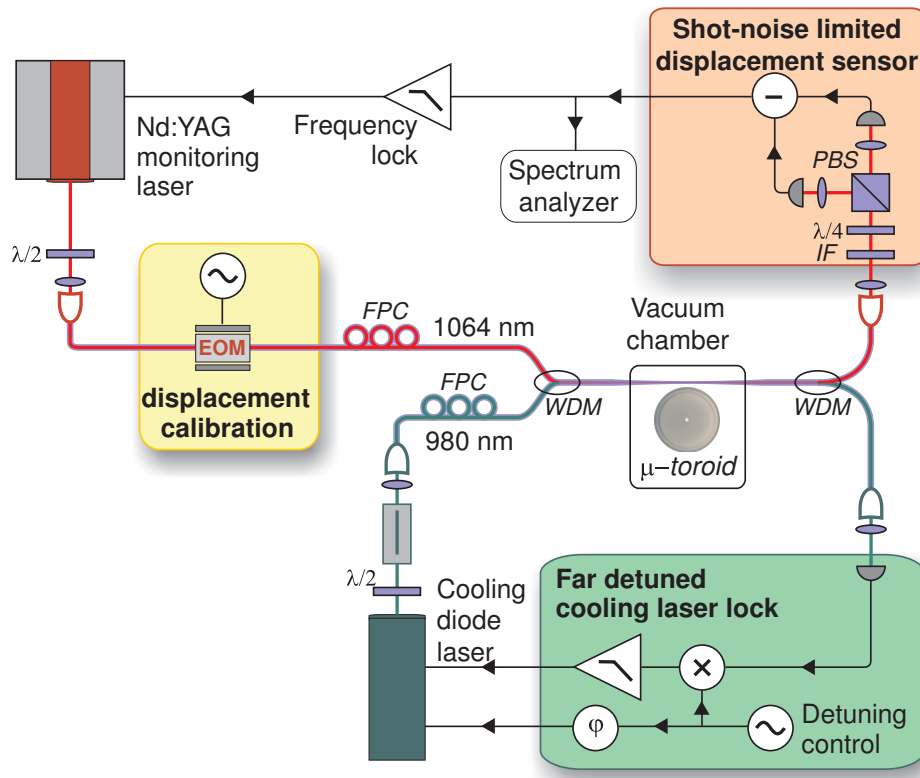


Figure 2.37: Setup used to implement resolved-sideband cooling and high-sensitivity monitoring of the RBM of silica toroidal microresonators. Two lasers are used, a diode laser at 980 nm for cooling by tuning and locking it to the lower sideband of a high-Q WGM, and a Nd:YAG laser at 1064 nm monitoring mechanical displacements using the Hänsch-Couillaud technique. More details are given in the text. Figure from ref. [8].

is shown in figure 2.40. A displacement sensitivity at the  $10^{-18} \text{ m}/\sqrt{\text{Hz}}$ -level is achieved. At low Fourier frequencies, the noise spectrum again reveals a thermorefractive background already discussed in section 2.4.

The strong peaks observed at 14.96, 28.58 and 40.59 MHz can be assigned to different radially symmetric modes in this sample. The latter peak belongs to the RBM, which has an effective mass of about 10 ng. If the cooling laser is tuned to the lower sideband of a  $\kappa/2\pi = 5.8 \text{ MHz}$ -wide WGM, cooling of the RBM is evident by the reduction of the RBM’s thermal noise (figure 2.40). It is interesting to note that the thermal noise in the other radially symmetric modes is not affected. In the resolved sideband regime, this is possible due to the fact that the absorption sidebands of the individual mechanical modes do not overlap, as they are as narrow as the optical resonance. Furthermore, we note that effects analogous to “sympathetic cooling”—due to, for example a preferential coupling of the RBM to other radially symmetric modes—is not observed.

The mode temperature  $T_m$  of the RBM is subsequently evaluated by integrating the displacement noise spectrum  $\bar{S}_{xx}(\Omega)$  (cf. section 2.5.2). The lowest mode temperature obtained with this sample is  $T_m \approx 11 \text{ K}$ , corre-

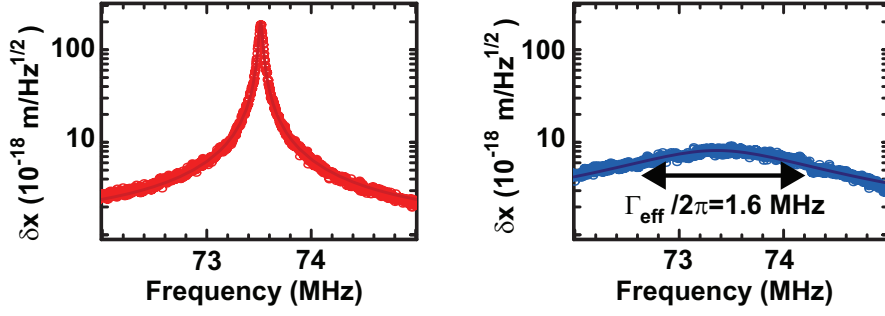


Figure 2.38: Displacement noise spectra of the RBM as recorded by the monitoring laser with the cooling laser off (left panel), and running at a power of 2.7 mW, when detuned to the lower sideband (right panel). Cooling rates up to 1.6 MHz can be achieved. Circles are data points and lines Lorentzian fits. Figure from ref. [8].

sponding to a residual occupation of  $\langle n \rangle \approx 5900$ . As in the experiments with the first sample, this is significantly above the value expected from the high cooling rates, reaching up to  $\Gamma_{\text{dba}}/2\pi = 119$  kHz with this sample. This discrepancy is attributed to excess heating by the cooling laser's frequency noise.

Indeed, an independent measurement reveals frequency fluctuations of the cooling laser at the level of  $\sqrt{\bar{S}_{\omega\omega}(\Omega_m)} = 2\pi \cdot 200$  Hz/ $\sqrt{\text{Hz}}$ , a value consistent with earlier measurements on the frequency noise at radio frequencies of a grating stabilized diode laser [247]. For a finite bath temperature  $T$ , the lowest occupation that can be attained can be estimated by

$$\langle n \rangle \approx \frac{\bar{S}_{FF}^{\text{ba,fn}}(\Omega_m) + \bar{S}_{FF}^{\text{th}}(\Omega_m)}{2m_{\text{eff}}\Gamma_{\text{dba}}}. \quad (2.174)$$

In the resolved-sideband limit  $\kappa \ll \Omega_m$ , the force noise due to frequency fluctuations from equation (2.171) simplifies to

$$\bar{S}_{FF}^{\text{ba,fn}}(\Omega_m) \approx \frac{4\eta_c^2 \bar{S}_{\omega\omega}(\Omega_m) P_{\text{in}}^2}{R^2 \Omega_m^4}, \quad (2.175)$$

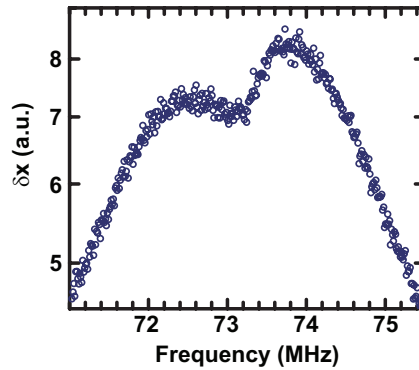


Figure 2.39: Resonance doublet observed in the power spectrum of the cooling laser for strong cooling powers. See text for more information.

## 2. Cavity optomechanics

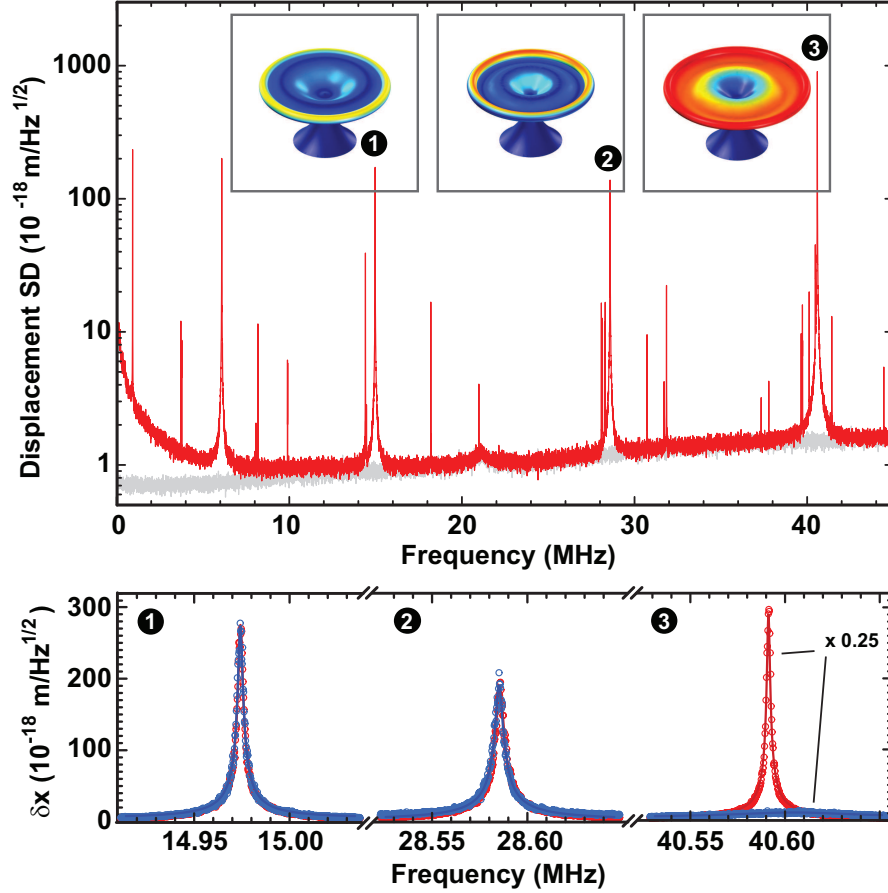


Figure 2.40: Resolved-sideband cooling of the RBM of a microtoroidal oscillator. Top panel shows a broadband displacement noise spectrum recorded using the Hänsch-Couillaud technique (red trace). Gray trace is background trace with the fiber taper retracted from the WGM near field. It is dominated by shot noise, its dependence on Fourier frequency is due to the weaker transduction of displacement fluctuations to phase fluctuations at Fourier frequencies beyond the cavity cutoff  $\kappa/2$ . The sensitivity is at the  $10^{-18} \text{ m}/\sqrt{\text{Hz}}$ -level. Insets show the displacement patterns of three radially symmetric modes, with the corresponding strain indicated in the color code. The bottom panel shows zooms on the displacement noise of these three modes, when the cooling laser is off (red traces) and on (blue traces), at a detuning of  $\bar{\Delta} = -\Omega_m$ . Clearly, only the RBM mode (number 3) is affected. The lowest achieved occupation in these measurements was  $\langle n \rangle \approx 5900$ . Figure from ref. [8].

## 2.6 Resolved-sideband cooling

and the cooling rate is approximately given by

$$\Gamma_{\text{dba}} \approx \frac{4g_0^2 \bar{a}^2 x_{\text{ZPF}}^2}{\kappa} = \frac{2g_0^2 \eta_c P_{\text{in}}}{m_{\text{eff}} \omega_l \Omega_m^3}. \quad (2.176)$$

As a consequence, the lowest temperature is obtained at a finite input power, and one finds  $n_{\text{min}} \approx \sqrt{2k_B T m_{\text{eff}} \Gamma_m \bar{S}_{\omega\omega}(\Omega_m) / \hbar |g_0|}$  [8]. For the parameters of this experimental run,  $T = 300$  K,  $m_{\text{eff}} = 10$  ng,  $\Gamma_m / 2\pi = 1.3$  kHz,  $\sqrt{\bar{S}_{\omega\omega}(\Omega_m) / \Omega_m^2} \approx 4 \mu\text{rad} / \sqrt{\text{Hz}}$ ,  $R = 38 \mu\text{m}$ ,  $\Omega_m / 2\pi = 40.6$  MHz,  $\omega / 2\pi \approx 300$  THz, one obtains  $n_{\text{min}} \approx 5200$ , close to the lowest observed occupation number.

### 2.6.4 Direct sideband spectroscopy

If the ground state of the mechanical oscillator is approached, it becomes increasingly difficult to reliably measure its occupation number. For example, if the method demonstrated here—using an independent motion transducer based on an optical phase measurement—the requirements on its performance are quite challenging. Even for a perfect implementation of such a measurement, in which the standard quantum limit can be reached (cf. section 2.4), the signal-to-noise ratio (SNR) at the mechanical resonance frequency would be only equal to unity at the mechanical resonance frequency when the resonator is in its ground state: for  $\langle n \rangle \rightarrow 0$ , the spectrum of displacement fluctuation is expected to peak at a value of

$$\bar{S}_{xx}^0(\Omega_m) = \frac{\hbar}{m_{\text{eff}} \Gamma_m \Omega_m} \quad (2.177)$$

which exactly equals  $\bar{S}_{xx}^{\text{SQL}}(\Omega_m)$ .

We note that our experiment reaches an imprecision level close to the SQL: For example, for the sample described above, we calculate  $\sqrt{\bar{S}_{xx}^0(\Omega_m)} \approx 2.2 \text{ am} / \sqrt{\text{Hz}}$ , and routinely achieve imprecision noise at the same level (cf. figure 2.40). However, as in most other experiments reporting similarly low imprecision levels [158, 248], backaction of these measurements is difficult to quantify and may impede cooling to the quantum ground state.

As an alternative approach to measure the residual occupation number for small  $\langle n \rangle$ , it has been suggested to directly monitor the individual motional sidebands of the cooling laser [118]. In theory, the optical spectrum<sup>11</sup> of the

---

<sup>11</sup>Note that here the high- $Q$  approximation for the mechanical susceptibility was used,  $((\Omega_m^2 - \Omega^2)^2 - \Omega^2 \Gamma_{\text{eff}}^2)^{-1} \approx (4\Omega_m^2 ((\Omega - \Omega_m)^2 + (\Gamma_{\text{eff}}/2)^2))^{-1}$ . We also emphasize that this spectrum lies in the optical domain, instead of the RF-domain of the spectra discussed previously.

## 2. Cavity optomechanics

---

cooling laser light coupled back into the taper is described by

$$\begin{aligned}
S_{\Phi\Phi}(\omega) = \eta_c & \left( \delta(\omega - \omega_1) \left( \frac{1}{\eta_c} - \frac{(1 - \eta_c)\kappa^2}{\Delta^2 + (\kappa/2)^2} \right) \bar{s}_{\text{in}}^2 \right. \\
& + \frac{\Gamma_{\text{eff}}/(2\pi)}{(\omega - (\omega_1 + \Omega_m))^2 + (\Gamma_{\text{eff}}/2)^2} A_- \langle n \rangle \\
& \left. + \frac{\Gamma_{\text{eff}}/(2\pi)}{(\omega - (\omega_1 - \Omega_m))^2 + (\Gamma_{\text{eff}}/2)^2} A_+ (\langle n \rangle + 1) \right), \quad (2.178)
\end{aligned}$$

where  $\Phi$  is the photon flux emerging from the cavity [118]. Next to the carrier at  $\omega_1$ , two sidebands are expected, their lineshape being given by the effective susceptibility of the mechanical oscillator. Most notably, the spectrally integrated photon flux of the individual sidebands is given by  $A_- \langle n \rangle$  and  $A_+ (\langle n \rangle + 1)$  for the upper and lower sidebands, respectively. As a consequence, the sideband asymmetry, given initially by the asymmetry in  $A_-$  and  $A_+$ , becomes balanced for sufficiently low  $\langle n \rangle$ . The change in the ratio of the sideband amplitudes could therefore serve as a gauge of the occupation [118].

Accessing the individual sidebands in a measurement necessitates the ability to individually resolve them against the much stronger carrier signal at the laser frequency. For typical parameters of an optomechanical experiment, this is difficult, as in the RSB regime the power even in the resonantly enhanced upper sideband is weaker by  $\sim \langle n \rangle g_0^2 4\eta_c^2 x_{\text{ZPF}}^2 / \Omega_m^2 \sim \langle n \rangle \mathcal{O}(10^{-9})$  than the carrier, and the lower sideband is again weaker by a factor of  $\kappa^2 / 16\Omega_m^2$ . As a consequence, sufficient suppression of the carrier using a (single) filtering cavity is hardly possible, as it would require sub-kHz cavity linewidth, which could not even simultaneously collect all light in the sidebands (typically  $\Gamma_{\text{eff}}/2\pi > 1$  kHz).

An alternative way of individually resolving the sidebands is to use a heterodyne technique. A similar technique has been demonstrated to enable resolving motional sidebands<sup>12</sup> of a laser-cooled ion [249]. In such an experiment, the cooling light which couples back to the fiber taper is mixed with a strong local oscillator beam at a different frequency  $\omega_1 - \Omega_{\text{AOM}}$  with  $\Omega_{\text{AOM}} > \Omega_m$ . Then the upper sideband, carrier, and lower sideband signals are detected at the radio frequencies  $\Omega_{\text{AOM}} + \Omega_m$ ,  $\Omega_{\text{AOM}}$  and  $\Omega_{\text{AOM}} - \Omega_m$ , respectively.

Figure 2.41 shows the implementation and results of a proof-of-principle experiment using this technique. When the laser is tuned close to resonance, the motional sidebands have roughly the same amplitude, which are again independently calibrated using a frequency-modulation technique. As  $\langle n \rangle \gg 1$ , the residual asymmetry in this case is attributed to a finite detuning from the WGM resonance. When the laser is further detuned, the asymmetry becomes more pronounced, as  $A_- \gg A_+$ . In this experiment, an asymmetry

---

<sup>12</sup>Note however that only micro-motion sidebands could be detected for a cold ion. To observe the secular motion, the ion was driven to large-amplitude oscillations in the trap.

## 2.7 Approaching the quantum ground state

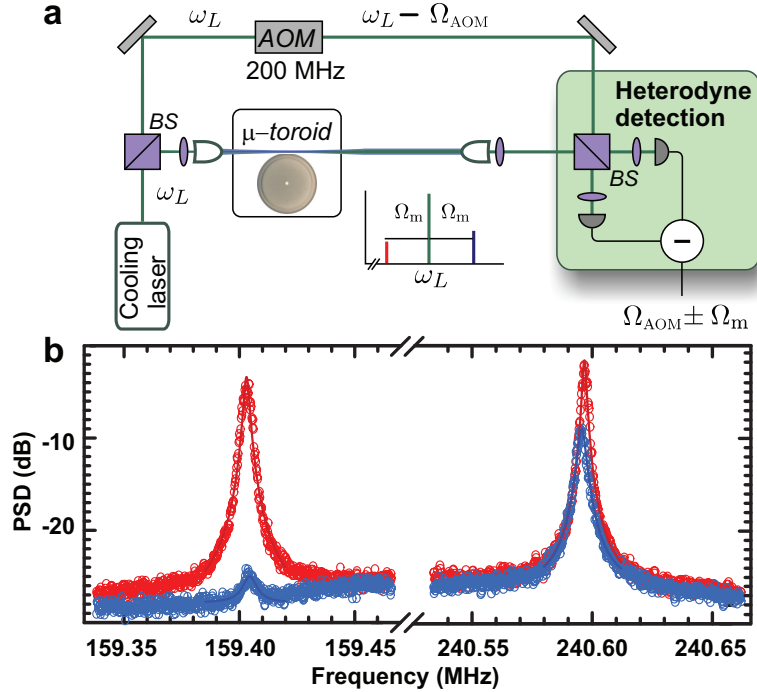


Figure 2.41: Heterodyne spectroscopy of the sidebands during cooling. (a) Experimental setup, in which a frequency-shifted laser beam is used as a heterodyne local oscillator. (b) Experimental results, showing the power spectral density of the differential photocurrent recorded in the heterodyne receiver. Red points are recorded with the cooling laser close to resonance, and blue points are recorded with a detuned cooling laser. Figure from ref. [8].

of more than 15 dB is reached. Higher values could not be observed due to the limited SNR. This limitation is due to the classical frequency noise of the cooling laser, which could be shown to induce the relatively high background noise level in this measurement.

We note however that his experiment was performed without actively driving the motion of the mechanical oscillator—in contrast to an experiment with trapped ions [249]. In our case, the oscillator is exclusively driven by thermal noise. In that sense, this measurement technique reveals in a very direct manner the physical process underlying cooling by dynamical backaction: enhanced anti-Stokes scattering and suppressed Stokes-scattering.

## 2.7 Approaching the quantum ground state

The work presented in the previous sections has clearly demonstrated the potential of resolved-sideband cooling. In the following, we present experimental results in which this technique is successfully implemented to cool a mechanical oscillator close to its quantum ground state, rivalling the results achieved with nanoelectromechanical systems engineered for this purpose for nearly a decade [127, 159, 246, 250, 251]. In our laboratory these results [10]

## 2. Cavity optomechanics

---

were achieved by combining laser cooling with efficient cryogenic precooling, a technique traditionally applied to nanoelectromechanical systems, but novel in the context of optomechanics.

As a second crucial feature, the vastly superior displacement sensitivity of our optomechanical system warrants the ability to monitor such an ultracold oscillator at levels close to the amplitude of its zero-point fluctuations  $x_{\text{ZPF}} = \sqrt{\hbar/2m_{\text{eff}}\Omega_m}$ —in spite of the fact that its mass is more than 1000-times higher than in typical nanomechanical systems.

Finally, considered from the perspective of quantum measurement, we are able to assess the backaction of the measurement performed on the ultracold oscillator. We will show that considering both imprecision and backaction of our measurement, one can conclude that the optical displacement transduction performs in a near-ideal manner.

### 2.7.1 Implementation

From the theoretical considerations of the previous sections, we can summarize the limits in cooling by dynamical backaction in the simple expression

$$\langle n \rangle \geq \frac{\Gamma_m}{\Gamma_m + \Gamma_{\text{dba}}} \frac{k_B T}{\hbar \Omega_m} + n_{\text{fn}} + \frac{A_+}{A_- - A_+}. \quad (2.179)$$

Reaching  $\langle n \rangle \rightarrow 0$  therefore requires low mechanical dissipation  $\Gamma_m$ , high cooling rates  $\Gamma_{\text{dba}}$ , a low environment temperature  $T$ , high mechanical resonance frequency  $\Omega_m$ , low frequency noise  $S_{\omega\omega}(\Omega_m) \propto n_{\text{fn}}$  of the cooling laser (or, more general, no technical noise of any kind), and operation in the resolved-sideband regime to achieve low  $A_+/(A_- - A_+) \approx \kappa^2/16\Omega_m^2$ .

After the optimization of the silica microtoroids for low dissipation, high frequency and operation deeply in the resolved-sideband regime, and the demonstration of very high cooling rates, the most significant performance improvements are expected for operation in a cryogenic experiment, and using a cooling laser bare of any technical noise at the relevant radio frequencies. In the following, we will briefly describe the implementation of these two advances.

### Cryogenic optomechanical experiment

For the successful cryogenic operation of an optomechanical cooling experiment, it is important that the concrete technical implementation provides a proper thermalization of the sample to the cryogen, even in presence of a microwatt-scale heat load through residual light absorption in the sample. This may be a non-trivial task, as strong thermal anchoring of the mechanically compliant device would in many cases imply designs opposite to the requirement of low clamping losses of the mechanical oscillator. For example, the highest mechanical quality factors in silica microresonators were achieved

## 2.7 Approaching the quantum ground state

---

with toroids held only on a sub-micrometric pillar [8], or suspended from silica spokes [6]. Therefore, heat transport from the region of the optical mode in the torus to a heat sink below the silicon chip can be expected to be prohibitively low.

For this reason, we chose to directly immerse the sample into the cryogen, a dilute helium gas, similar to an early experiment with silica microspheres [76] immersed in superfluid helium (figure 2.42). In contrast to other cryogenic experiments with optical microcavities [142, 252], this allows us to reliably thermalize the sample to the base temperature of the cryostat (1.6 K). At the same time, due its low pressure (typically held in the range 0.1 mbar-50 mbar), and the increased intrinsic damping of the mechanical mode due to two-level fluctuators (see section 2.3.2), the helium gas present in the sample chamber does not induce significant damping of the mechanical mode.

The employed commercial Optistat SXM cryostat (Oxford instruments) implements such a cooling scheme by providing two completely independent helium containers (cf. figure 2.42): A larger ( $V = 4.31$ ), thermally insulated reservoir contains liquid helium. From this reservoir, a rotary pump continuously draws helium through a capillary contained in a copper block. During this process, the helium evaporates and cools to temperatures down to 1.6 K. The copper block has a large central bore (49 mm diameter), and constitutes part of the wall of the second helium container—a ca. 50 cm-long tube filled with low-pressure helium gas. It therefore serves as a heat exchanger between the cold He gas from the reservoir and the buffer gas in the central chamber in which the sample is held. The temperature of the heat exchanger can be continuously tuned by controlling the evaporation rate of the He using a control valve. In addition, an electric heater in the copper block allows electronic temperature stabilization, and makes the whole temperature range up to 300 K accessible.

Successful coupling to the WGM in the toroids requires a stable, micrometer-scale gap between the fiber taper and the edge of the toroid. Low vibrations in the experimental assembly are therefore an important selection criterion. The chosen system has successfully been operated in many labs for the purpose of low-temperature scanning-probe microscopy—obviously very vibration-sensitive applications. Both the suspension of the experimental head from a  $\sim 0.5$  m-long metallic rod into the buffer gas, and our compact head design (figure 2.42) indeed renders the cryogenic coupling setup extremely stable [253]. Standard techniques to reduce the coupling of vibrations from the running pumps (heavy masses on the transfer pipes between cryostat and pump) are sufficient to eliminate vibrations to a degree that they cannot be observed in any experimental signal. At the same time, this cryostat allows convenient optical access from two orthogonal directions, providing both a side and top view of the silicon chip. Standard machine vision products (Navitar 12 $\times$ ) with large working distance ( $\sim 9$  cm) allow observa-

## 2. Cavity optomechanics

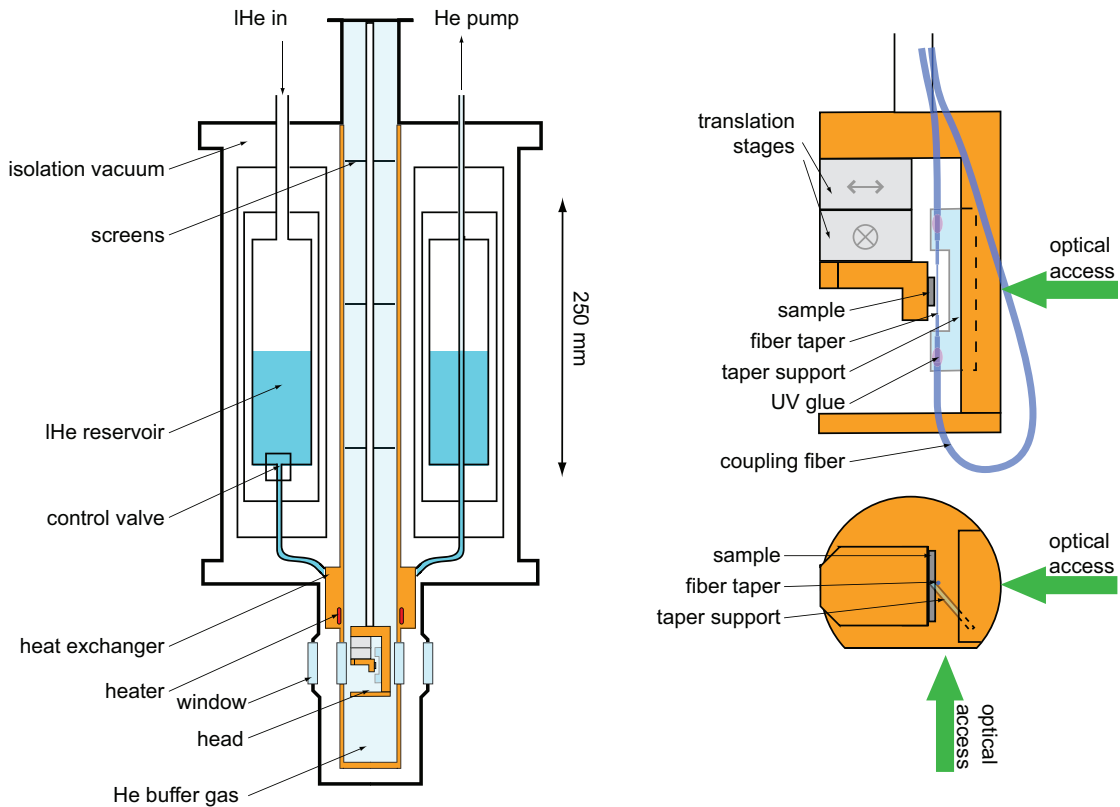


Figure 2.42: Implementation of cryogenic cooling. Left panel: schematic drawing of the employed buffer gas cryostat. Liquid  $^4\text{He}$ , kept in an isolated reservoir, evaporates when pumped through a capillary (“heat exchanger”) and thereby cools low-pressure (0.1 mbar–50 mbar)  $^4\text{He}$ -gas in the sample space to temperatures down to 1.6 K. However, a heater can also be used to stabilize the temperature of the buffer gas to a different value in the full range up to 300 K. The experimental assembly (“head”) is directly immersed into the buffer gas. Right panel: side (top) and bottom (bottom) view of the experimental head. The coupling taper, glued to a glass taper mount, is fixed, while the position of the chip containing the silica microresonators can be adjusted using stick-slip piezoelectric actuators. Optical access from two orthogonal directions allows convenient addressing the toroids on a chip, and precision positioning for coupling to the tapered fiber.

## 2.7 Approaching the quantum ground state

---

tion of the coupling region with up to  $\times 14$ -magnification. This is sufficient for convenient control of the chip's position, allowing to address various toroids on the chip, and to fine-tune its position for well-controlled coupling via the fixed fiber taper.

Preparation of a cryogenic cooling experiment includes two critical tasks: selection of an adequate cooling sample and preparation of a fiber taper mounted into the experiment. Sample preparation and testing proceeds along the lines outlined in chapter 1. In particular, the resonators on the chip are tested for high-Q WGM resonances allowing to enter the RSB regime ( $\kappa < \Omega_m$ ) and for low-mass, high-quality RBM modes. These measurements are done in standard room-temperature coupling setups. If an adequate sample is found, it is mounted into the cryogenic head.

The compactness of the cryogenic experiment renders the use of the bulky metallic taper holders used during taper fabrication impossible. Instead, tapers have to be transferred to a compact glass support made of a microscopy glass slide which, importantly, features the same coefficient of thermal expansion as the taper. In that manner, the taper tension remains constant during cooldown of the cryostat.

The fabrication and transfer of the fiber taper proceeds in several steps which are illustrated in figure 2.43. After the standard fabrication procedure in a hydrogen flame (cf. chapter 1) the taper, still in the fabrication holder, is placed in an auxiliary testing setup. Here, a microtoroid is approached until it touches the taper at its central position. If retracted again, the toroid pulls the taper with it for a certain distance due to proximity forces. Using a micrometer drive, the taper is strained by increasing the separation of the clamps ("elongation" in figure 2.43), and the tests are repeated until the distance over which the taper can be displaced by the toroid is in the range of  $10 \mu\text{m}$ . While not particularly quantitative, this simple test was found very helpful in the delicate task to mount a well-strained taper into the cryostat: sloppy tapers make coupling at low temperatures impossible, while too tightly strained tapers are prone to rupture during cooldown. The glass support, fabricated from a simple microscopy slide is then positioned underneath the taper with a 3d-translation stage. The taper is glued to the support with UV-hardening epoxy applied first on one side, hardened, and then on the other side. Then the fiber is released from the metal holder and transferred to the cryostat. We finally note that due to its reduced diameter and potentially lower quality of the available single-mode fiber material, creating a cryogenic fiber taper at shorter wavelength (e. g.  $780 \text{ nm}$  as in this work) is significantly more difficult than at near-IR wavelengths ( $1.5 \mu\text{m}$ ).

The slide carrying the taper is then mounted into the experimental head, and the fiber ends are guided to the top of the sample insert and leave the cryostat via a helium-tight feedthrough. We have achieved total optical transmission through the cryostat up to 80% from fiber end to fiber end. A toroid from the mounted sample can then be approached using the piezo-

## 2. Cavity optomechanics

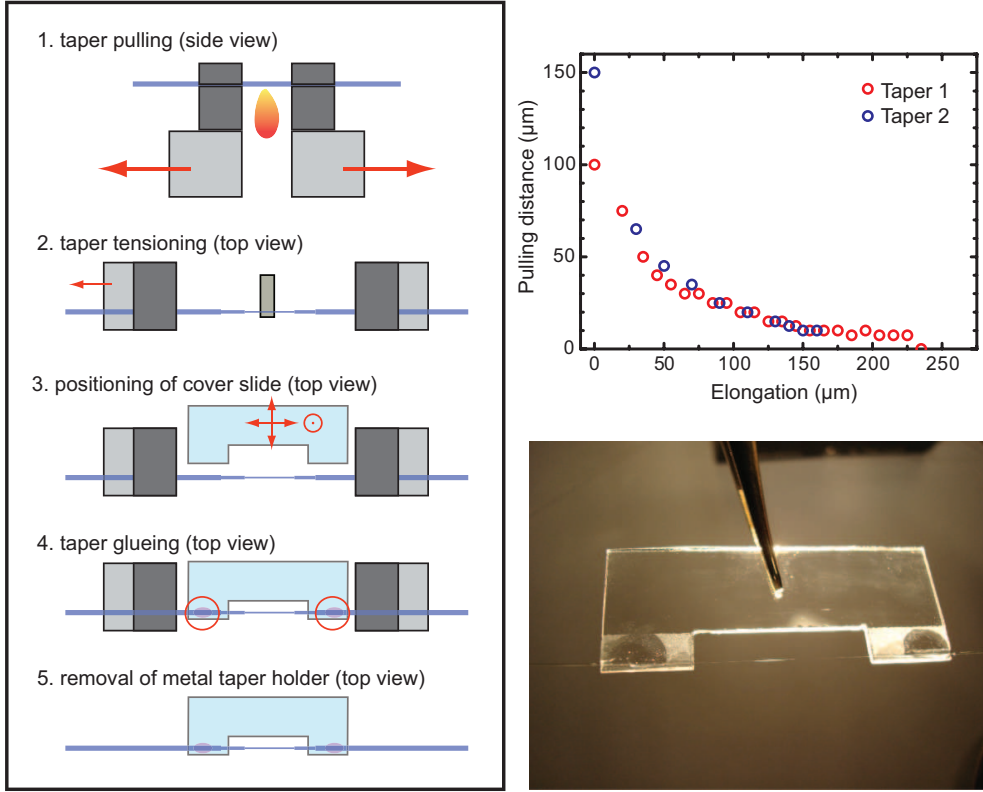


Figure 2.43: Five steps in the fabrication and transfer of a fiber taper to the compact glass support used in the cryogenic experiments (left panel). After pulling the taper over the flame of a hydrogen torch, its strain is tested using an auxiliary chip with microtoroids (upper right graph). If properly strained, the glass support (prepared from a cover slide) is positioned underneath the taper, and the fiber is glued to the support with an epoxy. After hardening the epoxy with UV light, the metal clamps of the fabrication holder are opened to release the taper now only held by the glass support (photograph bottom right). It can then be mounted into the experimental head. See text for more details.

electric stick-slip actuators (Attocube systems) that carry the sample chip. For testing purposes, and to check the correct alignment of the taper mount (position, tilt), these experiments can also be done with the sample insert (experimental head, suspension rod, and top vacuum flange) held outside the cryostat.

To verify the effectiveness of the buffer gas, a sample with microtoroids, and a coupling taper suited for 1550 nm-light was mounted into the cryostat. The cryostat was cooled down, and the mode temperature of this sample's RBM was determined using a displacement measurement based on the PDH technique (see section 2.4.2). To enhance the sensitivity, the weak probing light ( $< 2 \mu\text{W}$ ) from the employed low-noise fiber laser (BASIK, Koheras) was amplified using an erbium-doped amplifier after leaving the cryostat, allowing to measure displacement spectra down to the base temperature of the cryostat [11]. In figure 2.44, the mode temperature  $T_m$  extracted from the calibrated spectra is shown to closely follow the temperature of the helium

## 2.7 Approaching the quantum ground state

buffer gas down to about 1.8 K, or  $\langle n \rangle \approx 600$ . In spite of being exclusively in contact with the cold helium gas, this 62 MHz-RBM could therefore be thermalized to occupations which are, for lower frequency oscillators, often only attainable in dilution refrigerator systems.

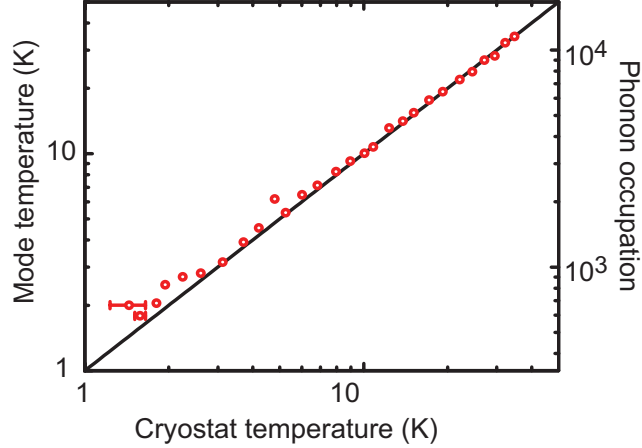


Figure 2.44: Thermalization of the 62 MHz-RBM of a silica microtoroid. The mode temperature  $T_m$  follows the temperature of the helium buffer gas down to 1.8 K, or  $\langle n \rangle \approx 600$ , proving the effectiveness of the buffer gas cooling. Figure from ref. [10].

Cryogenic cooling of the silica microresonators implies severe modifications of the properties of these devices. As discussed already in section 2.3.2, the mechanical quality factor critically depends on the temperature of the structure, due to coupling of the mechanical modes to two-level systems in the glass. In contrast, the change in the sound velocity, and therefore the mechanical resonance frequencies, is a relatively weak effect at the  $\mathcal{O}(10^{-2})$ -level [11]. At the same time, the thermorefractive ( $dn/dT$ ) and thermoelastic ( $\alpha$ ) coefficients are strongly modified. While  $\alpha$  tends to zero at low temperatures ( $T < 2 \cdot 10^{-9} \text{ K}^{-1}$  at 1.6 K), the thermorefractive coefficient continuously drops and changes sign at a temperature of about 8 K.<sup>13</sup> The resulting non-trivial temperature dependence of the optical resonance frequency gives rise to interesting thermal multistability effects when an optical resonance is probed using a laser powerful enough to heat the cavity above this temperature [11]. In the context of the cooling experiments, it is important to note that negative  $dn/dT$  implies that the red wing of an optical resonance is dynamically self-stable, relaxing dramatically the requirements on the laser frequency stability and locking speed when working red-detuned.

### Optical system

For a cooling experiment with the aim of reaching very low occupation it is mandatory to avoid excess backaction noise in the cooling laser beam, as this

<sup>13</sup>Note these observations [11] differ from a previous report [76].

## 2. Cavity optomechanics

---

leads to a limit [8,236,237] in the cooling performance. The grating-stabilized diode lasers employed in our previous cooling work was observed to exhibit excess frequency noise (cf. section 2.6.3). One possible strategy to eliminate this noise is to measure the noise using an independent, quiet cavity, and fast feedback on the frequency of the laser using e. g. the diode laser current as an actuator. Feedback with the required bandwidth exceeding 50 MHz however is technically difficult, as few meters of cable alone would already induce phase lags in the loop sufficient to render it ineffective.

As an alternative approach, a quiet cavity could be used in transmission to filter out the noise. In this manner, reduction of phase noise by 85 dB has been demonstrated at 1 MHz Fourier frequency [254]. However, the filtering reduces the available power by more than a factor of 5, so that the remaining available power of  $\sim 2$  mW is problematically low for cooling experiments. At the same time, the complex filtering setup derogates one important asset of a grating-stabilized diode laser: its convenient, wide-range, and fast tunability.

For these reasons, we chose to use a solid-state pumped continuous wave titanium-sapphire (Ti:S) laser (Matisse TX, Sirah Lasertechnik), which combines very wide tunability (750 to 870 nm) with high output power ( $> 0.5$  W) and quantum-limited noise in both amplitude and phase at the relevant Fourier frequencies. Figure 2.45 shows the schematic setup of this device. The laser is pumped with up to 6 W at 532 nm from a frequency-doubled diode-pumped solid-state laser (Millenia, Spectra Physics). The frequency of the laser is adjusted by a combination of intracavity filters: a Lyot birefringent filter narrows down the frequency range in which gain exceeds loss to a few hundred GHz, and a thin and a thick etalon, with free-spectral ranges of about 250 GHz and 20 GHz, respectively, single out one longitudinal mode of the laser to oscillate. Once the desired laser mode oscillates, electronic feedback loops are used to lock the etalons to keep their transmission maximum resonant with the laser mode. These loops are implemented by the controller of the laser and can be adjusted on a computer using an USB-interface.

Two mirrors mounted on piezo-electric transducers can then be used to fine-adjust the frequency of the laser. In particular, the “slow” transducer allows frequency scans up to about 60 GHz. The “fast” transducer, together with the intracavity electro-optic modulator, can be used for fast feedback to the laser frequency. In normal operation, these actuators are employed in a feedback-loop to lock the laser to an external, temperature-stabilized,  $\sim 30$  cm-long high-finesse ( $\mathcal{F} \sim 300$ ) cavity via the PDH technique, in order to eliminate low-frequency frequency noise of the laser, reducing the laser linewidth to  $< 30$  kHz. In this case, the laser frequency is controlled by tuning the resonance frequency of the reference cavity, again by displacing a cavity mirror mounted on a piezoelectric transducer.

The Ti:S laser can be tuned to arbitrary frequencies within its tuning range, however, continuous scanning over the whole range is not possible, as the various frequency selectors have to be readjusted if the laser has to be

## 2.7 Approaching the quantum ground state

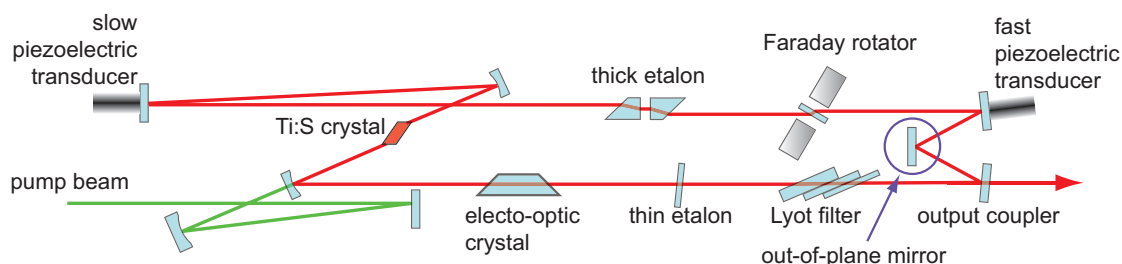


Figure 2.45: Layout of the Ti:S laser used for the cryogenic cooling experiments. The Ti:S crystal in the ring cavity is pumped optically at 532 nm (green beam). In order to select a single longitudinal mode within the tuning range of 750 to 870 nm, a Lyot filter, thick etalon and thin etalon are used. A Faraday rotator, one reflection point lying outside the plane of the rest of the cavity mode, and a number of Brewster-angled surfaces ensure unidirectional lasing. The frequency of the laser is controlled by displacing cavity mirrors using a fast, a slow piezo, as well as an intracavity electro-optic modulator.

tuned by more than about 30 GHz. We therefore resort to a tunable external cavity diode laser (DL) in Littman-Metcalf configuration (TLB-6300, New Focus) for pre-characterization of the toroids (figure 2.46).

Once a well-suited WGM resonance is found with the DL, the Ti:S laser is tuned close to the frequency of this resonance. For this purpose, the Ti:S frequency is coarsely adjusted first, using a grating spectrograph. For the subsequent fine-adjustment, it was found very useful to monitor the interference signal of the DL—scanning over a broader frequency range including the WGM resonance—and the slowly tuning Ti:S laser. When the DL scans through the Ti:S frequency, a transient interference signal is observed as long as the difference frequency is within the bandwidth of the receiver (125 MHz). This transient beat serves as a convenient marker of the Ti:S frequency, while the standard transmission signal of the DL indicates the WGM resonance frequency.

After the Ti:S has been tuned close to the WGM resonance, an optical switch based on MEMS<sup>14</sup>-technology is used to switch to the Ti:S laser as input to the experiment. The optical setup of the experiment corresponds essentially to a homodyne measurement (figure 2.46). To achieve the highest possible SNR, good interference contrast between the local oscillator and signal beams is crucial. For this reason, identical collimators in both beams are employed. Careful alignment then allowed to achieve interference contrast up to 90% (figure 2.47).

The phase of the local oscillator is locked by using the DC-part of the homodyne signal from the balanced receiver, forcing the average detected differential photocurrent to zero for a phase measurement. Note that this is slightly different to the technique described in 2.4.2, where an orthogonal polarization component (in both signal and LO beams) was used to derive the LO phase error signal. In this experiment, the length of the employed

<sup>14</sup>MEMS: microelectromechanical system

## 2. Cavity optomechanics

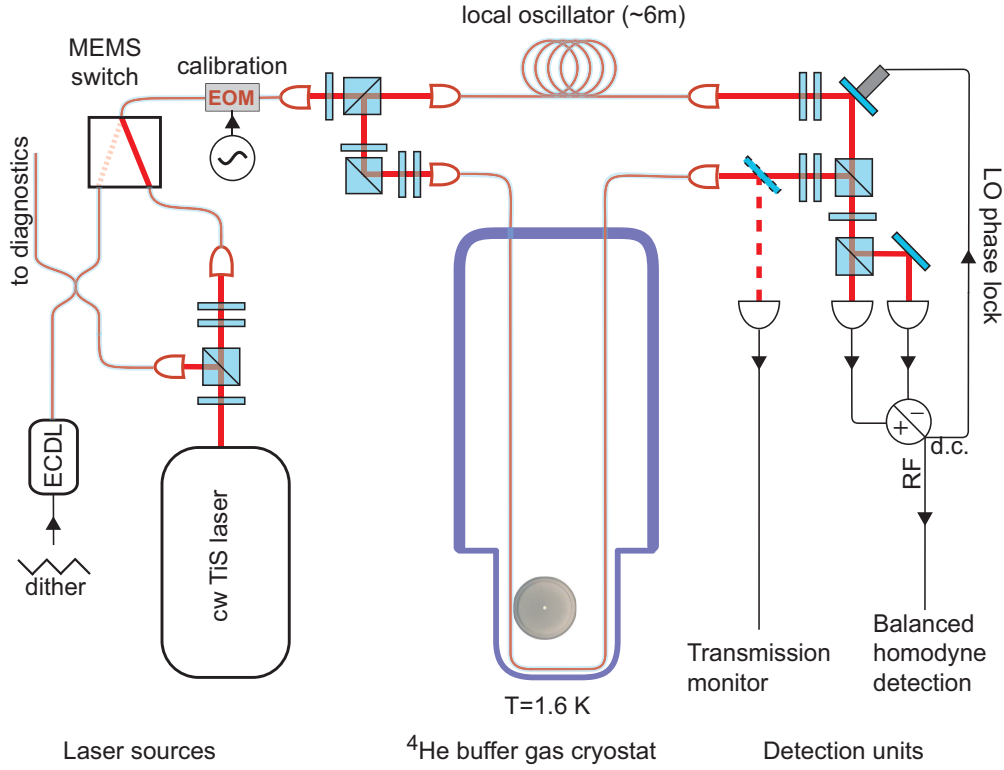


Figure 2.46: Schematic of the setup used for resolved-sideband laser cooling in a cryogenic environment. An external cavity diode laser (EC DL) is used for precharacterization of the optical modes. When a suited WGM resonance is found, the Ti:S laser is tuned to the frequency of the EC DL using the “diagnostics” optical output (see text). Then the input to the experiment is switched to the Ti:S using a MEMS switch. The subsequent optical setup is essentially a Mach-Zehnder interferometer, one arm of which contains the cryostat with the taper coupled to the WGM in a microtoroid. For testing purposes, the output of the taper can also directly be monitored by guiding the light to an auxiliary photoreceiver (dashed beam path). In normal operation, the transmitted light is spatially overlapped with the local oscillator in a polarizing beam splitter cube, albeit in orthogonal polarization modes. Projected into a different polarization basis using a waveplate and another polarizing cube, the modes interfere, and the interference signal is recorded with a balanced receiver. The phase of the local oscillator—and therefore also the detected signal quadrature—is locked using the DC-signal from the balanced receiver. The radio-frequency-part is sent to a spectrum analyzer to obtain the displacement noise spectra, calibrated again by the frequency modulation of probing laser using an electro-optic modulator (EOM). Waveplates and polarizing beam splitter cubes are used at various positions in the optical setup to adjust powers and polarizations of the beams.

## 2.7 Approaching the quantum ground state

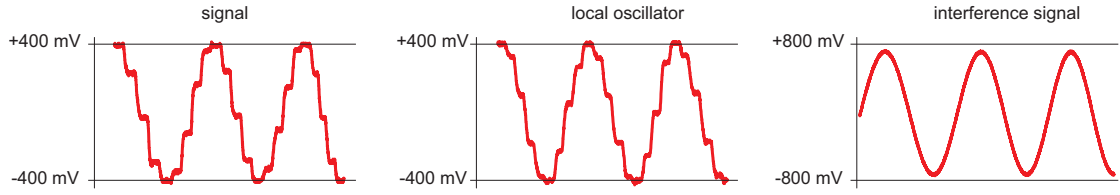


Figure 2.47: Interference contrast of the homodyne receiver. “Signal” and “local oscillator” traces are recorded by manually rotating the last  $\lambda/2$ -waveplate in front of the last polarizing beam splitter cube in steps of  $10^\circ$ , with the other input beam blocked. For this test, the powers in both beams are adjusted to yield a maximum signal of 400 mV. If both beams are opened, and the detection unit is properly aligned, a total signal amplitude of 1440 mV, corresponding to 90% interference contrast, is recorded.

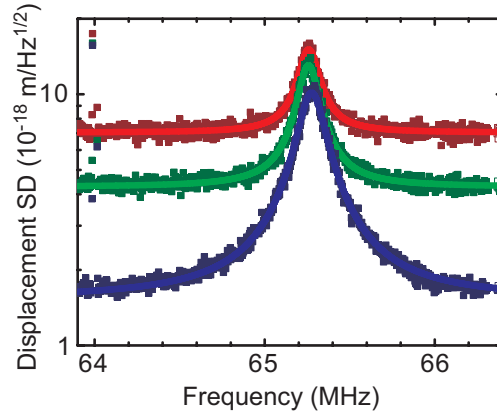


Figure 2.48: Displacement noise spectra of the RBM of a silica microtoroid held at a temperature of 2.4 K. The power used to probe the RBM was about  $3 \mu\text{W}$  (red trace),  $10 \mu\text{W}$  (green trace) and  $100 \mu\text{W}$  (blue trace). Points are measured data, lines are Lorentzian fits. Figure from ref. [10].

fibers renders this approach problematic due to apparent drifts in the polarization rotation in the fibers. Note also that it is necessary to match the total length of the fibers in both arms of the interferometer (excluding the potential propagation length in the toroid) in order to measure the correct signal quadrature at all Fourier frequencies.

Figure 2.48 shows typical displacement spectra of the 65.3 MHz-RBM of a silica microtoroid probed by homodyne spectroscopy with the Ti:S laser. The sample is held in the cryostat, at a temperature of 2.4 K, corresponding to  $\langle n \rangle \approx 770$ . Sensitivity at the  $10^{-18} \text{ m}/\sqrt{\text{Hz}}$ -level, as well as a SNR of nearly 20 dB (in noise power) is achieved, in spite of a mechanical quality factor which was as low as 540 in this case. Note that displacement noise measured at resonance is the sum of the thermal noise in the mechanical mode *plus* the imprecision background noise due to quantum noise in the detection, which reduces at higher probing powers.

## 2. Cavity optomechanics

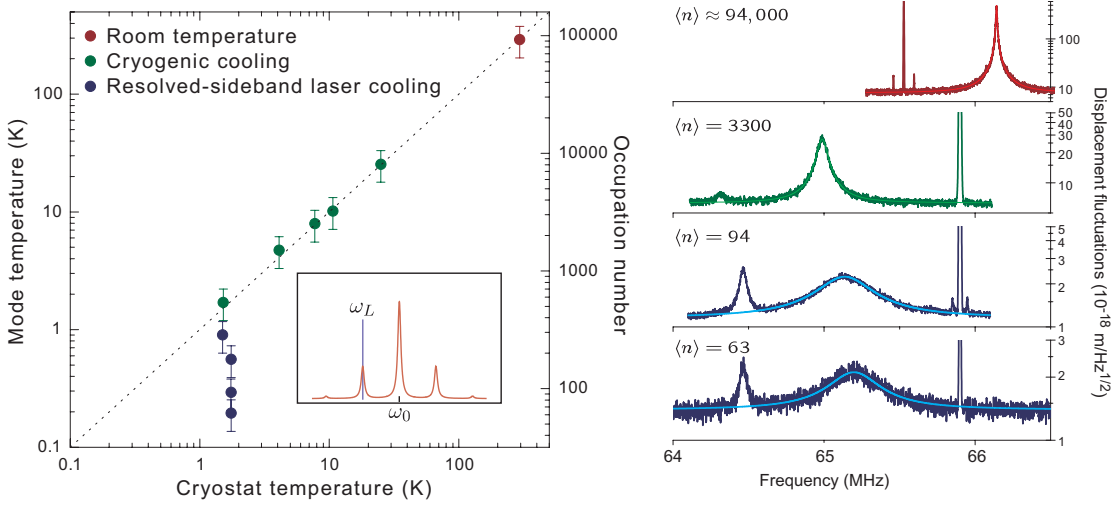


Figure 2.49: Left panel: Mode temperature and occupation number of the RBM, measured using noise thermometry, versus the temperature of the buffer gas in the cryostat, including a reference measurement at room temperature (red point). Green data points are taken with the laser tuned to the optical resonance, so no optical cooling takes place. When tuned to the lower mechanical sideband (inset), additional laser cooling is observed (blue points). Panels on the right show a selection of displacement noise spectra, from which the mode temperatures of the measurements were derived. Apart from the calibration peak these spectra also reveal a nearby second mechanical mode. Nonetheless, the spectrum of the RBM can be well-fit with a Lorentzian (thin lines). Figure from ref. [10].

### 2.7.2 Cooling towards the quantum ground state

To demonstrate the performance of combined optical and cryogenic cooling, we used a  $52\ \mu\text{m}$ -diameter sample with a WGM of  $5.5\ \text{MHz}$  intrinsic decay rate and  $9\ \text{MHz}$  mode splitting, loaded down to  $\kappa/2\pi \approx 19\ \text{MHz}$  using the fiber taper, corresponding to a finesse of about  $70,000$ . A room-temperature reference measurement (figure 2.48) of its RBM at  $65.2\ \text{MHz}$  reveals an effective mass of  $5.6\ \text{ng}$ , in good agreement with the simulated value of  $4.9\ \text{ng}$ . Note that the experimentally determined mass can only be as accurate as the displacement calibration and the knowledge of the actual temperature of the RBM is. We generally estimate the resulting systematic error to a level of  $30\%$ , arising from imperfections in the modulation scheme and temperature changes induced by dynamical backaction or absorption-induced heating.

Using this effective mass, it is possible to derive the mode temperature from subsequent displacement measurements during cooldown of the cryostat. The results again confirm proper thermalization of the sample (figure 2.49), down to an occupation of  $\langle n \rangle \approx 550$ . For further cooling, the Ti:S laser is tuned to the lower sideband at  $\bar{\Delta} = -\Omega_m$ . The signal from the homodyne receiver can still be used to measure mechanical displacements, however, due to the detuned operation, the spectrum of the phase quadrature now displays a more complicated dependence from the mechanical noise

## 2.7 Approaching the quantum ground state

spectrum. In contrast to the expression (2.118) for  $\bar{\Delta} = 0$ , we now obtain

$$\bar{S}_{qq}^{\text{out}}(\Omega) = 1 + \frac{4\bar{a}^2 g_0^2 \eta_c \kappa}{\bar{\Delta}^2 + (2\eta_c - 1)^2 (\kappa/2)^2} \times \frac{\bar{\Delta}^4 + 2\bar{\Delta}^2 (2\eta_c - 1) (\kappa/2)^2 + (2\eta_c - 1)^2 (\kappa/2)^2 ((\kappa/2)^2 + \Omega^2)}{\bar{\Delta}^4 + 2\bar{\Delta}^2 ((\kappa/2)^2 - \Omega^2) + ((\kappa/2)^2 + \Omega^2)^2} \bar{S}_{xx}(\Omega), \quad (2.180)$$

where 1 again is due to quantum noise.

We emphasize that the transduction of a frequency modulation into  $\bar{S}_{qq}$  has the same dependence on the relevant experimental parameters as the transduction of displacements  $\bar{S}_{xx}$ , so that the calibration scheme remains valid also in the detuned case. Rewriting (2.180) as a quantum-noise induced imprecision in the displacement measurement one obtains

$$\bar{S}_{xx}^{\text{im,qn}}(\Omega) = \frac{\bar{\Delta}^2 + (2\eta_c - 1)^2 (\kappa/2)^2}{4\bar{a}^2 g_0^2 \eta_c \kappa} \times \frac{\bar{\Delta}^4 + 2\bar{\Delta}^2 ((\kappa/2)^2 - \Omega^2) + ((\kappa/2)^2 + \Omega^2)^2}{\bar{\Delta}^4 + 2\bar{\Delta}^2 (2\eta_c - 1) (\kappa/2)^2 + (2\eta_c - 1)^2 (\kappa/2)^2 ((\kappa/2)^2 + \Omega^2)}. \quad (2.181)$$

For  $\kappa \gg \Gamma_{\text{eff}}$ , which is typically in the case in the experiments presented here, the spectral shape of this function can be assumed to be flat over the frequency range of interest, and we find as a useful approximation

$$\bar{S}_{xx}^{\text{im,qn}}(\Omega_m) \approx \frac{\Omega_m^2}{4\eta_c^2 g_0^2} \frac{\hbar\omega}{P_{\text{in}}} \quad (2.182)$$

in the resolved sideband regime ( $\bar{\Delta} = -\Omega_m \gg \kappa$ ). It is noteworthy that this value is only a factor of 4 higher than expected for resonant probing  $\bar{\Delta} = 0$  in this regime. However, in the resolved sideband regime, only a fraction of  $\sim (\kappa/4\Omega_m)^2$  of the launched power is coupled to the cavity.

Figure 2.49 shows displacement spectra and corresponding mode temperatures recorded during such a cooling run. As expected, the damping of the mechanical modes is optically increased, when the laser is detuned to  $\bar{\Delta} = -\Omega_m$ . Note that for these experiments, active stabilization of the laser frequency to the optical sideband of the WGM has not been necessary. Instead, a second electronic spectrum analyzer was used to demodulate the homodyne signal at the frequency  $\Omega_{\text{mod}}$  of the calibration modulation. As expected from (2.181), this signal displays local maxima at  $\bar{\Delta} = 0, \pm\Omega_{\text{mod}}$ . After the laser is tuned to  $\bar{\Delta} = -\Omega_m$ , the system is sufficiently stable during the averaging of typically several tens of seconds (small drifts can be manually compensated).

For the highest launched powers of  $\sim 0.2$  mW, the total damping rate was increased to  $\Gamma_{\text{eff}}/2\pi = 370$  kHz. At the same time, the mode temperature was reduced to  $T_m = 200 \pm 60$  mK, corresponding to an occupation

## 2. Cavity optomechanics

---

of  $\langle n \rangle = 63 \pm 20$  [10]. The error interval is due to potential calibration errors in the displacement measurement and the determination of the effective mass. This value is comparable to the lowest occupation achieved in nano-electromechanical systems, yet those experiments have to rely more heavily on advanced cryogenic machinery [246], and suffer from the insufficient signal-to-noise ratio.

### 2.7.3 Assessing measurement backaction

The strong suppression of thermal noise in the measurements presented here allows an interesting analysis of the data from the perspective of quantum measurement. As discussed in section 2.4.1, fundamentally, the achieved total uncertainty in the measurement of the displacement of the mechanical oscillator is limited by two effects: imprecision and backaction. The imprecision in our experiment is given by detection shot noise, in the detuned case discussed here it is described by equation (2.181).

On the other hand, the light used to measure the mechanical oscillator exerts backaction on it. Inevitably, intracavity photon number fluctuations give rise to a fluctuating force the spectrum of which can be derived to read [10]

$$\bar{S}_{FF}^{\text{ba,qn}}(\Omega) = \hbar^2 g_0^2 \bar{a}^2 \kappa \frac{\bar{\Delta}^2 + (\kappa/2)^2 + \Omega^2}{\bar{\Delta}^4 + 2\bar{\Delta}^2((\kappa/2)^2 - \Omega^2) + ((\kappa/2)^2 + \Omega^2)^2}. \quad (2.183)$$

These force fluctuations are usually referred to as quantum backaction, simplifying to

$$\bar{S}_{FF}^{\text{ba,qn}}(\Omega_m) \approx \frac{2g_0^2 P_{\text{in}} \eta_c \hbar}{\omega \Omega_m^2} \quad (2.184)$$

in the resolved-sideband regime ( $|\bar{\Delta}| = \Omega_m \gg \kappa$ ). Note that the spectra of imprecision and backaction noise, as well as their possible correlation  $S_{xF}(\Omega)$  reflect properties of the measurement device (the cavity pumped by a laser field)—independent of the mechanical oscillator.

Other sources of measurement backaction include excess noise in the intracavity photon number, which may arise from laser frequency fluctuations [8, 236, 237]. This effect can be ruled out in this work as the employed Ti:S is known to exhibit only quantum fluctuations at the Fourier frequencies of interest. Another possible source of measurement backaction is heating of the torus due to light absorption. This increases the temperature of the structure, and raises the level of Langevin force fluctuations driving the mechanical oscillator.

A series of cooling measurements (figure 2.50) indeed reveals a deviation from the simple relation (2.147), which can however be reproduced by introducing a heating term

$$T_m = \frac{\Gamma_m(T')}{\Gamma_m(T') + \Gamma_{\text{dba}}} T', \quad (2.185)$$

## 2.7 Approaching the quantum ground state

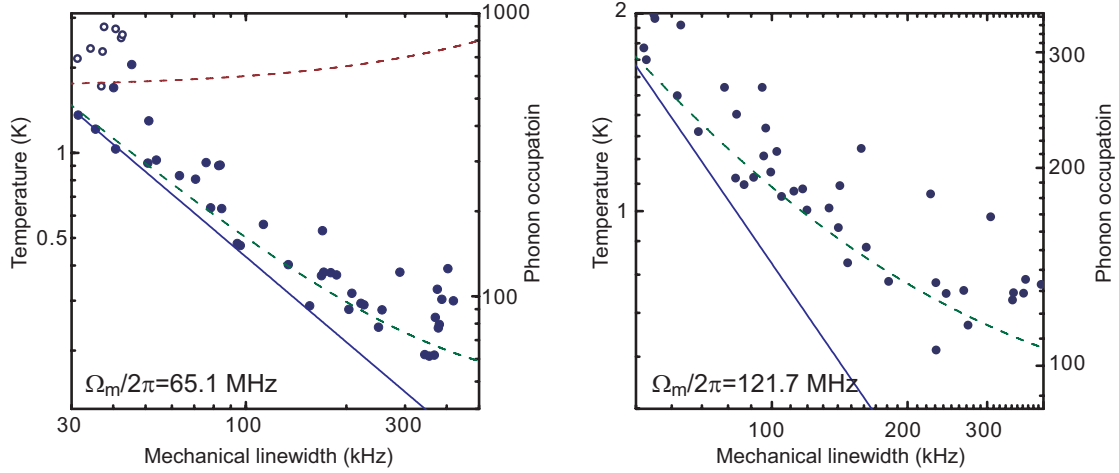


Figure 2.50: Resolved-sideband cooling of two samples with frequencies of  $\Omega_m/2\pi = 65.1$  MHz (left panel) and  $\Omega_m/2\pi = 121.7$  MHz (right panel). The graphs show the mechanical linewidth  $\Gamma_{\text{eff}}$  (abscissa) versus the derived mode temperature  $T_m$  (ordinate) during a cooling run. Open points correspond to measurements with the laser tuned close to the optical resonance (no optical cooling), and filled points to measurements with the laser tuned close to the lower sideband. When varying the power of the cooling laser, both linewidth and mode temperature are changed. Deviation from the simple cooling behavior (blue line) is attributed to an increase of the structures temperature (red dashed line), taken into account in a more elaborate model (green dashed line). Scatter is due to varying operation conditions, uncertainty in phonon occupation for each point is  $< 30\%$ . Figure from ref. [10].

with  $T' = T + \Delta T_{\text{abs}}$ , where  $\Delta T_{\text{abs}}$  is proportional to the power circulating in the cavity. In addition, we have taken also the temperature dependence of the mechanical damping  $\Gamma_m(T')$  into account. For the 65 MHz-oscillator below 2 K, with [11]  $d\Gamma_m/dT \approx 2\pi 16$  kHz/K, we find a heating of about 5 K per Watt of circulating power. Similar values were extracted from studies of optical multi-stability at low temperature at a wavelength of  $1.5 \mu\text{m}$ , corroborating the attribution of the observed backaction effect to laser-induced heating.

A comparison with a second cooling run with a different sample with  $\Omega_m/2\pi = 121.7$  MHz and  $Q_m = 2,200$ , but a broader WGM resonance with  $\kappa/2\pi = 155$  MHz emphasizes the importance of the resolved-sideband regime for the efficiency of cooling in the presence of laser absorption: A significantly more pronounced heating effect prevents reaching occupations below  $\langle n \rangle = 100$ , in spite of the higher mechanical frequency (figure 2.50).

From the data of the  $\langle n \rangle \approx 63$ -cooling run we can now extract quantitative values of the corresponding backaction force fluctuations. As a very conservative upper limit, we may use the *total* thermal force fluctuations  $\overline{S_{FF}^{\text{the}}}(\Omega) = 2m_{\text{eff}}\Gamma_m k_B T'$ , and find a value of  $\sqrt{\overline{S_{FF}^{\text{the}}}(\Omega_m)} = 8 \text{ fN}/\sqrt{\text{Hz}}$ . If we consider only the temperature *raise*  $\Delta T_{\text{abs}}$  caused by the laser absorption as the backaction of the measurement, a lower value of  $\sqrt{\overline{S_{FF}^{\text{ba}}}(\Omega_m)} = 4 \text{ fN}/\sqrt{\text{Hz}}$  is found. In these assessments, we benefit from the low occupation which al-

## 2. Cavity optomechanics

---

allows us to extract the effect of measurement backaction, as it large enough to be observed on top of the background of the thermal noise.

It is interesting to compare these findings with fundamental limits. Indeed, quantum mechanics imposes an inequality on imprecision and backaction noise, which, for the particular case of an optical measurement of a mechanical oscillator's displacement, can be written as simple as

$$\bar{S}_{xx}^{\text{im}}(\Omega) \cdot \bar{S}_{FF}^{\text{ba}}(\Omega) \geq \frac{\hbar^2}{4}. \quad (2.186)$$

This relation can be considered a manifestation of the Heisenberg uncertainty principle in the context of continuous position measurement [94].

Taking the force noise extracted from our data, and the experimental imprecision of  $\sqrt{\bar{S}_{xx}^{\text{im}}(\Omega_m)} \approx 1.4 \text{ am}/\sqrt{\text{Hz}}$  achieved in the same measurement, an upper limit from the backaction-imprecision product of

$$\sqrt{\bar{S}_{xx}^{\text{im}}(\Omega_m) \cdot \bar{S}_{FF}^{\text{the}}(\Omega_m)} \approx 220 \frac{\hbar}{2}$$

is found. Considering only the absorption-induced heating as a backaction mechanism, an even lower value of

$$\sqrt{\bar{S}_{xx}^{\text{im}}(\Omega_m) \cdot \bar{S}_{FF}^{\text{ba}}(\Omega_m)} \approx 100 \frac{\hbar}{2}$$

is found from our experiments. This is an order of magnitude lower than the values achieved with nanomechanical oscillators cooled in dilution refrigerators: Readout with an atomic point contact [255] achieved a backaction-imprecision product of  $1700 \pm 400 \hbar/2$ , while measurements using a sSET [246] have achieved a value<sup>15</sup> of  $\sim 800 \hbar/2$ .

## 2.8 Conclusion

In this chapter, we have reported on optomechanical interactions in high-finesse optical whispering gallery mode resonators. Careful analysis and understanding of these devices' properties has allowed us to optimize their performance for the purpose of cavity optomechanics. Among the various systems now designed and studied in this context, they offer a unique combination of high-frequency (30–120 MHz), high-quality ( $Q_m$  up to 80,000) mechanical modes and ultra-high finesse (intrinsic finesse  $\mathcal{F}_0 \approx 0.9 \cdot 10^6$ ) optical resonances. These key figures rival even the best optical cavities developed in the context of cavity quantum electrodynamics [256] in terms of finesse, and the mechanical quality factors of state-of-the art nano- and micromechanical oscillators [246, 257] in the same frequency range.

---

<sup>15</sup>Note that the number quoted in this manuscript,  $15 \hbar/2$ , is a theoretical estimate if shot-noise limited detection was possible. As discussed in the supplementary information, the actual imprecision noise in the experiment was 50-times higher [239, 246].

Together with an intrinsically strong parametric coupling of optical and mechanical degrees of freedom—with optical resonance frequency shifts of typically more than 10 kHz per femtometer displacement—this has enabled ultrasensitive optical monitoring of the mechanical mode. Adapting powerful tools from Quantum Optics as optical displacement meters limited only by optical quantum noise, sensitivities at the level of  $10^{-18}$  m/ $\sqrt{\text{Hz}}$  were achieved [8, 9]. This experimentally demonstrated imprecision is below the expected noise level associated with the zero-point fluctuations of the mechanical mode, a feat yet achieved only with much lighter nanomechanical oscillators [239, 246]. Reaching such a sensitivity is a crucial precondition for the experimental verification of the concepts of Quantum Measurement in the context of displacement measurements, such as quantum backaction and the emergence of the standard quantum limit [94, 124, 127]. Furthermore, this exquisite sensitivity may also be exploited to monitor nanomechanical oscillators brought into the near-field of the cavity mode [9], such as silicon nitride nanobeams or -membranes [12], graphene sheets or diamond nanowires. Beyond mechanical effects, this sensitivity has allowed studying fundamental thermal noise mechanisms, such as thermorefractive noise, which are of interest for the application of silica microresonators as frequency references [203, 258], as biophysical sensors [29, 259, 260] or for the proposed demonstration of Kerr squeezing [75].

Due to the high-finesse, the dramatically enhanced intracavity radiation pressure exerts a readily detectable force on the mechanical mode. This effect was directly measured in a “pump-probe”-type measurement, in which the displacements induced by modulated radiation-pressure is probed with a second laser. It was shown that the nonlinear cross-coupling of the two light fields is strongly dominated by radiation pressure induced mechanical displacement, and more than two orders of magnitude stronger than the well-known Kerr effect [1]. Furthermore, radiation pressure has also been shown to induce a modification of the dynamics of the mechanical mode, changing both its effective spring constant (optical spring) and its damping (amplification and cooling). Predicted as early as 1967 by Braginsky [97], this dynamical backaction was systematically studied over a wide regime of experimental parameters (detuning, photon storage time, mechanical oscillation period). Our experiments have demonstrated, for the first time, efficient optical cooling of a mechanical mode induced by dynamical backaction, both in the “Doppler” [1] and the resolved-sideband regime [8]. These techniques are now widely employed in experiments which aim to demonstrate ground-state cooling of a mechanical device (figure 2.51).

In our experiments, we have identified several important barriers on the way towards this ultimate goal. Frequency noise of the driving electromagnetic field, practically relevant in many systems [8, 236, 237], is shown here to be eliminated by resorting to a quantum-noise limited laser system. Furthermore, much in contrast to trapped atoms or ions, even very high-Q macro-

## 2. Cavity optomechanics

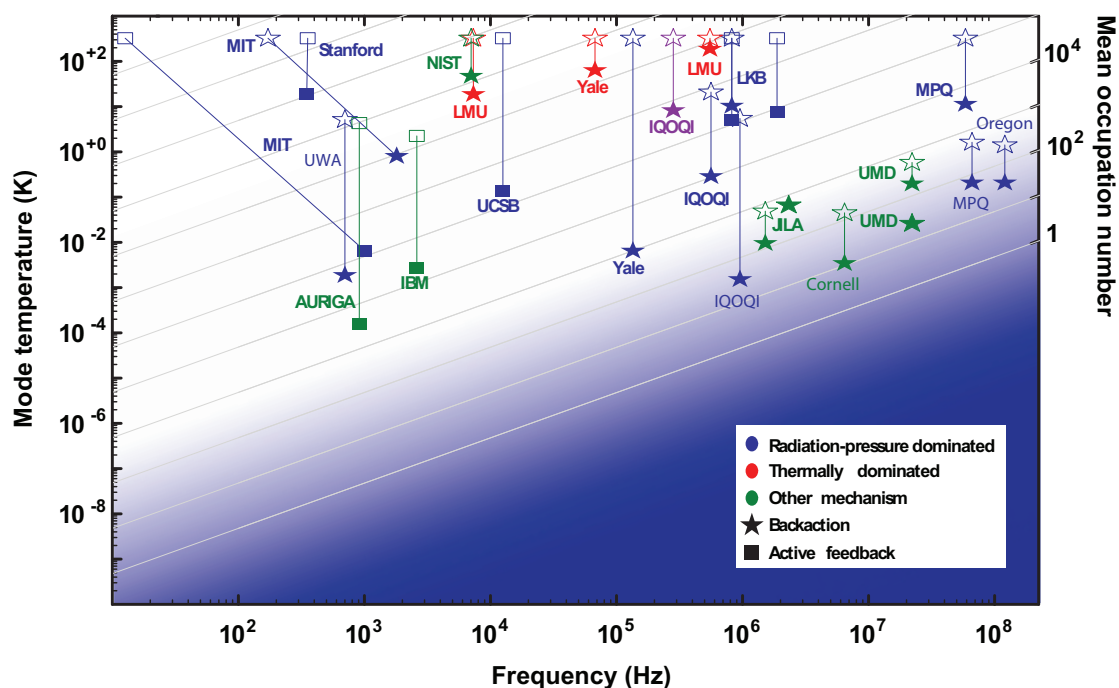


Figure 2.51: Cooling experiments performed in different laboratories around the globe, including both experiments based on dynamical backaction and active feedback cooling. The cooled oscillators span about 8 orders of magnitude in frequency. Open symbols indicate the reservoir temperature of the experiments, distinguishing cryogenic from room-temperature experiments. Full symbols indicate the lowest mode temperature achieved when optomechanical cooling is applied. The dashed line indicates the temperature for which  $\hbar\Omega_m \approx k_B T$ . The individual results are described in references: AURIGA [160], Cornell [41], IBM [150], IQOQI [141, 142, 164], JILA [157], LKB [130, 137, 138], LMU [135, 154], MIT [148, 149], MPQ [1, 8, 10], NIST [151], Oregon [261], Stanford [231], UCSB [144], UMD [246], UWA [156], Yale [152].

scopic oscillators are not very well isolated from their finite-temperature environment. Fluctuating thermal forces thus compete with laser cooling, limiting the occupancies achieved in room-temperature experiments to a few thousand quanta (figure 2.51).

To overcome this limit, we have implemented resolved-sideband laser cooling in a cryogenic environment [10]. The mechanical oscillator is cooled to an occupation of  $\langle n \rangle \approx 63 \pm 20$ . The optical detection scheme provides small enough displacement imprecision to enable monitoring even such an ultra-cold oscillator with appreciable signal-to-noise ratio. Even more, due to the low occupation, we are able to extract an upper limit on the *backaction* of the displacement measurement. The product of backaction and imprecision noise lies only a factor of 100 above the fundamental quantum limit [94], and constitutes the lowest value reported in the literature [239].

In conclusion, we have introduced an optomechanical system suited for the exploration of quantum effects in mesoscopic mechanical oscillators, by experimentally demonstrating (*i*) the possibility to monitor its displacements

with an imprecision below the standard quantum limit, *(ii)* a combination of cooling techniques based on radiation-pressure and standard cryogenics capable of cooling the oscillator close to its quantum ground state, and *(iii)* a near-ideal operation of the displacement transducer in the sense of quantum measurement (imprecision-backaction product). Leveraging quantum optical techniques, we have therefore established a route into the quantum realm of mesoscopic oscillators, which previously was thought to be uniquely accessible with nano-electromechanical systems [127].

## 2.9 Outlook

Notwithstanding such progress, true quantum effects of radiation pressure, or a mechanical oscillator, have not been observed in any experiment today.<sup>16</sup> Of the various theoretical proposals, it appears that cooling to the quantum ground state, and the observation of quantum backaction are closest to being possible with WGM microresonators. In the following, we briefly outline the strategies pursued in our laboratory to achieve these goals, and, concluding this chapter, point at other interesting optomechanical effects to explore.

The most severe antagonist to ground state cooling is the intrinsic damping  $\Gamma_m$  of the mechanical mode, coupling it to the environment at a finite temperature  $T$ . This coupling tries to maintain the mode and the environment in thermal equilibrium, essentially feeding the power  $\Gamma_m k_B(T - T_m)$  into the mechanical mode, which has to be continuously removed by laser cooling. There are two obvious ways to reduce this load: reducing the environment temperature  $T$ , and reducing the mechanical damping  $\Gamma_m$ . While the former is a technical task, the latter exhibits complex dependence on material, geometry and operation conditions.

In particular we have observed (sections 2.3.2 and 2.7.2) a strong increase of the mechanical damping at cryogenic temperatures due to relaxation of two-level systems (TLS) present in the silica material [11, 185]. This flaw is known, however, to ameliorate at sufficiently low temperatures  $\lesssim 1$  K, at which the damping due to TLS rolls off with  $\Gamma_m \propto \Omega_m/T^3$ . Thus, lowering the operation temperature of the experiment may be expected to enhance the cooling performance with a scaling up to  $T^{-4}$ . For this reason, a <sup>3</sup>He-cryogenic system is presently tested in our laboratory. A base temperature of 600 mK, and significantly higher mechanical quality factors ( $> 10^4$ ) than in the <sup>4</sup>He-cryostat were already measured. Resolved-sideband cooling, with the cooling rates of 1.5 MHz already demonstrated, would place a 70 MHz RBM directly in the quantum ground state. A very crucial issue in this context, however, is the suppression of heating by laser absorption, requiring very high-quality samples and operation deeply in the resolved sideband regime.

---

<sup>16</sup>There are, however, experiments that could be considered “quantum simulations” of mesoscopic mechanical oscillators—based on ultracold atoms [262, 263].

## 2. Cavity optomechanics

---

Optical absorption could be reduced by using ultrapure crystalline materials for the WGM resonators. Indeed, pioneering work at the Jet Propulsion Laboratory has demonstrated WGM resonators made of quartz [264],  $\text{MgF}_2$  and  $\text{CaF}_2$  [265] with optical quality factors up to  $6 \cdot 10^{10}$ . Machining and polishing WGM resonators down to a diameter of  $80 \mu\text{m}$  has also been achieved. At the same time, the pristine crystalline structure avoids mechanical losses due to two-level systems. At  $\sim 100 \text{ kHz}$ -frequencies, mechanical quality factors  $Q_m \gtrsim 10^8$  were measured in bulk  $\text{CaF}_2$  samples, both at room and cryogenic temperatures [266].

We have therefore started to explore the optomechanical properties of crystalline WGM resonators in our laboratory. Several different geometries were fabricated using a precision lathe and polished using diamond slurry. An example of such a resonator is shown in figure 2.52. We have achieved optical quality factors up to  $Q_0 = 1.2 \cdot 10^{10}$ , corresponding to a linewidth of  $\kappa/2\pi = 24 \text{ kHz}$  in a  $R = 1.8 \text{ mm}$  resonator (intrinsic Finesse  $\mathcal{F}_0 = 760,000$ ). We have also produced an  $800 \mu\text{m}$ -diameter,  $100 \mu\text{m}$  thick disk and achieved  $Q_0 \approx 10^9$  ( $\mathcal{F}_0 = 400,000$ ). Optical transduction techniques described in section 2.4 are used to measure mechanical modes in these structures, which are typically found in the range between  $0.5$  and  $5 \text{ MHz}$ . The highest measured mechanical quality factor was  $Q_m = 136,000$ . Already an encouraging value, there is strong evidence for this value to be still limited by clamping losses which can be mitigated by a more suitable design and suspension of the resonators. Furthermore, the rather high effective masses (around  $600 \mu\text{g}$ ) and the slightly weaker optomechanical coupling ( $|g_0|/2\pi \sim 1.5 \text{ kHz/fm}$ ) call for further miniaturization of the structures. For example, a  $80 \mu\text{m}$ -diameter,  $10 \mu\text{m}$  thick disk would possess  $m_{\text{eff}} = 90 \text{ ng}$  and  $\Omega_m/2\pi = 63 \text{ MHz}$ . If  $Q_m \sim 10^8$  can be reached, the power required to cool such a device from  $T = T_m = 1.6 \text{ K}$  to  $T_m \approx \hbar\Omega_m/k_B$  is as low as  $10 \mu\text{W}$  in the resolved-sideband regime. Heating due to absorption is likely to be totally negligible considering the optical quality of the crystals.

We finally point out that various crystalline materials may be amenable to this approach, combining optomechanical coupling with yet other functionality. As an example, we have tested various polished diamond spheres, and have observed WGMs with quality factors up to  $3 \cdot 10^6$  in a  $3 \text{ mm}$ -diameter sphere.

A somewhat opposite approach consists in decoupling optical and mechanical degrees of freedom. Keeping the silica WGM resonators as optical cavities, but placing an external mechanical oscillator in the near-field of the WGM allows independently engineered mechanical properties. For example, light-weight ( $m_{\text{eff}} \approx 1 \text{ pg}$ ) nanomechanical oscillators such as strained SiN strings, have been demonstrated to enable  $Q_m \approx 10^6$  at  $\sim 1 \text{ MHz}$ -resonance frequencies [267]. Placed in the near-field of a WGM, movement of the polarizable oscillator in the optical field gradient induces frequency shifts on the order of  $|g_0| \approx 10 \text{ MHz/nm}$ , without inducing detectable optical loss of the

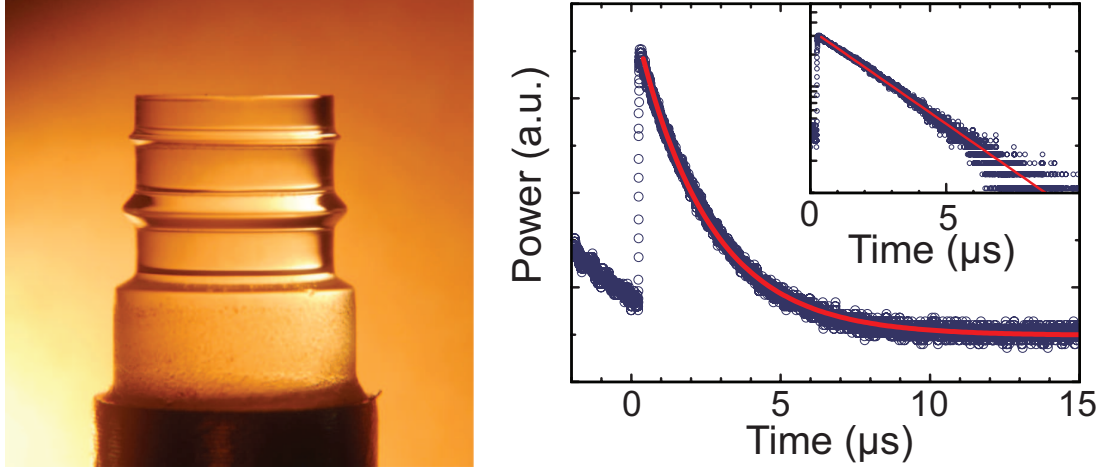


Figure 2.52: Whispering gallery mode resonator made of calcium fluoride. The rims of the protrusions support WGM with extreme photon storage times. Left panel is a photograph of a 6 mm-diameter prototype resonator produced at MPQ. Right panel shows a ringdown trace for a critically coupled resonator. The ringdown time of  $2.5 \mu\text{s}$  corresponds to an intrinsic quality factor of  $1.2 \cdot 10^{10}$ .

WGM. A measurement imprecision below the noise level associated with zero-point fluctuations, and dynamical backaction induced by the optical dipole force have been demonstrated with such a system in our laboratory [12].

These results are very encouraging for studies pertaining to the observation of quantum backaction. Usually masked by the much stronger thermal noise, this effect may become detectable if the ratio  $\bar{S}_{FF}^{\text{ba,qn}}(\Omega_m)/\bar{S}_{FF}^{\text{the}}(\Omega_m) \approx \bar{a}^2 g_0^2 \kappa \hbar^2 \Omega_m^{-2} / 2m_{\text{eff}} \Gamma_m kT$  (assuming the limit  $\Omega_m \gtrsim \kappa/2$ ) approaches unity. Leveraging the low mass and high quality factor available with nanomechanical oscillators it appears feasible to approach this regime, with moderate optical probing powers of  $\sim 100 \mu\text{W}$  even *at room temperature*. To differentiate the added noise induced by quantum backaction from potentially present absorption induced heating, correlation measurements [133] or backaction cancellation [132] between two oscillators with slightly different frequencies may be employed.

As a last example of near-future research projects enabled by the progress presented in this thesis is an investigation of the regime of strong optomechanical coupling [240] in the yet unexplored optical domain. As our analysis shows, the strong—but tunable—coupling of the optical mode to the mechanical mode via the mean photon field  $\bar{a}$  gives rise to features very similar to the effect of electromagnetically induced transparency (EIT) in atomic physics [112, 268].

The basic idea of such an experiment is illustrated in figure 2.53. The strong field  $\bar{a}$  of the coupling (formerly “cooling”) laser oscillates at frequency  $\omega_1 = \omega_c - \Omega_m$ , and thereby couples the levels  $2 \leftrightarrow 3$  by processes in which a phonon is removed upon the addition of a photon to the intracavity field (red-sideband transitions). A second, very weak laser oscillating at  $\omega_p = \omega_1 + \Omega$ ,

## 2. Cavity optomechanics

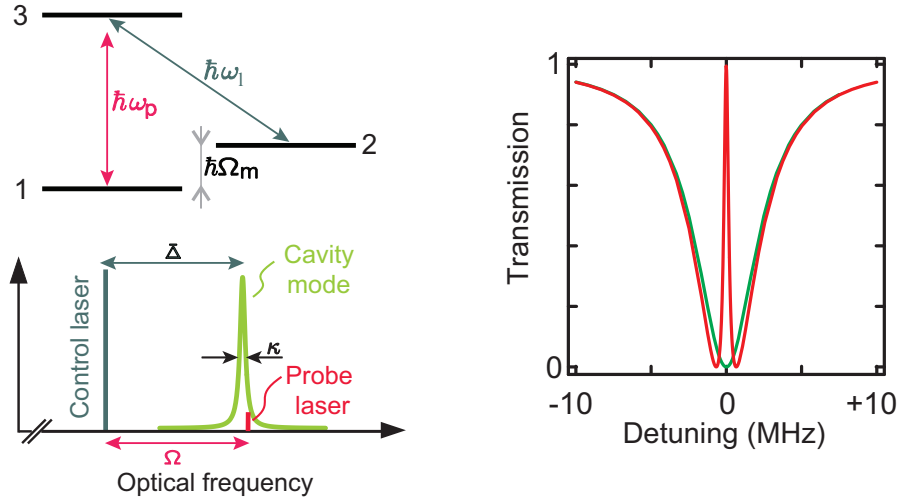


Figure 2.53: Optomechanically induced transparency. Left: A coupling laser of frequency  $\omega_1$  drives red sideband transitions between (sets of) levels 2 and 3, which differ both in the number of optical and mechanical excitation quanta (each time a phonon is added to the coupling field, a phonon in the mechanical degree of freedom is removed). A probing laser tuned close to the  $1 \rightarrow 3$  transition of the unperturbed systems actually interacts with a superposition of levels 2 and 3, leading to the opening of a transmission window in the case of an optomechanical system. Right panel shows the resulting power transmission of the probe laser through a taper-toroid system for  $\bar{\Delta} = -\Omega_m$  versus the detuning  $(\Omega - \Omega_m)/2\pi$  of the probe laser. Numerical parameters are typical for silica microtoroids, with  $\Omega_m/2\pi = 40$  MHz,  $\Gamma_m/2\pi = 1.3$  kHz,  $\kappa/2\pi = 5$  MHz,  $R =$ ,  $m_{\text{eff}} = 10$  ng,  $R = 40$   $\mu\text{m}$  and  $\bar{s}_{\text{in}}^2 \hbar\omega_1 = 300$   $\mu\text{W}$  (red line) or  $\bar{s}_{\text{in}}^2 \hbar\omega_1 = 0$   $\mu\text{W}$  (green line).

probes “carrier” transitions  $1 \leftrightarrow 2$ , in which originally no phonons are added or removed. Due to the strong optomechanical coupling induced by the coupling field, it effectively interacts with a hybrid optomechanical resonance. Similar to EIT, this hybridization opens up a *tunable* transmission window for the probing laser at the center of the optical resonance. We therefore refer to this effect as “optomechanically induced transparency”.

A simple model for this scheme can be set up directly from the Langevin equation (2.50). Neglecting thermal and quantum noise for an elementary analysis, one obtains for the (power) transmission of the probing laser

$$T_p = \left| 1 - \frac{1 + if(\Omega)}{-i(\bar{\Delta} + \Omega) + \kappa/2 + 2\bar{\Delta}f(\Omega)} \eta_c \kappa \right|^2 \quad (2.187)$$

with

$$f(\Omega) = \hbar g_0^2 \bar{a}^2 \frac{\chi(\Omega)}{i(\bar{\Delta} - \Omega) + \kappa/2}. \quad (2.188)$$

At a basic level, this effect can be understood from the fact that for  $\omega_p - \omega_1 = \Omega \approx \Omega_m$ , the beat of coupling and probing laser drives the mechanical oscillator. The anti-Stokes field generated, in turn, from the coupling field interferes with the incoming probing light.

The formal analogy with atomic EIT is even more obvious in the limiting case of: (i) a high- $Q$  oscillator  $\Omega_m \gg \Gamma_m$  (ii) the resolved-sideband regime  $\Omega_m \gg \kappa$  and (iii) the detuning  $\bar{\Delta} = -\Omega_m$ . Using the abbreviation  $\Delta' \equiv \Omega - \Omega_m$  one can then simplify the equation system to

$$(-i\Delta' + \kappa/2) \delta\hat{a}(\Omega) = +ig_0\bar{a}\delta\hat{x}(\Omega) + \sqrt{\eta_c\kappa} \delta\hat{s}_{\text{in}}(\Omega) \quad (2.189)$$

$$(-i\Delta' + \Gamma_m)\delta\hat{x}(\Omega) = i\frac{\hbar g_0\bar{a}}{m_{\text{eff}}\Omega_m}\delta\hat{a}(\Omega) \quad (2.190)$$

directly analogous to the EIT case [269], with the well-known solution

$$\delta\hat{a}(\Omega) = \frac{\eta_c\kappa}{(-i\Delta' + \kappa/2) + \frac{2\bar{a}^2 g_0^2 x_{\text{ZPF}}^2}{i\Delta' + \Gamma_m}}. \quad (2.191)$$

Mechanical and optical oscillator play the role of two dipole transitions, where a pump laser couples two of the involved three levels. As in EIT, the modification of the transmission for the probe laser may be used for tuning optical group velocities to generate slow or fast light [269–271], or, in designs hosting large arrays of optomechanical systems, even storage of light in mechanical states [272–274] may be envisioned.

## 2. Cavity optomechanics

---

## Chapter 3

# Generation of frequency combs in silica microresonators\*

### 3.1 Introduction

Optical frequency combs [275–277] provide equidistant frequency markers across wide spectral regions of electromagnetic radiation from the infrared to the extreme ultraviolet [278, 279]. T. W. Hänsch and coworkers have realized in their early work on mode-locked lasers that the periodic pulse train emitted by these devices intrinsically constitutes an optical frequency comb in the spectral domain, which can be used to measure unknown optical frequencies [280, 281]. Such an optical frequency comb is characterized by only two degrees of freedom, its mode spacing  $f_r$  and the carrier-envelope-offset frequency  $f_{\text{ceo}}$  [282]. The mode spacing  $f_r$  is directly given by the pulse repetition rate, whereas  $f_{\text{ceo}}$  determines the frequency offset of the comb teeth from integer multiples of the repetition rate. In time domain,  $f_{\text{ceo}}$  describes the phase slippage rate of the pulse envelope with respect to the carrier. The frequency of any comb line in the spectrum of a frequency comb can therefore be written as

$$f_m = f_{\text{ceo}} + m f_r, \quad (3.1)$$

where  $m$  is an integer.

As a consequence, the frequency of every comb tooth is uniquely determined by the experimentally controlled quantities  $f_{\text{ceo}}$  and  $f_r$ . Any arbitrary optical frequency within the spectrum of the comb may therefore be synthesized. And, vice versa, any given optical frequency within this spectrum can be phase coherently compared to the (typically radio-frequency) entities  $f_{\text{ceo}}$  and  $f_r$ , which can in turn be referenced to today's microwave time

---

\*The material presented in this chapter has also been published in reference [13], and is reproduced here with permission from Taylor&Francis.

### 3. Generation of frequency combs in silica microresonators

---

the development and practical use of time standards in the optical domain if used as a clockwork mechanism, transducing the  $\sim 10^{14}$  Hz-fast pace of an optical primary oscillator to countable radio frequencies [276, 277, 285, 286]. Very recently, novel applications of frequency combs have also been developed in the domain of broadband, ultra-sensitive absorption spectroscopy as employed, for example, for trace gas sensing [287–290].

The first attempts to compare the frequencies of radio-frequency (RF) and optical electromagnetic radiation were based on many stages of auxiliary oscillators, whose frequency was multiplied using nonlinear radiation mixers. Both at the National Bureau of Standards (NBS, now National Institute of Standard and Technology, NIST) in Boulder, USA, and at the Physikalisch-Technische Bundesanstalt (PTB) in Braunschweig, Germany, links between a Cs atomic clock reference and oscillators at optical frequencies were established in this manner [291]. For the somewhat simpler task of phase-coherently linking two optical frequencies, researchers at the Max Planck Institute of Quantum Optics (MPQ) in Garching, Germany, had used another approach: An optical frequency interval divider chain was implemented using compact semiconductor lasers, bisecting the frequency gap in several steps until a direct microwave signal could be measured [292]. For the same purpose, Kouroggi, in 1993, had already demonstrated [293] that narrow optical frequency combs can be generated by inserting a phase modulator inside a cavity, into which resonant continuous wave laser radiation is injected. This led to the generation of a cascade of optical sidebands spaced by the driving frequency of the phase modulator. Limited by the dispersion of the cavity and phase modulator, combs generated in this way could span several THz. This approach was refined in later research at the Joint Institute for Laboratory Astrophysics (JILA) [294, 295].

Frequency combs derived from mode-locked lasers have dramatically simplified all of these tasks [282, 296]. For their practical use, however, it is essential to measure and control both  $f_r$  and  $f_{ceo}$ . The pulse repetition rate  $f_r$  can be measured by simply detecting the laser’s power with a fast photodetector, the signal of which is directly modulated at  $f_r$  and its harmonics. Control of  $f_r$  is possible by actuating the effective round-trip length of the light pulse in the laser cavity. Measuring and locking the carrier-envelope offset frequency  $f_{ceo}$  is more challenging. A powerful technique devised for that purpose is a non-linear interferometer (“ $f - 2f$ ” interferometer) comparing the frequency of one comb component with another comb component close to twice the optical frequency of the first. Such a measurement, however, requires an optical spectrum that spans a full octave. Only with the advent of photonic crystal fibers which exhibited a zero dispersion wavelength in the 800 nm-range, it became possible to broaden the output spectrum of a Ti:Sapphire laser system to a full octave and thereby measure (and stabilize) the carrier envelope offset frequency [283, 284, 286].

## 3.2 Physics of the comb generation process

An entirely novel comb generator based on the silica WGM cavities described in chapter 1 was reported at the Max Planck Institute of Quantum Optics in 2007. This has allowed a dramatic reduction in size and enabled access to ultra-high repetition rates, exceeding 40 GHz, while normal mode-locked lasers typically only offer rates below 1 GHz. The approach is based on the  $\chi^{(3)}$  nonlinearity of the device's host material, giving rise to parametric frequency conversion<sup>1</sup>. The cavities' high optical finesse and small mode volume make them uniquely suited for optical frequency conversion [298] due to the significantly reduced threshold power for nonlinear optical processes.

Figure 3.1 illustrates the comb generation process. A high-Q ( $Q \sim 10^8$ ) WGM resonance of a 75  $\mu\text{m}$ -diameter toroidal microcavity is pumped with a monochromatic laser in the 1550 nm-range at a power of about 60 mW. Such a power corresponds to an intracavity intensity of more than 1 GW/cm<sup>2</sup>, and thus far exceeds the threshold for parametric oscillations [75]. In this case, a comb-like spectrum consisting of several bright emission lines spaced by about 7 nm (cf. figure 3.1) is measured using an optical spectrum analyzer. This spacing corresponds approximately to the cavity FSR

$$\nu_{\text{FSR}} = \frac{c}{2\pi R n_{\text{eff}}}, \quad (3.2)$$

with the cavity radius  $R$  and  $n_{\text{eff}}$  the effective refractive index. The observed process is very efficient, generating strong (typically  $> 1$  mW or 0 dBm) sidebands spanning several hundreds of nanometers of spectral width.

The underlying physical mechanism is a cavity-enhanced cascaded four-wave mixing (FWM) process. It is mediated by the intensity-dependent refractive index of silica as introduced in subsection 1.5.3. At low pump powers this process gives rise to a single pair of signal and idler sidebands at frequencies  $\nu_S$  and  $\nu_I$ , respectively. In a quantum picture, this corresponds to the conversion of two pump photons into a pair of signal and idler photons, and energy conservation requires  $\nu_S + \nu_I = \nu_{\text{pump}} + \nu_{\text{pump}}$ . If idler, signal and pump frequencies all coincide with optical modes of the microresonator, this mechanism is resonantly enhanced by the cavity. This effect was observed both in silica microtoroidal resonators [75] and crystalline CaF<sub>2</sub> WGM resonators [299] at very low thresholds (tens of  $\mu\text{W}$ ). We have also been able to generate frequency combs from the crystalline resonators introduced in section 2.9.

At higher powers, the generation of sidebands can cascade via non-degenerate four-wave mixing among pump and first-order sidebands. This gives rise to higher order sidebands, as shown in figure 3.1. Energy conservation (for example,  $\nu_{\text{pump}} + \nu_I = \nu_{II} + \nu_S$ ) again ensures that the difference of pump and first-order sidebands  $|\nu_{\text{pump}} - \nu_I| = |\nu_S - \nu_{\text{pump}}|$  is exactly transferred

---

<sup>1</sup>This process has also been referred to as *hyperparametric* frequency conversion [297].

### 3. Generation of frequency combs in silica microresonators

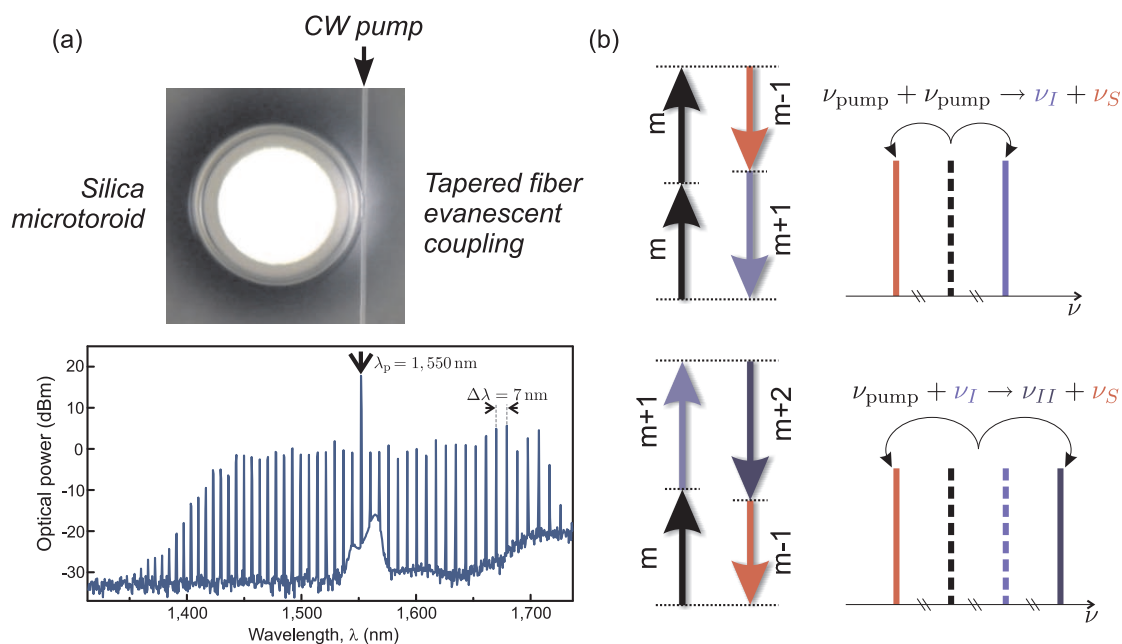


Figure 3.1: Frequency comb generation in an optical microresonator. (a) Optical micrograph of a silica toroid employed for frequency comb generation, and a spectrum measured at the output of the tapered optical fiber. The individual modes are approximately spaced by the FSR (7 nm) of the cavity. Below the pump line at 1550 nm, amplified spontaneous emission due to the employed erbium-doped fiber amplifier is also observed. (b) Principle of the comb generation process, involving both degenerate (top panel) and non-degenerate four-wave mixing (bottom panel) processes.

to all higher-order inter-sideband spacings. If the cavity exhibits a sufficiently equidistant mode spacing, the frequencies of higher-order sidebands remain resonant with the corresponding WGMs. The cavity then resonantly enhances successive four-wave mixing to higher orders, leading to the generation of phase-coherent sidebands with equal spacing over a large spectral range—an optical frequency comb. However, dispersion due to the cavity geometry or material may render the cavity resonances non-equidistant (cf. figure 3.2). If the resulting walk-off of the cavity modes from the oscillating sidebands therefore exceeds the WGMs' linewidth, the broadening of the comb ceases [299].

Dispersion in a microcavity arises from both its geometry and the intrinsic dispersion of the resonator's material. Advantageously, these two contributions can cancel if they are of similar magnitude but opposite sign. This is indeed the case for silica WGM cavities in the 1550-nm spectral window. Measurements have verified that the WGM of a cold cavity deviate by only around 20 MHz from equidistance over a 100-nm span. This deviation is still comparable to the width of slightly overcoupled WGM resonances as typically used in this work. Furthermore, non-linear mode pulling (self- and cross-modulation) can contribute to compensate residual dispersion [75].

### 3.3 Verification of the comb components' equidistance

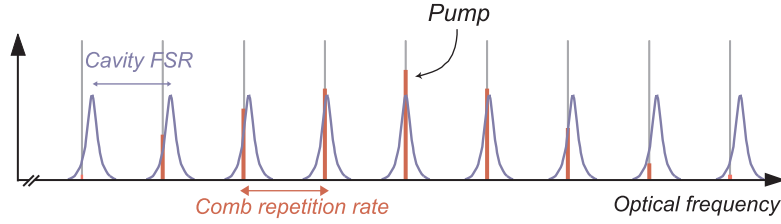


Figure 3.2: The role of dispersion in optical frequency comb generation. Cavity dispersion renders the free spectral range (FSR) dependent on the optical frequency. As a consequence, the cavity resonances (blue Lorentzians), are not equidistant in frequency space, while the generated optical sidebands are. If the walk-off exceeds the WGMs' linewidth, the cavity enhancement of the four-wave mixing process is reduced. Therefore, uncompensated cavity dispersion can eventually limit the comb bandwidth.

### 3.3 Verification of the comb components' equidistance

Importantly, the FWM process could in principle produce pairs of signal/idler sidebands which are only pair-wise equidistant but not mutually equidistant as required for a comb. Therefore, it is necessary to verify the equidistance of the lines in the generated spectrum. This can be accomplished by comparison with another comb. At present, the most accurate references for optical frequency differences are provided by optical frequency combs derived from mode-locked femtosecond lasers [276, 277, 300]. In the following, we describe two experiments in which the mode spacing of a microcavity frequency comb is compared against such a femtosecond laser frequency comb to verify the equidistance of the mode spacing [3].

Multiheterodyne spectroscopy [288] is a particularly convenient measurement scheme for this purpose. For this technique, two light beams both containing a large number of optical fields oscillating at discrete frequencies (such as two frequency combs) are brought to interference on a beam splitter, giving rise to power modulation (a *beat*) of the output beams at the various difference frequencies of the incident modes. A single detector can record all beats within its detection bandwidth simultaneously, and the beats can be analyzed in the Fourier domain. If the two input fields are equidistant frequency combs, the frequencies of the resulting beats are expected to be equally equidistant, and the measured signal constitutes a “frequency comb” in the RF domain. However, any deviation from equidistance—of either input—is also directly apparent in this signal.

In our experiment (figure 3.3), we have used an erbium-fiber-based mode-locked femtosecond laser [301] as a reference frequency comb. It emits a spectrum containing modes at the frequencies  $f_{\text{ceo}} + n f_r$ , with  $f_r \sim 100$  MHz and  $n \sim 2 \times 10^6$ . If the spectrum emitted by a strongly pumped microcavity constitutes a frequency comb, it can be written as  $\nu_0 + j \Delta\nu$  ( $j$  integer). In order to measure the beat notes, the repetition rate of the reference comb has to be adjusted properly such that a multiple of it is close to the microcavity comb mode spacing,  $j_0 f_r \approx \Delta\nu$  with an integer  $j_0$ . If the microcavity comb

### 3. Generation of frequency combs in silica microresonators

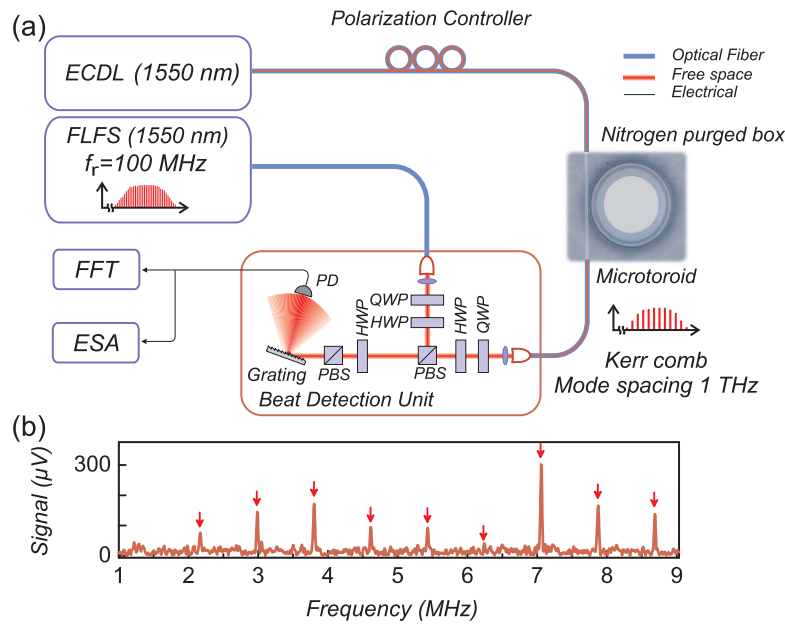


Figure 3.3: Verification of comb equidistance using the multiheterodyne technique (a) Experimental setup. The comb spectrum from the microresonator is combined with reference light from a fiber-laser frequency comb (FLFC) using a beat detection unit. ECDL, external cavity diode laser; FLFS, femtosecond laser frequency comb; PBS, polarizing beam splitter; HWP, half-wave retarder plate; QWP, quarter-wave retarder plate; PD, photodiode; FFT, fast-Fourier transform analyzer; ESA, electronic spectrum analyzer. Details are given in the text. (b) RF spectrum of the beats induced by nine simultaneously oscillating microcavity modes beating against reference comb modes. Adapted from ref. [3].

is equidistant, the generated RF beat notes should also be equidistant, their frequencies being given by  $f_0 + k \Delta f$  with  $\Delta f = (\Delta\nu \bmod f_r)$  and  $k$  integer.

To generate the sideband cascade in the cavity, a 1550-nm external cavity diode laser (ECDL) is coupled to a high-Q WGM of the microresonator using a fiber taper (section 1.4), and the resulting frequency comb is coupled back into the same tapered fiber. This output is split into several branches (not shown in figure 3.3), and its total power, and optical spectrum are continuously monitored. Another part of the output is fed into a *beat detection unit* (BDU). In this optical setup, light from the microcavity comb and the reference comb are first merged into the same spatial, but orthogonal polarization modes using a polarizing beam splitter. A subsequent  $\lambda/2$ -retarder plate and a second PBS enforce interference between the two input beams with an adjustable power ratio of the input beams. After selecting a spectral region of interest using a grating, the beam is sent to a  $\sim 125$  MHz-bandwidth InGaAs-photoreceiver (Menlo Systems). The amplified photocurrent signal is analyzed using a fast Fourier transform (FFT) or electronic spectrum analyzer. As discussed above, by adjusting the repetition rate  $f_r$  of the reference comb, the spacing  $\Delta f$  of the resulting beats can be easily tuned to values as low as  $\sim 1$  MHz, so that all beat frequencies  $f_0 + k \Delta f$  of interest fall in the

### 3.3 Verification of the comb components' equidistance

---

window between DC and  $f_r/2$ .

In such a measurement, no deviation from equidistance of nine microcavity comb lines spanning 50 nm (6.5 THz) can be found at the level of 5 kHz, limited by the acquisition time of the FFT analyzer (figure 3.3). This corresponds to a relative deviation below  $10^{-9}$ , or  $10^{-11}$  when referenced to the optical carrier. Note that higher resolutions and signal-to-noise ratios (SNRs) would in principle be possible with this method by simply extending the measurement time. However, mutual fluctuations of the two free-running combs preclude such improvements in practice.

To achieve higher measurement resolution, these fluctuations have to be reduced. This can be accomplished by locking the ECDL generating the microcavity comb to the reference comb using an offset lock. For this purpose, a beat note between the ECDL and the closest reference comb mode is detected in an auxiliary BDU. The phase of this RF beat is compared to a stable RF signal at the *offset frequency*  $f_0$ , which is obtained from a synthesizer referenced to the MPQ in-house maser. The two RF signals are held in phase by feeding back a correction signal on the frequency of the ECDL. On times scales longer than the feedback loop's response time, the frequency of the pump laser is locked to the closest reference comb mode with an offset of  $f_0$ . To improve the measurement stability further, the repetition rate of the reference comb is locked to around 100 MHz using standard techniques.

Much longer measurement runs, up to several hundreds of seconds have been possible using these techniques without degradation of the beat signals due to mutual fluctuations. Precise measurement of the beat's radio frequencies on such time scales is most conveniently accomplished using RF counters. Reliable counting requires a good SNR. Therefore each beat to be counted was measured in a dedicated BDU, which could be individually optimized. The achieved SNR exceeding 30 dB in a 500-kHz bandwidth proved sufficient, in spite of still lacking about 26 dB to the shot-noise limit [302] of  $\text{SNR} \simeq \eta P_{\text{rcm}}/h\nu \text{RBW}$ , for a detection efficiency  $\eta \sim 0.5$ , power of the reference comb mode beating with the microcavity Kerr comb mode  $P_{\text{rcm}} \simeq 50 \text{ nW}$ , optical frequency  $\nu \simeq 200 \text{ THz}$  and detection bandwidth  $\text{RBW} = 500 \text{ kHz}$ .

At least three modes have to be measured simultaneously to verify the equidistance of the microcavity comb (figure 3.4) [3]. The pump laser can be considered as the first comb component; its offset to the closest reference comb line is locked to  $f_0$ . In two additional BDUs, two further microcavity comb components are measured against the closest reference comb modes. The counted beat frequencies  $f_1$  and  $f_2$ , in this experiment, correspond to microcavity comb lines at five and seven FSRs from the pump laser. To quantify the maximum deviation from a perfectly equidistant mode spacing consistent with the measured beat frequencies we can calculate the entity  $\varepsilon = (f_2 - f_1)/(7 - 5) - (f_1 - f_0)/5$ , which should be zero for a perfectly equidistant comb. To rule out technical artifacts, all counters were also

### 3. Generation of frequency combs in silica microresonators

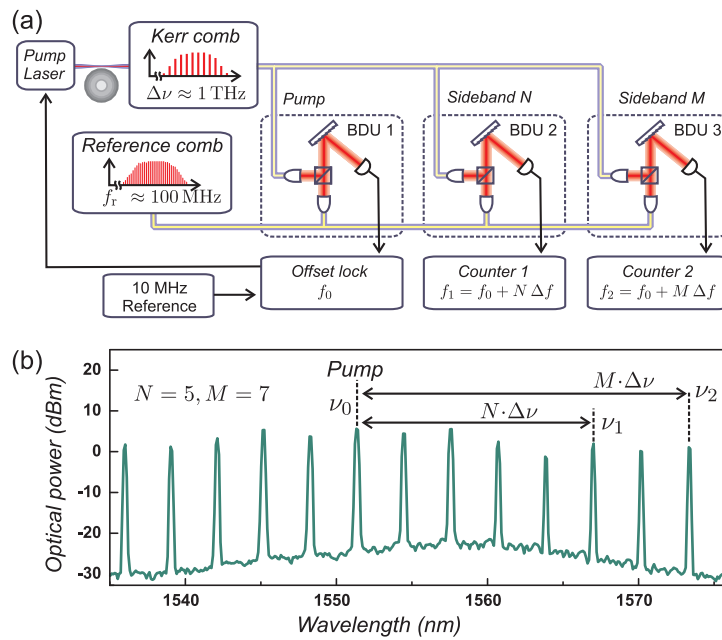


Figure 3.4: Verification of comb equidistance by counting three individual beats. (a) Schematic of the setup, in which three independent BDUs are used. BDU1 is used for the offset lock of the pump laser. BDU2 and BDU3 allow counting the beats of the 5<sup>th</sup> and 7<sup>th</sup> sideband of the pump laser against reference comb modes. (b) Optical spectrum of the microcavity comb measured in this experiment. Adapted from ref. [3].

referenced to the hydrogen maser and triggered by a common trigger signal.

In an alternative configuration of the RF electronics, even slightly more accurate measurements could be made: Mixing the outputs of BDU2 and BDU3 with the offset frequency  $f_0$ , the frequencies  $f_1 - f_0$  and  $f_2 - f_0$  can be obtained from analog RF mixers. By directly counting the frequency ratio  $r = (f_2 - f_0)/(f_1 - f_0)$ , the deviation  $\varepsilon$  can be simply derived from  $\varepsilon = (r - 7/5) \cdot (f_1 - f_0)$ , where  $f_1 - f_0$  provides only a scale factor and needs not to be known very accurately. The observed improvement of the measurement results can be attributed to the reduced effect of trigger latencies in the counters, possibly degrading the temporal overlap of the measurements.

Taking a large number of measurements in both the “two-counter” and “frequency ratio” configurations, the deviation  $\varepsilon$  can be measured extremely accurately. The results from a large data set in the two-counter-configuration are shown in figure 3.5. The results of individual measurements of  $\varepsilon$  were found to be normally distributed around a mean of  $(-0.91 \pm 5.5)$  mHz with a standard deviation of 322 mHz. Taking all recorded data sets into account, with a total measurement time of several hours, the mean deviation from equidistance could be bracketed to  $(-0.8 \pm 1.4)$  mHz [3]. This corresponds to a deviation of the comb component’s frequency of only  $7.3 \times 10^{-18}$  relative to the optical carrier, and  $5.2 \times 10^{-16}$  relative to the 2.1 THz span of the measured microcavity comb lines.

### 3.4 Dispersion in toroidal microresonators

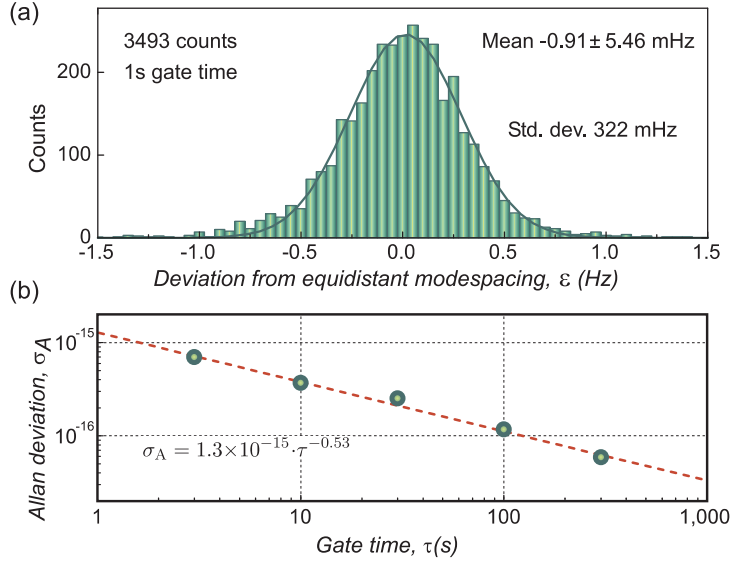


Figure 3.5: Deviation from equidistant mode spacing. (a) Statistics of the measurement results for  $\varepsilon$  measured in a 1-s gate time. A normal distribution is found. (b) Allan deviation for different gate times  $\tau$ , displaying an approximately inverse square-root dependence. Adapted from ref. [3].

### 3.4 Dispersion in toroidal microresonators

The resonant enhancement of four-wave mixing requires the microcavity frequency comb modes to coincide in frequency with the high-Q whispering-gallery modes of the microresonator. Therefore, the resonator's dispersion is of crucial importance to the generation of combs [75, 299, 303]. As already discussed in the previous section, both the geometry of the resonator and its material contribute to the total resonator dispersion.

To assess the contribution of resonator geometry to the variation of the FSR, it is possible to approximate the resonances of a toroid by those of a microsphere [39]. As discussed in section 1.2, the resonance frequency of the fundamental mode ( $\ell = |m|$ ) of a microsphere is approximately given by [47]

$$\nu_\ell = \frac{c}{2\pi nR} \left( \ell + 1/2 + \eta_1 \left( \frac{\ell + 1/2}{2} \right)^{1/3} + \dots \right), \quad (3.3)$$

where  $c$  is the vacuum speed of light,  $n$  the refractive index,  $R$  the cavity radius and  $-\eta_1$  the first zero of the Airy function ( $\eta_1 \approx 2.34$ ). As a consequence, the variation of the free spectral range

$$\Delta\nu_{\text{FSR}} = (\nu_{\ell+1} - \nu_\ell) - (\nu_\ell - \nu_{\ell-1}) \approx \frac{\partial^2 \nu_\ell}{\partial \ell^2} \quad (3.4)$$

is given by

$$\Delta\nu_{\text{FSR}} = -\frac{c}{2\pi nR} \cdot \frac{\eta_1}{18} \left( \frac{\ell + 1/2}{2} \right)^{-5/3} \approx -0.41 \frac{c}{2\pi nR} \ell^{-5/3} < 0. \quad (3.5)$$

### 3. Generation of frequency combs in silica microresonators

---

The FSR *reduces* with increasing frequency, which corresponds to a negative group velocity dispersion (GVD). If there was exclusively geometric dispersion, low frequency modes would exhibit a shorter round trip time than high frequency modes (i. e. dispersion is normal). In an intuitive picture, this can be understood as resulting from the fact that higher frequency modes are located closer to the cavity boundary, making the classical optical trajectory longer.

The refractive index of the silica constituting the resonator is a function of frequency, and therefore of the mode number  $\ell$ ,  $n \equiv n(\ell)$ . This leads to a second contribution to dispersion and a consequent variation of the FSR of

$$\Delta\nu_{\text{FSR}} \approx \frac{\partial^2}{\partial \ell^2} \left( \frac{c}{2\pi n(\ell)R} \cdot \ell \right) \approx \frac{c^2 \lambda^2}{4\pi^2 n^3 R^2} \cdot \text{GVD}, \quad (3.6)$$

where

$$\text{GVD} = -\frac{\lambda}{c} \frac{\partial^2 n}{\partial \lambda^2} \quad (3.7)$$

is the group velocity dispersion of the material.

The GVD of silica is well-known to change its sign in the 1300-nm wavelength region from about  $-100$  ps/(nm km) at 800 nm (normal dispersion) to  $+20$  ps/(nm km) at 1550 nm (anomalous dispersion). The positive GVD in this wavelength region can cancel the geometric dispersion of silica microresonators to some extent as shown in figure 3.6. Taking into account both geometric and material dispersion for microspheres of  $80 \mu\text{m}$  and  $160 \mu\text{m}$  radius, a zero dispersion point occurs close to the operating wavelength of 1550 nm [3]. We finally note that finite element modeling of the optical modes of silica microtoroids [36] suggests shorter resonance wavelengths for the same mode number  $\ell$ . As a consequence, the zero dispersion points is expected to shift to shorter wavelengths in toroids as compared to spheres [304]. We anticipate that accurate, fast and reliable assessment and eventually engineering of resonator dispersion will be a key ingredient to future research pursuing the generation of ultra-broad optical frequency combs from monolithic microresonators.

### 3.5 Conclusion

In this chapter, we have introduced a novel approach to the generation of optical frequency combs. It is based on four-wave-mixing in optical microcavities pumped only by a strong continuous-wave laser. Such a comb generator is unique in several ways. Its compact size and reduced complexity bodes well for full integration of the generator into a micro-photonic platform, potentially including even the driving laser. Furthermore, as the approach does not rely on the use of atomic or molecular resonances, the generation process can be efficient over a wide frequency window, limited, in principle, only by material absorption or dispersion. Owing to the large transparency

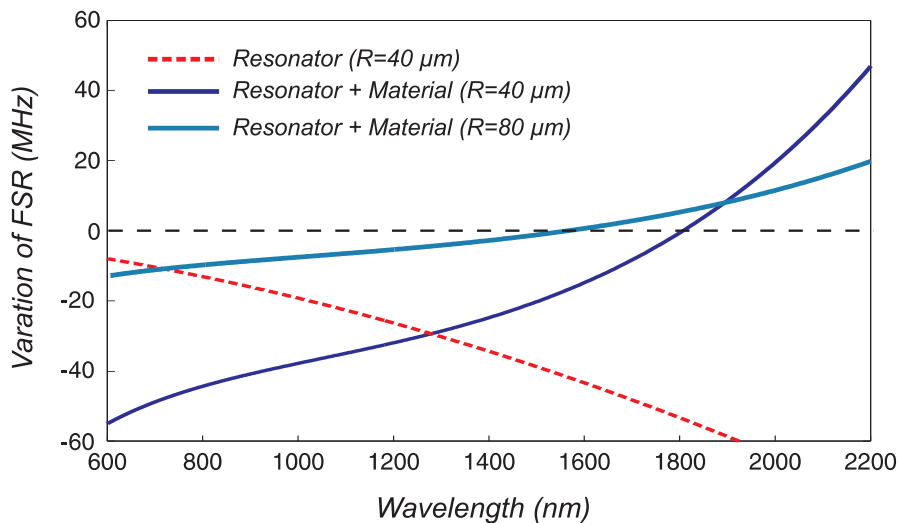


Figure 3.6: Variation of the FSR of microsphere resonators of radii  $40 \mu\text{m}$  and  $80 \mu\text{m}$ , due to geometric dispersion only (red curve) and taking both geometric and material dispersion into account (blue curves). A zero-dispersion point occurs close to  $1550 \text{ nm}$ .

window of glass, frequency comb generation may be possible from the UV into the intermediate infrared beyond  $2 \mu\text{m}$ , and wider windows may even be available in crystalline WGM resonators. Very importantly, monolithic microresonators enable the generation of frequency combs with ultra-high mode spacing. Conventional femtosecond laser frequency combs are approaching  $10 \text{ GHz}$  repetition rates, but the corresponding cavity length of  $3 \text{ cm}$  is difficult to reduce further. Fiber-based mode-locked lasers generally operate at even lower repetition rates. With the approach introduced here, very large mode spacings in the range of  $50 \text{ GHz}$  up to  $1 \text{ THz}$  are accessible. This may be crucial for applications in which the access to individual comb modes is required, such as optical waveform synthesis, spectrometer calibration, direct comb spectroscopy, or high capacity telecommunications.

### **3. Generation of frequency combs in silica microresonators**

# Appendix A

## Constants, symbols and relations

### A.1 Silica material constants

|                                      |   |
|--------------------------------------|---|
| Refractive index (780 nm) [69]       | $n=1.45$                                    |
| Intensity dependent refractive index | $n_2=3 \cdot 10^{-20} \text{ m}^2/\text{W}$ |
| Thermorefractive coefficient [69]    | $dn/dT=10 \cdot 10^{-6} \text{ K}^{-1}$     |
| Thermal expansion [69]               | $\alpha=0.55 \cdot 10^{-6} \text{ K}^{-1}$  |
| Density [69]                         | $\rho=2203 \text{ kg/m}^3$                  |
| Thermal conductivity [69]            | $k=1.4 \text{ W/K m}$                       |
| Specific heat [69]                   | $c_p=750 \text{ J/K kg}$                    |
| Young's modulus                      | $E=73.1 \text{ GPa}$                        |
| Poisson ratio [69]                   | $\sigma=0.17$                               |
| Longitudinal sound velocity          | $v_0=5970 \text{ m/s}$                      |
| Transverse sound velocity            | $v_1 = v_2=3770 \text{ m/s}$                |
| Lamé factor                          | $\lambda=16.1 \text{ GPa}$                  |
| Lamé factor                          | $\mu=31.2 \text{ GPa}$                      |

## A. Constants, symbols and relations

---

### A.2 Table of symbols

| symbol                              | meaning   | unit                    | definition |
|-------------------------------------|---|-------------------------|------------|
| $\omega_l$                          | laser frequency   | rad/s                   |            |
| $\omega_c$                          | cavity resonance frequency  | rad/s                   |            |
| $\Delta$                            | detuning  | rad/s                   |            |
| $Q$                                 | optical quality factor  | 1                       | (1.13)     |
| $Q_0$                               | intrinsic optical quality factor                                    | 1                       | (1.16)     |
| $\kappa$                            | optical linewidth (FWHM)  | rad/s                   | (1.12)     |
| $\mathcal{F}$                       | optical finesse   | 1                       | (1.31)     |
| $\eta_c$                            | coupling parameter  | 1                       | (1.32)     |
| $\bar{a}$                           | mean intracavity mode amplitude                                     | $\sqrt{1} (\sqrt{J})$   |            |
| $\bar{s}_{\text{in}}$               | mean drive amplitude  | $\sqrt{1/s} (\sqrt{W})$ |            |
| $x_n(t)$                            | optically measured displacement of mode $n$                         | m                       | (2.97)     |
| $g_0$                               | optomechanical coupling   | rad/s/m                 | (2.1)      |
| $G$                                 | optomechanical coupling rate  | rad/s                   | (2.165)    |
| $\Omega_m$                          | mechanical resonance frequency                                      | rad/s                   |            |
| $\Gamma_m$                          | mechanical damping rate   | rad/s                   |            |
| $Q_m$                               | mechanical quality factor   | 1                       | (2.78)     |
| $x_{\text{ZPF}}$                    | zero-point fluctuations   | m                       | (2.160)    |
| $m_{\text{eff}}$                    | effective mass  | kg                      | (2.99)     |
| $M_n$                               | moving mass   | kg                      | (2.96)     |
| $\bar{\Delta}$                      | equilibrium detuning  | rad/s                   | (2.17)     |
| $\vec{u}$                           | displacement  | m                       |            |
| $\chi(\Omega)$                      | mechanical susceptibility   | m/N                     | (2.125)    |
| $\chi_{\text{eff}}(\Omega)$         | effective mechanical susceptibility induced by dynamical backaction | m/N                     | (2.28)     |
| $F_{\text{rp}}$                     | radiation pressure force  | N                       | (2.39)     |
| $\bar{S}_{XX}(\Omega)$              | symmetrized noise spectrum of quantity $X$                          | $[X^2]/\text{Hz}$       |            |
| $\bar{S}_{xx}^{\text{im}}(\Omega)$  | apparent position noise (imprecision)                               | $\text{m}^2/\text{Hz}$  |            |
| $\bar{S}_{FF}^{\text{ba}}(\Omega)$  | backaction force noise  | $\text{N}^2/\text{Hz}$  |            |
| $\bar{S}_{FF}^{\text{the}}(\Omega)$ | thermal (Langevin) force noise                                      | $\text{N}^2/\text{Hz}$  | (2.137)    |
| $T$                                 | sample temperature  | K                       |            |
| $T_m$                               | mode temperature  | K                       | (2.144)    |

### A.3 Frequently used relations

$$\kappa = \tau_0^{-1} + \tau_{\text{ex}}^{-1}, \quad \eta_c = \frac{\tau_0}{\tau_0 + \tau_{\text{ex}}}, \quad \tau_{\text{ex}}^{-1} = \eta_c \kappa, \quad \tau_0^{-1} = (1 - \eta_c) \kappa$$

$$\Delta = \omega_l - \omega_c$$

$$\mathcal{F} = \frac{c}{nR\kappa}$$

$$x_{\text{ZPF}} = \sqrt{\frac{\hbar}{2m_{\text{eff}}\Omega_m}}$$

$$\bar{S}_{xx}(\Omega_m) \approx \frac{\hbar}{m_{\text{eff}}\Gamma_m\Omega_m} \cdot 2\langle n \rangle$$

$$\bar{S}_{FF}^{\text{th},n}(\Omega) = \hbar m_{\text{eff}} \Gamma_m \Omega \coth\left(\frac{\hbar\Omega}{2k_B T}\right) \approx 2m_{\text{eff}} \Gamma_m k_B T$$

Fourier transform of the entity  $X$

$$X(\Omega) = \int_{-\infty}^{+\infty} X(t) e^{+i\Omega t} dt$$

spectral resolution of fluctuations

$$S_{XX}(\Omega) = 2\pi\delta(\Omega + \Omega') \langle X(\Omega)X(\Omega') \rangle$$

$$\bar{S}_{XX}(\Omega) = \frac{1}{2} (S_{XX}(+\Omega) + S_{XX}(-\Omega))$$

## A. Constants, symbols and relations

---

## Appendix B

# Calculations

### B.1 Integrating displacement spectra

It is frequently required to integrate a mechanical displacement noise spectrum of Lorentzian shape in order to obtain the rms-displacement fluctuations or the energy of the mode. As shown below, this can be accomplished in a straightforward manner using the residue theorem. We assume in

$$\langle \delta x^2 \rangle = \int_{-\infty}^{+\infty} \bar{S}_{xx}(\Omega) \frac{d\Omega}{2\pi} = \int_{-\infty}^{+\infty} |\chi(\Omega)|^2 \bar{S}_{FF}(\Omega) \frac{d\Omega}{2\pi} \quad (\text{B.1})$$

that  $\bar{S}_{FF}(\Omega)$  is sufficiently flat in the narrow frequency range where  $|\chi(\Omega)|^2$  is significant, and write

$$\langle \delta x^2 \rangle \approx \frac{\bar{S}_{FF}(\Omega_m)}{m_{\text{eff}}^2} \int_{-\infty}^{+\infty} \frac{1}{(\Omega_m^2 - \Omega^2)^2 + \Gamma_m^2 \Omega^2} \frac{d\Omega}{2\pi}. \quad (\text{B.2})$$

In order to apply the residue theorem, we replace the real integration variable  $\Omega$  by the complex number  $z$  and call  $a(z) = 1$  and  $b(z) = (\Omega_m^2 - z^2)^2 + \Gamma_m^2 z^2$ . The integrand  $f(z) = a(z)/b(z)$  is analytical in the entire upper half  $z$ -plane and converges gleichmaessig to 0 in the upper half plane including the real axis for  $|z| \rightarrow \infty$ . Thus the integral along the half circle in the upper half plane vanishes (Jordan's lemma) and the integral along the real axis can be calculated from the residues of the singularities in the upper half plane at

$$z_1 = \frac{1}{2} \left( +\sqrt{4\Omega_m^2 - \Gamma_m^2} + i\Gamma_m \right) \quad (\text{B.3})$$

$$z_2 = \frac{1}{2} \left( -\sqrt{4\Omega_m^2 - \Gamma_m^2} + i\Gamma_m \right) \quad (\text{B.4})$$

The residues can be calculated according to

$$\text{Res} \left[ \frac{a(z)}{b(z)} \right]_{z=z_k} = \frac{a(z_k)}{b'(z_k)} = \frac{1}{i\Gamma_m(4\Omega_m^2 - \Gamma_m^2) \mp \Gamma_m^2 \sqrt{4\Omega_m^2 - \Gamma_m^2}} \quad (\text{B.5})$$

## B. Calculations

---

and

$$\begin{aligned} 2\pi i \sum_{k=1,2} \operatorname{Res} \left[ \frac{a(z)}{b(z)} \right]_{z=z_k} &= 2\pi i \frac{2i\Gamma_m(4\Omega_m^2 - \Gamma_m^2)}{-\Gamma_m^2(4\Omega_m^2 - \Gamma_m^2)^2 - \Gamma_m^4(\Omega_m^2 - \Gamma_m^2)} = \\ &= \frac{\pi}{\Omega_m^2 \Gamma_m} \end{aligned} \quad (\text{B.6})$$

so that

$$\langle \delta x^2 \rangle \approx \frac{\bar{S}_{FF}(\Omega_m)}{2m_{\text{eff}}^2 \Omega_m^2 \Gamma_m}. \quad (\text{B.7})$$

For the thermal noise Langevin force

$$\bar{S}_{FF}^{\text{the}}(\Omega) = \hbar m_{\text{eff}} \Gamma_m \Omega \coth \left( \frac{\hbar \Omega}{2k_B T} \right) \approx 2k_B T m_{\text{eff}} \Gamma_m \quad (\text{B.8})$$

one gets

$$\langle \delta x^2 \rangle = \frac{k_B T}{m_{\text{eff}} \Omega_m^2} \quad (\text{B.9})$$

as expected. Similarly, to spectrally integrate momentum fluctuations (to calculate the kinetic energy) the integral

$$m_{\text{eff}}^2 \langle \delta \dot{x} \rangle^2 \approx \bar{S}_{FF}(\Omega_m) \int_{-\infty}^{+\infty} \frac{\Omega^2}{(\Omega_m^2 - \Omega^2)^2 + \Gamma^2 \Omega^2} \frac{d\Omega}{2\pi}, \quad (\text{B.10})$$

with  $a(z) = z^2$  and  $b(z) = (\Omega_m^2 - z^2)^2 + \Gamma_m^2 z^2$  now yields the residues (the singularities are the same)

$$\operatorname{Res} \left[ \frac{a(z)}{b(z)} \right]_{z=z_k} = \frac{a(z_k)}{b'(z_k)} = \frac{1}{4i\Gamma_m} \mp \frac{i\Gamma_m}{\sqrt{-4\Omega_m^2 + \Gamma_m^2}} \quad (\text{B.11})$$

so that with  $2\pi i \sum_k \operatorname{Res}[z_k] = \pi/\Gamma_m$

$$m_{\text{eff}}^2 \langle \delta \dot{x} \rangle^2 \approx \frac{\bar{S}_{FF}(\Omega_m)}{2\Gamma_m} \quad (\text{B.12})$$

and

$$m_{\text{eff}}^2 \langle \delta \dot{x} \rangle^2 \approx k_B T m_{\text{eff}} \quad (\text{B.13})$$

for the thermal Langevin force.

## B.2 Noise transfer of a lossy cavity

In the following we calculate the transduction of noise in the input quadratures to noise in the output quadratures induced by an optical cavity. Starting from the standard linearized quantum Langevin equations

$$(-i(\bar{\Delta} + \Omega) + \kappa/2) \delta \hat{a}[\Omega] = \sqrt{\eta_c \kappa} \delta \hat{s}_{\text{in}}[\Omega] + \sqrt{(1 - \eta_c) \kappa} \delta \hat{s}_{\text{vac}}[\Omega] \quad (\text{B.14})$$

$$(+i(\bar{\Delta} - \Omega) + \kappa/2) \delta \hat{a}^\dagger[\Omega] = \sqrt{\eta_c \kappa} \delta \hat{s}_{\text{in}}^\dagger[\Omega] + \sqrt{(1 - \eta_c) \kappa} \delta \hat{s}_{\text{vac}}^\dagger[\Omega] \quad (\text{B.15})$$

we write them, for convenience, in matrix form (omitting the frequency arguments)

$$C_{\bar{\Delta}, \Omega, \kappa} \begin{pmatrix} \delta \hat{a} \\ \delta \hat{a}^\dagger \end{pmatrix} = \sqrt{\eta_c \kappa} \begin{pmatrix} \delta \hat{s}_{\text{in}} \\ \delta \hat{s}_{\text{in}}^\dagger \end{pmatrix} + \sqrt{(1 - \eta_c) \kappa} \begin{pmatrix} \delta \hat{s}_{\text{vac}} \\ \delta \hat{s}_{\text{vac}}^\dagger \end{pmatrix} \quad (\text{B.16})$$

with

$$C_{\bar{\Delta}, \Omega, \kappa} = \begin{pmatrix} -i(\bar{\Delta} + \Omega) + \kappa/2 & 0 \\ 0 & +i(\bar{\Delta} - \Omega) + \kappa/2 \end{pmatrix} \quad (\text{B.17})$$

Next we determine the phase angle of input and output mean fields (we chose the intracavity mean field to be real): From (1.28) we have

$$\begin{aligned} \bar{s}_{\text{in}} &= \frac{-i\bar{\Delta} + \kappa/2}{\sqrt{\eta_c \kappa}} \bar{a} = \\ &= \frac{-i\bar{\Delta} + \kappa/2}{\sqrt{\bar{\Delta}^2 + (\kappa/2)^2}} |\bar{s}_{\text{in}}| =: e^{-i\theta_{\text{in}}} |\bar{s}_{\text{in}}| \end{aligned} \quad (\text{B.18})$$

while

$$\begin{aligned} \bar{s}_{\text{out}} &= \bar{s}_{\text{in}} - \sqrt{\eta_c \kappa} \bar{a} = \\ &= \frac{-i\bar{\Delta} + (\frac{1}{2} - \eta_c) \kappa}{\sqrt{\eta_c \kappa}} \bar{a} = \\ &= \frac{-i\bar{\Delta} + (\frac{1}{2} - \eta_c) \kappa}{\sqrt{\bar{\Delta}^2 + (\frac{1}{2} - \eta_c)^2 \kappa^2}} |\bar{s}_{\text{out}}| =: e^{-i\theta_{\text{out}}} |\bar{s}_{\text{out}}| \end{aligned} \quad (\text{B.19})$$

Note that the phase of the *mean* output field, with respect to which the quadratures are *defined*, changes upon changing coupling conditions!

Using the general relation between quadrature and creation/annihilation operators fluctuations for a mean field at angle  $\theta$

$$\begin{pmatrix} \delta \hat{s} \\ \delta \hat{s}^\dagger \end{pmatrix} = \frac{1}{2} \begin{pmatrix} e^{-i\theta} & +ie^{-i\theta} \\ e^{+i\theta} & -ie^{+i\theta} \end{pmatrix} \begin{pmatrix} \delta \hat{p} \\ \delta \hat{q} \end{pmatrix} =: M_\theta \begin{pmatrix} \delta \hat{p} \\ \delta \hat{q} \end{pmatrix} \quad (\text{B.20})$$

we get

$$\begin{pmatrix} \delta \hat{a} \\ \delta \hat{a}^\dagger \end{pmatrix} = C_{\bar{\Delta}, \Omega, \kappa}^{-1} \left( \sqrt{\eta_c \kappa} M_{\theta_{\text{in}}} \begin{pmatrix} \delta \hat{p}_{\text{in}} \\ \delta \hat{q}_{\text{in}} \end{pmatrix} + \sqrt{(1 - \eta_c) \kappa} M_0 \begin{pmatrix} \delta \hat{p}_{\text{vac}} \\ \delta \hat{q}_{\text{vac}} \end{pmatrix} \right) \quad (\text{B.21})$$

## B. Calculations

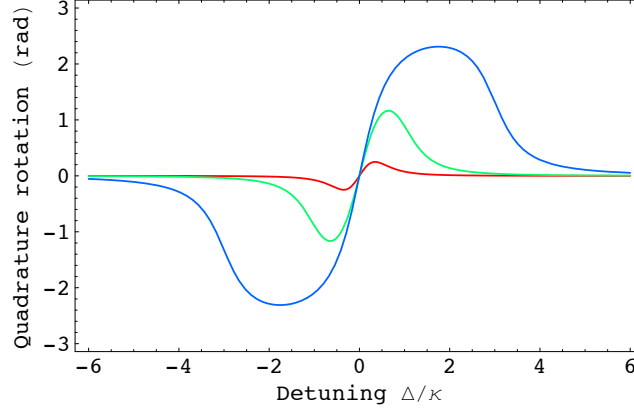


Figure B.1: Quadrature rotation for noise at  $\Omega = \kappa/3$  (red),  $\Omega = \kappa$  (green) and  $\Omega = 3\kappa$  (blue).

and using

$$\begin{pmatrix} \delta \hat{s}_{\text{out}} \\ \delta \hat{s}_{\text{out}}^\dagger \end{pmatrix} = \begin{pmatrix} \delta \hat{s}_{\text{in}} \\ \delta \hat{s}_{\text{in}}^\dagger \end{pmatrix} - \sqrt{\eta_c \kappa} \begin{pmatrix} \delta \hat{a} \\ \delta \hat{a}^\dagger \end{pmatrix} \quad (\text{B.22})$$

finally

$$\begin{aligned} \begin{pmatrix} \delta \hat{p}_{\text{out}} \\ \delta \hat{q}_{\text{out}} \end{pmatrix} &= M_{\theta_{\text{out}}}^{-1} \left( I - \eta_c \kappa C_{\bar{\Delta}, \Omega, \kappa}^{-1} \right) M_{\theta_{\text{in}}} \begin{pmatrix} \delta \hat{p}_{\text{in}} \\ \delta \hat{q}_{\text{in}} \end{pmatrix} \\ &\quad - \sqrt{(1 - \eta_c) \eta_c \kappa} M_{\theta_{\text{out}}}^{-1} C_{\bar{\Delta}, \Omega, \kappa}^{-1} M_0 \begin{pmatrix} \delta \hat{p}_{\text{vac}} \\ \delta \hat{q}_{\text{vac}} \end{pmatrix} \end{aligned} \quad (\text{B.23})$$

where  $I$  is the identity matrix.

For the simplest case  $\eta_c = 1$  one gets

$$M_{\theta_{\text{out}}}^{-1} \left( I - \kappa C_{\bar{\Delta}, \Omega, \kappa}^{-1} \right) M_{\theta_{\text{in}}} = \begin{pmatrix} R_{11} & R_{12} \\ R_{21} & R_{22} \end{pmatrix} \quad (\text{B.24})$$

with

$$R_{11} = R_{22} = \frac{\left( \bar{\Delta}^2 + \frac{\kappa^2}{4} \right)^2 - \left( \bar{\Delta}^2 - \frac{\kappa^2}{4} \right) \Omega^2}{\left( \bar{\Delta}^2 + \frac{\kappa^2}{4} \right) \left( \bar{\Delta}^2 + \left( \frac{\kappa}{2} - i\Omega \right)^2 \right)} \quad (\text{B.25})$$

$$R_{12} = -R_{21} = \frac{\bar{\Delta} \kappa \Omega^2}{\left( \bar{\Delta}^2 + \frac{\kappa^2}{4} \right) \left( \bar{\Delta}^2 + \left( \frac{\kappa}{2} - i\Omega \right)^2 \right)} \quad (\text{B.26})$$

see also [247]. This matrix actually rotates the quadratures by an angle  $\arctan(R_{12}/R_{11})$  which is shown in figure B.1.

## B.2 Noise transfer of a lossy cavity

---

This leads to

$$\bar{S}_{pp}^{\text{out}} = \alpha_1 \bar{S}_{pp}^{\text{in}} + \alpha_2 \bar{S}_{qq}^{\text{in}} \quad (\text{B.27})$$

$$\bar{S}_{qq}^{\text{out}} = \alpha_2 \bar{S}_{pp}^{\text{in}} + \alpha_1 \bar{S}_{qq}^{\text{in}} \quad (\text{B.28})$$

$$\alpha_1 = \frac{\left( \left( \bar{\Delta}^2 + \frac{\kappa^2}{4} \right)^2 - \left( \bar{\Delta}^2 - \frac{\kappa^2}{4} \right) \Omega^2 \right)^2}{\left( \bar{\Delta}^2 + \frac{\kappa^2}{4} \right) \left( \frac{\kappa^2}{4} + (\bar{\Delta} + \Omega)^2 \right) \left( \frac{\kappa^2}{4} + (\bar{\Delta} - \Omega)^2 \right)} \quad (\text{B.29})$$

$$\alpha_2 = \frac{4\bar{\Delta}^2 \frac{\kappa^2}{4} \Omega^4}{\left( \bar{\Delta}^2 + \frac{\kappa^2}{4} \right) \left( \frac{\kappa^2}{4} + (\bar{\Delta} + \Omega)^2 \right) \left( \frac{\kappa^2}{4} + (\bar{\Delta} - \Omega)^2 \right)} \quad (\text{B.30})$$

## B. Calculations

---

The general case of arbitrary coupling conditions produces rather lengthy expressions:

$$\bar{S}_{pp}^{\text{out}} = \left( \beta_1 \bar{S}_{pp}^{\text{in}} + \beta_2 \bar{S}_{qq}^{\text{in}} + \beta_3 \bar{S}_{pp}^{\text{vac}} + \beta_4 \bar{S}_{qq}^{\text{vac}} \right) / \beta_5 \quad (\text{B.31})$$

$$\bar{S}_{qq}^{\text{out}} = \left( \beta_2 \bar{S}_{pp}^{\text{in}} + \beta_1 \bar{S}_{qq}^{\text{in}} + \beta_4 \bar{S}_{pp}^{\text{vac}} + \beta_3 \bar{S}_{qq}^{\text{vac}} \right) / \beta_5 \quad (\text{B.32})$$

$$\begin{aligned} \beta_1 &= 16 \left( 4\bar{\Delta}^2 + (1 - 2\eta_c)\kappa^2 \right)^2 \Omega^4 + \left( 4\bar{\Delta}^2 + \kappa^2 \right)^2 \left( 4\bar{\Delta}^2 + (1 - 2\eta_c)^2 \kappa^2 \right)^2 \\ &\quad - 8 \left( 4\bar{\Delta}^2 + (1 - 2\eta_c)\kappa^2 \right) \left( 4\bar{\Delta}^2 + (2\eta_c - 1)\kappa^2 \right) \left( 4\bar{\Delta}^2 + (2(\eta_c - 1)\eta_c + 1)\kappa^2 \right) \Omega^2 \\ \beta_2 &= 256\bar{\Delta}^2 \eta_c^2 \kappa^2 \Omega^2 \left( (\eta_c - 1)^2 \kappa^2 + \Omega^2 \right) \\ \beta_3 &= 4\eta_c(1 - \eta_c)\kappa^2 \left( \left( 4\bar{\Delta}^2 + (2\eta_c - 1)\kappa^2 \right)^2 + 4(1 - 2\eta_c)^2 \kappa^2 \Omega^2 \right) \left( 4\bar{\Delta}^2 + \kappa^2 \right) \\ \beta_4 &= 64\bar{\Delta}^2 \eta_c(1 - \eta_c)\kappa^2 \left( (\kappa - \eta_c\kappa)^2 + \Omega^2 \right) \left( 4\bar{\Delta}^2 + \kappa^2 \right) \\ \beta_5 &= \left( 4\bar{\Delta}^2 + \kappa^2 \right) \left( 4\bar{\Delta}^2 + (1 - 2\eta_c)^2 \kappa^2 \right) \left( 4(\bar{\Delta} - \Omega)^2 + \kappa^2 \right) \left( 4(\bar{\Delta} + \Omega)^2 + \kappa^2 \right) \end{aligned} \quad (\text{B.33})$$

where

$$(\beta_1 + \beta_2 + \beta_3 + \beta_4) / \beta_5 = 1 \quad (\text{B.34})$$

is easily verified.

# Appendix C

## Useful experimental techniques

### C.1 Fiber loop cavity

For many purposes (some applications are described below), simple, high- $Q$  reference cavities are a useful tool for the experiments described in this work. Inspired by the toroid-taper geometry, we have frequently used so-called fiber-loop cavities (FLCs). They are “set up” as easily as connecting one output port of a standard fused coupler back to one input as shown in figure C.1. The fiber loop then constitutes a low-finesse ( $\mathcal{F} \lesssim 20$ ), yet, due to its significant length, reasonably high- $Q$  ( $\kappa/2\pi \sim 10$  MHz) cavity. If the fiber loop is kept quiet, such a cavity is stable enough for a number of simple reference measurements.

Figure C.1 shows a trace recorded by slowly scanning a quiet laser over the resonances of a FLC. Clean Lorentzian fringes are observed. By calibrating the frequency axis, using a frequency modulation of the laser at a well-known frequency, it was possible to derive the tuning coefficient (frequency shift vs. applied control voltage) of the Ti:S laser. At the same time, the frequency range over which mode-hop free scans are possible could be measured.

Another possible application is the calibration of the modulation depth induced by a phase modulator. This is an important measurement, as a frequency modulation induced by such a modulator later serves for the calibration of mechanical displacements. Phase-modulating the laser of frequency  $\omega_1$  with a peak-to-peak modulation depth  $\delta\varphi$  at a frequency  $\Omega_{\text{mod}}$  results in an input amplitude

$$\begin{aligned} s_{\text{in}}(t) &= \bar{s}_{\text{in}} \exp(i(\omega_1 t - \delta\varphi \cos(\Omega_{\text{mod}} t))) = \\ &= \sum_{n=-\infty}^{+\infty} \bar{s}_{\text{in}} (-i)^n J_n(\delta\varphi) \exp(i(\omega_1 + n\Omega_{\text{mod}}) t) \end{aligned}$$

where  $J_n$  is the Bessel function of the first kind. This can be considered as an infinite array of lasers, oscillating at frequencies  $\omega_1 + n\Omega_{\text{mod}}$ , with powers

## C. Useful experimental techniques

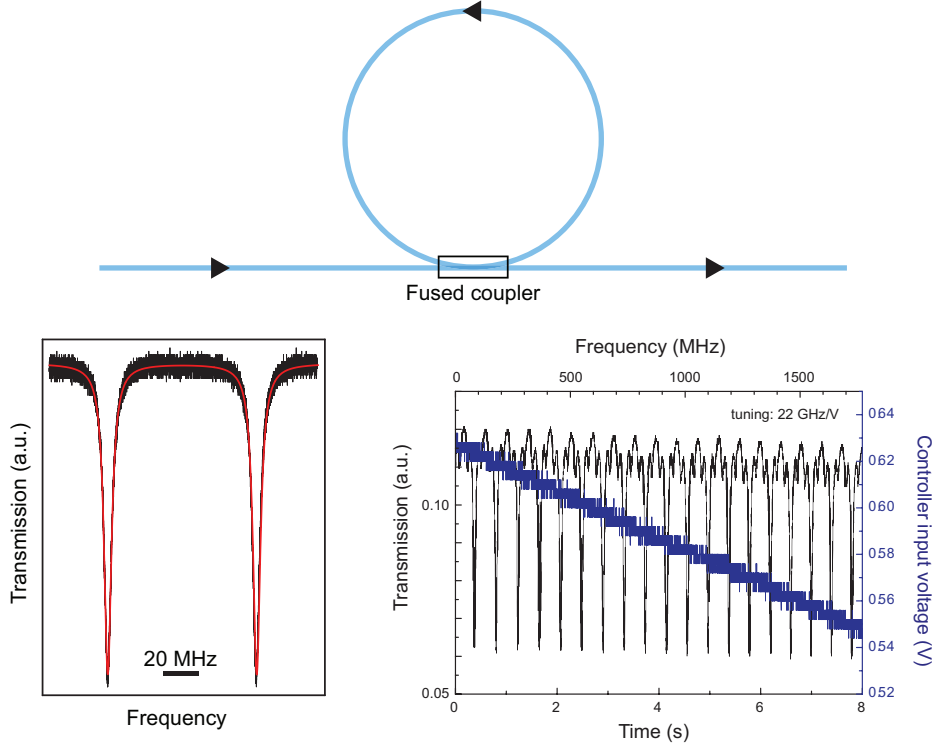


Figure C.1: Fiber loop cavity configuration (top) and narrow Lorentzian resonance fringes (bottom left). Bottom right panel shows a measurement in which the laser was frequency-modulated at 30 MHz to induce sidebands to the resonances used for frequency calibration. In this manner, the tuning coefficient of one of the frequency actuators in the Ti:S laser was derived.

$P_n \propto E_0^2 J_n(\delta\varphi)^2$ . If only the average transmission is recorded, one simply expects the sum of the transmitted powers of the individual sidebands

$$T(\omega_1) \propto \left( 1 - \eta_c(1 - \eta_c) \sum_n J_n(\delta\varphi)^2 \frac{\kappa^2}{(\kappa/2)^2 + (\omega_1 + n\Omega_{\text{mod}} - \omega_c)^2} \right),$$

compare (1.35). Such transmission spectra (scanning the laser and its sidebands at  $\omega_1 + n\Omega_{\text{mod}}$  through the cavity resonance at  $\omega_c$ ) are recorded for different RF-powers applied to the modulator. For each trace, the ratio of the depth of the carrier and first sideband dips  $J_0(\delta\varphi)^2/J_{\pm 1}(\delta\varphi)^2$  can be extracted by using the above fit model. It is expected to be a function of RF power according to the dependence of the phase modulation amplitude

$$\delta\varphi = \frac{\sqrt{2}\sqrt{P_{\text{RF}} \cdot 50 \text{ Ohm}}}{V_\pi} \cdot \pi$$

One can thus extract  $V_\pi$  from the measurement ( $V_\pi$  is the voltage necessary to induces a  $\pi$ -phase shift in the light field). Or, even more direct, extract the proportionality coefficient  $\lambda = \pi\sqrt{2 \cdot 50 \text{ Ohm}}/V_\pi$  with  $\delta\varphi = \lambda\sqrt{P_{\text{RF}}}$ .

## C.2 Locking of the cooling laser

---

Another useful application for FLCs is the measurement of high-Fourier frequency noise of a laser. For example, the laser can be locked to the center of a fringe of the FLC using one of the techniques described in section 2.4 with a feedback loop. Fluctuations in the error signal at Fourier frequencies beyond the bandwidth of the (slow) feedback loop are due to laser frequency fluctuations, and can be easily analyzed using a spectrum analyzer. The recorded spectra can be again calibrated by effecting a *known* frequency modulation on the laser using a phase modulator. For Fourier frequencies beyond the cavity cutoff, the reduced sensitivity of this measurement method has to be taken into account, however. Zhang *et al.* [247] describes another possibility to determine laser frequency noise using a Fabry-Perot cavity, which can easily be adapted to the virtually alignment-free FLCs.

## C.2 Locking of the cooling laser

The experimental observation of cooling requires a negative detuning, and therefore makes a stabilization of the laser frequency to the red wing of the optical resonance necessary. Due to the strong thermal non-linearities, reaching the bistability threshold for light powers well below a microwatt (see section 1.5.1), this poses a significant experimental difficulty, as the red wing is dynamically unstable under small fluctuations of laser or cavity frequency fluctuations. To counteract this instability, a fast control loop to the laser frequency was implemented. As described in figure 2.28, the detuning error signal is directly derived from the residual transmission of the pump laser through the taper. After applying an offset, the signal is split and sent to two proportional-integral controllers (“lock-boxes”).

The error signal is pre-amplified with a low noise amplifier (DC-1 MHz), the two outputs of which are fed to two custom-built proportional-integral controllers with bandwidths on the order of 1 kHz and 1 MHz. Both controllers allow to apply an offset to the error signal input, enabling continuous variation of the control setpoint and thus detuning from line center. Without further amplification, the output of the slower controller is applied to a piezoelectric element actuating the grating in the laser to tune the laser emission frequency. For the compensation of fast fluctuations, the output from the faster controller is applied to a field-effect transistor parallel to the laser diode. The consequent temporary change of diode current leads to the desired laser frequency adjustment via a temperature and carrier dispersion change. Laser emission power is affected only on the order of 5% and, since the output of the fast controller is high-pass filtered (cut-off  $> 10$  Hz), remains unmodified on average.

To implement resolved-sideband cooling, the direct transmission signal cannot be used as an error signal, as its slope is too flat far away from the WGM resonance. Instead, a frequency modulation technique is used (figure C.2). In essence, this scheme resembles the PDH method, including

## C. Useful experimental techniques

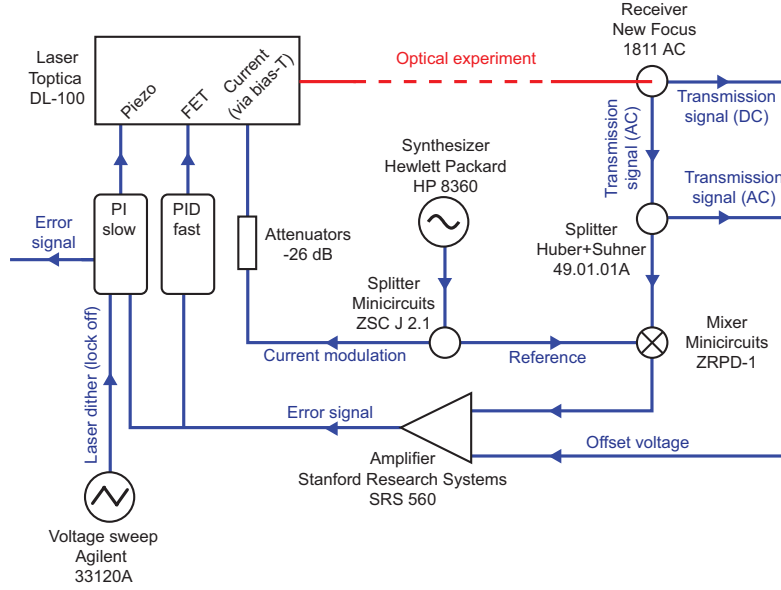


Figure C.2: Electronic feedback loop to stabilize the laser to the lower mechanical sideband of a WGM resonance in the deeply resolved sideband regime. FET is a field effect transistor controlling the current applied to the laser diode. See text for more information.

frequency modulation of the cooling laser and subsequent demodulation of the transmission signal at the modulation frequency. It is important however, to choose a modulation frequency that differs from the mechanical resonance frequency in order to avoid driving the oscillator with the beat of the laser carrier and the modulation sideband in the cavity. In order to still be able to lock to a detuning of precisely  $-\Omega_m$ , the phase of the demodulation reference is adjusted to yield an absorptive, instead of dispersive shape (as is the case for the PDH signal). For the high radio frequencies involved here, adjusting this phase can be accomplished by simply changing the length of the cable providing this signal. An error signal similar to the trace shown in figure 1.5 is then obtained, with positive and negative dips when a modulation sideband is scanned through the resonance. Application of an appropriate offset to this error signal then allows locking the upper modulation sideband to the wing of the optical resonance. In this configuration, the laser carrier is detuned by the mechanical resonance frequency, while the modulation frequency differs from the mechanical resonance frequency by  $\sim \kappa/2 \gg \Gamma_m$ , so that the mechanical oscillator is not driven.

# Bibliography

- [1] A. Schliesser, P. Del’Haye, N. Nooshi, K.J. Vahala, and T. Kippenberg. Radiation pressure cooling of a micromechanical oscillator using dynamical backaction. *Physical Review Letters*, 97:243905, 2006.
- [2] A. Schliesser, C. Gohle, T. Udem, and T. W. Hänsch. Complete characterization of a broadband high-finesse cavity using an optical frequency comb. *Optics Express*, 14(13):5975–5983, 2006.
- [3] P. Del’Haye, A. Schliesser, O. Arcizet, T. Wilken, R. Holzwarth, and T. Kippenberg. Optical frequency comb generation from a monolithic microresonator. *Nature*, 450:1214–1217, 2007.
- [4] C. Gohle, B. Stein, A. Schliesser, T. Udem, and T. W. Hänsch. Frequency Comb Vernier Spectroscopy for Broadband, High-Resolution, High-Sensitivity Absorption and Dispersion spectra. *Physical Review Letters*, 99:263902, 2007.
- [5] R. Ma, A. Schliesser, P. Del’Haye, A. Dabirian, G. Anetsberger, and T. Kippenberg. Radiation-pressure-driven vibrational modes in ultrahigh-Q silica microspheres. *Optics Letters*, 32:2200–2202, 2007.
- [6] G. Anetsberger, R. Rivière, A. Schliesser, O. Arcizet, and T. J. Kippenberg. Ultralow-dissipation optomechanical resonators on a chip. *Nature Photonics*, 2:627–633, 2008.
- [7] P. Del’Haye, O. Arcizet, A. Schliesser, R. Holzwarth, and T. J. Kippenberg. Full stabilization of a microresonator-based optical frequency comb. *Physical Review Letters*, 101:053903, 2008.
- [8] A. Schliesser, R. Rivière, G. Anetsberger, O. Arcizet, and T. Kippenberg. Resolved-sideband cooling of a micromechanical oscillator. *Nature Physics*, 4:415–419, 2008.
- [9] A. Schliesser, G. Anetsberger, R. Rivière, O. Arcizet, and T. J. Kippenberg. High-sensitivity monitoring of micromechanical vibration using

## BIBLIOGRAPHY

---

- optical whispering gallery mode resonators. *New Journal of Physics*, 10:095015, 2008.
- [10] A. Schliesser, O. Arcizet, R. Rivière, G. Anetsberger, and T. Kippenberg. Resolved-sideband cooling and position measurement of a micromechanical oscillator close to the Heisenberg uncertainty limit. *Nature Physics*, 5:509–514, 2009.
- [11] O. Arcizet, R. Rivière, A. Schliesser, G. Anetsberger, and T. J. Kippenberg. Cryogenic properties of optomechanical silica microcavities. *Physical Review A*, 80:021803(R), 2009.
- [12] G. Anetsberger, O. Arcizet, Q. P. Unterreithmeier, R. Rivière, A. Schliesser, E. M. Weig, J. P. Kotthaus, and T. J. Kippenberg. Near-field cavity optomechanics with nanomechanical oscillators. *Nature Physics*, accepted, 2009.
- [13] O. Arcizet, A. Schliesser, P. Del’Haye, R. Holzwarth, and T. J. Kippenberg. Optical frequency comb generation in monolithic microresonators. In A. Matsko, editor, *Practical applications of microresonators in optics and photonics*, chapter 11, pages 483–506. CRC press, 2009.
- [14] A. Schliesser and T. J. Kippenberg. Cavity optomechanics with silica microresonators. In E. Arimondo, P. Berman, and C. C. Lin, editors, *Advances in atomic, molecular and optical physics*, volume 58. Elsevier Academic Press, 2010. (in preparation).
- [15] C. Gohle, A. Schliesser, and T. W. Hänsch. Method and device for optical Vernier spectroscopy. European (EP 06026763) and US (US 12/520577) patent applications, 2007.
- [16] P. Del’Haye, T. Kippenberg, and A. Schliesser. Method and apparatus for optical frequency comb generation using a monolithic microresonator. European (EP 07009067) and US (US 60.916045) patent applications, 2007.
- [17] V. B. Braginsky, M. L. Gorodetsky, and V. S. Ilchenko. Quality-factor and nonlinear properties of optical whispering-gallery modes. *Physics Letters A*, 137(7-8):393–397, 1989.
- [18] L. Collot, V. Lefèvre-Seguin, M. Brune, J. M. Raimond, and S. Haroche. Very high-Q whispering-gallery mode resonances observed on fused silica microspheres. *Europhysics Letters*, 23(5):327–334, 1993.
- [19] D. W. Vernooy, V. S. Ilchenko, H. Mabuchi, W. W. Sreed, and H. J. Kimble. High-Q measurements of fused-silica microspheres in the near infrared. *Optics Letters*, 23(4):247–249, 1998.

## BIBLIOGRAPHY

---

- [20] S. M. Spillane, T. J. Kippenberg, and K. J. Vahala. Ultralow-threshold Raman laser using a spherical dielectric microcavity. *Nature*, 415(6872):621–623, 2002.
- [21] B. K. Min, T. J. Kippenberg, and K. J. Vahala. Compact, fiber-compatible, cascaded Raman laser. *Optics Letters*, 28(17):1507–1509, 2003.
- [22] V. Sandoghdar, F. Treussart, J. Hare, V. Lefèvre-Seguin, J.-M. Raimond, and S. Haroche. Very low threshold whispering-gallery-mode microsphere laser. *Physical Review A*, 54(3):R1777–R1780, 1996.
- [23] M. Cai, O. Painter, K. J. Vahala, and P. C. Sercel. Fiber-coupled microsphere laser. *Optics Letters*, 25(19):1430–1432, 2000.
- [24] M. Cai and K. Vahala. Highly efficient hybrid fiber taper coupled microsphere laser. *Optics Letters*, 26(12):884–886, 2001.
- [25] H. J. Kimble. Structure and dynamics in cavity quantum electrodynamics. In P. R. Berman, editor, *Cavity Quantum Electrodynamics*, Advances in Atomic, Molecular and Optical Physics. Academic Press, 1994.
- [26] D. W. Vernooy, A. Furusawa, A. P. Georgiades, V. S. Ilchenko, and H. J. Kimble. Cavity QED with high-Q whispering gallery modes. *Physical Review A*, 57:R2293–R2296, 1998.
- [27] J. R. Buck, Jr. *Cavity QED in Microsphere and Fabry-Perot Cavities*. PhD thesis, California Institute of Technology, 2003.
- [28] F. Vollmer, D. Braun, A. Libchaber, M. Khoshshima, I. Teraoka, and S. Arnold. Protein detection by optical shift of a resonant microcavity. *Applied Physics Letters*, 80(21):4057–4059, 2002.
- [29] F. Vollmer, S. Arnold, and D. Keng. Single virus detection from the reactive shift of a whispering-gallery mode. *PNAS*, 105:20701–20704, 2009.
- [30] D. K. Armani, T. J. Kippenberg, S. M. Spillane, and K. J. Vahala. Ultra-high-Q toroid microcavity on a chip. *Nature*, 421:925–928, 2003.
- [31] T. J. Kippenberg, S. M. Spillane, and K. J. Vahala. Demonstration of ultra-high-Q small mode volume toroid microcavities on a chip. *Applied Physics Letters*, 85(25):6113–6115, 2004.
- [32] T. J. Kippenberg, S. M. Spillane, D. K. Armani, B. Min, L. Yang, and K. J. Vahala. Fabrication, coupling and nonlinear optics of ultra-high-Q

## BIBLIOGRAPHY

---

- micro-sphere and chip-based toroid microcavities. In K. Vahala, editor, *Optical microcavities*, volume 5 of *Advanced series in applied physics*, chapter 5. World Scientific, 2004.
- [33] G. Mie. Beiträge zur Optik trüber Medien, speziell kolloidaler Metallösungen. *Annalen der Physik*, 25:377–445, 1908.
- [34] J. Strutt (Lord Rayleigh). The problem of the whispering gallery. *Philosophical Magazine*, 20:1001–1004, 1910.
- [35] S. M. Spillane. *Fiber-coupled Ultra-high-Q Microresonators for Nonlinear and Quantum Optics*. PhD thesis, California Institute of Technology, 2004.
- [36] T. J. A. Kippenberg. *Nonlinear Optics in Ultra-high-Q Whispering-Gallery Optical Microcavities*. PhD thesis, California Institute of Technology, July 2004.
- [37] S. M. Spillane, T. J. Kippenberg, K. J. Vahala, K. W. Goh, W. Wilcut, and H. J. Kimble. Ultrahigh-Q toroidal microresonators for cavity quantum electrodynamics. *Physical Review A*, 71:013807, 2005.
- [38] M. Gorodetsky and A. E. Fomin. Geometrical theory of whispering-gallery modes. *IEEE Journal of Selected Topics in Quantum Electronics*, 12:33–39, 2006.
- [39] B. Min, L. Yang, and K. Vahala. Perturbative analytic theory of an ultrahigh-Q toroidal microcavity. *Physical Review A*, 76(1):013823, 2007.
- [40] M. Oxborrow. Traceable 2-d finite-element simulation of the whispering-gallery modes of axisymmetric electromagnetic resonators. *IEEE Transactions on Microwave Theory and Techniques*, 55:1209–1218, 2007.
- [41] J. B. Hertzberg, T. Rocheleau, T. Ndukum, M. Savva, A. A. Clerk, and K. C. Schwab. Back-action evading measurements of nanomechanical motion. *arxiv:0906.0967*, 2009.
- [42] P. Debye. Der Lichtdruck auf Kugeln von beliebigem Material. *Annalen der Physik*, 335:57–136, 1909.
- [43] F. Treussart. *Étude expérimentale de l’effet laser dans des microsphères de silice dopées avec des ions neodyme*. PhD thesis, Université Paris VI, 1997.
- [44] A. N. Oraevsky. Whispering-gallery waves. *Quantum Electronics*, 32(5):377–400, 2002.

## BIBLIOGRAPHY

---

- [45] J. C. Knight, N. Dubreuil, V. Sandoghdar, J. Hare, V. Lefèvre-Seguin, J. M. Raimond, and S. Haroche. Mapping whispering-gallery modes in microspheres with a near-field probe. *Optics Letters*, 20(14):1515–1517, 1995.
- [46] J. C. Knight, N. Dubreuil, V. Sandoghdar, J. Hare, V. Lefèvre-Seguin, J.-M. Raimond, and S. Haroche. Characterizing whispering-gallery modes in microspheres by direct observation of the optical standing-wave pattern in the near field. *Optics Letters*, 21(10):698–700, 1996.
- [47] S. Schiller. Asymptotic expansion of morphological resonance frequencies in Mie scattering. *Applied Optics*, 32(12):2181–2185, 1993.
- [48] P. Del’Haye, O. Arcizet, R. Holzwarth, and T. J. Kippenberg. Broadband precision spectroscopy with a frequency comb and a scanning diode laser. *Nature Photonics*, 3:529–533, 2009.
- [49] M. L. Gorodetsky, A. A. Savchenkov, and V. S. Ilchenko. Ultimate Q of optical microsphere resonators. *Optics Letters*, 21(7):453–455, 1996.
- [50] M. L. Gorodetsky, A. D. Pryamikov, and V. S. Ilchenko. Rayleigh scattering in high-Q microspheres. *Journal of the optical society of America B - Optical physics*, 17(6):1051–1057, 2000.
- [51] H. Rokhsari, S. M. Spillane, and K. J. Vahala. Loss characterization in microcavities using the thermal bistability effect. *Applied Physics Letters*, 85(15):3029–3031, 2004.
- [52] H. F. Winters and J. W. Coburn. The etching of silicon with XeF<sub>2</sub> vapor. *Applied Physics Letters*, 34(1):70–73, 1979.
- [53] K. Sugano and O. Tabata. Reduction of surface roughness and aperture size effect for etching of Si with XeF<sub>2</sub>. *Journal of Micromechanics and Microengineering*, 12:911–916, 2002.
- [54] T. J. Kippenberg, S. M. Spillane, D. K. Armani, and K. J. Vahala. Fabrication and coupling to planar high-Q silica disk microcavities. *Applied Physics Letters*, 83:797–799, 2003.
- [55] T. Kippenberg, J. Kalkman, A. Polman, and K. J. Vahala. Demonstration of an erbium-doped microdisk laser on a silicon chip. *Physical Review A*, 74:051802(R), 2006.
- [56] A. D. McLachlan and F. P. Meyer. Temperature dependence of the extinction coefficient of silica for CO<sub>2</sub> laser wavelengths. *Applied Optics*, 26:1728–1731, 1987.
- [57] H. A. Haus. *Waves and fields in optoelectronics*. Prentice-Hall, 1984.

## BIBLIOGRAPHY

---

- [58] H. A. Haus. *Electromagnetic Noise and Quantum Optical Measurements*. Springer, 2000.
- [59] B. E. Little, J. P. Laine, and H. A. Haus. Analytic theory of coupling from tapered fibers and half-blocks into microsphere resonators. *Journal of Lightwave Technology*, 17(4):704–715, 1999.
- [60] T. A. Birks and Y. W. Li. The shape of fiber tapers. *Journal of Lightwave Technology*, 10:432–438, 1992.
- [61] M. Cai, O. Painter, and K. J. Vahala. Observation of critical coupling in a fiber taper to a silica-microsphere whispering-gallery mode system. *Physical Review Letters*, 85(1):74–77, 2000.
- [62] S. M. Spillane, T. J. Kippenberg, O. J. Painter, and K. J. Vahala. Ideality in a fiber-taper-coupled microresonator system for application to cavity quantum electrodynamics. *Physical Review Letters*, 91(4):043902, 2003.
- [63] D. S. Weiss, V. Sandoghdar, J. Hare, V. Lefèvre-Seguin, J. M. Raimond, and S. Haroche. Splitting of high-Q Mie modes induced by light backscattering in silica microspheres. *Optics Letters*, 20(18):1835–1837, 1995.
- [64] T. J. Kippenberg, S. M. Spillane, and K. J. Vahala. Modal coupling in traveling-wave resonators. *Optics Letters*, 27(19):1669–1671, 2002.
- [65] A. Mazzei, S. Götzinger, L. de S. Menezes, G. Zumofen, O. Benson, and V. Sandoghdar. Controlled coupling of counterpropagating whispering-gallery modes by a single Rayleigh scatterer: a classical problem in a quantum optical light. *Physical Review Letters*, 99:173603, 2007.
- [66] D. C. Bjorklund, M. D. Levenson, W. Lenth, and C. Ortiz. Frequency Modulation (FM) Spectroscopy. *Applied Physics B*, 32:145–152, 1983.
- [67] V. S. Ilchenko and M. L. Gorodetskii. Thermal nonlinear effects in optical whispering gallery microresonators. *Laser Physics*, 2(2):1004–1009, 1992.
- [68] T. Carmon, L. Yang, and K. J. Vahala. Dynamical thermal behavior and thermal selfstability of microcavities. *Optics Express*, 12:4742–4750, 2004.
- [69] M. Weber. *Handbook of Optical Materials*. CRC Press, Boca Raton, 2003.
- [70] R. W. Boyd. *Nonlinear Optics*. Academic Press, 2003.

- [71] M. Gorodetsky. private communication (2009).
- [72] T. J. Kippenberg, S. A. Spillane, B. Min, and K. J. Vahala. Theoretical and experimental study of stimulated and cascaded raman scattering in ultrahigh-Q optical microcavities. *IEEE Journal of Selected Topics in Quantum Electronics*, 10(5):1219–1228, 2004.
- [73] T. J. Kippenberg, S. M. Spillane, D. K. Armani, and K. J. Vahala. Ultralow-threshold microcavity raman laser on a microelectronic chip. *Optics Letters*, 29(11):1224–1226, 2004.
- [74] B. Min, L. Yang, and K. Vahala. Controlled transition between parametric and raman oscillations in ultrahigh-Q silica toroidal microcavities. *Applied Physics Letters*, 87:181109, 2005.
- [75] T. J. Kippenberg, S. M. Spillane, and K. J. Vahala. Kerr-nonlinearity optical parametric oscillation in an ultrahigh-Q toroid microcavity. *Physical Review Letters*, 93(8):083904, 2004.
- [76] F. Treussart, V. S. Ilchenko, J.-F. Roch, J. Hare, V. Lefèvre-Seguin, J.-M. Raimond, and S. Haroche. Evidence for intrinsic Kerr bistability of high-Q resonators in suprafluid helium. *European Physical Journal D*, 1:235–238, 1998.
- [77] H. Rokhsari and K. J. Vahala. Observation of Kerr nonlinearity in microcavities at room temperature. *Optics Letters*, 30(4):427–429, 2005.
- [78] A. E. Woodruff. The radiometer and how it does not work. *The Physics Teacher*, 6:358–363, 1968.
- [79] P. Lebedew. Untersuchungen über die Druckkräfte des Lichtes. *Annalen der Physik*, 311:433–458, 1901.
- [80] E. F. Nichols and G. F. Hull. A preliminary communication on the pressure of heat and light radiation. *Physical Review*, 13:307–320, 1901.
- [81] E. F. Nichols and G. F. Hull. The pressure due to radiation. *Physical Review*, 17:26–50, 1903.
- [82] E. F. Nichols and G. F. Hull. The pressure due to radiation. *Physical Review*, 17:91–104, 1903.
- [83] T. W. Hänsch and A. L. Schawlow. Cooling of gases by laser radiation. *Optics Communications*, 13:68–69, 1975.
- [84] D. J. Wineland and H. Dehmelt. Proposed  $10^{14} \delta\nu < \nu$  Laser Fluorescence Spectroscopy on  $\text{Tl}^+$  Ion Mono-Oscillator. *Bulletin of the American Physical Society*, 20:637, 1975.

## BIBLIOGRAPHY

---

- [85] D. J. Wineland and W. M. Itano. Laser cooling of atoms. *Physical Review A*, 20:1521–1540, 1979.
- [86] A. Ashkin. Trapping of atoms by resonance radiation pressure. *Physical Review Letters*, 40:729–732, 1978.
- [87] S. Chu, L. Hollberg, J. E. Bjorkholm, A. Cable, and A. Ashkin. Three-dimensional viscous confinement and cooling of atoms by resonance radiation pressure. *Physical Review Letters*, 55(1):48–51, Jul 1985.
- [88] W. M. Itano, J. C. Bergquist, J. J. Bollinger, and D. J. Wineland. *Laser cooling of trapped ions*, pages 519–537S. Laser Manipulation of Atoms and Ions. North-Holland, Amsterdam, 1992.
- [89] F. Diedrich, J. C. Bergquist, Wayne M. Itano, and D. J. Wineland. Laser cooling to the zero-point energy of motion. *Physical Review Letters*, 62(4):403–406, Jan 1989.
- [90] C. Monroe, D. M. Meekhof, B. E. King, S. R. Jefferts, W. M. Itano, D. J. Wineland, and P. Gould. Resolved-sideband raman cooling of a bound atom to the 3d zero point energy. *Physical Review Letters*, 75(22):4011–4014, 1995.
- [91] S. E. Hamann, D. L. Haycock, G. Klose, P. H. Pax, I. H. Deutsch, and P. S. Jessen. Resolved-sideband Raman cooling to the ground state of an optical lattice. *Physical Review Letters*, 80(19):4149–4152, May 1998.
- [92] D. Leibfried, R. Blatt, C. Monroe, and D. Wineland. Quantum dynamics of single trapped ions. *Review of Modern Physics*, 75(1):281–324, Mar 2003.
- [93] V. B. Braginsky, Y. I. Vorontsov, and K. Thorne. Quantum Nondemolition Measurements. *Science*, 209:547–557, 1980.
- [94] V. B. Braginsky and F. Y. Khalili. *Quantum Measurement*. Cambridge University Press, 1992.
- [95] V. B. Braginsky and F. Ya. Khalili. Quantum nondemolition measurements: the route from toys to tools. *Reviews of Modern Physics*, 68:1–11, 1996.
- [96] V. B. Braginsky, M. L. Gorodetsky, F. Ya. Khalili, A. B. Matsko, K. S. Thorne, and S. P. Vyatchanin. Noise in gravitational-wave detectors and other classical-force measurements is not influenced by test-mass quantization. *Physical Review D*, 67:082001, 2003.

## BIBLIOGRAPHY

---

- [97] V. B. Braginskii and A. B. Manukin. Ponderomotive effects of electromagnetic radiation. *Soviet Physics JETP Letters*, 25(4):653–655, 1967.
- [98] V. B. Braginskii, A. B. Manukin, and M. Yu. Tikhonov. Investigation of dissipative ponderomotive effects of electromagnetic radiation. *Soviet Physics JETP*, 31:829–830, 1970.
- [99] V. B. Braginsky and A. B. Manukin. *Measurement of Weak Forces in Physics Experiments*. University of Chicago Press, 1977.
- [100] V. B. Braginsky, S. E. Strigin, and V. P. Vyatchanin. Parametric oscillatory instability in Fabry-Perot interferometer. *Physics Letters A*, 287(5-6):331–338, 2001.
- [101] M. I. Dykman. Heating and cooling of local and quasilocal vibrations by a nonresonance field. *Soviet Physics - Solid State*, 20:1306–1311, 1978.
- [102] V. B. Braginsky and S. P. Vyatchanin. Low quantum noise tranquilizer for Fabry-Perot interferometer. *Physics Letters A*, 293:228–234, 2002.
- [103] C. M. Caves. Quantum-mechanical radiation-pressure fluctuations in an interferometer. *Physical Review Letters*, 45(2):75–79, Jul 1980.
- [104] C. M. Caves. Quantum-mechanical noise in an interferometer. *Physical Review D*, 23:1693, 1981.
- [105] V. B. Braginsky, Yu. I. Vorontsov, and F. Ya. Khalili. *Soviet Physics JETP*, 46:705, 1977.
- [106] A. Heidmann, Y. Hadjar, and M. Pinard. Quantum non-demolition measurement by optomechanical coupling. *Applied Physics B*, 64:173–180, 1997.
- [107] C. Fabre, M. Pinard, S. Bourzeix, A. Heidmann, E. Giacobino, and S. Reynaud. Quantum-noise reduction using a cavity with a movable mirror. *Physical Review A*, 49:1337–1343, 1994.
- [108] S. Mancini and P. Tombesi. Quantum noise reduction by radiation pressure. *Physical Review A*, 49:4055–4065, 1994.
- [109] S. Bose, K. Jacobs, and P. L. Knight. Preparation of nonclassical states in cavities with a moving mirror. *Physical Review A*, 56:4175–4186, 1997.
- [110] W. Marshall, Ch. Simon, R. Penrose, and D. Bouwmeester. Towards Quantum Superpositions of a Mirror. *Physical Review Letters*, 91:130401, 2003.

## BIBLIOGRAPHY

---

- [111] S. Mancini, V. Giovannetti, D. Vitali, and P. Tombesi. Entangling Macroscopic Oscillators Exploiting Radiation Pressure. *Physical Review Letters*, 88:120401, 2002.
- [112] J. Zhang, K. Peng, and S. L. Braunstein. Quantum-state transfer from light to macroscopic oscillators. *Physical Review A*, 68:013808, 2003.
- [113] M. Pinard, A. Dantan, D. Vitali, O. Arcizet, T. Briant, and A. Heidmann. Entangling movable mirrors in a double-cavity system. *Europhysics Letters*, 72:747–753, 2005.
- [114] M. Bhattacharya, P. L. Giscard, and P. Meystre. Entangling the rovibrational modes of a macroscopic mirror using radiation pressure. *Physical Review A*, 77(3):030303, MAR 2008.
- [115] D. Vitali, S. Gigan, A. Ferreira, H. R. Bohm, P. Tombesi, A. Guerreiro, V. Vedral, A. Zeilinger, and M. Aspelmeyer. Optomechanical entanglement between a movable mirror and a cavity field. *Physical Review Letters*, 98:030405, 2007.
- [116] M. Bhattacharya, P. L. Giscard, and P. Meystre. Entanglement of a Laguerre-Gaussian cavity mode with a rotating mirror. *Physical Review A*, 77(1):013827, JAN 2008.
- [117] I. Wilson-Rae, P. Zoller, and A. Imamoglu. Laser cooling of a nanomechanical resonator mode to its quantum ground state. *Physical Review Letters*, 92(7):075507, 2004.
- [118] I. Wilson-Rae, N. Nooshi, W. Zwerger, and T. J. Kippenberg. Theory of ground state cooling of a mechanical oscillator using dynamical backaction. *Physical Review Letters*, 99(9):093901, 2007.
- [119] F. Marquardt, J. P. Chen, A. A. Clerk, and S. M. Girvin. Quantum theory of cavity-assisted sideband cooling of mechanical motion. *Physical Review Letters*, 99:093902, 2007.
- [120] M. Bhattacharya and P. Meystre. Trapping and cooling a mirror to its quantum mechanical ground state. *Physical Review Letters*, 99(7):073601, AUG 17 2007.
- [121] C. Genes, D. Vitali, P. Tombesi, S. Gigan, and M. Aspelmeyer. Ground-state cooling of a micromechanical oscillator: Comparing cold-damping and cavity-assisted cooling schemes. *Physical Review A*, 77:033804, 2008.
- [122] A. Dantan, C. Genes, D. Vitali, and M. Pinard. Self-cooling of a movable mirror to the ground state using radiation pressure. *Physical Review A*, 77:011804(R), 2008.

## BIBLIOGRAPHY

---

- [123] M. F. Bocko and R. Onofrio. On the measurement of a weak classical force coupled to a harmonic oscillator: experimental progress. *Review of Modern Physics*, 68:755–799, 1996.
- [124] I. Tittoonen, G. Breitenbach, T. Kalkbrenner, T. Müller, R. Conradt, S. Schiller, E. Steinsland, N. Blanc, and N. F. de Rooij. Interferometric measurements of the position of a macroscopic body: Towards observations of quantum limits. *Physical Review A*, 59:1038–1044, 1999.
- [125] Y. Hadjar, P. F. Cohadon, C. G. Aminoff, M. Pinard, and A. Heidmann. High-sensitivity optical measurement of mechanical Brownian motion. *Europhysics Letters*, 47(5):545–551, 1999.
- [126] T. Caniard, T. Briant, P.-F. Cohadon, M. Pinard, and A. Heidmann. Ultrasensitive optical measurement of thermal and quantum noises. *Optics and Spectroscopy*, 103:225–230, 2007.
- [127] K. C. Schwab and M. L. Roukes. Putting mechanics into quantum mechanics. *Physics Today*, 58(7):36–42, 2005.
- [128] T. J. Kippenberg and K. Vahala. Cavity Opto-Mechanics. *Optics Express*, 15:17172–17205, 2007.
- [129] T. J. Kippenberg and K. J. Vahala. Cavity Optomechanics: Back-Action at the Mesoscale. *Science*, 321:1172–1176, 2008.
- [130] P.-F. Cohadon, A. Heidmann, and M. Pinard. Cooling of a mirror by radiation pressure. *Physical Review Letters*, 83:3174–3177, 1999.
- [131] M. Pinard, P. F. Cohadon, T. Briant, and A. Heidmann. Full mechanical characterization of a cold damped mirror. *Physical Review A*, 63:013808, 2000.
- [132] T. Caniard, P. Verlot, T. Briant, P.-F. Cohadon, and A. Heidmann. Observation of back-action noise cancellation in interferometric and weak force measurements. *Physical Review Letters*, 99:110801, 2007.
- [133] P. Verlot, A. Tavernarakis, T. Briant, P.-F. Cohadon, and A. Heidmann. Scheme to probe optomechanical correlations between two optical beams down to the quantum level. *Physical Review Letters*, 102:103601, 2008.
- [134] O. Hahtela, K. Nera, and I. Tittoonen. Position measurement of a cavity mirror using polarization spectroscopy. *Journal of Optics A*, 6:S115–S120, 2004.
- [135] C. Hühberger Metzger and K. Karrai. Cavity cooling of a microlever. *Nature*, 432:1002–1005, 2004.

## BIBLIOGRAPHY

---

- [136] M. Ludwig, C. Neuenhanh, C. Metzger, A. Ortlieb, I. Favero, K. Karrai, and F. Marquardt. Self-induced oscillations in an optomechanical system driven by bolometric backaction. *Physical review Letters*, 101:133903, 2008.
- [137] O. Arcizet, P.-F. Cohadon, T. Briant, M. Pinard, A. Heidmann, J.-M. Mackowski, C. Michel, L. Pinard, O. Francais, and L. Rousseau. High-sensitivity optical monitoring of a micromechanical resonator with a quantum-limited optomechanical sensor. *Physical Review Letters*, 97:133601, 2006.
- [138] O. Arcizet, P.-F. Cohadon, T. Briant, M. Pinard, and A. Heidmann. Radiation-pressure cooling and optomechanical instability of a micromirror. *Nature*, 444:71–74, 2006.
- [139] O. Arcizet, C. Molinelli, P.-F. Briant, T. anf Cohadon, A. Heidmann, J.-M. Mackowksi, C. Michel, L. Pinard, O. Francais, and L. Rousseau. Experimental optomechanics with silicon micromirrors. *New Journal of Physics*, 10:125021, 2008.
- [140] H. R. Böhm, S. Gigan, F. Blaser, A. Zeilinger, M. Aspelmeyer, G. Langer, D. Bäuerle, J. B. Hertzberg, and K. C. Schwab. High reflectivity high-Q micromechanical Bragg mirror. *Applied Physics Letters*, 89:223101, 2006.
- [141] S. Gigan, H. R. Böhm, M. Paternosto, F. Blaser, G. Langer, J. B. Hertzberg, K. C. Schwab, D. Bäuerle, M. Aspelmeyer, and A. Zeilinger. Self-cooling of a micromirror by radiation pressure. *Nature*, 444:67–70, 2006.
- [142] S. Gröblacher, S. Gigan, H. R. Böhm, A. Zeilinger, and M. Aspelmeyer. Radiation pressure self-cooling of a micromirror in a cryogenic environment. *Europhysics Letters*, 81:54003, 2008.
- [143] G. D. Cole, S. Gröblacher, S. Gugler, K. Gigan, and M. Aspelmeyer. Monocrystalline  $\text{Al}_x\text{Ga}_{1-x}\text{As}$  heterostructures for high-reflectivity high-Q micromechanical resonators in the megahertz regime. *Applied Physics Letters*, 92:261108, 2008.
- [144] D. Kleckner and D. Bouwmeester. Sub-kelvin optical cooling of a micromechanical resonator. *Nature*, 444:75–78, 2006.
- [145] D. Kleckner, W. Marshall, J. M. A. De Dood, N. D. Khodadad, B.-J. Pors, W. T. M. Irvine, and D. Bouwmeester. High finesse optomechanical cavity with a movable thirty-micron-size mirror. *Physical Review Letters*, 96:173901, 2006.

## BIBLIOGRAPHY

---

- [146] Y. S. Park and H. L. Wang. Radiation pressure driven mechanical oscillation in deformed silica microspheres via free-space evanescent excitation. *Optics Express*, 15:16471–16477, 2007.
- [147] T. Carmon and K. J. Vahala. Modal spectroscopy of optoexcited vibrations of a micron-scale on-chip resonator at greater than 1 GHz frequency. *Physical Review Letters*, 98:123901, 2007.
- [148] T. Corbitt, Y. Chen, E. Innerhofer, H. Muller-Ebhardt, D. Ottaway, H. Rehbein, D. Sigg, S. Whitcomb, Ch. Wipf, and N. Mavalvala. An all-optical trap for a gram-scale mirror. *Physical Review Letters*, 98(15):150802, 2007.
- [149] T. Corbitt, Ch. Wipf, T. Bodiya, D. Ottaway, D. Sigg, N. Smith, S. Whitcomb, and N. Mavalvala. Optical dilution and feedback cooling of a gram-scale oscillator to 6.9 mK. *Physical Review Letters*, 99(16):160801, 2007.
- [150] M. Poggio, L. Degen, J. J. Mamin, and D. Rugar. Feedback cooling of a cantilever’s fundamental mode below 5 mK. *Physical Review Letters*, 99:017201, 2007.
- [151] K. R. Brown, J. Britton, R. J. Epstein, J. Chiaverini, D. Leibfried, and D. J. Wineland. Passive cooling of a micromechanical oscillator with a resonant electric circuit. *Physical Review Letters*, 99(13):137205, 2007.
- [152] J. D. Thomson, B. M. Zwickl, A. M. Jayich, F. Marquardt, S. M. Girvin, and J. G. E. Harris. Strong dispersive coupling of a high finesse cavity to a micromechanical membrane. *Nature*, 452:72–75, 2008.
- [153] B. M. Zwickl, W. E. Shanks, A. M. Jayich, C. Yang, C. Bleszynski Jayich, J. D. Thomson, and J. G. E. Harris. High quality mechanical and optical properties of commercial silicon nitride membranes. *Applied Physics Letters*, 92:103125, 2008.
- [154] I. Favero, C. Metzger, S. Camerer, D. König, H. Lorenz, J. P. Kotthaus, and K. Karrai. Optical cooling of a micromirror of wavelength size. *Applied Physics Letters*, 90:104101, 2007.
- [155] M. Eichenfield, C. P. Michael, R. Perahia, and O. Painter. Actuation of micro-optomechanical systems via cavity-enhanced optical dipole forces. *Nature Photonics*, 1:416–422, 2007.
- [156] C. M. Mow-Lowry, A. J. Mullavey, S. Goler, M. B. Gray, and D. E. McClelland. Cooling of a gram-scale cantilever flexure to 70 mK with a servo-modified optical spring. *Physical Review Letters*, 100:010801, 2008.

## BIBLIOGRAPHY

---

- [157] J. D. Teufel, J. D. Harlow, C. A. Regal, and K. W. Lehnert. Dynamical backaction of microwave fields on a nanomechanical oscillator. *Physical Review Letters*, 101:197203, 2008.
- [158] C. A. Regal, J. D. Teufel, and K. W. Lehnert. Measuring nanomechanical motion with a microwave cavity interferometer. *Nature Physics*, 4:555–560, 2008.
- [159] T. Rocheleau, T. Ndukum, C. Macklin, J. B. Hertzberg, A. A. Clerk, and K. C. Schwab. Preparation and detection of a mechanical resonator near the ground state of motion. *arxiv:0907.3313v1*, 2009.
- [160] A. Vinante, M. Bionotto, M. Bonaldi, M. Cerdonio, L. Conti, P. Falferi, N. Liguori, R. Longo, R. Mezzena, A. Ortolan, G. A. Prodi, F. Salemi, L. Taffarello, G. Vedovato, S. Vitale, and J.-P. Zendri. Feedback cooling of the normal modes of a massive electromechanical system to submillikelvin temperature. *Physical Review Letters*, 101:033601, 2008.
- [161] M. Li, W. H. P. Pernice, C. Xiong, T. Baehr-Jones, M. Hochberg, and H. X. Tang. Harnessing optical forces in integrated photonic circuits. *Nature*, 456:480–484, 2008.
- [162] M. Eichenfield, R. Camacho, J. Chan, K. Vahala, and O. Painter. A picogram and nanometer scale photonic crystal opto-mechanical cavity. *arXiv:0812.2953*, 2009.
- [163] LIGO scientific collaboration. Observation of a kilogram-scale oscillator near its quantum ground state. LIGO report LIGO-P070135-00-Z.
- [164] S. Gröblacher, J. B. Hertzberg, M. R. Vanner, S. Gigan, K. C. Schwab, and M. Aspelmeyer. Demonstration of an ultracold micro-optomechanical oscillator in a cryogenic cavity. *Nature Physics*, 5:485–488, 2009.
- [165] I. Favero, S. Stapfner, D. Hunger, P. Paulitschke, J. Reichel, H. Lorenz, E. M. Weig, and K. Karrai. Fluctuating nanomechanical systems in a high finesse optical microcavity. *Optics Express*, 17:12813–12820, 2009.
- [166] Q. Lin, J. Rosenberg, X. Jiang, K. J. Vahala, and O. Painter. Mechanical oscillation and cooling actuated by the optical gradient force. *arxiv:0905.2716*, 2009.
- [167] M. Eichenfield, J. Chan, R. M. Camacho, K. J. Vahala, and O. Painter. Optomechanical crystals. *arxiv:0906.1236*, 2009.
- [168] K. Vahala, M. Herrmann, S. Knünz, V. Batteiger, G. Saathoff, T. W. Hänsch, and Th. Udem. A phonon laser. *Nature Physics*, Advance online publication, 2009.

## BIBLIOGRAPHY

---

- [169] J. Hofer, A. Schliesser, and T. J. Kippenberg. Cavity optomechanics with ultra-high Q crystalline micro-resonators. *arXiv:0911.1178*, 2009.
- [170] A. Dorsel, J. D. McCullen, P. Meystre, E. Vignes, and H. Walther. Optical bistability and mirror confinement induced by radiation pressure. *Physical Review Letters*, 51(17):1550–1553, 1983.
- [171] A. Gozzini, F. Maccarrone, F. Mango, I. Longo, and S. Barbarino. Light-pressure bistability at microwave frequencies. *Journal of the Optical Society of America B*, 2:1841, 1985.
- [172] C. K. Law. Interaction between a moving mirror and radiation pressure: A Hamiltonian formulation. *Physical Review A*, 51:2537–2541, 1995.
- [173] V. Giovannetti and D. Vitali. Phase-noise measurement in a cavity with a movable mirror undergoing quantum Brownian motion. *Physical Review A*, 63:023812, 2001.
- [174] C. W. Gardiner and P. Zoller. *Quantum Noise*. Springer, 2004.
- [175] L. D. Landau and E. M. Lifshitz. *Theory of elasticity*, volume 7 of *Course of Theoretical Physics*. Pergamon Press, 2 edition, 1970.
- [176] J. R. Hutchinson. Axisymmetric flexural vibrations of a thick free circular plate. *Journal of Applied Mechanics*, 46:139–144, 1979.
- [177] J. R. Hutchinson. Vibrations of solid cylinders. *Journal of Applied Mechanics*, 47:901–907, 1980.
- [178] S.-I. Tamura. Vibrational cavity modes in a free cylindrical disk. *Physical Review B*, 79:054302, 2009.
- [179] A. E. H. Love. *A treatise on the mathematical theory of elasticity*. Cambridge University Press, 1906.
- [180] COMSOL Multiphysics GmbH. COMSOL. Göttingen, Germany.
- [181] T. J. Kippenberg, H. Rokhsari, T. Carmon, A. Scherer, and K. J. Vahala. Analysis of Radiation-Pressure Induced Mechanical Oscillation of an Optical Microcavity. *Physical Review Letters*, 95:033901, 2005.
- [182] T. J. Kippenberg, H. Rokhsari, and K. Vahala. Scanning probe microscopy of thermally excited mechanical modes of an optical microcavity. *arxiv:0602234*, 2006.
- [183] L. D. Landau and E. M. Lifshitz. *Fluid Mechanics*, volume 6 of *Course of Theoretical Physics*. Pergamon Press, 2 edition, 1987.

## BIBLIOGRAPHY

---

- [184] I. Wilson-Rae. Intrinsic dissipation in nanomechanical resonators due to phonon tunneling. *Physical Review B*, 77:245418, 2008.
- [185] R. O. Pohl, X. Liu, and E. Thompson. Low-temperature thermal conductivity and acoustic attenuation in amorphous solids. *Review of Modern Physics*, 74:991–1013, 2002.
- [186] J. Jäckle. On the ultrasonic attenuation in glasses at low temperature. *Zeitschrift für Physik*, 257:212–223, 1972.
- [187] R. Vacher, E. Courtens, and M. Foret. Anharmonic versus relaxational sound damping in glasses. II. Vitreous silica. *Physical Review B*, 72:214205, 2005.
- [188] U. Bartell and S. Hunklinger. Pressure dependence of the low-temperature acoustic anomalies in vitreous silica. *Journal de Physique Colloques*, 43:498, 1982.
- [189] D. Tielbürger, R. Merz, R. Ehrenfels, and S. Hunklinger. Thermally activated relaxation processes in vitreous silica: An investigation by Brillouin scattering at high pressures. *Physical Review B*, 45:2750–2760, 1992.
- [190] S. Hunklinger, W. Arnold, and S. Stein. Anomalous ultrasonic attenuation in vitreous silica at low temperatures. *Physics Letters*, 45A:311–312, 1973.
- [191] C. Zener. Internal friction in solids i. theory of internal friction in reeds. *Physical Review*, 52:230–235, 1937.
- [192] C. Zener. Internal friction in solids II. General theory of thermoelastic internal friction. *Physical Review*, 53:90–99, 1938.
- [193] K. L. Ekinici and M. L. Roukes. Nanoelectromechanical systems. *Review of Scientific Instruments*, 76:061101, 2005.
- [194] M. Pinard, Y. Hadjar, and A. Heidmann. Effective mass in quantum effects of radiation pressure. *European Physics Journal D*, 7:107–116, 1999.
- [195] S. Arnold, M. Khoshima, I. Teraoka, S. Holler, and F. Vollmer. Shift of whispering-gallery modes in microspheres by protein adsorption. *Optics Letters*, 28:272–274, 2003.
- [196] C. R. Locke and M. E. Tobar. Measurement of the strain-induced coefficient of permittivity of sapphire using whispering gallery modes excited in a high-Q acoustic sapphire oscillator. *Measurement Science and Technology*, 15:2145–2149, 2004.

## BIBLIOGRAPHY

---

- [197] V. Ilchenko, P. S. Volikov, V. L. Velichanski, V. L. Treussart, V. Lefèvre-Seguin, J.-M. Raimond, and S. Haroche. Strain-tunable high-Q optical microresonator. *Optics Communications*, 145:86–90, 1998.
- [198] R. W. Dixon. Photoelastic properties of selected materials and their relevance for applications to acoustic light modulators and scanners. *Journal of Applied Physics*, 38:5149, 1967.
- [199] A. Gillespie and F. Raab. Thermally excited vibrations of the mirrors of laser interferometer gravitational wave detectors. *Physical Review D*, 52:577–585, 1995.
- [200] L. D. Landau and E. M. Lifshitz. *Electrodynamics of continuous media*, volume 8 of *Course of Theoretical Physics*. Pergamon Press, 2 edition, 1984.
- [201] R. N. C. Pfeifer, T. A. Nieminen, N. R. Heckenberg, and H. Rubinsztein-Dunlop. Colloquium: Momentum of an electromagnetic wave in dielectric media. *Reviews of Modern Physics*, 79:1197–1216, 2007.
- [202] V. S. Ilchenko, M. L. Gorodetsky, and S. P. Vyatchanin. Coupling and tunability of optical whispering-gallery modes: a basis for coordinate meter. *Optics Communications*, 107:41–48, 1994.
- [203] A. B. Matsko, A. A. Savchenko, N. Yu, and L. Maleki. Whispering-gallery-mode resonators as frequency references. I. fundamental limitations. *Journal of the Optical Society of America B*, 24:1324–1335, 2007.
- [204] L. D. Landau and E. M. Lifshitz. *Statistical Physics*, volume 5 of *Course of Theoretical Physics*. Pergamon Press, 3rd edition, 1980.
- [205] M. L. Gorodetsky and I. S. Grudinin. Fundamental thermal fluctuations in microspheres. *Journal of the Optical Society of America B*, 21:697–705, 2004.
- [206] V. B. Braginsky, M. L. Gorodetsky, and S. P. Vyatchanin. Thermodynamical fluctuations and photo-thermal shot noise in gravitational wave antennae. *Physics Letters A*, 264:1–10, 1999.
- [207] V. B. Braginsky, M.L. Gorodetsky, and S.P. Vyatchanin. Thermo-refractive noise in gravitational wave antennae. *Physics Letters A*, 271:303–307, 2000.
- [208] H. P. Yuen and V. W. S. Chan. Noise in homodyne and heterodyne detection. *Optics Letters*, 8:177–179, 1983.

## BIBLIOGRAPHY

---

- [209] T. Briant, P.-F. Cohadon, A. Heidmann, and M. Pinard. Optomechanical characterization of acoustic modes in a mirror. *Physical Review A*, 68:033823, 2003.
- [210] T. W. Hänsch and B. Couillaud. Laser frequency stabilization by polarization spectroscopy of a reflecting reference cavity. *Optics Communications*, 35(3):441–444, 1980.
- [211] R. W. P. Drever, J. L. Hall, F. V. Kowalski, J. Hough, G. M. Ford, A. J. Munley, and H. Ward. Laser Phase and Frequency Stabilization Using an Optical Resonator. *Applied Physics B*, 31:97–105, 1983.
- [212] E. D. Black. An introduction to Pound-Drever-Hall laser frequency stabilization. *American Journal of Physics*, 69:79–87, 2001.
- [213] O. Arcizet. *Mesure optique ultrasensible et refroidissement par pression de radiation d'un micro-résonateur mécanique*. PhD thesis, Université Paris VI, 2007.
- [214] H. Rehbein, J. Harms, R. Schnabel, and K. Danzmann. Optical transfer functions of Kerr nonlinear cavities and interferometers. *Physical Review Letters*, 95:193001, 2005.
- [215] D. G. Blair, E. N. Ivanov, M. E. Tobar, P. J. Turner, F. van Kann, and I. S. Heng. High sensitivity gravitational wave antenna with parametric transducer readout. *Physical Review Letters*, 74:1908–1911, 1995.
- [216] B. D. Cuthbertson, M. E. Tobar, N. Ivanov, E, and D. G. Blair. Parametric back-action effects in a high-Q cryogenic sapphire transducer. *Review of Scientific Instruments*, 67:2435–2442, 1996.
- [217] C. R. Locke, M. E. Tobar, E. N. Ivanov, and D. G. Blair. Parametric interaction of the electric and acoustic fields in a sapphire monocrystal transducer with a microwave readout. *Journal of Applied Physics*, 84:6523–6527, 1998.
- [218] T. Carmon, H. Rokhsari, L. Yang, T. J. Kippenberg, and K. J. Vahala. Temporal behavior of radiation-pressure-induced vibrations of an optical microcavity phonon mode. *Physical Review Letters*, 94(22):223902, 2005.
- [219] H. Rokhsari, T. J. Kippenberg, T. Carmon, and K. J. Vahala. Radiation-pressure-driven micro-mechanical oscillator. *Optics Express*, 13:5293–5301, 2005.

## BIBLIOGRAPHY

---

- [220] H. Rokhsari, T. J. Kippenberg, T. Carmon, and K. J. Vahala. Theoretical and experimental study of radiation pressure-induced mechanical oscillations (parametric instability) in optical microcavities. *IEEE Journal of Selected Topics in Quantum Electronics*, 12(1):96–107, 2006.
- [221] M. Hossein-Zadeh, H. Rokhsari, A. Hajimiri, and K. J. Vahala. Characterization of a radiation-pressure-driven micromechanical oscillator. *Physical Review A*, 74:023813, 2006.
- [222] B. S. Sheard, M. B. Gray, C. M. Mow-Lowry, D. E. McClelland, and S. E. Whitcomb. Observation and characterization of an optical spring. *Physical Review A*, 69:051801, 2004.
- [223] M. Hossein-Zadeh and K. Vahala. Observation of optical spring effect in a microtoroidal optomechanical resonator. *Optics Letters*, 32(12):1611–1613, 2007.
- [224] F. Marquardt, J. G. E. Harris, and S. M. Girvin. Dynamical multistability induced by radiation pressure in high-finesse micromechanical optical cavities. *Physical Review Letters*, 96(10):103901, 2006.
- [225] T. Carmon, M. C. Cross, and K. J. Vahala. Chaotic quivering of micron-scaled on-chip resonators excited by centrifugal optical pressure. *Physical Review Letters*, 98:167203, 2007.
- [226] K. J. Vahala. Back-action limit of linewidth in an optomechanical oscillator. *Physical Review A*, 78:023832, 2008.
- [227] M. Ludwig, B. Kubala, and F. Marquardt. The optomechanical instability in the quantum regime. *New Journal of Physics*, 10:095013, 2008.
- [228] J. M. W. Milatz, J. J. van Zolingen, and B. B. van Iperen. The reduction in the Brownian motion in electrometers. *Physica*, 19:195–207, 1953.
- [229] J. M. W. Milatz and J. J. van Zolingen. The Brownian motion of electrometers. *Physica*, 19:181–194, 1953.
- [230] D. Möhl, G. Petrucci, L. Thorndahl, and S. van der Meer. Physics and technique of stochastic cooling. *Physics Reports*, 58:73–102, 1980.
- [231] D. M. Weld and A. Kapitulnik. Feedback control and characterization of a microlever using optical radiation pressure. *Applied Physics Letters*, 89:164102, 2006.

## BIBLIOGRAPHY

---

- [232] J. G. E. Harris, B. M. Zwickl, and A. M. Jayich. Stable, mode-matched, medium-finesse optical cavity incorporating a micromechanical cantilever. *Review of Scientific Instruments*, 78:013107, 2007.
- [233] W. Nowacki. *Dynamic problems of thermoelasticity*. Springer, 1975.
- [234] X. Zhou, O. Arcizet, A. Schliesser, R. Rivière, and T. Kippenberg. *in preparation*, 2009.
- [235] G. K. White. Thermal expansion of vitreous silica at low temperatures. *Physical Review Letters*, 34:204–205, 1975.
- [236] L. Diósi. Laser linewidth hazard in optomechanical cooling. *Physical Review A*, 78:021801, 2008.
- [237] P. Rabl, C. Genes, K. Hammerer, and M. Aspelmeyer. Phase-noise induced limitations in resolved-sideband cavity cooling of mechanical resonators. *arxiv:0903.1637*, 2009.
- [238] S. Stenholm. The semiclassical theory of laser cooling. *Reviews of Modern Physics*, 58:699–739, 1986.
- [239] A. A. Clerk, M. H. Devoret, S. M. Girvin, F. Marquardt, and R. J. Schoelkopf. Introduction to Quantum Noise, Measurement and Amplification. *arXiv:0810.4729*, 2008.
- [240] J. M. Dobrindt, I. Wilson-Rae, and T. J. Kippenberg. Parametric normal-mode splitting in cavity optomechanics. *Physical Review Letters*, 101:263602, 2008.
- [241] S. Gröblacher, K. Hammerer, M. R. Vanner, and M. Aspelmeyer. Observation of strong coupling between a micromechanical resonator and an optical cavity field. *Nature*, 460:724–727, 2009.
- [242] L. Tian and P. Zoller. Coupled ion-nanomechanical systems. *Physical Review Letters*, 93(26):266403, 2004.
- [243] I. Martin, A. Shnirman, L. Tian, and P. Zoller. Ground-state cooling of mechanical oscillators. *Physical Review B*, 69:125339, 2004.
- [244] M. P. Blencowe and E. Buks. Quantum analysis of a linear dc squid mechanical displacement detector. *Physical Review B*, 76:014511, 2007.
- [245] M. P. Blencowe, J. Imbers, and A. D. Armour. Dynamics of a nanomechanical resonator coupled to a superconducting single-electron transistor. *New Journal of Physics*, 7:236, 2005.

## BIBLIOGRAPHY

---

- [246] A. Naik, O. Buu, M. D. LaHaye, A. D. Armour, A. A. Clerk, M. P. Blencowe, and K. C. Schwab. Cooling a nanomechanical resonator with quantum back-action. *Nature*, 443:193–196, 2006.
- [247] T. C. Zhang, J. Ph. Poizat, et al. Quantum noise of free-running and externally-stabilized laser diodes. *Quantum and semiclassical optics*, 7:601–613, 1995.
- [248] J. D. Teufel, R. Donner, M. A. Castellanos-Beltran, J. W. Harlow, and K. W. Lehnert. Nanomechanical motion measured with precision beyond the standard quantum limit. *arxiv*, 2009.
- [249] Ch. Raab, J. Eschner, J. Bolle, H. Oberst, F. Schmidt-Kaler, and R. Blatt. Motional sidebands and direct measurement of the cooling rate in the resonance fluorescence of a single trapped ion. *Physical Review Letters*, 85(3):538, 2000.
- [250] R. G. Knobel and A. N. Cleland. Nanometre-scale displacement sensing using a single-electron transistor. *Nature*, 424:291–293, 2003.
- [251] M. D. LaHaye, O. Buu, B. Camarota, and K. C. Schwab. Approaching the quantum limit of a nanomechanical resonator. *Science*, 304:74–77, 2004.
- [252] K. Srinivasan and O. Painter. Optical fiber taper coupling and high-resolution wavelength tuning of microdisk resonators at cryogenic temperatures. *Applied Physics Letters*, 90:031114, 2007.
- [253] R. Rivière, O. Arcizet, A. Schliesser, G. Anetsberger, and T. Kippenberg. Design and operation of a cryogenic taper-coupling setup for cavity optomechanical experiments. 2010. (in preparation).
- [254] J. Hald and V. Ruseva. Efficient suppression of diode-laser phase noise by optical filtering. *Journal of the Optical Society of America B*, 22(11):2338–2344, 2005.
- [255] N. E. Flowers-Jacobs, D. R. Schmidt, and K. W. Lehnert. Intrinsic noise properties of atomic point contact displacement detectors. *Physical Review Letters*, 98:096804, 2007.
- [256] G. Rempe, R. J. Thomson, H. J. Kimble, and R. Lalezari. Measurement of ultralow losses in an optical interferometer. *Optics Letters*, 17:363–365, 1992.
- [257] S. S. Verbridge, D. F. Shapiro, H. G. Craighead, J. M. Parpia, and M. Jeevak. Macroscopic tuning of nanomechanics: Substrate bending for reversible control of frequency and quality factor of nanostring resonators. *Nano Letters*, 7:1728–1735, 2007.

## BIBLIOGRAPHY

---

- [258] V. V. Vassiliev, V. L. Velichansky, V. S. Ilchenko, M. L. Gorodetsky, L. Hollberg, and A. V. Yarovitsky. Narrow-line-width diode laser with a high-Q microsphere resonator. *Optics Communications*, 158(1-6):305–312, 1998.
- [259] A. M. Armani, R. P. Kulkarni, S. E. Fraser, R. C. Flagan, and K. J. Vahala. Label-free, single-molecule detection with optical microcavities. *Science*, 317:783–787, 2007.
- [260] B. Schröter, C. Reich, O. Arcizet, J. O. Rädler, B. Nickel, and T. J. Kippenberg. Chip based, lipid bilayer functionalized microresonators for label-free, ultra sensitive and time-resolved molecular detection. *submitted*, 2008.
- [261] Y.-S. Park and H. Wang. Resolved-sideband and cryogenic cooling of an optomechanical resonator. *Nature Physics*, 2009.
- [262] K. W. Murch, K. L. Moore, S. Gupta, and D. M. Stamper-Kurn. Observation of quantum-measurement backaction with an ultracold atomic gas. *Nature Physics*, 4:561–564, 2008.
- [263] F. Brennecke, S. Ritter, T. Donner, and T. Esslinger. Cavity optomechanics with a Bose-Einstein condensate. *Science*, 322:235–238, 2008.
- [264] V. S. Ilchenko, A. A. Savchenkov, J. Byrd, A. B. Solomatine, I. Matsko, D. Seidel, and L. Maleki. Crystal quartz optical whispering-gallery resonators. *Optics Letters*, 33:1569–1571, 2008.
- [265] I. Grudinin, V. S. Ilchenko, and L. Maleki. Ultrahigh optical Q factors of crystalline resonators in the linear regime. *Physical Review A*, 74:063806, 2006.
- [266] R. Nawrodt, A. Zimmer, T. Koettig, S. Nietzsche, M. Thürk, M. Vodel, and P. Seidel. High mechanical Q-factor measurements on calcium fluoride at cryogenic temperatures. *European Physical Journal - Applied Physics*, 38:53–59, 2007.
- [267] S. S. Verbridge, H. G. Craighead, and J. M. Parpia. A megahertz nanomechanical resonator with room temperature quality factor over a million. *Applied Physics Letters*, 92:013112, 2008.
- [268] M. Fleischhauer, A. Imamoglu, and J. P. Marangos. Electromagnetically induced transparency: Optics in coherent media. *Review of Modern Physics*, 77:633–673, 2005.
- [269] P. W. Milonni. *Fast light, slow light and left-handed light*. Taylor and Francis, 2005.

## BIBLIOGRAPHY

---

- [270] M. M. Kash, V. A. Sautenkov, A. S. Zibrov, L. Hollberg, G. R. Welch, M. D. Lukin, Y. Rostovtsev, E. S. Fry, and M. O. Scully. Ultraslow group velocity and enhanced nonlinear optical effects in a coherently driven hot atomic gas. *Physical Review Letters*, 82:5229–5232, 1999.
- [271] L. V. Hau, S. E. Harris, Z. Dutton, and C. H. Behroozi. Light speed reduction to 17 metres per second in an ultracold atomic gas. *Nature*, 397:594–598, 1999.
- [272] M. Fleischhauer and M. D. Lukin. Dark-state polaritons in electromagnetically induced transparency. *Physical Review Letters*, 84:5094–5097, 2000.
- [273] C. Liu, Z. Dutton, C.H. Behroozi, and L.V. Hau. Observation of coherent optical information storage in an atomic medium using halted light pulses. *Nature*, 409:490–493, 2001.
- [274] D. F. Phillips, A. Fleischhauer, A. Mair, R. L. Walsworth, and M. D. Lukin. Storage of light in atomic vapor. *Physical Review Letters*, 86:783–786, 2001.
- [275] T. W. Hänsch. Passion for Precision (Nobel Lecture). *ChemPhysChem*, 7:1170–1187, 2006.
- [276] S. T. Cundiff and J. Ye. Colloquium: Femtosecond optical frequency combs. *Reviews of Modern Physics*, 75(1):325, 2003.
- [277] Th. Udem, R. Holzwarth, and T. W. Hänsch. Optical frequency metrology. *Nature*, 416:233–237, 2002.
- [278] J. R. Jones, K. D. Moll, M. J. Thorpe, and J. Ye. Phase-coherent frequency combs in the vacuum ultraviolet via high-harmonic generation inside a femtosecond enhancement cavity. *Physical Review Letters*, 94:193201, 2005.
- [279] C. Gohle, Th. Udem, M. Herrmann, J. Rauschenberger, R. Holzwarth, H. A. Schuessler, F. Krausz, and T. W. Hänsch. A frequency comb in the extreme ultraviolet. *Nature*, 436:234–237, 2005.
- [280] U. Keller. Recent developments in compact ultrafast lasers. *Nature*, 424(6950):831–838, 2003.
- [281] J. N. Eckstein, A. I. Ferguson, and T. W. Hänsch. High-resolution two-photon spectroscopy with picosecond light pulses. *Physical Review Letters*, 40:847–850, 1978.

## BIBLIOGRAPHY

---

- [282] Th. Udem, J. Reichert, R. Holzwarth, and T. W. Hänsch. Absolute optical frequency measurement of the cesium D<sub>1</sub> line with a mode-locked laser. *Physical Review Letters*, 82:3568–3571, 1999.
- [283] D. J. Jones, S. A. Diddams, J. K. Ranka, A. Stentz, R. S. Windeler, J. L. Hall, and S. T. Cundiff. Carrier-envelope phase control of femtosecond mode-locked lasers and direct optical frequency synthesis. *Science*, 288:635–639, 2000.
- [284] R. Holzwarth, T. Udem, T. W. Hänsch, J. C. Knight, W. J. Wadsworth, and P. S. J. Russell. Optical frequency synthesizer for precision spectroscopy. *Physical Review Letters*, 85:2264–2267, 2000.
- [285] J. Reichert, M. Niering, R. Holzwarth, M. Weitz, Th. Udem, and T. W. Hänsch. Phase coherent vacuum-ultraviolet to radio frequency comparison with a mode-locked laser. *Physical Review Letters*, 84:3232–3235, 2000.
- [286] S. A. Diddams, D. J. Jones, J. Ye, S. T. Cundiff, J. L. Hall, J. K. Ranka, R. S. Windeler, R. Holzwarth, T. Udem, and T. W. Hänsch. Direct link between microwave and optical frequencies with a 300 THz femtosecond laser comb. *Physical Review Letters*, 84:5102–5105, 2000.
- [287] F. Keilmann, C. Gohle, and R. Holzwarth. Time-domain mid-infrared frequency-comb spectrometer. *Optics Letters*, 29:1542–1544, 2004.
- [288] A. Schliesser, M. Brehm, F. Keilmann, and D. W. van der Weide. Frequency-comb infrared spectrometer for rapid, remote chemical sensing. *Optics Express*, 13:9029–9038, 2005.
- [289] S. A. Diddams, L. Hollberg, and V. Mbele. Molecular fingerprinting with the resolved modes of a femtosecond laser frequency comb. *Nature*, 445:627–630, 2007.
- [290] M. J. Thorpe, K. D. Moll, R. J. Jones, B. Safdi, and J. Ye. Broadband cavity ringdown spectroscopy for sensitive and rapid molecular detection. *Science*, 311(5767):1595–1599, 2006.
- [291] H. Schnatz, B. Lipphardt, J. Helmcke, F. Riehle, and G. Zinner. First phase-coherent frequency measurement of visible radiation. *Physical Review Letters*, 76:18–21, 1996.
- [292] T. Udem, A. Huber, B. Gross, J. Reichert, M. Prevedelli, M. Weitz, and T. W. Hänsch. Phase-coherent measurement of the hydrogen 1s-2s transition frequency with an optical frequency interval divider chain. *Physical Review Letters*, 79:2646–2649, 1997.

## BIBLIOGRAPHY

---

- [293] M. Kourogi, K. Nakagawa, and M. Ohtsu. Wide-span optical frequency comb generator for accurate optical frequency difference measurement. *Ieee Journal Of Quantum Electronics*, 29:2693–2701, 1993.
- [294] S. A. Diddams, L.-S. Ma, J. Ye, and J. L. Hall. Broadband optical frequency comb generation with a phase-modulated parametric oscillator. *Optics Letters*, 24:1747–1749, 1999.
- [295] J. Ye. *Ultrasensitive High-Resolution Laser Spectroscopy and its Application to Optical Frequency Standards*. PhD thesis, University of Colorado, 1997.
- [296] Th. Udem, J. Reichert, R. Holzwarth, and T. W. Hänsch. Accurate measurement of large optical frequency differences with a mode-locked laser. *Optics Letters*, 24:881–883, 1999.
- [297] D.N. Klyshko. *Photons and Nonlinear Optics*. Gordon and Breach Science Publishers, 1988.
- [298] K. J. Vahala. Optical microcavities. *Nature*, 424(6950):839–846, 2003.
- [299] A. A. Savchenkov, A. B. Matsko, D. Strekalov, M. Mohageg, V. S. Ilchenko, and L. Maleki. Low threshold optical oscillations in a whispering gallery mode CaF<sub>2</sub> resonator. *Physical Review Letters*, 93:243905, 2004.
- [300] J. Ye and S. T. Cundiff. *Femtosecond Optical Frequency Comb: Principle, Operation and Applications*. Springer, 2005.
- [301] P. Kubina, P. Adel, F. Adler, G. Grosche, T. W. Hansch, R. Holzwarth, A. Leitenstorfer, B. Lipphardt, and H. Schnatz. Long term comparison of two fiber based frequency comb systems. *Optics Express*, 13:904–909, 2005.
- [302] J. Reichert, R. Holzwarth, Th. Udem, and T.W. Hänsch. Measuring the frequency of light with mode-locked lasers. *Optics Communications*, 172:59–68, 1999.
- [303] A. B. Matsko, A. A. Savchenkov, D. Strekalov, V. S. Ilchenko, and L. Maleki. Optical hyperparametric oscillations in a whispering-gallery-mode resonator: Threshold and phase diffusion. *Physical Review A*, 71:033804, 2005.
- [304] I. H. Agha, Y. Okawach, M. A. Foster, J. E. Sharping, and A. L. Gaeta. Four-wave-mixing parametric oscillations in dispersion-compensated high-Q silica microspheres. *Physical Review A*, 76:043837, 2007.